



**Iwona Bernacka-Wojcik**

Mestrado em Ciência dos Materiais

## **Design and development of a microfluidic platform for use with colorimetric gold nanoprobe assays**

Dissertação para obtenção do Grau de Doutor  
em Nanotecnologias e Nanociências

Orientador: Doutor Rodrigo Ferrão de Paiva Martins, Professor  
Catedrático, Faculdade de Ciências e Tecnologia da  
Universidade Nova de Lisboa

Co-orientador: Doutor Pedro Viana Baptista, Professor Associado com  
Agregação, Faculdade de Ciências e Tecnologia da  
Universidade Nova de Lisboa

Doutor Hugo Águas, Professor Auxiliar, Faculdade de  
Ciências e Tecnologia da Universidade Nova de Lisboa

Júri:

Presidente: Doutora Ana Maria Félix Trindade Lobo, Professora Catedrática da  
Faculdade de Ciências e Tecnologia da Universidade Nova de Lisboa

Arguentes: Doutor João Lemos Pinto, Professor Catedrático da Universidade de  
Aveiro

Doutora Graça Maria Henriques Minas, Professora Associada da  
Escola de Engenharia da Universidade do Minho

Vogais: Doutor Rodrigo Ferrão de Paiva Martins, Professor Catedrático da  
Faculdade de Ciências e Tecnologia da Universidade Nova de Lisboa  
Doutora Elvira Maria Correia Fortunato, Professora Catedrática da  
Faculdade de Ciências e Tecnologia da Universidade Nova de Lisboa  
Doutor Adélio Miguel Magalhães Mendes, Professor Associado com  
Agregação da Faculdade de Engenharia da Universidade do Porto  
Doutor Pedro Miguel Ribeiro Viana Baptista, Professor Associado com  
Agregação da Faculdade de Ciências e Tecnologia da Universidade  
Nova de Lisboa

Doutora Maria Goreti Ferreira Sales, Professora Adjunta do Instituto  
Superior de

Engenharia do Porto do Instituto Politécnico do Porto

Doutor Abel González Oliva, Investigador Auxiliar do Instituto de  
Tecnologia Química

e Biológica António Xavier da Universidade Nova de Lisboa



**FACULDADE DE  
CIÊNCIAS E TECNOLOGIA  
UNIVERSIDADE NOVA DE LISBOA**

**Março de 2014**



**Iwona Bernacka-Wojcik**

Mestrado em Ciência dos Materiais

## **Design and development of a microfluidic platform for use with colorimetric gold nanoprobe assays**

Dissertação para obtenção do Grau de Doutor  
em Nanotecnologias e Nanociências

Orientador: Doutor Rodrigo Ferrão de Paiva Martins, Professor  
Catedrático, Faculdade de Ciências e Tecnologia da  
Universidade Nova de Lisboa

Co-orientador: Doutor Pedro Viana Baptista, Professor Associado com  
Agregação, Faculdade de Ciências e Tecnologia da  
Universidade Nova de Lisboa

Doutor Hugo Águas, Professor Auxiliar, Faculdade de  
Ciências e Tecnologia da Universidade Nova de Lisboa

Júri:

Presidente: Doutora Ana Maria Félix Trindade Lobo, Professora Catedrática da  
Faculdade de Ciências e Tecnologia da Universidade Nova de Lisboa

Arguentes: Doutor João Lemos Pinto, Professor Catedrático da Universidade de  
Aveiro

Doutora Graça Maria Henriques Minas, Professora Associada da  
Escola de Engenharia da Universidade do Minho

Vogais: Doutor Rodrigo Ferrão de Paiva Martins, Professor Catedrático da  
Faculdade de Ciências e Tecnologia da Universidade Nova de Lisboa  
Doutora Elvira Maria Correia Fortunato, Professora Catedrática da  
Faculdade de Ciências e Tecnologia da Universidade Nova de Lisboa  
Doutor Adélio Miguel Magalhães Mendes, Professor Associado com  
Agregação da Faculdade de Engenharia da Universidade do Porto  
Doutor Pedro Miguel Ribeiro Viana Baptista, Professor Associado com  
Agregação da Faculdade de Ciências e Tecnologia da Universidade  
Nova de Lisboa

Doutora Maria Goreti Ferreira Sales, Professora Adjunta do Instituto  
Superior de

Engenharia do Porto do Instituto Politécnico do Porto

Doutor Abel González Oliva, Investigador Auxiliar do Instituto de  
Tecnologia Química

e Biológica António Xavier da Universidade Nova de Lisboa



**FACULDADE DE  
CIÊNCIAS E TECNOLOGIA  
UNIVERSIDADE NOVA DE LISBOA**

**Março de 2014**





Design and development of a microfluidic platform for use with colorimetric gold nanoprobe assays

Copyright: Iwona Bernacka-Wojcik  
FCT/UNL e UNL

A Faculdade de Ciências e Tecnologia e a Universidade Nova de Lisboa têm o direito, perpétuo e sem limites geográficos, de arquivar e publicar esta dissertação através de exemplares impressos reproduzidos em papel ou de forma digital, ou por qualquer outro meio conhecido ou que venha a ser inventado, e de a divulgar através de repositórios científicos e de admitir a sua cópia e distribuição com objectivos educacionais de investigação, não comerciais, desde que seja dado crédito ao autor e editor.



## Acknowledgements

*I am very grateful to all the people that contributed and supported me directly and indirectly during this PhD studies.*

*To Prof. Rodrigo Martins, for enabling me to carry a new research area within the group, for providing all necessary facilities, for possibility to present the results on international meetings and for all provided support.*

*To Prof. Pedro Viana Baptista, for your constructive critics, possibility to work with your truly golden DNA detection method, for showing wider aspect of the issues and for all your help.*

*To Prof. Hugo Águas, for the countless emails and hours of discussions and personal support.*

*To Prof. Elvira Fortunato for the ideas, effort to provide all needed help, time spent for papers improvement.*

*To co-workers that provided me their expertise in various areas: Dr. Paulo Lopes, Dr. Abel Oliva, Dr. Loic Hilliou, Dr. Sergej Filonovich, Dr. Rohan Seneedera, for all the discussions and co-operation.*

*To my co-workers, MSc. David Barata, MSc. Fabio Pereira, Dr. Leonardo Silva, BSc. Teresa Lobato, MSc. Pedro Urbano Alves, MSc. Ana Catarina Vaz and MSc. Iracema Martinho, for brainstorming, for your ideas, for sharing the joy of successful experiments and cheering after the worse ones.*

*To my co-workers from Life Science Department: MSc. Bruno Veigas, MSc. Fabio Carlos and Dr. Gonçalo Doria, for sharing with me your gold and for fruitful discussions and cooperation.*

*To all the members from MEON group, for the help and support that I received from you during the PhD studies, specially to MSc. António Vicente, MSc. Mafalda Costa, Dr. Daniela Gomes, Dr. Luis Pereira, Dr. Pedro Barquinha, MSc. Sonia Pereira, MSc. Alexandra Gonçalves, Dr. Rita Branquinho, Dr. Gonçalo Gonçalves, Dr. Tito Busani, Dr. Joana Vaz Pinto, MSc. Raquel Barros and Dr. Ana Pimental.*

*To Ricardo Ferreira, Carlos Alcobia, Salomão Lopes, Manuel Quintela, for the professional help with technical tasks.*

*To Carla Saldanha, MSc. Paulo Manteigas, Sara Oliveira, Susana Mendes, Valéria Gomes, Patricia Carrão and Sonia Seixas, for the help with administrative issues.*

*I would like to thank Portuguese Science Foundation (FCT-MCTES) for financing my work through the PhD grant (SFRH/BD/44258/2008) and to “SMART-EC” project.*

*The PhD studies time was made enjoyable in large part due to the many friends that became a part of my life.*

*To Dr. Vitor Figueiredo, MSc. Jonas Deuermeier, MSc. Ricardo Correia, MSc. Kasra Kardarian, MSc. Bertrand Soulé, MSc. Paolo Sberna, MSc. Michele Pavan, MSc. Diana Gaspar, MSc. Javier Contreras, Dr. Andriy Lyubchyk and MSc. Ana Baptista, for the huge doses of humour and our open-minded meetings.*

*To Katarzyna Karpowicz-Osowska, Maciej Osowski Maria Osowska and Iza Stapor, for your friendship that was really priceless during this PhD studies. You are like family to me.*

*To Joana Kulwikowska, Marcin Kulwikowski, Madalena Kulwikowska, Małgorzata Zakrzewska, João Franco, Ines Franco, Sara Franco, Adalgiza Fonseca, Błażej Nowacki, José Reis, Julia Nunes, Pedro Nunes, Fernando Belo, Marina Filonovich and Nastia Filonovich, for the good time that we spent together and for your support.*

*I would like to take this opportunity to express my gratitude to those that make my life better and more beautiful before I started this stage of my life.*

*To Dominika Dyminska, Ewelina Kaczmarczyk and Katarzyna Maksymow for being my beloved soul-mates.*

*To people that play very special role in my life: Roksana Jamska, Anna Waksmundzka, Katarzyna Salwa, Monika Lefek, Agata Gądek, Mari Carmen Guisande, Moncho Fernández, Iris Fernández Guisande, Isabel Iglesias, Maria Montero, Ewa Heda, Joanna Winnicka-Bilska, Rafał Szymkowiak, Andrzej Kania, Wiesław Michalek, Oliwia Puczyłowska, Agata Stępień and Sebastian Jary. I am very grateful that I have met you.*

*To whole my wonderful family, you are so many that I have no space to name you all! For the way that you all support each other and for our fun together.*

*To all the Wójciks, my in-laws, for making me part of the family.*

*If I have forgotten anyone in the above then I am sincerely sorry, please remind me the first chance you get.*

*There are a few people for whom thanks seem never enough.*

*To my parents, Maria Bernacka and Andrzej Bernacki: Mum and Dad, you keep surprising me with the greatness of your love. I cannot find words to express my gratitude...*

*Ola, “my little sis”, for being my person and for your special skills in cheering me up.*

*Paweł, for your love, friendship and support in the difficult moments. For your passion that you put in nearly everything you do, for sharing with me your talents that make my life much more colorful and better.*

*Aniela, I thank you for melting my heart, for coloring my life, for your juicy kisses and re-discovering the world beauty with you. You are my Miracle!*

*The last, but not the least,*

*‘Thank You just for being  
for the impossibility of grasping You with our too nervous hearts  
for our doing nothing for You, but everything thanks to You’*

*Jan Twardowski*

## Resumo

Devido à importância das análises de ADN, existe uma necessidade premente de desenvolver biossensores capazes de as tornar disponíveis no mercado a baixo custo, de forma a que sejam acessíveis a todos. Assim, o objectivo desta tese de Doutoramento é o de otimizar um biosensor colorimétrico de ADN com base em nanossondas de ouro partindo da tecnologia desenvolvida e existente no CEMOP.

Numa primeira fase, conseguiu-se reduzir o custo do biossensor, substituindo os fotodetectores de Si por fotodetectores que utilizam  $\text{TiO}_2$  como material semicondutor (células sensibilizadas por corante). Para além disso, o novo método de microfabricação, utilizando a tecnologia de impressão, desenvolvida para este trabalho, permitiu o aumento da área superficial do fotodetector, bem como a redução de custos na fabricação do biossensor.

Numa segunda fase procedeu-se à optimização do biossensor de ADN utilizando técnicas de microfluidica que permitiram a sua miniaturização, um menor consumo de amostras/reagentes e um aumento do desempenho e funcionalidade do sistema ao integrar diferentes componentes numa única plataforma. O percurso óptico foi estendido de forma a permitir uma leitura ao longo do microcanal, e a luz utilizada para a detecção óptica é transmitida através de fibras ópticas. Os chips de microfluidica foram fabricados em PDMS a partir de moldes em SU-8. Conseguiu-se obter estruturas com elevados rácios ( $\sim 13$ ) e paredes lisas e verticais. Os testes efectuados com nano-sondas de ouro na plataforma aqui descrita permitiram a detecção de *Mycobacterium tuberculosis* usando 3  $\mu\text{l}$  de solução de ADN, um volume 20 vezes menor que o mencionado no último estado da arte. A plataforma bio-microfluidica foi optimizada em termos de custo, processamento de sinal eléctrico e sensibilidade à variação de cor, tendo sido verificada uma melhoria de 160% na análise colorimétrica de nano-sondas de ouro.

Numa terceira fase, foram incorporadas no chip microlentes com o objectivo de colimar a luz de saída da fibra óptica na câmara de detecção e focá-la no núcleo da fibra óptica de colecção da luz. Isto permitiu aumentar em 6 vezes a razão entre o sinal e o ruído do dispositivo. Esta plataforma optimizada permitiu a detecção de um polimorfismo de nucleótido único associado com o risco de obesidade (gene *FTO*), usando concentrações de ADN alvo abaixo do limite de detecção das microplacas de leitura convencionais (15  $\text{ng}/\mu\text{l}$ ) e volumes 10 vezes menores de solução (3  $\mu\text{l}$ ). A combinação das propriedades únicas das nanossondas de ouro com a plataforma de microfluidica resultou num sensor preciso para a detecção de nucleótidos de polimorfismo únicos usando baixos volumes de solução e sem a necessidade de funcionalizar a plataforma ou de utilizar instrumentação sofisticada.

Finalmente, para permitir a mistura dos reagentes dentro do chip, foi desenvolvido e optimizado um micro-misturador passivo em PDMS. O dispositivo foi optimizado para a obtenção da maior

eficiência de mistura, menor quebra de pressão e menor distância de mistura. Para  $Re = 0.1$ , obteve-se valores de 80%, 33 Pa e 2.5 mm, respectivamente, satisfazendo os requisitos para a aplicação da plataforma microfluidica em análise de ADN.

*Palavras Chave: microfluidos, biosensor de ADN, PDMS, SU-8, fibras ópticas, micromixing,  $TiO_2$ , fotodetector, nanopartículas de ouro*

## Abstract

Due to the importance and wide applications of the DNA analysis, there is a need to make genetic analysis more available and more affordable. As such, the aim of this PhD thesis is to optimize a colorimetric DNA biosensor based on gold nanoprobe developed in CEMOP by reducing its price and the needed volume of solution without compromising the device sensitivity and reliability, towards the point of care use.

Firstly, the price of the biosensor was decreased by replacing the silicon photodetector by a low cost, solution processed  $\text{TiO}_2$  photodetector. To further reduce the photodetector price, a novel fabrication method was developed: a cost-effective inkjet printing technology that enabled to increase  $\text{TiO}_2$  surface area.

Secondly, the DNA biosensor was optimized by means of microfluidics that offer advantages of miniaturization, much lower sample/reagents consumption, enhanced system performance and functionality by integrating different components. In the developed microfluidic platform, the optical path length was extended by detecting along the channel and the light was transmitted by optical fibres enabling to guide the light very close to the analysed solution. Microfluidic chip of high aspect ratio ( $\sim 13$ ), smooth and nearly vertical sidewalls was fabricated in PDMS using a SU-8 mould for patterning. The platform coupled to the gold nanoprobe assay enabled detection of *Mycobacterium tuberculosis* using 3  $\mu\text{l}$  on DNA solution, i.e. 20 times less than in the previous state-of-the-art.

Subsequently, the bio-microfluidic platform was optimized in terms of cost, electrical signal processing and sensitivity to colour variation, yielding 160% improvement of colorimetric AuNPs analysis. Planar microlenses were incorporated to converge light into the sample and then to the output fibre core increasing 6 times the signal-to-losses ratio. The optimized platform enabled detection of single nucleotide polymorphism related with obesity risk (*FTO*) using target DNA concentration below the limit of detection of the conventionally used microplate reader (i.e. 15  $\text{ng}/\mu\text{l}$ ) with 10 times lower solution volume (3  $\mu\text{l}$ ). The combination of the unique optical properties of gold nanoprobe with microfluidic platform resulted in sensitive and accurate sensor for single nucleotide polymorphism detection operating using small volumes of solutions and without the need for substrate functionalization or sophisticated instrumentation.

Simultaneously, to enable on chip reagents mixing, a PDMS micromixer was developed and optimized for the highest efficiency, low pressure drop and short mixing length. The optimized device shows 80% of mixing efficiency at  $Re = 0.1$  in 2.5 mm long mixer with the pressure drop of 6 Pa, satisfying requirements for the application in the microfluidic platform for DNA analysis.

*Keywords: microfluidics, DNA biosensor, PDMS, SU-8, optical fibres, micromixing,  $\text{TiO}_2$  photodetector, gold nanoparticles*





## Table of contents

<b>Chapter 1. General introduction .....</b>	<b>5</b>
<b>Summary.....</b>	<b>5</b>
<b>1.1. Biosensors .....</b>	<b>5</b>
<b>1.2. DNA biosensors based on gold nanoparticles.....</b>	<b>6</b>
<b>1.3. Microfluidic devices .....</b>	<b>10</b>
<b>1.4. Fluid behaviour at microscale.....</b>	<b>12</b>
<b>1.5. Microfluidics materials.....</b>	<b>14</b>
1.5.1. Silicon and glass .....	15
1.5.2. Polymers .....	15
1.5.3. Paper .....	20
1.5.4. Materials overview .....	21
<b>1.6. Nanofluidics .....</b>	<b>22</b>
<b>1.7. Miniaturisation of absorbance-based detection .....</b>	<b>25</b>
<b>1.8. Motivation and objectives .....</b>	<b>27</b>
<b>1.9. Thesis outline.....</b>	<b>28</b>
<b>1.10. List of publications.....</b>	<b>29</b>
<b>1.11. List of presentations.....</b>	<b>29</b>
 <b>Chapter 2. Fabrication and characterisation techniques .....</b>	 <b>37</b>
<b>Summary.....</b>	<b>37</b>
<b>2.1. Fabrication techniques .....</b>	<b>37</b>
2.1.1. “Doctor blade” method.....	37
2.1.2. Inkjet printing .....	38
2.1.3. Spin coating .....	40
2.1.4. Photolithography.....	40
2.1.5. Replica moulding soft-lithography .....	42
<b>2.2. Chip fabrication .....</b>	<b>43</b>
2.2.1. Before the SU-8 processing .....	45
2.2.2. SU-8 spin coating .....	45
2.2.3. Soft bake .....	46
2.2.4. Exposure .....	47
2.2.5. Post bake.....	54
2.2.6. Development.....	54
2.2.7. Casting of PDMS mould.....	55
2.2.8. Casting of epoxy mould.....	56
2.2.9. Casting of PDMS chips .....	56
2.2.10. Sealing of PDMS chips.....	57
<b>2.3. Characterisation techniques.....</b>	<b>60</b>
2.3.1. Scanning electron microscopy .....	62

2.3.2. Spectrophotometry.....	62
2.3.3. Stylus profilometry .....	64
2.3.4. Determination of features' thickness using optical microscopy .....	65
2.3.5. Confocal scanning microscopy .....	66
<b>Chapter 3. Inkjet printed and “doctor blade” TiO<sub>2</sub> photodetectors for DNA biosensors</b>	
.....	<b>71</b>
<b>Summary.....</b>	<b>71</b>
<b>3.1. Introduction.....</b>	<b>71</b>
<b>3.2. Experimental section .....</b>	<b>74</b>
3.2.1. Fabrication of photodetectors .....	74
3.2.2. Characterisation of photodetectors .....	77
3.2.3. Preparation of DNA-functionalized gold nanoparticles .....	77
3.2.4. Detection procedure.....	77
<b>3.3. Results and discussion .....</b>	<b>78</b>
3.3.1. Photodetectors' fabrication and characterisation.....	78
3.3.2. Colorimetric AuNPs analysis.....	80
3.3.3. Detection of DNA from <i>M. tuberculosis</i> .....	81
3.3.4. Optimization of inkjet printed TiO <sub>2</sub> photodetector .....	82
<b>3.4. Conclusions.....</b>	<b>87</b>
<b>Chapter 4. Bio-microfluidic platform for gold nanoprobe based DNA detection—</b>	
<b>    application to <i>Mycobacterium tuberculosis</i>.....</b>	<b>93</b>
<b>Summary.....</b>	<b>93</b>
<b>4.1. Introduction.....</b>	<b>93</b>
<b>4.2. Experimental details .....</b>	<b>99</b>
4.2.1. Fabrication of macro-machined PDMS containers.....	99
4.2.2. Fabrication of microfluidic chip .....	99
4.2.3. Opto-electronic set-up .....	100
4.2.4. Sample DNA preparation .....	101
4.2.5. Au-nanoprobe synthesis and characterisation.....	102
4.2.6. Au-nanoprobe colorimetric assay .....	102
4.2.7. Detection procedure and analysis .....	103
<b>4.3. Results and discussion .....</b>	<b>103</b>
4.3.1. Development of macro-machined PDMS containers .....	103
4.3.2. Microfluidic chip development.....	108
4.3.3. Optical performance .....	113
4.3.4. <i>M. tuberculosis</i> detection via the microfluidic platform.....	115
<b>4.4. Conclusions.....</b>	<b>118</b>
<b>Chapter 5. Single nucleotide polymorphism detection using gold nanoprobe and</b>	
<b>    optimized bio-microfluidic platform with embedded microlenses.....</b>	<b>125</b>

<b>Summary.....</b>	<b>125</b>
<b>5.1. Introduction.....</b>	<b>125</b>
<b>5.2. Experimental details .....</b>	<b>127</b>
5.2.1. Fabrication of microfluidic chip .....	127
5.2.2. Opto-electronic set-up .....	128
5.2.3. Sample DNA preparation .....	129
5.2.4. Au-nanoprobe synthesis and characterisation.....	129
5.2.5. Au-nanoprobe colorimetric assay .....	129
5.2.6. Detection procedure and analysis .....	130
<b>5.3. Results and discussion .....</b>	<b>130</b>
5.3.1. Set-up optimization.....	130
5.3.2. Microlenses design and fabrication .....	132
5.3.3. Effect of microlenses on colorimetric AuNPs analysis .....	137
5.3.4. SNP detection using the optimized system.....	139
<b>5.4. Conclusions.....</b>	<b>144</b>
 <b>Chapter 6. Experimental optimization of a passive planar rhombic micromixer with                   obstacles for effective mixing in a short channel length .....</b>	 <b>149</b>
<b>Summary.....</b>	<b>149</b>
<b>6.1. Introduction.....</b>	<b>149</b>
<b>6.2. Experimental details .....</b>	<b>153</b>
6.2.1. Fabrication of microfluidic device.....	153
6.2.2. Assessment of mixing efficiency.....	154
6.2.3. Pressure drop measurements.....	155
6.2.4. Statistical analysis.....	155
<b>6.3. Results and discussion .....</b>	<b>156</b>
6.3.1. Mixer design and fabrication .....	156
6.3.2. Mixing efficiency and mechanism.....	158
6.3.3. Pressure drop .....	162
6.3.4. Statistical analysis of the results.....	165
<b>6.4. Conclusions.....</b>	<b>171</b>
 <b>Chapter 7. General conclusions .....</b>	 <b>177</b>
<b>Summary.....</b>	<b>177</b>
<b>7.1. Conclusions.....</b>	<b>177</b>
<b>7.2. Future work.....</b>	<b>179</b>
7.2.1. Integration of microfluidic waveguides to facilitate the chip exchange .....	179
7.2.2. Integration of the optical detection chip with the micromixer.....	180
7.2.3. Miniaturization of further laboratory tasks towards “bleed and read” device .....	180
 <b>Appendix 1. SU-8 run sheet for 125 <math>\mu</math>m thick layer.....</b>	 <b>183</b>

**References ..... 185**

## List of Figures

Fig. 1.1. Schematic representation of biosensor principle: specific interaction of bioreceptor with analyte results in physical or chemical change analysed by transducer and then converted into measurable signal. Adapted from (Martins et al. 2013).....	6
Fig. 1.2. Colours of gold nanoparticle solutions; corresponding absorption spectra and transmission electron micrographs showing their inter-particles distance: (A) monodispersed AuNPs solution and (B) aggregated AuNPs solution. Adapted from (Schofield et al. 2007).....	7
Fig. 1.3. Principle of colorimetric DNA detection method based on non-cross-linking hybridisation of Au-nanoprobe at high salt concentration (Baptista et al. 2005). After salt addition, only the presence of complementary DNA target prevents the Au-nanoprobe aggregation remaining the red colour of the solution. ....	8
Fig. 1.4. (A) Colour wheel presenting the relationship between a colour of object and its absorption of light. (B) Schematic representation of biosensor used for detection of colorimetric changes of DNA solution. The light from green LED is transmitted through the solution and then is detected by photodetector. The light allowed through the solution reaches the sensor that generates a photocurrent. ....	9
Fig. 1.5. Portable, integrated biosensor for colorimetric DNA detection based on non-cross-linking aggregation of Au-nanoprobes. The light from RBGA LED is transmitted through the solution and then is detected by amorphous/nanocrystalline silicon photodetector generating photocurrent. The analog signal is filtered, amplified, converted to a digital signal and transmitted to a computer via a serial communication protocol. Adapted from (Silva et al. 2011).....	10
Fig. 1.6. Lab-on-chip concept: scaling down of several laboratory processes on a chip-format ( <a href="http://Lab-on-Chip.gene-quantification.info">http://Lab-on-Chip.gene-quantification.info</a> retrieved in 2014.03).....	11
Fig. 1.7. Evolution of the number of (A) publications and (B) citations in the microfluidics field indexed within Web of Science Core Collections from 2004 to 2013 (query: ‘microfluidics’). The number of publications increases linearly with time, while the citations’ number—exponentially.	12
Fig. 1.8. (A) Reynolds’ sketch of his 1883 experiment that allowed observation and explanation of various flow regimes: a dye-coloured water was injected with various velocities into clear water. (B) Laminar flow: smooth, ordered with constant fluid velocity.(C) Transitional flow: intermittent pulses of turbulence. (D) Turbulent flow: disorganised with the formation of eddy current. Retrieved from (Reynolds 1883). ....	13
Fig. 1.9. Market share of materials used in microfluidic devices field in 2010 (retrieved from (Yole Développement 2011). In diagnostics, POC tests and pharmaceutical research, the polymers constitute the most used group due to their low cost and wide range of properties. In the	

applications involving more aggressive chemicals, silicon, metal and ceramics are more commonly used.....	15
Fig. 1.10. PDMS cross-linking: linear vinyl ended PDMS polymers react with curing agent in the presence of platinum catalyser forming a cross-linked network (Esteves et al. 2009).....	17
Fig. 1.11. (A) Chemical structure of compounds of SU-8 photoresist: SU-8 epoxy resin molecule; cyclopentanone—solvent used in SU-8 series 2000 (in conventional SU-8 series, gamma-butyrolacton is used) and photoinitiator: triarylium-sulfonium salt. Eight reactive epoxy functionalities allow a high degree of cross-linking after photoactivation. (B) Chemical reaction for photoacid generation upon UV exposure. The generated acid acts as a catalyst in the cross-linking of the epoxy molecules. Adapted from (Al-Mumen et al. 2013).....	19
Fig. 1.12. The most promising materials for microfluidic chip fabrication and comparison of the resulting devices' cost. Retrieved from (Ren et al. 2013). Thermosets, inorganic materials and hydrogels have properties suitable for the research level use, while paper may constitute the most spread material in commercial microfluidics.....	21
Fig. 1.13. (A) Principle of the single DNA molecule detection and sorting. As each fluorescently labelled molecule passed through the input inspection volume its fluorescence signature was detected, evaluated in real time and used to actuate a sorting trigger to electrically direct the flow towards the sorted output. (B) Nanofluidic platform: nanofluidic device was mounted onto a confocal fluorescence microscope and illuminated by two overlapped lasers to excite molecule fluorescence simultaneously. Single molecule fluorescence was imaged using an optical fibre array connected to single photon counting avalanche photodiodes (APDs). Real-time fluorescence analysis at the input inspection volume was performed and used to trigger a high voltage (HV) sorting circuit to direct the electrokinetic flow of a molecule to the sorted or default output. Adapted from (Cipriany et al. 2012).....	24
Fig. 1.14. Photograph of the lab-on-chip for absorbance measurements with integrated microfluidic dye laser, waveguides, microchannels and photodiodes. All the optical and fluidic components were fabricated in SU-8, while planar c-Si n-type diodes are embedded in a c-Si p-type substrate. This device proves the feasibility of fully-integrated lab-on-chip for absorbance measurements, however its cost is relatively high due to use of c-Si and SU-8 as structural material. Retrieved from (Balslev et al. 2006). .....	26
Fig. 2.1. Principle of “doctor blade” method: suspension of ceramic particles (e.g. $\text{TiO}_2$ ) with additives is placed on a substrate and spread by sliding a glass rod (squeegee) over the substrate to form homogeneous and smooth layer.....	38

Fig. 2.2. Main characteristics, requirements, possibilities and challenges of the inkjet printing technology. Retrieved from (Teichler et al. 2012).....	39
Fig. 2.3. Photographs of inkjet printers used in this work: (A) desktop printed (Canon PIXMA IP4500) used for fabrication of the TiO <sub>2</sub> photodetector prototype and (B) lab-scale printer (LP50 PixDRO) used in the TiO <sub>2</sub> optimization. ....	39
Fig. 2.4. (A) Schematic representation of spin coating process: the sample is rotated at high speed spreading the material and forming thin film layer. (B) The thickness distribution of spin coated layer showing the edge bead formed along wafer borders. Retrieved from (Nima 2013). ....	40
Fig. 2.5. Principle of the photolithography process: irradiation through a mask a photosensitive resist layer. The irradiation initiates physico-chemical reactions in the polymer, which enable selective removal of resist in the development. In positive resists, the exposed areas become more soluble in the developer, and in negative resists, the exposed parts become insoluble ( <a href="http://www.objective.com/metaldeposition">http://www.objective.com/metaldeposition</a> retrieved in 2014.03). ....	41
Fig. 2.6. (A) Mask aligner MA6 used for the SU-8 photolithography: the sample is placed on the substrate chuck, while the mask is placed in the mask holder and i-line filter is inserted into the UV400 optics to cut off radiation below 365 nm. After alignment process, the sample is UV exposed. (B) Layout of the photolithographic mask used for micromixers fabrication: dark mask regions define SU-8 regions that are dissolved in the developer. ....	42
Fig. 2.7. Photographs of fabrication of PDMS microfluidic chip by replica moulding technique. A liquid mixture of PDMS pre-polymer and curing agent is poured on top of the SU-8 master and then cured. After cross-linking, the replica is peeled off the mould. ....	43
Fig. 2.8. Schematic representation of the SU-8 master fabrication: after SU-8 spin coating, the samples are soft-baked to evaporate solvent and then UV irradiated to initiate the cross-linking process that is thermally accelerated during the post bake. The unexposed SU-8 regions are removed in the developer bath and on the end, the samples are isopropanol rinsed and dried ( <a href="http://www.elveflow.com/microfluidic-reviews-and-tutorials/su-8-baking">http://www.elveflow.com/microfluidic-reviews-and-tutorials/su-8-baking</a> retrieved in 2014.03). ....	44
Fig. 2.9. (A) SU-8 2050 dispensed on a substrate prior to spin coating process. (B) Film thickness as a function of spin speed at ambient temperature of 21 °C ( <a href="http://www.microchem.com">http://www.microchem.com</a> retrieved in 2014.03). To obtain a desired spin speed, the values suggested in the manufacturer datasheet should be experimentally optimized. ....	46
Fig. 2.10. (A) Transmission spectrum of 1 mm thick unexposed SU-8 (Gersteltec's courtesy); (B) spectral irradiance of MA6 mask aligner with UV400 optics and (C) transmission curve of i-line filter. SU-8 absorbs light of wavelength below 350 nm, therefore for homogenous exposure of the	

whole SU-8 layer, a filter should be used to eliminate the light of wavelength below 350 nm emitted by the UV400 optics. Adapted from the mask aligner and filter datasheets. ....	48
Fig. 2.11. Scanning electron micrographs of SU-8 features (20 $\mu\text{m}$ high on glass substrates): top view of samples exposed (A) without filter (7 s) and (B) with i-line filter (18 s) and cross-section of SU-8 channel exposed (C) without filter indicating the negative side walls and (D) through the i-line filter indicating nearly vertical side walls (89 degrees). ....	49
Fig. 2.12. The microscopic images of SU-8 microchannels cross section (20 $\times$ 20 $\mu\text{m}^2$ on silicon wafer) fabricated using chromium mask: (A) 100 $\times$ magnification and (B) 200 $\times$ magnification. The microchannels were fabricated on silicon wafers exposing through the i-line filter. The use of the high resolution and high contrast mask enabled to eliminate the irregularities on the channels bottom visible in Fig. 2.11 and Table 2.1. ....	51
Fig. 2.13. SEM images of $\sim$ 125 $\mu\text{m}$ high SU-8 features fabricated with exposure dose of 309 $\text{mJ}/\text{cm}^2$ on silicon wafer: (A) top view indicating good features definition; (B) profile indicating smooth and nearly vertical side walls (87.8 degrees) and (C) zoom on the interface SU-8 / wafer indicating good adhesion. ....	54
Fig. 2.14. The process of the chip microfabrication: the moulding process starts with the fabrication of the SU-8 master mould (A), then instead of casting PDMS repeatedly from this mould, PDMS is casted once (B) and used as mould for the patterning of an epoxy mould (C), which can then be used to produce many PDMS replicas (D) without suffering delamination problems. ....	57
Fig. 2.15. (A) Schematic illustration of sealing of PDMS chips. The reversible sealing can be obtained basing on PDMS elasticity, while proper PDMS oxidation enables its irreversible sealing: generated highly active oxygen species remove the methyl groups from the PDMS surface forming polar silanol groups. When plasma treated surfaces are brought into contact, the condensation reaction occurs forming covalent bonds between those surfaces, sealing them irreversibly. Adapted from (Sun and Rogers 2007). (B) Photograph showing the strength of the PDMS sealing based on the oxidation process: it is easier to break PDMS than separate it from glass. ....	59
Fig. 2.16. Acquisition of solution spectra by miniature fibre optic spectrometer integrated with microfluidic chip. (A) The automatic measurement mode (absorbance wizard) was used to determine the optimum integration time. (B) Spectra were acquired using a manual measurement mode to enable more freedom during tests. After the dark and light reference spectra were stored in the intensity mode, the solvent and sample absorption spectra were acquired. ....	63
Fig. 2.17. Characterisation of the SU-8 feature by stylus profilometry. For such high thickness range (550 $\mu\text{m}$ ), the stylus force is fixed at the maximum value, so stylus may scratch the SU-8 layer surface. ....	65



- Fig. 2.18. Determination of features' thickness using optical microscopy: PDMS slab was immobilized perpendicularly under microscope using a bigger block of PDMS and the feature height and sidewall angle were measured..... 66
- Fig. 3.1. (A) Working principle of dye sensitized photodetector/solar cell: 1. dye photo-oxidation; 2. injection of the excited electron to the semiconductor conduction band; 3. percolation of the electron through porous semiconductor layer towards transparent conductive oxide layer and to counter electrode through external load; 4. injection of electron to a redox system of electrolyte; 5. reduction of the dye to its original state by the electrolyte (<http://www.solaronix.com/technology/dyesolarcells> retrieved in 2014.03). (B) Photograph of dye sensitized solar cells module fabricated using sensitizing dyes of various colours (<http://www.solarisnano.com> retrieved in 2014.03). ..... 73
- Fig. 3.2. Schematic of the TiO<sub>2</sub> photodetector fabrication by “doctor blade” and inkjet printing technique. The scanning electron micrograph presented the surface morphology of the TiO<sub>2</sub> film prepared by inkjet printing technology after sintering at 450 °C. The film is about 4 μm thick, no cracks on the surface are observed which indicates a very high inter-particle connectivity. The average diameter of TiO<sub>2</sub> particles is 25 nm..... 76
- Fig. 3.3. Incident photon to current conversion efficiency (IPCE) of the photodetector obtained by “doctor blade” method (DBP) and by inkjet printing (IPP). The TiO<sub>2</sub> layer of DBP is about 1.75 times thicker than in the case of the IPP, which may explain the observed difference at the IPCE. Inset: Absorption spectrum of the ethanol solution of Ruthenium N3 dye..... 79
- Fig. 3.4. Responses of the sensor with (A) “doctor blade” photodetector and (B) inkjet printed photodetector for different AuNP concentrations. Non-aggregated (red squares) and aggregated by salt addition (blue circles). The detection response ( $R_{det}$ )—difference in the photocurrent densities generated by photodetector when illuminating through the reference solution and through the sample solution. Measurements using a high power LED with 530 nm and 35 nm spectral half-width. *Inset*: Corresponding spectrophotometric measurements: absorption peak area integral from 520 to 540 nm as a function of AuNP concentration. Standard deviation bars were determined from 6 independent measurements. .... 81
- Fig. 3.5. (A) Schematic representation of DNA detection of the developed biosensor ( $W_f$ —the photon flux and  $R_{det}$ —detection responses). (B) The Au-nanoprobe based assays for *M. tuberculosis* DNA with the novel sensors with DBP and IPP: POS—complementary DNA target; NEG—non-complementary DNA target;  $R_{det}$ —difference in the photocurrent densities generated by photodetector when illuminating through the reference solution and through the sample solution. *Inset*: Absorption spectra of DNA solutions (in arbitrary units). The absorption spectrum of NEG was shifted for the same absorbance value at  $\lambda = 400$  nm as POS (shift =  $-0.0067$  a.u.) so as to

allow better colour change visualization. DNA detection was carried out with the appropriate oligonucleotide target at a final concentration of 1.33 $\mu\text{M}$ and Au-nanoprobes at a final concentration of 2.5 nM. Standard deviation bars were determined from 6 independent measurements.....	82
Fig. 3.6. Profiles and optical micrographs of $\text{TiO}_2$ layers of various thicknesses fabricated using the Solaronix paste by (A) “doctor blade” and (B) inkjet printing technique with sintering ramp of 10 $^\circ\text{C}/\text{min}$ and (C) 50 $^\circ\text{C}/\text{min}$ . During the inkjet printing process, the stage was heated to 70 $^\circ\text{C}$ . The $\text{TiO}_2$ films that resulted in functioning devices were labelled in green, while the malfunctioning—in red. ....	84
Fig. 3.7. SEM images of $\text{TiO}_2$ films fabricated using the Solaronix paste by (A) “doctor blade” (3.4 $\mu\text{m}$ thick) and (B) inkjet printing technique (1.6 $\mu\text{m}$ thick) with sintering ramp of 10 $^\circ\text{C}/\text{min}$ . The higher porosity of the inkjet printed $\text{TiO}_2$ films is most probably caused by the solvent evaporation during the droplet fly from the nozzle to the substrate that is additionally enhanced by the applied heating of printing stage (70 $^\circ\text{C}$ ).....	85
Fig. 3.8. Energy conversion efficiency of photodetectors incorporating $\text{TiO}_2$ films fabricated using the Solaronix paste by (A) “doctor blade” and (B) inkjet printing technique (the connecting lines are for eyes guidance only).....	87
Fig. 4.1. (A) Schematic representation of the DNA detection method based on non-cross-linking DNA hybridisation of Au-nanoprobes. (B) Diagram of the developed microfluidic platform. Solution to be analysed is dispensed into the inlet well and injected to the channel by the withdrawing from the outlet using a syringe pump. Optical fibres guide the light from the LEDs to the microfluidic detection channel and then to the photodiode. The bulk part of the PDMS is not shown to not darken the image. ....	95
Fig. 4.2. Absorption spectra of disperse and aggregated MTBC Au-nanoprobes solution (2.5 nM Au-nanoprobe in 10 mM phosphate buffer (pH 8)) attained via standard 384 well micro-plate. The aggregation was induced by salt addition $[\text{MgCl}_2] = 0.04 \text{ M}$ . Spectra values are normalised, i.e. spectrum of aggregated solution was shifted for the same absorbance value at $\lambda = 400 \text{ nm}$ as disperse solution. The dashed lines correspond to the dominant wavelengths [530 nm (green) and 625 nm (red)] of the LEDs used in the detection and for determination of $R_s$ ratio.....	96
Fig. 4.3. Microfluidic chip. (A) 3D schematic representation of the microfluidic chip design and zoom in on the detection area (the bulk part of the PDMS is not shown to not darken the images). The light is guided to the microchannel by the optical fibres that are self-aligned by the insertion grooves in the chip. (B) Photograph and microscopic image of the channel filled with gold nanoparticles solution and illuminated by the green LED.....	98

Fig. 4.4. Circuit diagram used for optical-to-electrical signal conversion and amplification. The electrical signal from the photodiode was provided to the input of operation amplifier circuit with a feedback loop resistance of 20 M $\Omega$ and supplied by $\pm 15$ V. ....	101
Fig. 4.5. Portable, integrated colorimetric DNA biosensor with <i>chip carrier</i> for insertion of photodetector and macro-machined PDMS containers. The light from RGB LED is transmitted vertically through the solution placed in PDMS container and afterwards is detected by photodetector placed underneath the container. The photocurrent generated by photodetector is filtered, amplified, converted to a digital signal and transmitted to a computer via a serial communication protocol. Adapted from (Silva 2010). ....	104
Fig. 4.6. Design of (A) the macro-machined polyacetal mould and (B) the resulting PDMS containers to be used in the colorimetric DNA biosensor. ....	105
Fig. 4.7. Absorption spectra of dispersed and aggregated AuNPs ( $\sim 2.5$ nM) in various containers. Reference: air in the water spectrum and respective container filled with water for AuNPs spectra. ....	107
Fig. 4.8. Absorption spectra of the Au-nanoprobe assay for <i>M. tuberculosis</i> detection in the macro-machined PDMS container (optical path: 2 mm, volume of the solution: 50 $\mu$ l): probe; blank (without DNA), POS—complementary DNA target; NEG—non-complementary DNA target. The spectra were taken 30 min after salt addition using a container filled with phosphate buffer (pH 8, 10 mM) as a reference. [Au-nanoprobe] = 2.5 nM; [MgCl <sub>2</sub> ] = 0.04 M; [oligonucleotide target] = 1.33 $\mu$ M. ....	108
Fig. 4.9. SEM characterisation of microfluidic chip. SEM images showing: (A) side wall angle of the SU-8 feature (achieved aspect ratio: 12) and (B) microchannel in PDMS patterned by the SU-8 mould. Perfectly flat and smooth walls are clearly visualised. ....	109
Fig. 4.10. (A) Profilometer measurement of a SU-8 mould feature with 126 $\mu$ m of height. (B) Optical specular transmittance of PDMS slabs of various thicknesses. ....	110
Fig. 4.11. Fabrication process. Microscopic images of top views and cross sections of the test features fabricated in each fabrication step (scale bar length: 100 $\mu$ m). The smallest feature is 10 $\mu$ m wide with aspect ratio of 12. ....	111
Fig. 4.12. Fabrication process. Confocal scanning microscope images, showing the definition obtained in each fabrication step: (A) SU-8 master; (B) first PDMS mould cast from the SU-8 master; (C) epoxy mould cast from the first PDMS mould and (D) final PDMS replica cast from the epoxy mould clearly replicating the features of the original SU-8 master. ....	112
Fig. 4.13. Microscopic image of an optical fibre immobilized in a PDMS groove. The proper dimensions of the groove allow thigh immobilization of the fibres and consequently their	

- alignment with each other and with the detection channel. The funnel shape of the entrance facilitates the insertion and reduces probability of fibre breaking. .... 113
- Fig. 4.14. Optical sensing with the microfluidic platform. (A) Output voltage generated by the platform for the chip of 2 mm long microchannel filled with water as a function of LEDs current; (B) sensitivity of the developed microfluidic platform defined as a difference between the detection responses (calculated from equation (4.1)) for the non-aggregated and aggregated AuNPs solutions. The tests were done for various optical path lengths (OPL) with LEDs powered with 300 mA and 920 mA. The data points represent the average of three readout measurements and the error bars indicate the standard deviation (the connecting lines are for eyes guidance only)..... 114
- Fig. 4.15. (A) Estimation of the beam width at the end of the chamber containing the microfluidic channel of a length of 0.5 mm. This estimation is intended for power loss evaluation. (B) Percentage of available power reaching the collecting optical fibre as a function of the optical path length in the developed microfluidic chips (for  $NA = 0.275$  and  $n = 1.33$ )..... 114
- Fig. 4.16. *M. tuberculosis* detection via proposed bio-microfluidic platform. Au-nanoprobe assay mixtures (2.5 nM Au-nanoprobe 30 ng/ $\mu$ l of sample DNA in 10 mM phosphate buffer (pH 8)) after 15 min of incubation following salt addition  $[MgCl_2] = 0.04$  M. Results obtained using: (A) PDMS microfluidic platform with LEDs powered with 300 mA and (B) with 920 mA (see eq. 4.1). The bars represent the average of independent measurements and the error bars indicate standard deviation. The horizontal line represents the threshold of 1 considered for discrimination between positive and negative. Statistical analysis was performed using Prism 5 graph pad, using one-way ANOVA with Tukey's Multiple Comparison test;  $***=p<0.0001$ ,  $n \geq 5$ . .... 116
- Fig. 4.17. Microplate reader results of Au-nanoprobe assay for MTBC detection: MTBC standard assay performed in a microplate reader. Au-nanoprobe aggregation as measured by ratio of aggregation for the assay mixtures [2.5 nM Au-nanoprobe, 10  $\mu$ g/ml of sample DNA in 10 mM phosphate buffer (pH 8)] after 15 min of incubation following salt addition  $[MgCl_2] = 0.04$  M. The bars represent the average of independent measurements and the error bars indicate standard deviation. The horizontal line represents the threshold of 1 considered for discrimination between positive and negative. Statistical analysis was performed using Prism 5 graph pad, using one-way ANOVA with Tukey's Multiple Comparison test;  $***=p<0.0001$ ,  $n \geq 5$ . .... 117
- Fig. 4.18. The detection response ( $R_s$ ; eq. 4.1) as a function of the gold nanoparticles concentration. The detection response increases linearly with AuNPs concentration (adjusted  $R$ -square coefficient = 0.95937). The measurements were taken with the LEDs powered with 400 mA. .... 118
- Fig. 5.1. Principle of colorimetric DNA detection method based on non-cross-linking hybridisation of Au-nanoprobes: at high salt concentration, only the presence of fully complementary DNA prevents aggregation and the solution remains red. .... 126

- Fig. 5.2. (A) Emission spectra of SMD LEDs used for the colorimetric analysis. The spectra were acquired using miniature fiber optic spectrophotometer (Ocean Optics USB4000) integrated with an empty microfluidic chip (integration time: 8 ms; LEDs supplied with 0.4 A). (B) Circuit diagram used for optical-to-electrical signal conversion and amplification. .... 128
- Fig. 5.3. 2D schema of light propagation in PDMS chip of 2 mm long optical path: (A) uncollimated; (B) with input and output air lenses and (C) with PDMS input lens and output air lenses (to scale). .... 133
- Fig. 5.4. (A) 3D schema of light propagation in chip of 2 mm long optical path without lenses and (B) with 2D air microlenses (the schema is drawn to scale; only the light propagation in the plane of the channel is considered as the light in vertical direction remains diverged). (C) Top view microscopic images of channel filled with water illuminated by green LED (0.9 A) in chip without lenses and (D) with 2D air microlenses. .... 135
- Fig. 5.5. Scanning electron micrographs of the PDMS chip: (A) main chip features; (B) input air microlens; (C) input PDMS microlens and (D) output air lenses. The images B – D were taken with the stage 20 degrees tilted to visualize better the aspect ratio. .... 136
- Fig. 5.6. Confocal microscope images of fabricated 2D microlenses: (A) input air lens; (B) input PDMS lens and (C) output air lenses. .... 136
- Fig. 5.7. (A) The detection response ( $R_s$ , eq. (5.1)) of the microfluidic platform for dispersed (in red) and aggregated (in blue) AuNPs solutions using microfluidics chips without lenses (before and after system optimization described in section 3.1), with air microlenses and with PDMS microlenses (LEDs powered with 0.4 A). The horizontal dashed line represents the threshold of 1 considered for discrimination between red and blue colour solutions. (B) The propagation of the signal-to-loss ratio along the channel in chip without lenses and chip with the air microlenses based on the analysis of the pixels intensity in Fig. 5.4C and D. .... 138
- Fig. 5.8. Absorption spectra acquired using miniature fibre optic spectrophotometer integrated with a microfluidic chip ('chip'; 3  $\mu$ l; 2 mm long optical path; integration time: 610 ms) and using conventional microplate reader (30  $\mu$ l; 10 mm long optical path). (A) Spectra of the dispersed and aggregated AuNPs (3 min after salt addition). (B) Spectra of the Au-nanoprobe assay for the *FTO* single nucleotide polymorphism detection: blank (without DNA), positive (POS) and negative (NEG) assay (30 ng/ $\mu$ l of target DNA). The spectra were taken 30 min after salt addition. The absorption spectra of blank, POS and NEG were shifted for the same absorbance value at  $\lambda = 400$  nm as probe, so as to allow better visualisation. .... 139
- Fig. 5.9. Transmission spectra of green and red LEDs acquired using miniature fiber optic spectrophotometer integrated with microfluidic chip with air lenses filled with water, the Au-

- nanoprobe and blank (8 min; 15 min and 30 min after salt addition; the samples were injected into the channel directly after salt addition). LEDs powered with 0.4 A; reference: empty chip; integration time: 8 ms. .... 141
- Fig. 5.10. Results of the colorimetric DNA detection (eq. 5.1) of the *FTO* single nucleotide polymorphism using Au-nanoprobes and the optimized bio-microfluidic platform with chip with air lenses using 3  $\mu$ l of solution with 15 and 30 ng/ $\mu$ l of target DNA. The horizontal dashed line represents the threshold of 1 considered for discrimination between positive and negative. .... 142
- Fig. 5.11. Microscopic images of chip with air microlenses illuminated by halogen lamp taken in dark conditions using Stereo Microscope and Pentax K100 camera with long exposure time (30 s). (A) AuNPs 10 to 60 min after salt addition (the solutions were injected into the channel directly after salt addition). (B) The positive and negative colorimetric Au-nanoprobe assays for *FTO* single mismatch detection (target DNA concentration: 30 ng/ $\mu$ l) taken 30; 40 and 50 min after salt addition (the solutions were injected to the channel 26 min after salt addition). .... 143
- Fig. 6.1(A) Schematic diagram of the designed rhombic micromixer with stepped diamond-shaped obstacles and rectangular contractions between rhombi. (B) PDMS micromixer fabricated using SU-8 mould and epoxy mediating mould. (C) Optical microscopy images taken at different locations along a micromixer with  $w_t = 100 \mu\text{m}$  and  $d = 140 \mu\text{m}$  at  $Re = 8.2$ . Mixing efficiency was analysed along the channel in the middle of the first contraction,  $M(1)$ , second contraction,  $M(2)$  and third contraction,  $M(3)$ , as indicated by the vertical dotted lines. .... 158
- Fig. 6.2. Optical microscopy images taken at the first contraction for various flow conditions. (A) Influence of the contraction width ( $w_t$ ) on fluid mixing at  $Re = 1.2$ ;  $Re = 5.9$  and  $Re = 88.2$ , in mixers with inter-obstacles distance  $d = 140 \mu\text{m}$ . At lower  $w_t$  and higher  $Re$ , strong acceleration and subsequent deceleration of flows leads to formation of vortices. (B) Comparison of vortices generated at  $Re = 28.4$ ;  $Re = 58.8$  and  $Re = 117.6$  in mixer with  $w_t = 100 \mu\text{m}$ . (C) Influence of the inter-obstacles distance ( $d$  varying from  $60 \mu\text{m}$  to  $140 \mu\text{m}$ ) for micromixers with  $w_t = 400 \mu\text{m}$  at  $Re = 5.9$ . For  $d = 60 \mu\text{m}$ , the fluids flow mainly next to the channel walls due to low inter-obstacles channel width. .... 161
- Fig. 6.3. Experimental mixing efficiency ( $M$ ; given in %) of mixers with various configurations at the middle of the first contraction ( $M(1)$ ; red line), second contraction ( $M(2)$ ; blue line) and third contraction ( $M(3)$ ; green line). Data points labelled *a* and *b* were determined from two different images taken from the first chip, while data points labelled *c* and *d* were determined from two different images taken from the second chip. Connecting lines are for eye guidance only. .... 162
- Fig. 6.4(A) Shear rate dependence of the shear viscosity computed from the pressure drop ( $dP$ ) and the volumetric flow rate ( $Q$ ) measured with chip of  $w_t = 100 \mu\text{m}$ ;  $d = 60 \mu\text{m}$  for two values of the effective channel width ( $w$ ):  $20 \mu\text{m}$  (squares) and  $32 \mu\text{m}$  (triangles). The red dashed horizontal line

indicates the viscosity ( $8 \times 10^{-3} \text{ Pa} \times \text{s}$ ) of water at 28 °C measured with a rotational rheometer. Inset: stress dependence of the apparent shear rate. The red line is a linear fit to the data with slope of $1.08 \pm 0.07$ indicating a Newtonian behavior. (B) Experimental pressure drop ( $dP$ ) for micromixers of various configurations ( $w_t$ and $d$ are given in $\mu\text{m}$ ). (C) Zoom in on the low $Re$ region. For low $dP$ values (usually below 12), there is no linear dependence between $dP$ and $Re$ due to the detection limit of the pressure sensor. ....	164
Fig. 6.5. Results obtained from mathematical fitting to the experimental data points (A) of mixing efficiency (given in %) measured at the middle of the first contraction ( $M(1)$ ); (B) at the second contraction ( $M(2)$ ); (C) at the third contraction ( $M(3)$ ) and (D) of pressure drop ( $dP$ ; given in kPa) measured after three rhombi. (E) Desirability results ( $D_n$ ) defined as maximum values of $M(1)$ ; $M(2)$ and $M(3)$ and minimum of $dP$ .....	169
Fig. 7.1. Schematic representation of fabrication of the PDMS waveguides based on a capillary filling technique. The channels patterned in the cladding material can be capillary filled with the core material pre-polymer that is cured afterwards, forming solid state, stretchable waveguides. Adapted from (Missinne et al. 2014). ....	180
Fig. 7.2. Layout proposal of a lab-on-chip device for colorimetric DNA detection starting from unamplified target DNA and Au-nanoprobes: (A) top view; (B) three-dimensional representation. ....	181





## List of Tables

Table 1.1. Main characteristics of the most used materials for microfluidic chip fabrication. Based on (Becker and Gärtner 2008; Ren et al. 2013). .....	22
Table 2.1. The scanning electron micrographs of microchannels ( $20 \times 20 \mu\text{m}^2$ ) fabricated in SU-8 on glass or silicon wafer exposed through the i-line filter for 18 s. Various post-development treatments were applied to eliminate the irregularities of bottom part of channels. ....	50
Table 2.2. Microscopic images of $140 \mu\text{m}$ thick SU-8 layer fabricated using various exposure doses on silicon wafers. The exposure dose of $330 \text{ mJ/cm}^2$ gives a higher aspect ratio and more homogenous SU-8 structure.....	53
Table 2.3. Minimum size of features and channel for various exposure doses based on scale bar results presented on Table 2.2. ....	53
Table 2.4. Characterisation techniques used in this PhD work.....	61
Table 4.1. Dimensions of developed PDMS containers (*total volume of container = volume of cylinder + volume of inlet and outlet). ....	105
Table 5.1. Main characteristics of the operational amplifiers used in various system optimization stages.....	132
Table 5.2. The curvatures ( $R$ ), distances ( $d$ ) and the characteristics of the resulting light beam ( $\gamma$ and $\theta$ ) for the input bi-concave air microlens and the input bi-convex PDMS microlens.....	133
Table 5.3. The curvatures ( $R$ ), distances ( $d$ ) and the characteristics of the resulting light beam ( $\gamma$ and $\theta$ ) for the output bi-concave and bi-convex air microlens. ....	134
Table 6.1. Summary of planar passive micromixer designs with respective performance reported in the literature (*data obtained through simulations). ....	151
Table 6.2. Summary of data sieving and corresponding model validation parameters based on least square regression. $N$ is the number of observations.....	166
Table 7.1. Comparison of the biosensor performance along the optimization process. The normalized colorimetric discrimination, i.e. $\Delta R_s(\text{normalized})$ , was defined as the AuNPs colorimetric discrimination (the difference between the detection response for dispersed AuNPs and aggregated AuNPs solutions) normalized to the detection response for the dispersed AuNPs (see eq. 7.1). ...	178



## List of symbols, acronyms and abbreviations

ANOVA	- analysis of variance
AuNPs	- gold nanoparticles
c-Si	- crystalline silicon
$D$	- inter-obstacles distance
$D$	- diffusion coefficient
DBP	- “doctor blade” photodetector
DNA	- deoxyribonucleic acid
$dP$	- pressure drop
FTO	- fluorine doped tin oxide
$h$	- channel height
$I$	- pixel intensity
ITO	- indium tin oxide
IPP	- inkjet printed photodetector
$k_B$	- Boltzmann’s constant
$l$	- characteristic dimension
$L$	- length
LED	- light emitting diode
LOC	- lab-on-chip
$M$	- mixing efficiency (1, i.e. 100%, for perfectly mixed streams)
OPL	- optical path length
PCI	- Peripheral Component Interconnect
PCR	- polymerase chain reaction
PDMS	- polydimethylsiloxane
$Pe$	- Peclet number
PMMA	- poly(methyl methacrylate)

POC	- point of care
$Q$	- volumetric flow (m <sup>3</sup> /s)
$Re$	- Reynolds number
SEM	- scanning electron microscopy
$t$	- time
TCO	- transparent conductive oxide
UV	- ultra violet electromagnetic radiation (300 – 400 nm)
$v$	- velocity
vis	- visible electromagnetic radiation (400 – 765 nm)
$w_c$	- channel width
$w_t$	- width of the contraction between rhombi
$x$	- mean distance that a molecule diffuses in time $t$
$\sigma$	- mixing index (0 for perfectly mixed streams)
$\mu$	- fluid viscosity
$\mu_o$	- viscosity of the dyed water
$\mu$ FLs	- microfluidics
$\mu$ TAS	- micro total analysis systems
$\rho$	- density of water
$\langle I \rangle$	- average greyscale intensity of all pixels in image
2D	- two-dimensional structure
3D	- three-dimensional structure

# **Chapter 1**

## General introduction



<b>Chapter 1. General introduction .....</b>	<b>5</b>
<b>Summary.....</b>	<b>5</b>
<b>1.1. Biosensors .....</b>	<b>5</b>
<b>1.2. DNA biosensors based on gold nanoparticles.....</b>	<b>6</b>
<b>1.3. Microfluidic devices .....</b>	<b>10</b>
<b>1.4. Fluid behaviour at microscale.....</b>	<b>12</b>
<b>1.5. Microfluidics materials.....</b>	<b>14</b>
1.5.1. Silicon and glass .....	15
1.5.2. Polymers .....	15
1.5.3. Paper .....	20
1.5.4. Materials overview .....	21
<b>1.6. Nanofluidics .....</b>	<b>22</b>
<b>1.7. Miniaturisation of absorbance-based detection .....</b>	<b>25</b>
<b>1.8. Motivation and objectives .....</b>	<b>27</b>
<b>1.9. Thesis outline.....</b>	<b>28</b>
<b>1.10. List of publications.....</b>	<b>29</b>
<b>1.11. List of presentations.....</b>	<b>29</b>





## **Chapter 1. General introduction**

### **Summary**

This chapter includes fundamental background related with biosensors, DNA detection and microfluidics and short state-of-the-art of microfluidic devices for absorbance-based detection giving the broader view for to the introduction sections given in each results chapter. The motivation of the chosen scope and research objectives are also provided stating the relationship among the presented articles. On the end of this chapter, the thesis structure is described.

### **1.1. Biosensors**

Biosensor, according to IUPAC, is a device that uses specific biochemical reactions to detect chemical compounds usually by electrical, thermal or optical signals (McNaught and Wilkinson). It consists of a biological recognition system, often called a bioreceptor, and a transducer. The specific interaction of the bioreceptor with the target analyte is designed to produce an effect measured by the transducer (physical or chemical change), which converts the information into measurable effect, such as an electrical signal. The basic structure of biosensor is shown in Fig. 1.1. Biosensors can be classified either by their bioreceptor or their transducer type. As bioreceptor, a biological molecular species (e.g. an antibody, an enzyme, a protein, or a nucleic acid) or a living biological system (e.g. cells, tissue or whole organisms) can be used. Basing on the type of measured change, biosensors can be classified into optical, electrochemical, thermal, acoustic and magnetic (naming few), where the most common are optical biosensors (Zhai et al. 1997). In principle, any receptor may be combined with any suitable transducer to produce an operational biosensor.

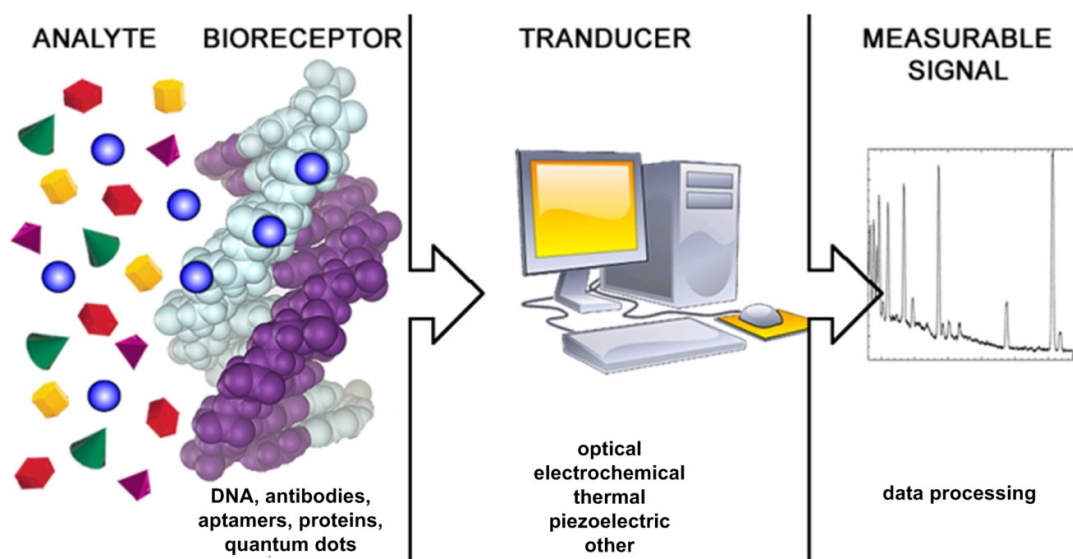


Fig. 1.1. Schematic representation of biosensor principle: specific interaction of bioreceptor with analyte results in physical or chemical change analysed by transducer and then converted into measurable signal. Adapted from (Martins et al. 2013).

One of the fastest growing segment of worldwide diagnostics market is point of care (POC) analysis (Ehrmeyer and Laessig 2007), i.e. ‘tests designed to be used at or near the site where the patient is located, that do not require permanent dedicated space, and that are performed outside the physical facilities of the clinical laboratories’ as defined by College of American Pathologists ([www.cap.org](http://www.cap.org)). POC tests may make biological analysis widely available and provide opportunities for better screening of at-risk patients and better monitoring of treatment, saving lives and costs. Many diseases are largely treatable with drug therapy, however the main issue is lack of available diagnostic tests (Soper et al. 2006). For POC tests, extensive cleaning is not acceptable, so disposable devices are favoured by the end user. On the other hand, disposing of all biosensor components would make these devices too costly to be used as point of care. Therefore, POC biosensor systems tend to be divided into disposable chips or cartridges and a non-disposable host device (or instrument) (Adams et al. 2003).

## 1.2. DNA biosensors based on gold nanoparticles

DNA biosensors attract much interest due to their selectivity, sensitivity and numerous applications, e.g. clinical diagnostics of inherited diseases and pathogenic infections (Bora et al. 2013). Recently, gold nanoparticles (AuNPs) are becoming more and more popular as markers in DNA analysis proving low-cost and sensitive detection system taking advantage of their unique optical properties.

Due to localized surface plasmon resonance (LSPR, i.e. the collective resonant oscillation of conduction electrons at the surface of a metal nanoparticle under the perturbation of incident light), the colour of AuNPs solution is dependent on the nanoparticles' size, shape, optical properties of surrounding media and inter-particle distance (Doria et al. 2012; Veigas 2012). In the latter case, when individual spherical AuNPs come into close proximity (i.e. the center-to-center distance smaller than 2.5 times of the AuNP diameter), the surface plasmon of individual AuNPs combines (inter-particle plasmon coupling), which results in the change of solution colour from red to blue (Fig. 1.2). The colour difference is a macroscopic response which derives from phenomenon occurring at a nanometer scale. Although silver nanoparticles exhibit sharper and stronger SPR bands, AuNPs are much more popular for biological applications due to their inert nature, biocompatibility and easy functionalization with biomolecules through thiol bond (Petryayeva and Krull 2011).

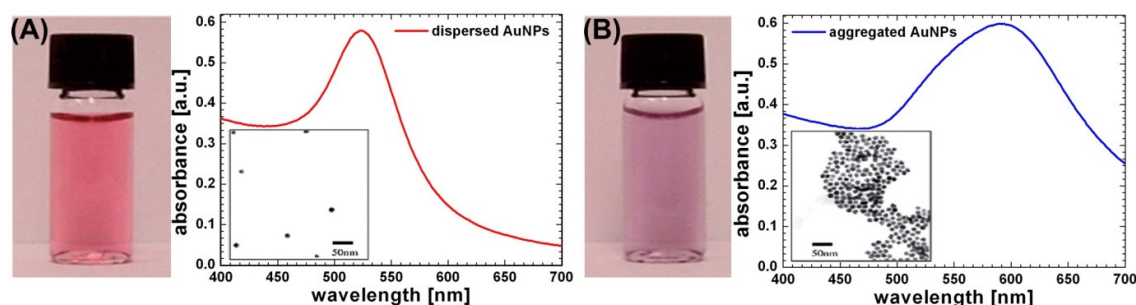


Fig. 1.2. Colours of gold nanoparticle solutions; corresponding absorption spectra and transmission electron micrographs showing their inter-particles distance: (A) monodispersed AuNPs solution and (B) aggregated AuNPs solution. Adapted from (Schofield et al. 2007).

The inter-particle distance dependent AuNP colours have been extensively applied for colorimetric biodetection (Baptista 2012; Doria et al. 2012; Dykman and Khlebtsov 2012). In particular, optical properties of AuNPs together with specificity of DNA interactions based on hybridisation process have resulted in very sensitive DNA detection methods (single base mismatch detection) that require very simple instrumentation (light source and photodetector).

In 1996, Mirkin and co-workers have functionalized AuNPs with thiol-modified oligonucleotides forming so called gold nanoprobes (Au-nanoprobes). To detect specific DNA sequences in the target DNA, two probes of sequences complementary to half of the target were used. When hybridisation occurs, Au-nanoprobes will approach to each other by target DNA forming a network (*cross-linking* method), i.e. they self-assemble into aggregates. The approaching of the probe causes inter-particle plasmon coupling with visible change of colour from red to blue. The network can be disassembled by thermal denaturation at specific temperature enabling detection of single nucleotide polymorphism.

Subsequently, various DNA detection methods have been developed basing on differential non-cross-linking aggregation of single Au-nanoprobe induced by increasing ionic strength of the solution in the presence of target DNA (Baptista et al. 2005; Sato et al. 2003). In the method developed by Baptista and co-workers, at increasing salt concentration, Au-nanoprobe aggregate in the presence of non-complementary/mismatch DNA target giving blue solution, while the presence of complementary DNA prevents aggregation of Au-nanoprobe and the solution remains red (Baptista et al. 2005), see Fig. 1.3. This method has allowed detection of pathogens (Baptista et al. 2006; Costa et al. 2009) and single base mismatches related with drug resistance (Veigas 2010).

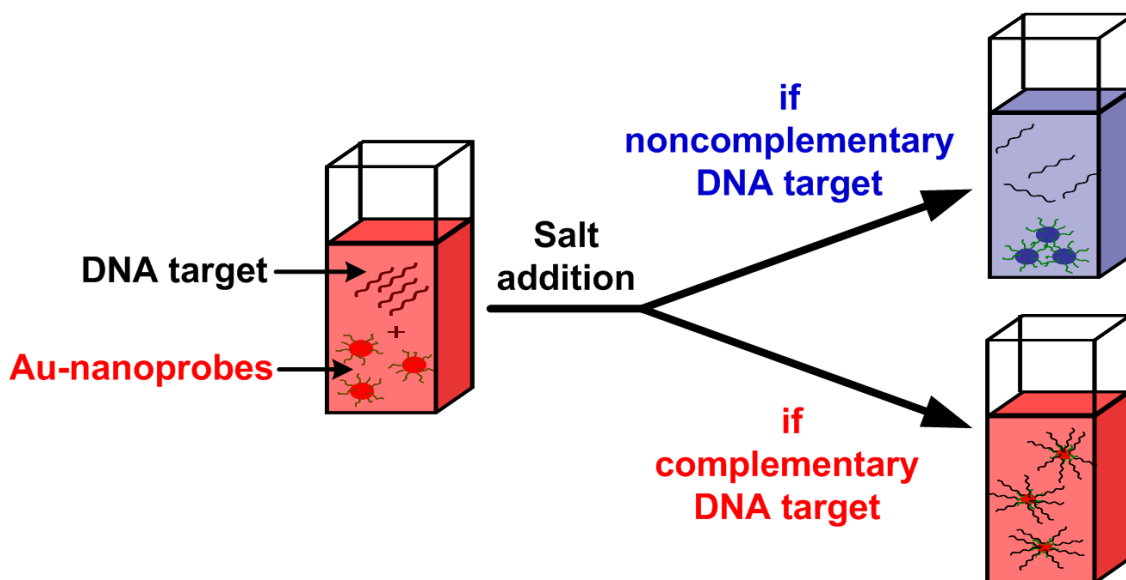


Fig. 1.3. Principle of colorimetric DNA detection method based on non-cross-linking hybridisation of Au-nanoprobe at high salt concentration (Baptista et al. 2005). After salt addition, only the presence of complementary DNA target prevents the Au-nanoprobe aggregation remaining the red colour of the solution.

The difference between positive and negative solution colours can be observed by naked-eye, however in order to quantify results or to reduce amount of needed solution, the biorecognition event should be converted into a measurable signal, e.g. by acquiring the absorption spectrum of the solution. Our group has simplified the transducer by integrating this colorimetric DNA detection method with an optoelectronic platform, using a high intensity green light source and a colour sensitive amorphous/nanocrystalline silicon photodetector, so as to create a biosensor that can be used for the detection of specific DNA sequences (Martins et al. 2008; Silva et al. 2008). In order to detect whether the DNA solution after the salt addition is red or blue, we take advantage of the fact that a positive solution (red colour) has a stronger absorption in the green region than a negative solution

(blue solution). A photodetector sensitive to green light can detect these light intensity changes proving indirectly information of the colour of the solution being analysed, i.e. presence or absence of specific DNA sequence (Fig. 1.4). Alternatively, a system with a red light source and a photodetector sensitive for red light can be used.

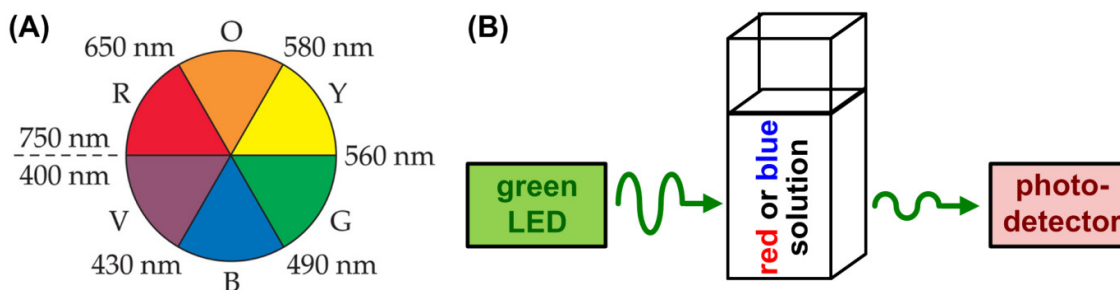


Fig. 1.4. (A) Colour wheel presenting the relationship between a colour of object and its absorption of light. (B) Schematic representation of biosensor used for detection of colorimetric changes of DNA solution. The light from green LED is transmitted through the solution and then is detected by photodetector. The light allowed through the solution reaches the sensor that generates a photocurrent.

Subsequently, the developed DNA biosensor have been optimized by the use of a tuneable double colour light emitting diode (LED; here RGBA LED that emits red, green, blue and amber colour light) and a broad band colour sensitive amorphous/nanocrystalline silicon photodetector, yielding increased results accuracy. Furthermore, signal acquisition and processing electronics with associated software for direct data evaluation via USB port for PC connection and an user friendly interface have been developed (Fig. 1.5; Silva et al. 2011). Such optimized biosensor has been incorporated into an integrated, portable ( $13 \times 6 \text{ cm}^2$ ) prototype platform that requires 60  $\mu\text{l}$  of solution volume per assay (optical path length: 10 mm).

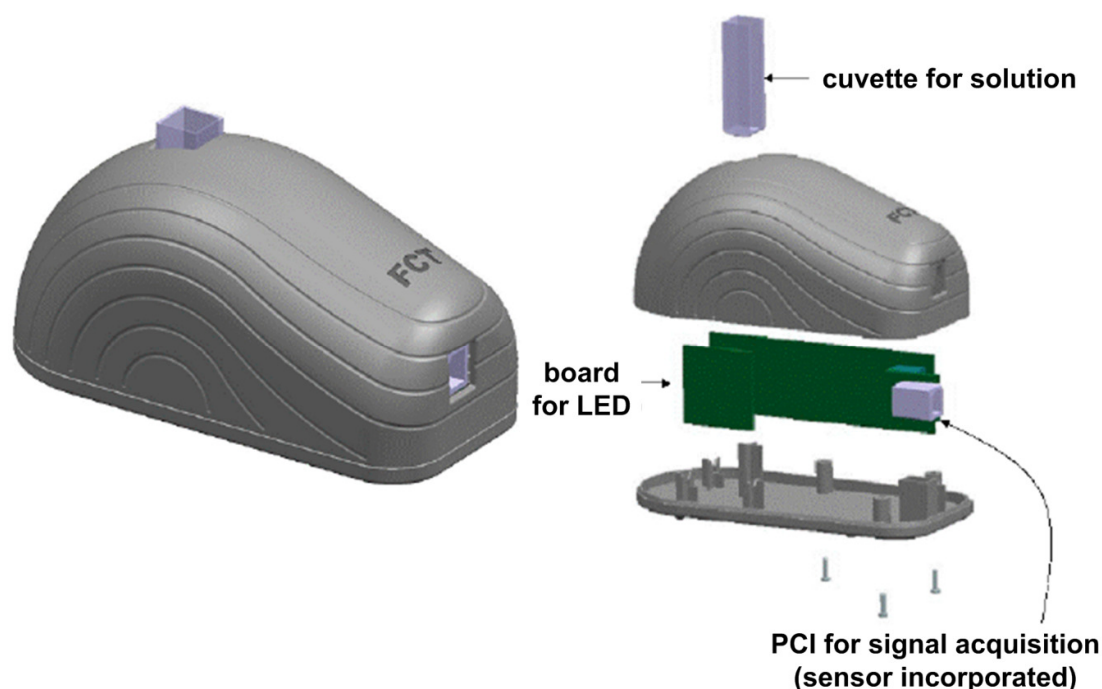


Fig. 1.5. Portable, integrated biosensor for colorimetric DNA detection based on non-cross-linking aggregation of Au-nanoprobes. The light from RBGA LED is transmitted through the solution and then is detected by amorphous/nanocrystalline silicon photodetector generating photocurrent. The analog signal is filtered, amplified, converted to a digital signal and transmitted to a computer via a serial communication protocol. Adapted from (Silva et al. 2011).

### 1.3. Microfluidic devices

Microfluidics is the science and technology of controlling fluids at microscale (Whitesides 2006). Strictly speaking, ‘lab-on-chip’ (LOC) refers to the scaling down of *several* laboratory processes on a chip-format (Fig. 1.6), while ‘micro-total analysis systems’ ( $\mu$ TAS) refers to integration of *all* laboratory processes required for an analysis on a single chip. In reality, many researchers use the terms *microfluidics*, *BioMEMS*, *BioChips*, *lab-on-chip* and  $\mu$ TAS interchangeably (Weigl et al. 2007). Microfluidic ( $\mu$ FL) devices offer numerous advantages over conventional chemical or biological methods due to the micro-scale dimensions, the resulting high surface-area-to-volume ratio and consequential microscale phenomena (see section 1.4). Microfluidic structures usually require only from 100 nl to 10  $\mu$ l of sample and reagents, making this technology ideal for handling costly or hazardous reagents (Janasek et al. 2006; Soper et al. 2006). The small size of these devices results in faster reaction times, better temperature control, lower energy consumption, parallelisation and portability.  $\mu$ FL devices may give more reliable analysis results due to their closed architecture that reduces the risk of contamination (Price et al. 2009; Wang 2000). Furthermore, by devices automation



the risk of operator error can be greatly reduced. Therefore, microfluidic devices are very promising candidates for the point of care use (Yager et al. 2008).

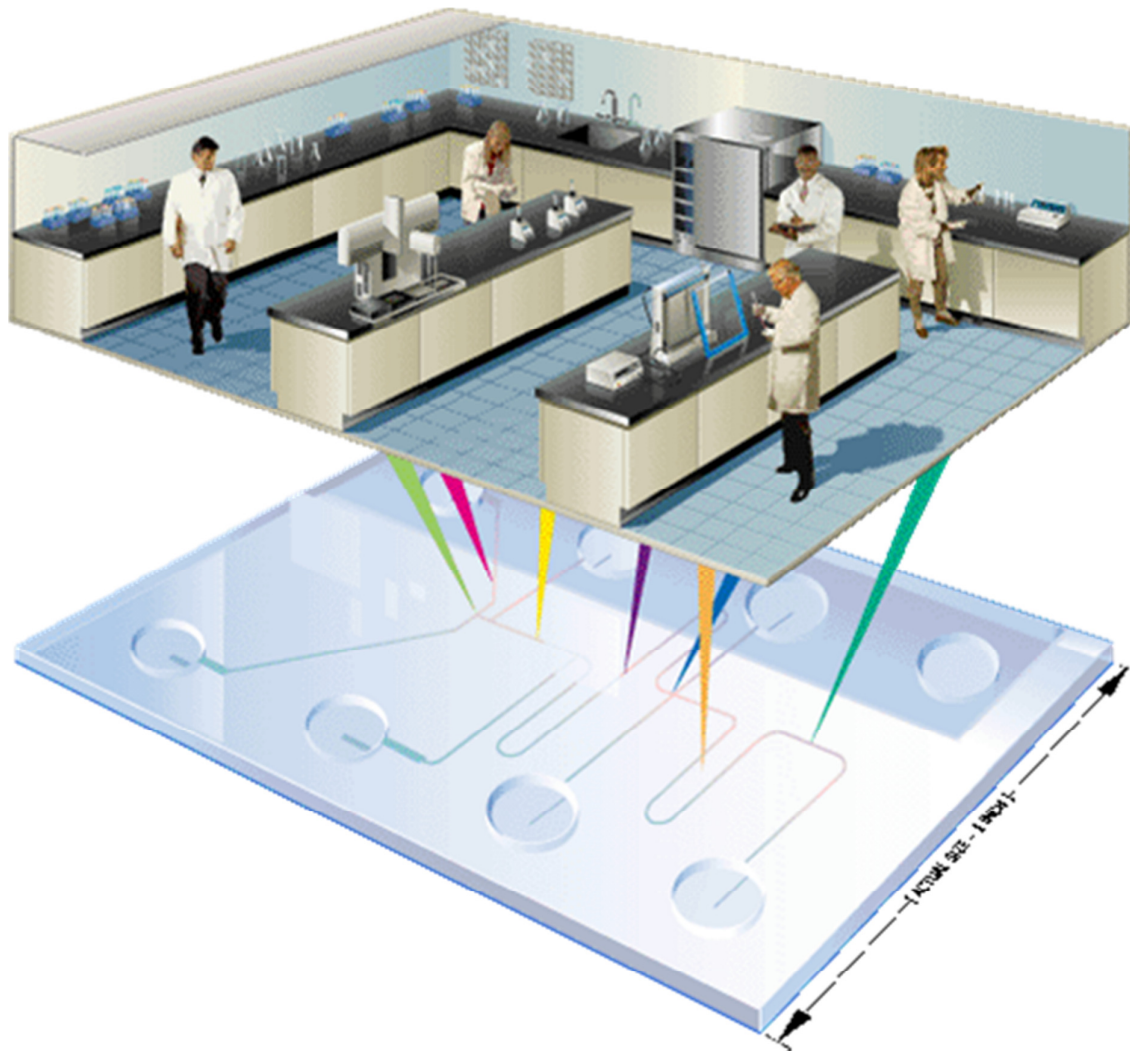


Fig. 1.6. Lab-on-chip concept: scaling down of several laboratory processes on a chip-format (<http://Lab-on-Chip.gene-quantification.info> retrieved in 2014.03).

The range of applications for microfluidic systems is increasing rapidly as more and more researchers become aware of the significant benefits of this technology (Fig. 1.7), while the most highly integrated chips have been developed in the DNA analysis (Erickson and Li 2004; Hahn et al. 2003; van den Berg et al. 2010). The area has considerably grown and a number of specialized reviews and books have been published (Chin et al. 2012; Han et al. 2013; Lei 2012; Lin 2011; Medina-Sanchez et al. 2012; Sollier et al. 2011).

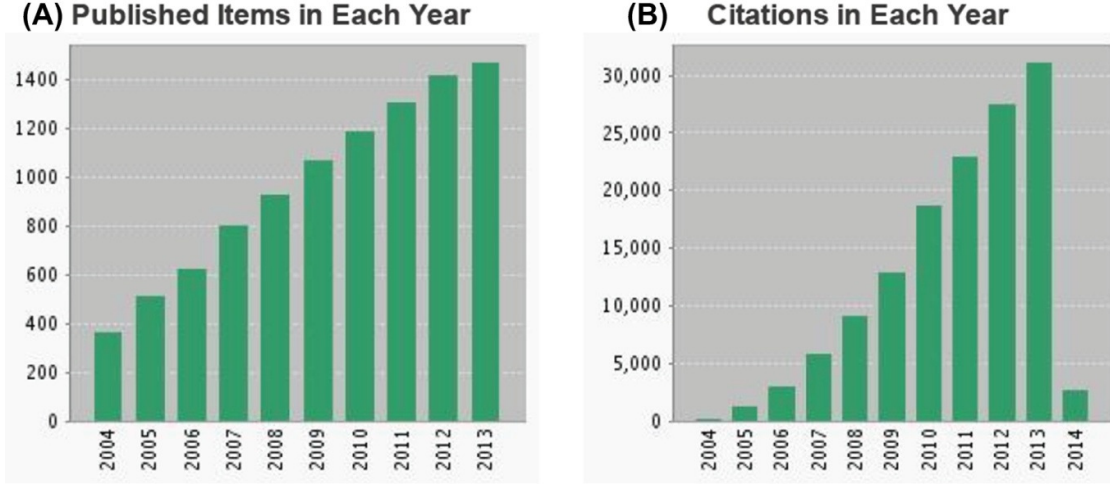


Fig. 1.7. Evolution of the number of (A) publications and (B) citations in the microfluidics field indexed within Web of Science Core Collections from 2004 to 2013 (query: ‘microfluidics’). The number of publications increases linearly with time, while the citations’ number—exponentially.

#### 1.4. Fluid behaviour at microscale

Many phenomena do not simply scale linearly from large to small implementations due to increased surface area-to-volume ratio (eq. 1.1) (Weigl et al. 2008).

$$\frac{\text{surface\_forces}}{\text{volume\_forces}} = \frac{l^2}{l^3} = l^{-1} \xrightarrow{l \rightarrow 0} \infty \quad \text{eq. (1.1)}$$

The relative importance of the inertial versus viscous forces in the flow (i.e. the ratio of the momentum of the fluid to the friction force imparted on the fluid by the walls) is described by Reynolds number (eq. 1.2).

$$Re = \frac{\text{inertial}}{\text{viscous}} = \frac{\rho v L}{\mu} \quad \text{eq. (1.2)}$$

in which  $\rho$  is fluid density;  $v$  is velocity;  $L$  is characteristic dimension (often the smallest length scale of the system, e.g. the smallest width of a channel);  $\mu$  is fluid viscosity. At high Reynolds number, inertial force dominates and the flow is turbulent: irregular with random variation of flow properties (e.g. velocity, pressure, etc.) in both time and space coordinates simultaneously, so advective mass transport occurs in all directions (Weigl et al. 2007). The turbulent flow dominates in everyday life, e.g. river flow, stirring cream in coffee, water filling a sink. At low Reynolds number, the fluid is dominated by viscous force and the flow is laminar: smooth, ordered with constant fluid velocity. The laminar flow is not common in nature, but it can be observed in our daily life with viscous fluids, e.g. pouring honey, squeezing toothpaste, glacier flow. The transition between laminar and turbulent flow



is usually around  $Re = 2000$ , although depending on the system (channel shape, surface roughness, aspect ratio etc.), the turbulence may occur for  $Re > 1000$  (Capretto et al. 2011). For Reynolds numbers from 1 to 1000, non-turbulent inertial effects may occur such as secondary flows in curved channels (Di Carlo 2009). The non-turbulent inertial effects are often used to enhance mixing of the fluids in microsystems.

Fig. 1.8 shows images from Reynolds' 1883 paper, in which various flow regimes were determined and explained. Coloured water was injected with various velocities into clear water (Fig. 1.8A) forming various streak shapes (Fig. 1.8B) and basing on this observation, Reynolds had defined mathematical conditions for forming various flows.

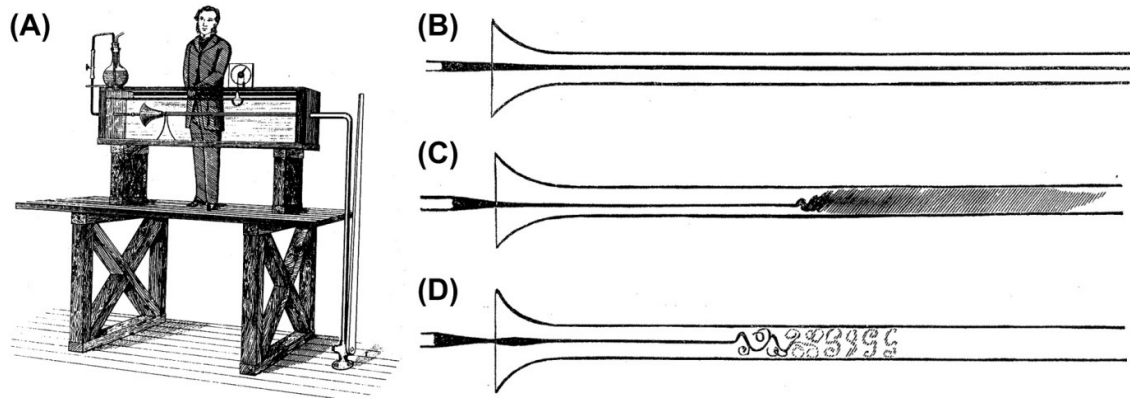


Fig. 1.8. (A) Reynolds' sketch of his 1883 experiment that allowed observation and explanation of various flow regimes: a dye-coloured water was injected with various velocities into clear water. (B) Laminar flow: smooth, ordered with constant fluid velocity. (C) Transitional flow: intermittent pulses of turbulence. (D) Turbulent flow: disorganised with the formation of eddy current. Retrieved from (Reynolds 1883).

In the microfluidic systems,  $Re$  is usually below 1 due to low values of the characteristic dimension. The flow is essentially laminar, where two fluid streams flow in parallel and the mass is transported only in the direction of fluid flow. The only mixing that occurs is the result of diffusion (i.e. process of spreading molecules from a region of higher concentration to one of lower concentration by Brownian motion) across the interface between the fluids (Whitesides 2006). The distance that a molecule will diffuse in time  $t$  is given by eq. 1.3.

$$x = 2\sqrt{Dt} \quad \text{eq. (1.3)}$$

in which  $D$  is diffusion coefficient of the solute in the solvent defined by equation 1.4.

$$D = \frac{k_B T}{6\pi\eta} \quad \text{eq. (1.4)}$$

in which  $k_B$  is Boltzmann's constant,  $T$  the temperature,  $\eta$  liquid viscosity and  $r$  molecule radius. The *advection* (*convection* if heat is being transferred) is a transport mechanism in which molecules are carried along by the local velocity of the fluid (Capretto et al. 2011). The relative importance of advection to diffusion in proving the mass transport associated with mixing is described by Peclet number (eq. 1.5).

$$\frac{\text{advective\_mass\_transport}}{\text{diffusive\_mass\_transport}} = \frac{\frac{L^2}{D}}{\frac{L}{v}} = \frac{vL}{D} \equiv Pe \quad \text{eq. (1.5)}$$

in which  $v$  is the fluid velocity. When  $Pe < 1000$ , molecular diffusion becomes more effective than stirring for mixing (Weigl et al. 2007).

In microscale systems,  $Pe$  is usually low, so mixing is slow requiring long channels and increasing chip footprint. Thus, the mixing efficiency should be enhanced actively (using additional energy source, e.g. ultrasounds) or passively (by channel geometries that increase the contact surface area, e.g. using obstacles) (Capretto et al. 2011).

The advantage of working at low  $Pe$  is that the diffusion distance can be made very small, especially if hydrodynamic focusing is used. Therefore, diffusion-controlled chemical reactions occur more rapidly than in comparable macroscopic reaction vessels (Weigl and Bardell 2004) .

### 1.5. Microfluidics materials

The function of a microfluidic device is greatly influenced by the used structural material. Each material has advantages and disadvantages that determine its applicability. Fig. 1.9 shows the report of the share of various materials for fabrication of microfluidic devices in 2010. Below, main materials for microfluidic device fabrication will be shortly described, indicating their main physical properties, benefits/drawbacks and typical application. The properties of materials used in this PhD work, namely PDMS and SU-8, will be depicted in more details.

## Materials distribution 2010

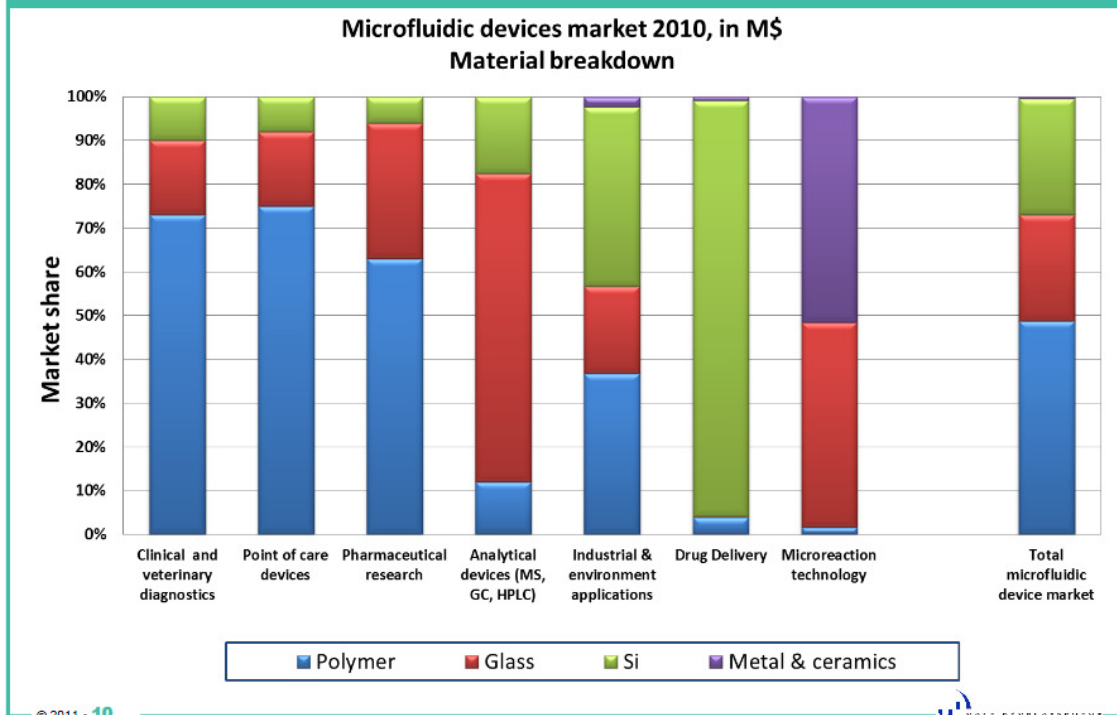


Fig. 1.9. Market share of materials used in microfluidic devices field in 2010 (retrieved from (Yole Développement 2011)). In diagnostics, POC tests and pharmaceutical research, the polymers constitute the most used group due to their low cost and wide range of properties. In the applications involving more aggressive chemicals, silicon, metal and ceramics are more commonly used.

### 1.5.1. Silicon and glass

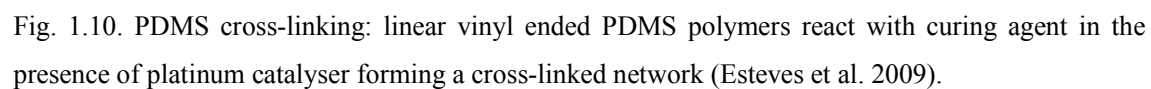
Originally, microfluidic devices were fabricated using technologies adapted from the semiconductor industry (etching and photolithography), so called “hard lithography” in silicon or glass (Abgrall 2007; Hunt and Wilkinson 2008). These techniques are related with fabrication difficulties, high cost and long processing times. Nevertheless, due to their excellent chemical resistance and high thermoconductivity, there are the preferred materials for analytical and microreaction devices (see Fig. 1.9).

### 1.5.2. Polymers

“Hard lithography” materials have largely been displaced by polymers (“soft lithography”) that are usually cheap and can be manufactured using techniques suitable for the mass scale production: once

a high-resolution mould has been made, no more clean-room work is required since a large number of devices can be made quickly by injection moulding, casting or hot embossing. Polymers represent a broad class of materials, providing a wide range of material properties: various optical properties, glass transition temperatures and chemical resistance (Hunt and Wilkinson 2008). The use of polymer-based microsystem techniques leads to devices with a very competitive cost of test (Schuenemann and Harvey 2007), therefore they clearly constitute the most used group, especially in the fields of clinical and veterinary diagnostics and point of care devices, where the unit cost is a critical issue (Yole Développement 2011). Majority of polymers have lower resistivity to non-aqueous solvents, lower melting point and have tendency to adsorb reagents, so their application in drug discovery or chemical production is limited (Becker and Gärtner 2008). Basing on physical properties and related fabrication process, polymers can be divided into elastomers, thermosets and thermoplastics.

Elastomers (e.g. polydimethylsiloxane, PDMS) display rubber-like elasticity due to their chemical structure: they consist in long polymeric chains that do not interact chemically and are only physically entangled. When an external force is applied, the chains disentangle, so the elastomers can easily stretch or compress and then return to original shape when force is withdrawn. Elastomers offer advantages of low cost, the ability to reproduce features with very high fidelity by simple methods like replica moulding (McDonald et al. 2000) and their elasticity is advantageous when fabricating some microfluidic components like pumps and valves (Whitesides 2006). PDMS, one of the most widespread used materials in microfluidics, is biocompatible, thermally stable up to 150 °C, has ability to replicate features with ~1 nm resolution (Feng et al. 2006) and excellent optical properties: high optical transmittance down to 280 nm and low autofluorescence. Fig. 1.10 illustrates the mechanism of the PDMS cross-linking: linear vinyl ended PDMS polymers react with curing agent in the presence of platinum catalyser forming a cross-linked network. PDMS devices can be sealed reversibly onto substrates by conformal contact due to its elasticity or irreversibly without adhesives by plasma or UVO treatment (Becker and Locascio 2002). For that reason, powerful microscale research platforms are commonly fabricated in this material, e.g. a three-dimensional microfluidic platform capable of nucleic acid amplification, rapid isolation and detection of cancer cells (Lien et al. 2010) or ‘organs-on-chips’ devices (Huh et al. 2011). PDMS has high gas permeability which is beneficial when performing long term living cells studies, but is detrimental in quantitative analysis because any loss of water vapour may lead to a drift in pH and disturb the analysis (Sun and Kwok 2006). PDMS disadvantages include poor chemical resistance, hydrophobicity, limited mechanical strength and risk of adsorption/absorption of molecules (Ren et al. 2013; Schuenemann and Harvey 2007). Replica moulding technique has low capital investment cost, but in mass production, the cost per unit does not decrease, therefore it is mainly used for low-volume-manufacturing of microfluidic devices, e.g. in research prototyping (Becker and Gärtner 2008).



Thermosets (also called resins, e.g. SU-8) consist in inflexible three-dimensional chain network. The cross-linking is mediated by heating or radiation exposure and from irreversible chemical bonds, therefore once cross-linked, the thermosets do not soften before decomposition, so cannot be reshaped. Due to their rigid molecular structure, thermosets exhibit high mechanical, thermal and electrical stability and allow to produce high aspect ratio features and also three-dimensional submicron structures (del Campo and Greiner 2007). Their processing is expensive; therefore thermosets are usually used as mould material for high aspect ratio microfluidic devices. SU-8, a high contrast epoxy-based negative photoresist allows obtaining aspect ratio above 20 and layering up to 650  $\mu\text{m}$  by single coating. Due to its high optical transparency, viscosity and high photosensitivity, SU-8 has enabled big progress in microfluidic technologies as with previously used conventional photoresists only features up to 3  $\mu\text{m}$  height could be fabricated, while high aspect ratio features were fabricated by very complex X-ray LIGA process requiring use of synchrotron radiation (Becker and Gärtner 2008; Tabeling 2006). It is biocompatible and allows for fabrication of smooth and vertical side-wall features.

SU-8 consists of three components (Fig. 1.11):

- (i) an epoxy oligomer (EPON SU-8 resin, Shell Chemical) that has eight reactive epoxy group per molecule (hence '8' in the name);
- (ii) a solvent: gamma-butyrolacton in conventional SU-8 series or cyclopentanone in newer series 2000. Cyclopentanone, more polar solvent, gives better coating quality and also evaporates much faster, which is of particular importance for high structures (e.g. for 150  $\mu\text{m}$  high features, in series GM1070 soft bake at 95 °C takes 4 hours, while for SU-8 2050 takes 30 min);
- (iii) a photoinitiator: triarylium-sulfonium salt that upon ultraviolet irradiation generates acid which act then as a catalysts in the cross-linking of the epoxy molecules.

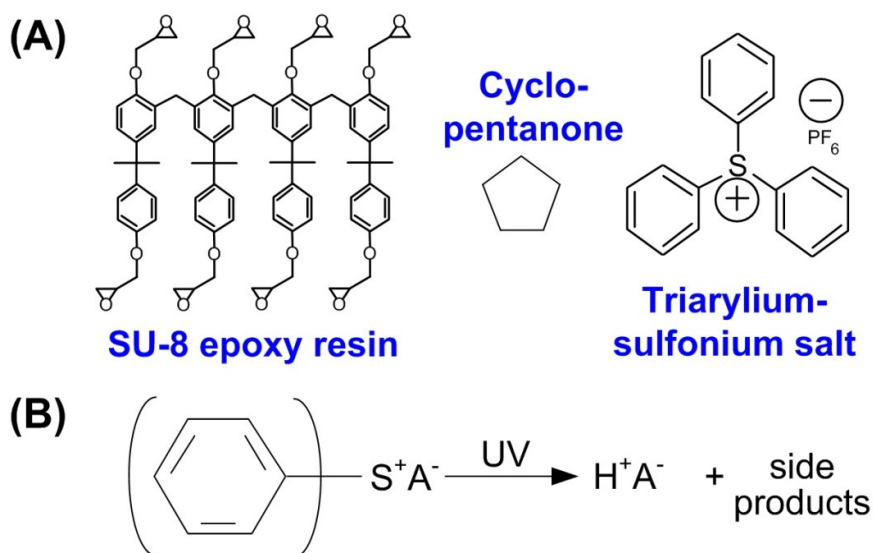


Fig. 1.11. (A) Chemical structure of compounds of SU-8 photoresist: SU-8 epoxy resin molecule; cyclopentanone—solvent used in SU-8 series 2000 (in conventional SU-8 series, gamma-butyrolacton is used) and photoinitiator: triarylium-sulfonium salt. Eight reactive epoxy functionalities allow a high degree of cross-linking after photoactivation. (B) Chemical reaction for photoacid generation upon UV exposure. The generated acid acts as a catalyst in the cross-linking of the epoxy molecules. Adapted from (Al-Mumen et al. 2013).

The cross-linking process is too slow to be completed at ambient temperature; therefore it should be speed up by post baking in temperature above SU-8 glass transition temperature (55 °C). The cross-linking process of the exposed SU-8 regions results in very dense structure due to the presence of eight epoxy group per molecule. The cross-linked SU-8 is insoluble in the subsequent development process and due to the high degree of cross-linking it has excellent mechanical, thermal and chemical properties (del Campo and Greiner 2007).

Thermoplastics (e.g. PMMA, polystyrene) consist in thermo-reversible network that forms or breaks up as the temperature is changed, therefore can be patterned at elevated temperature using injection moulding or hot embossing. It is the most commonly used polymer in commercial macro- and microdevices due to the low cost of their mass scale production. However, due to high initial investment cost (mould fabrication in metal or silicon), thermoplastics are not economical for research prototyping. Their main limitations are related with poor chemical resistance and insufficient gas permeability for long term cell studies.

### **1.5.3. Paper**

Recently, unconventional materials for microfluidic chip fabrication become increasingly popular like paper (Bruzewicz et al. 2008) or hydrogel (Sharma et al. 2011). Fig. 1.12 presents the most promising materials for microfluidic chip fabrication and their cost. Paper is a hydrophilic, porous cellulose matrix, therefore paper itself is a network of channels. To guide a liquid, hydrophobic barriers are embedded in paper, e.g. by wax printing. Paper-based microfluidics are definitely the cheapest microfluidic devices developed so far due to the low material/fabrication cost and transport of liquid by capillary action (Li et al. 2012b). Therefore, they are very promising in the point of care use that is highly sensitive to test cost. Main issues of paper-based microfluidics is ineffective sample consumption due to liquid evaporation (usually 50% reaches the detection zone), poor sensitivity, and low resolution ( $\sim 200\text{ }\mu\text{m}$ ) that hampers high density integration. Besides, solvents of surface tension higher than a critical value may penetrate the hydrophobic channel walls, while the fact that cellulose fibres partially fill the channels increase the complexity of the flow (Thuo et al. 2014).



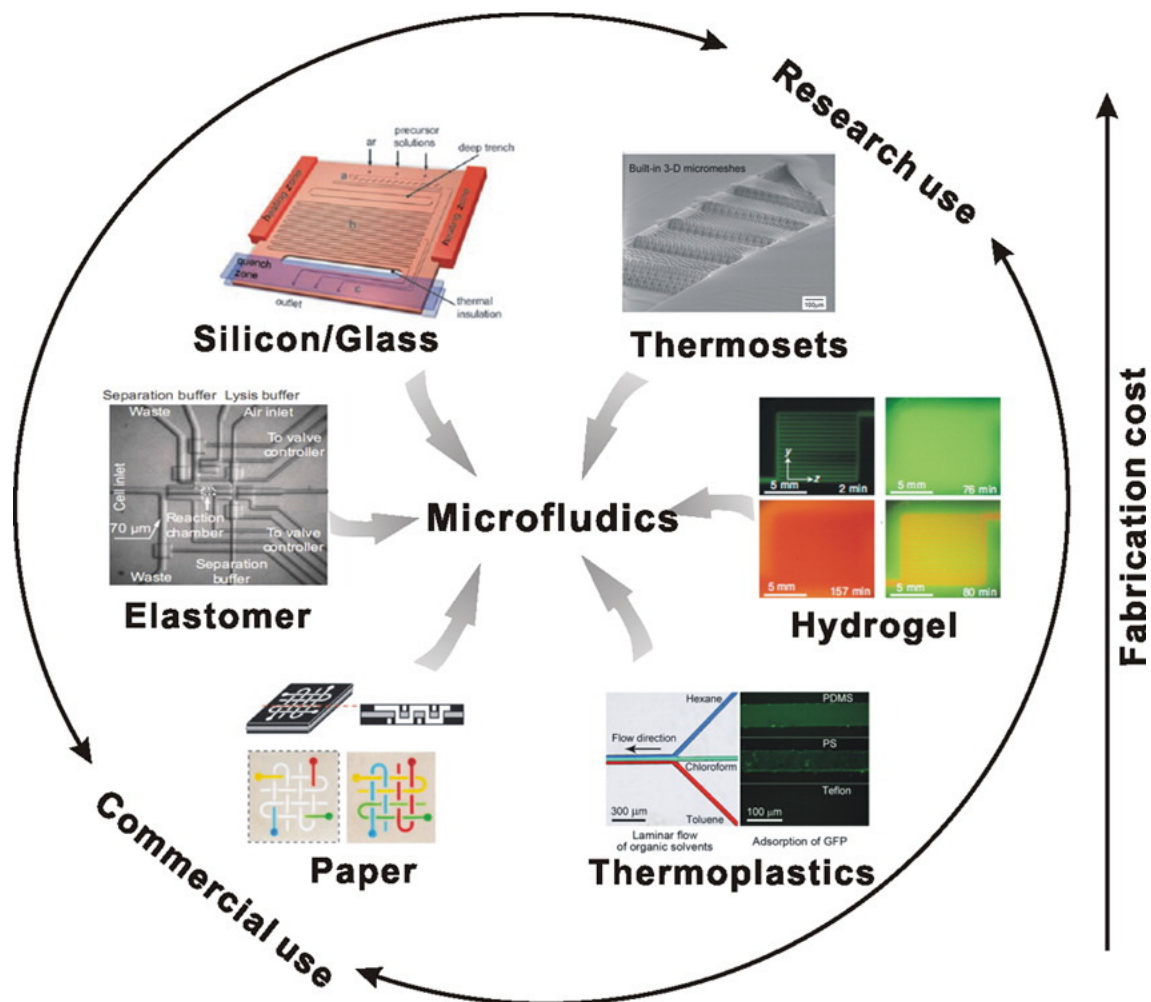


Fig. 1.12. The most promising materials for microfluidic chip fabrication and comparison of the resulting devices' cost. Retrieved from (Ren et al. 2013). Thermosets, inorganic materials and hydrogels have properties suitable for the research level use, while paper may constitute the most spread material in commercial microfluidics.

#### 1.5.4. Materials overview

Table 1.1 presents overview of the main materials for microfluidic chip fabrication comparing their fabrication processes, stability, price and main advantages/disadvantages.

Table 1.1. Main characteristics of the most used materials for microfluidic chip fabrication. Based on (Becker and Gärtner 2008; Ren et al. 2013).

	silicon and glass	polymers			paper
		elastomers	thermosets	thermoplastics	
<b>common technique for microfabrication</b>	wet and dry etching	casting	photolithography	thermomoulding	photolithography; printing
<b>smallest channel dimension</b>	< 100 nm	< 1 $\mu$ m	< 100 nm	~100 nm	~200 $\mu$ m
<b>mechanical stability</b>	very high	low	high	medium	very low
<b>solvent compatibility</b>	very high	low	high	medium	medium
<b>cost</b>	high	medium	medium-high	medium-low	low
<b>main advantage</b>	high chemical, mechanical and thermal stability	low investment cost; oxygen permeability	good chemical, mechanical and thermal stability	low cost in mass production	low cost;
<b>main drawback</b>	very high cost	difficult to scale up	high cost	high investment cost	sample evaporation; low sensitivity
<b>main application</b>	capillary electrophoresis; microreactors	cell-based studies; research platforms	complex research platforms requiring high chemical or thermal stability; moulds for elastomers	mass-scale production of conventional microfluidic devices	colorimetric analysis; mass-scale production

## 1.6. Nanofluidics

Nanofluidics, a research area that emerged in the begging of the 2000s, is a study and application of fluid flow in channels with at least one characteristic dimension below 100 nm (Duan et al. 2013). Ultra high surface-to-volume ratio, size comparable with the range of various surface forces and with size of biomolecules leads to altered behaviour in nanofluidics making this field very promising in biological and energy-related studies. For instance, single molecule analysis may allow observing different subpopulation hidden underneath in conventional studies carried out with large population (Levy and Craighead 2010). The fluid consists of fewer molecules, so discrete nature of molecules can become important (Sparreboom et al. 2010). Nanofluidic devices may enable to answer many fundamental biological questions (e.g. the role of methylation in gene expression, see Fig. 1.13) as

they allow studying the dynamics of single biomolecules in experimentally tuneable nanostructures (Levy and Craighead 2010). On the other hand, the hydrodynamic resistance of the fluid in nanochannels is very high, therefore the pressure driving is not sufficient and it should be combined with the electrical driving.

Recently, the number of publication in nanofluidics field has strongly increased and many patents were published (Dutta and Morse 2008; Michael Chen 2012). Its growing popularity is related with advances in nanofabrication and nano-scale analysis tools. The fabrication of nanofluidics is more complex than in the case of regular nanostructures, because it requires sealing of the nanostructures without collapsing and also connection to fluidic network for sample delivery (Duan et al. 2013).

Nanofluidics may provide a high resolution optical and electrical genetic analysis. The developed so far nanofluidic devices for the continuous and rapid sorting of DNA molecules show results comparable with other technologies (Levy and Craighead 2010). Recently, a nanofluidic platform for real-time detection, automated sorting of individual methylated DNA molecules and collection of sorted molecules has been developed, see Fig. 1.13 (Cipriany et al. 2012). The methylated DNA molecules were recognized using a two-colour fluorescent labels that were used afterwards to actuate sorting. The sorted material was collected and amplified for further post-sorting analysis, proofing the principle. Nevertheless, a low cost, high efficiency, highly sensitive nanofluidic platform for DNA analysis is yet to be developed, however taking into account the progress in the fabrication and integration of nanochannels, it is believed that is not too distant (Deying et al. 2012).

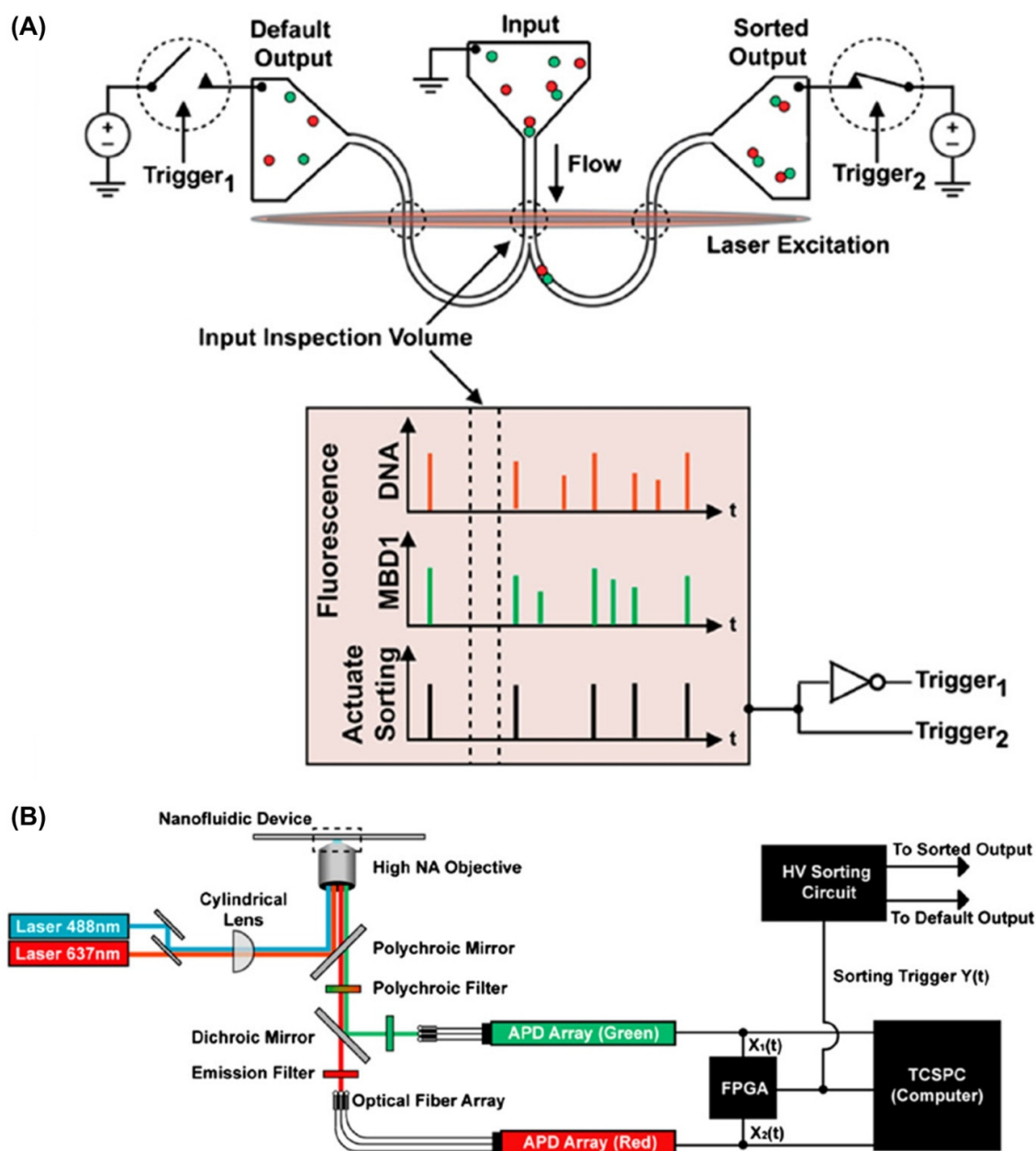


Fig. 1.13. (A) Principle of the single DNA molecule detection and sorting. As each fluorescently labelled molecule passed through the input inspection volume its fluorescence signature was detected, evaluated in real time and used to actuate a sorting trigger to electrically direct the flow towards the sorted output. (B) Nanofluidic platform: nanofluidic device was mounted onto a confocal fluorescence microscope and illuminated by two overlapped lasers to excite molecule fluorescence simultaneously. Single molecule fluorescence was imaged using an optical fibre array connected to single photon counting avalanche photodiodes (APDs). Real-time fluorescence analysis at the input inspection volume was performed and used to trigger a high voltage (HV) sorting circuit to direct the electrokinetic flow of a molecule to the sorted or default output. Adapted from (Cipriany et al. 2012).

### 1.7. Miniaturisation of absorbance-based detection

Optical detection techniques are the most commonly used methods in biology and life sciences in macroscale detection (Bashir 2004). Therefore, it is very attractive to adopt these in lab on chip microsystems and clearly, optical detection approaches have become the most widely applied methods used in connection with miniaturised analytical devices due to its non-invasive nature and rapid response (Lin et al. 2011). All conventional optical detection methods, including absorbance, chemiluminescence, interferometry, surface plasmon resonance and fluorescence have been implemented in microfluidics, while the latter is the most commonly used. Nevertheless, so far only few optical microchips have been commercialized (Myers and Lee 2008). The main issue of miniaturisation of optical detection is poor detection limit due to the small amount of sample at a particular point in time in the miniaturised microchannels. Another problem is related with packaging challenges and the difficulties in coupling the light into and out of channels. Since biosensor systems usually consist in disposable chips and a non-disposable host device, the exchange of the chips should be easy and operator-independent. Therefore, to be more user friendly, the light source and the photodetector should be integrated in the holder, while on-chip coupling optics should be included in the chips to allow large alignment tolerances (Mogensen and Kutter 2009). If these issues would be overcome, optical detection could become a very popular in POC devices, because it enables high scale multiplexing, as commercial CCD image sensors could detect numerous reactions simultaneously (Gotz and Karst 2007). Besides, the optical detection offers advantage of cheap instrumentation thanks to the rapid reduction in the cost of optoelectronic components like image sensors and diodes (Myers and Lee 2008).

Detection through optical absorption is the most widely used detection method in common macro-structure sensing systems (Kuswandi et al. 2007), employing either direct absorption in the UV/visible wavelength range or a colorimetric assay (Hunt and Wilkinson 2008). In absorption-based detection, changes in optical density are usually sufficient for diagnosis, so instrumentation is much simpler than for other optical methods. However, the popularity of absorption detection has not translated to the microscale systems, because the reduction in path length within the microdevice directly impacts the absorption sensitivity as described by the Lambert–Beer law:

$$A = \epsilon lc \quad \text{eq. (1.6)}$$

where  $A$  is the absorbance,  $\epsilon$  the analyte's molar extinction coefficient,  $l$  the path length and  $c$  the analyte concentration (King et al. 2014). A diversity of attempts to overcome limitation of short optical path in microsystems has been recently highlighted and discussed in several reviews (Gotz and Karst 2007; Hunt and Wilkinson 2008; King et al. 2014; Kuswandi et al. 2007; Viskari and Landers 2006). The path length in microfluidic systems can be extended by detecting along a channel segment in the plane of the device, the use of integrated optical fibbers with longitudinal transmission,

detection cells with extended light paths (*e.g.* Z-shaped and U-shaped microchannels) (Mogensen et al. 2001) or multi-reflection cells (Llobera et al. 2007), among others. In order to facilitate chip exchange, waveguides can be integrated for the coupling of light into the detection region (Baig et al. 2013; Feidenhans'l et al. 2014; Garcia et al. 2012; Missinne et al. 2014). On the other hand, as light from an optical fibre is highly divergent, both fibres usually need to be very close to yield sufficient transmittance. This problem can be overcome by incorporating additional on-chip optical components, such as microlenses to reduce light divergence (Camou et al. 2003; Mohammed and Desmulliez 2013) and microapertures to block stray light (Ro et al. 2005). Furthermore, light source (*e.g.* dye laser) and photodetectors can be incorporated on chip to reduce the optical losses and proving the feasibility of fully-integrated, operator-independent lab-on-chip for absorbance measurements, see Fig. 1.14 (Balslev et al. 2006). Nevertheless, the cost of this device is relatively high due to use of SU-8 as structural material, requiring expensive processing. More recently, other integrated chips for absorbance measurements have been developed, however their processing is probably still too expensive to be used in the point of care (deMello et al. 2009; Krishnaswamy et al. 2013; Watts et al. 2012).

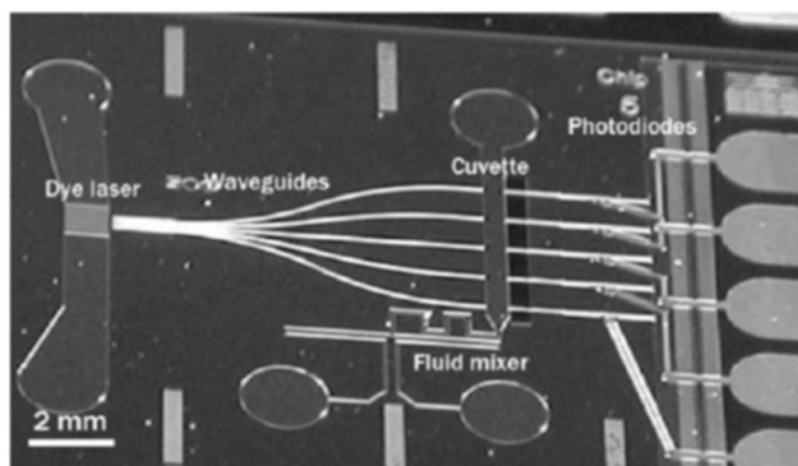


Fig. 1.14. Photograph of the lab-on-chip for absorbance measurements with integrated microfluidic dye laser, waveguides, microchannels and photodiodes. All the optical and fluidic components were fabricated in SU-8, while planar c-Si n-type diodes are embedded in a c-Si p-type substrate. This device proves the feasibility of fully-integrated lab-on-chip for absorbance measurements, however its cost is relatively high due to use of c-Si and SU-8 as structural material. Retrieved from (Balslev et al. 2006).

Lately, paper-based microfluidics are becoming increasingly popular, especially in colorimetric detection, owing to their low cost and the ease in use (Veigas et al. 2012; Yetisen et al. 2013), however they suffer from low sensitivity and liquid evaporation, therefore their applicability is limited.

### **1.8. Motivation and objectives**

Due to the importance and wide applications of the DNA analysis, there is a need to make genetic analysis more available and more affordable. The colorimetric DNA biosensor based on non-cross-linking Au-nanoprobe hybridisation and amorphous/nanocrystalline silicon photodetector shows advantage of low cost, portability, sensitivity and simple instrumentation using 60  $\mu$ l of solution per assay (10 mm long optical path length; Fig. 1.5). However, to meet requirements for POC use, this biosensor should be further optimized. As such, the main objective of this PhD work is to improve the colorimetric DNA biosensor based on non-cross-linking Au-nanoprobes hybridisation by reducing its price and minimizing the needed volume of solution without compromising the device sensitivity and reliability.

The first objective was to reduce the biosensor cost by replacing the silicon-based photodetector by an inexpensive, solution-processed device. The  $\text{TiO}_2$  photodetector has been chosen for this purpose due to its low cost and colour sensitivity that can be easily tuned by changing the dyes used in sensitization. Among various solution-processed techniques, we have selected inkjet printing because it enables to obtain more uniform coverings spanning larger areas and to deposit material layer by layer, so highly porous structure can be achieved increasing the device photosensitivity.

The cost per tests could be also reduced by lowering the needed volume of solution to minimize the reagents consumption. Initially, we have developed macro-machined PDMS containers to be integrated in chip carrier for vertical colorimetric detection. Nevertheless, it was challenging to significantly reduce the volume using macro-machining tools (minimum achieved solution volume: 50  $\mu$ l; 2 mm long optical path) and also the biosensor sensitivity was not sufficient to detect the colorimetric changes in these containers, most probably due to high optical losses.

At that point, we have realized that the developed biosensor performance could be greatly improved by integration of microfluidic devices as they may allow to considerably reduce the solution volume, integrate all biosensors elements, automatically mix reagents, amplify DNA target and perform sample purification, providing a “bleed and read” device for DNA analysis. Furthermore, these tasks could be performed much faster and with better temperature control than in macroscale and with high degree of parallelisation allowing simultaneous acquisition of the control tests.

In the first step towards the lab-on-chip device for integrated DNA analysis, a bio-microfluidic platform for colorimetric DNA detection should be developed. The aimed device should enable detection with much lower volume than in the state-of-the-art biosensor; clearly distinguish between positive and negative assays of various DNA targets with single mismatch sensitivity and low detection limit.

In the second step towards lab-on-chip device, to enable reagents mixing on chip, micromixers should be developed. These micromixers should allow efficient mixing of water based solutions at wide Reynolds number range, but in particular at  $Re$  below 1 (typical range for microfluidic systems) with minimal pressure drop.

## **1.9. Thesis outline**

This PhD thesis is structured in article-based form: each results chapter (chapter 3–6) is based on manuscripts already published or under preparation. The articles have been edited for the thesis consistency and also to provide additional results. The articles' Supplementary information has been merged into the article text for the reading flow. In the summary of each results chapter, there is provided information how the chapter differs from the corresponding article.

The general introduction (chapter 1) provides fundamental background, literature overview and objectives of this work giving the broader view for to the introduction sections given in each results chapter. It also states the relationship among the presented articles.

Chapter 2 gives supplementary information to the experimental details given in each results chapter to facilitate the reproduction of performed tests. The emphasis is put on the most critical step: optimization of the chips' microfabrication process.

Chapter 3 describes the optimization of the colorimetric DNA biosensor by development of low cost  $\text{TiO}_2$  photodetectors. Chapters 4–6 are related with the miniaturisation the biosensor by means of microfluidic technology. The development of bio-microfluidics platform for optical detection is described in chapter 4 presenting the design, fabrication and characterisation of microfluidic chips' and proof of the concept. Chapter 5 depicts the platform optimization by incorporation of microlenses to enable detection of single nucleotide polymorphism. Chapter 6 is devoted to the design, performance tests and results statistical evaluation of micromixers to be applied for reagents mixing in the miniaturised biosensor.

Finally, chapter 7 presents the general conclusions for the thesis as a whole and suggestions for the future work.



## 1.10. List of publications

*Included in this thesis:*

- Bernacka-Wojcik, I., Senadeera, R., Wojcik, P.J., Silva, L.B., Doria, G., Baptista, P.V., Aguas, H., Fortunato, E., Martins, R., 2010. Inkjet printed and “doctor blade” TiO<sub>2</sub> photodetectors for DNA biosensors. *Biosensors and Bioelectronics*, 1229–1234.
- Bernacka-Wojcik, I., Lopes, P., Vaz, A.C., Veigas, B., Wojcik, P.J., Simões, P., Barata, D., Fortunato, E., Baptista, P.V., Águas, H., Martins, R., 2013. Bio-microfluidic platform for gold nanoprobe based DNA detection—application to *Mycobacterium tuberculosis*. *Biosensors and Bioelectronics* 48(0), 87–93.
- Bernacka-Wojcik, I., Ribeiro, S., Wojcik, P.J., Alves, P., Busani, T., Fortunato, E., Baptista, P.V., Águas, H., Hilliou, L., Martins, R. 2014. Experimental optimization of a passive planar rhombic micromixer with obstacles for effective mixing in a short channel length.. *RSC Advances*. DOI: 10.1039/C4RA10160J.

*Not included in this thesis:*

- Filonovich, S.A., Águas, H., Bernacka-Wojcik, I., Fortunato, E., Martins R., 2009. Highly conductive p-type nanocrystalline silicon films deposited by rf-PECVD using silane and trimethylboron mixtures at high pressure. *Vacuum* 83, 1253–1256.
- Águas, H., Filonovich, S.A., Bernacka-Wojcik, I., Fortunato, E., Martins, R., 2010. Role of trimethylboron to silane ratio on the properties of p-type nanocrystalline silicon thin film deposited by radio frequency Plasma Enhanced Chemical Vapour Deposition. *Journal of Nanoscience and Nanotechnology* 10, 2547–2551.
- Tillak, J.B., Bernacka-Wojcik, I., Barata, D., Jorge, P.A.S., Águas, H., Oliva, A.G., 2011. Towards single cell spectroscopy and refractometry in microfluidic chip platforms. *Proc. of SPIE* 8001, 800112.
- Ribeiro, A.R., Martinho, I., Tillak, J.B., Bernacka-Wojcik, I., Barata, D., Jorge, P.A.S., Águas, H., Oliva, A.G., 2012. Microfluidic chip for spectroscopic and refractometric analysis. *Proc. of SPIE* 8421, 84211Y.

## 1.11. List of presentations

*Oral presentations:*

- Bernacka-Wojcik, I., Águas, H., Wojcik, P.J., Barquinha, P., Vilà, A., Font, J., Oliva, A., Fortunato, E., Martins, R., 2009. Optimization of fabrication process for microchannels

utilizing SU-8 photoresist. V International Materials Symposium MATERIAIS 2009. Lisbon, Portugal.

- Bernacka-Wojcik, I., Senadeera, R., Wojcik, P.J., Silva, L.B., Doria, G., Baptista, P., Aguas, H., Fortunato, E., Martins, R., 2009. From gold nanoparticles to "toothpaste" for DNA detection. Workshop Nano09, Braga, Portugal.
- Bernacka-Wojcik, I., Senadeera, R., Wojcik, P.J., Silva, L.B., Doria, G., Baptista, P., Aguas, H., Fortunato, E., Martins, R., 2010. Colorimetric DNA biosensor based on gold nanoparticles and inkjet printed TiO<sub>2</sub> photodetector. Jornadas Tecnologicas da FCT 2010 (JORTEC), Caparica, Portugal.
- Bernacka-Wojcik, I., Águas, H., Lopes, P., Veigas, B., Wojcik, P.J., Simões, P., Igreja, R., Fortunato, E., Baptista, P.V., Martins, R., 2014, Bio-Microfluidic platform for gold nanoprobe based DNA detection with embedded microlenses for improved performance. Biosensors 2014, Melbourne, Australia. Accepted for oral presentation.

*Contribution in oral presentations:*

- Wojcik, P.J., Bernacka-Wojcik, I., Fortunato, E., Martins, R., 2010. Inkjet printed dye sensitized solar cells, The International Chemical Congress of Pacific Basin Societies—PacifiChem 2010, Honolulu, USA.
- Tillak, J.B., Bernacka-Wojcik, I., Barata, D., Jorge, P.A.S., Águas, H., Oliva, A.G., 2011. Towards single cell spectroscopy and refractometry in microfluidic chip platforms. International Conference on Applications of Optics and Photonics, Braga, Portugal.
- Oliva, A.G., Tillak, J.B., Bernacka-Wojcik, I., Barata, D., Jorge, P.A.S., Águas, H., 2011. Development of a microfluidic platform for erythrocyte monitoring under opto-electronic sensors. Workshop “Microfluidics, from single molecule to cell biology” INTERBIO IECB, Bordeaux, France.
- Ram, S.K. Bernacka-Wojcik, I., Vicente, A., Barata, D., Wojcik, P.J., Busani, T., Diaconu, B., Águas, H., Fortunato, E., Martins, R., 2011. Single step preparation technique of multidimensional microfluidic system. E-MRS Fall 2011, Symposisum F, Warsaw, Poland.
- Filonovich, S.A., Águas, H., Araujo, A., Bernacka-Wojcik, I., Ram, S.K., Busani, T., Ferreira, I., Fortunato, E., Martins, R., 2011. Structural and electrical characterization of very thin p-type nanocrystalline Si thin films. E-MRS Fall 2011, Symposisum B, Warsaw, Poland.
- Ram, S.K. Bernacka-Wojcik, I., Vicente, A., Wojcik, P.J., Busani, T., Barata, D., Diaconu, B., Águas, H., Fortunato, E., Martins, R., 2011. Non-lithographic approach to create periodic nanowrinkled microchannels for ultrasensitive sensors detection. E-MRS Fall 2011, Symposisum F, Warsaw, Poland.

- Jorge, P.A.S., Ribeiro, A., Martinho, I., Bernacka-Wojcik, I., Águas, H., Martins, R., Oliva, A.G., Guerreiro, A., Soperra, O., Marques, P., 2013. Advances in Optofluidics: Integration of Optical Control and Photonics with Microfluidics. MPNS COST Action 1205—Working Group Meeting, and ESR workshop in conjunction with NOMA 2013 Conference, Cetraro, Italy.

*Posters:*

- Bernacka-Wojcik, I., Senadeera, R., Wojcik, P.J., Silva, L.B., Doria, G., Baptista, P.V., Aguas, H., Fortunato, E., Martins, R., 2009. Inkjet printed and “doctor blade” TiO<sub>2</sub> photodetectors for DNA biosensors. NanoBioTech 2009 Conference, Montreux, Switzerland
- Bernacka-Wojcik, I., Águas, H., Baptista, P., Fortunato, E., Martins, R., 2009. Optimization of profile of microchannels fabricated in SU-8. NanoBioTech 2009 Conference, Montreux, Switzerland
- Bernacka-Wojcik, I., Senadeera, R., Wojcik, P.J., Silva, L.B., Doria, G., Baptista, P., Aguas, H., Fortunato, E., Martins, R., 2010. Colorimetric DNA biosensor based on gold nanoparticles and inkjet printed nanocrystalline TiO<sub>2</sub> photodetector, The 3rd International Conference on Advanced Nano Materials (ANM 2010), Agadir, Marocco.
- Bernacka-Wojcik, I., Senadeera, R., Wojcik, P.J., Silva, L.B., Doria, G., Baptista, P., Aguas, H., Fortunato, E., Martins, R., 2010. Inkjet printed and “doctor blade” TiO<sub>2</sub> photodetectors for DNA biosensors. Biosensors 2010 Congress, Glasgow, United Kingdom.
- Bernacka-Wojcik, I., Aguas, H., Hilliou, L., Ribeiro, S., Wojcik, P.J., Baptista, P., Covas, J., Fortunato, E., Martins, R., 2014. Mixing performance of passive rhombic micromixer with diamond-shape obstacles for DNA biosensor application. Biosensors 2014, Melbourne, Australia. Accepted for poster presentation.

*Contribution in posters:*

- Wojcik, P.J., Bernacka-Wojcik, I., Senadeera, R., Baptista, P., Fortunato, E., Martins, R., 2009. Inkjet printed titanium dioxide for dye sensitized photodetectors, Plastic Electronics Europe 2009, Dresden, Germany.
- Tillak, J.B., Jorge, P.A.S., Bernacka-Wojcik, I., Águas, H., Barata, D., Oliva, A.G., 2010. Evaluation of different strategies for single cell refractometry in microfluidic chips. EWOFs'2010. 4<sup>th</sup> European Workshop on optical fibre sensors, Porto, Portugal.
- Tillak, J.B., Jorge, P.A.S., Bernacka-Wojcik, I., Águas, H., Barata, D., Oliva, A.G., 2010. Evaluation of different strategies for single cell refractometry in microfluidic chips. SEON 2010—VIII Symposium on Enabling Optical Networks, Porto, Portugal.

- Ram, S.K. Vicente, A., Bernacka-Wojcik, I., Busani, T., Diaconu, B., Águas, H., Fortunato, E., Martins, R., 2011. Fabrication of doped and undoped Silicon Nanowires on Transparent Conducting Oxide Coated Substrates for Photovoltaic Applications. E-MRS Fall 2011, Symposium H, Warsaw, Poland.
- Tillak, J.B., Bernacka-Wojcik, I., Barata, D., Jorge, P.A.S., Águas, H., Oliva, A.G., 2012. Microfluidic Chip for Simultaneous Spectroscopic and Refractometric Cell Analysis. Eurotrode XI, Barcelona, Spain.
- Pereira, F., Aguas, H., Barreiros, M., Amorim, A., Horta, S., Bernacka-Wojcik, I., Igreja, R., Fortunato, E., Martins, R., Oliva, A.G., 2014. Single cell analysis in microfluidic chip using impedance spectroscopy—development of instrumentation. Biosensors 2014, Melbourne, Australia. Accepted for poster presentation.
- Pereira, F., Aguas, H., Bernacka-Wojcik, I., Ribeiro, R.S., Jorge, P., Fortunato, E., Martins, R., Oliva, A.G., 2014. Construction of an optical-electrical hybrid microfluidic chip platform for individual cell characterization. Flow14 Conference, Twente, Netherlands. Accepted for poster presentation.
- Pereira, F., Aguas, H., Barreiros, M., Amorim, A., Horta, S., Bernacka-Wojcik, I., Igreja, R., Fortunato, E., Martins, R., Oliva, A.G., 2014. Single cell analysis in microfluidic chip using impedance spectroscopy—development of instrumentation. Flow14 Conference, Twente, Netherlands. Accepted for poster presentation.

## **Chapter 2**

### **Fabrication and characterisation techniques**



<b>Chapter 2. Fabrication and characterisation techniques .....</b>	<b>37</b>
<b>Summary.....</b>	<b>37</b>
<b>2.1. Fabrication techniques .....</b>	<b>37</b>
2.1.1. “Doctor blade” method .....	37
2.1.2. Inkjet printing .....	38
2.1.3. Spin coating .....	40
2.1.4. Photolithography.....	40
2.1.5. Replica moulding soft-lithography .....	42
<b>2.2. Chip fabrication .....</b>	<b>43</b>
2.2.1. Before the SU-8 processing .....	45
2.2.2. SU-8 spin coating .....	45
2.2.3. Soft bake .....	46
2.2.4. Exposure .....	47
2.2.5. Post bake .....	54
2.2.6. Development.....	54
2.2.7. Casting of PDMS mould.....	55
2.2.8. Casting of epoxy mould.....	56
2.2.9. Casting of PDMS chips .....	56
2.2.10. Sealing of PDMS chips.....	57
<b>2.3. Characterisation techniques.....</b>	<b>60</b>
2.3.1. Scanning electron microscopy .....	62
2.3.2. Spectrophotometry.....	62
2.3.3. Stylus profilometry .....	64
2.3.4. Determination of features’ thickness using optical microscopy .....	65
2.3.5. Confocal scanning microscopy .....	66





## **Chapter 2. Fabrication and characterisation techniques**

### **Summary**

The experimental details are provided in each results chapter (chapters 2–6), whereas in this section, additional information will be given to facilitate reproduction of performed tests. Firstly, main fabrication techniques will be shortly represented, then the chip fabrication—the most critical and most time consuming process—will be described with more details to allow their easy reproduction and also to simplify to other users the optimization of SU-8 processing for other layer thicknesses. Besides, the characterisation techniques used for all studied materials/devices will be summarized and the most used methods will be shortly depicted.

### **2.1. Fabrication techniques**

#### **2.1.1. “Doctor blade” method**

“Doctor blade” method, called also sliding method or tape casting, is a common technique for producing thin films on large area surfaces. A well mixed suspension of ceramic particles (e.g.  $\text{TiO}_2$ ) with additives, (such as solvent, binders, dispersants) is placed on a substrate and spread by sliding a glass rod (squeegee) over the substrate to form homogeneous and smooth layer (preferably, the rod should be moved in one direction) (Aegerter et al. 2004). For the patterning, adhesive tape can be used to form a channel where the paste can flow (Fig. 2.1). Thickness of tape will determine thickness of resulting  $\text{TiO}_2$  layer, so more layers of tape can be used to increase thickness. Then, the paste excess is removed and the layer is left to dry naturally. When the layer becomes almost transparent, the tape is carefully removed.

In the case of producing of  $\text{TiO}_2$  photodetector by “doctor blade” method, the paste consists in  $\text{TiO}_2$  powder (0.2 g; e.g. P-25), acetic acid (0.2 ml; to reduce pH) and Triton X-100 (1 drop; to decrease surface tension for stress reduction). These ingredients should be mixed well and then left to rest for 30 min. Grinding continuously for 30 min, 3 ml of ethanol is slowly added. The resulting paste should be thicker than water, but thinner than wall paint.

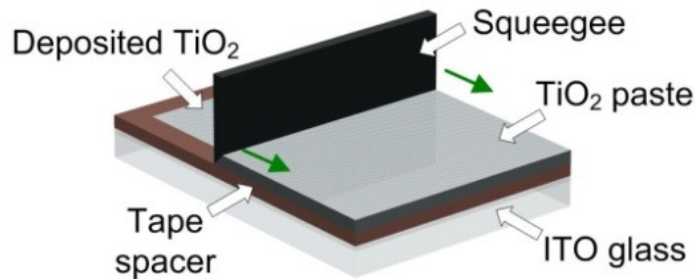


Fig. 2.1. Principle of “doctor blade” method: suspension of ceramic particles (e.g.  $\text{TiO}_2$ ) with additives is placed on a substrate and spread by sliding a glass rod (squeegee) over the substrate to form homogeneous and smooth layer.

Due to the low viscosity of the  $\text{TiO}_2$  paste, it is difficult to get thick enough crack-free films by “doctor blade” method (Senadeera et al. 2005b). Besides, as the layer thickness is determined by tape thickness, it is difficult to finely-tune film thickness.

### 2.1.2. Inkjet printing

Inkjet printing is a solution-processed, automated deposition method based on expelling of picoliter droplets of liquid ink from the nozzle one at a time while moving the print-head above the substrate. Fig. 2.2 indicates main characteristics, requirements, possibilities and challenges of the inkjet printing technology (Teichler et al. 2012). It allows non-contact patterning on almost any type of substrate (Dang et al. 2013). Inkjet printing is highly material-efficient, additive method as it uses only material that is needed for the pattern, while in subtractive methods like spin coating, majority of the applied material is wasted. Layer of thickness from hundreds of nanometres up to of tens of micrometres can be obtained with possibility of fine tuning of the film thickness. Inkjet printing is data driven, i.e. does not requiring tooling such as mask or screens, and the patterning is controlled directly by CAD data, so it is highly flexible.

The quality of the printed films depends strongly on the printing parameters (e.g. the dot spacing) and proper formulation of stable, printable inks (e.g. viscosity, surface tension). To prevent nozzle clogging, size of particles should at least 100 times smaller than nozzle diameter. Inkjet printed films are formed by picolitre drops and it is challenging to control properly the position of these drops, therefore the layer homogeneity might be an issue (Teichler et al. 2012). Due to the low printing speed, printing of thick layers is time consuming, thus inkjet printing is more adequate for thinner layers patterning.

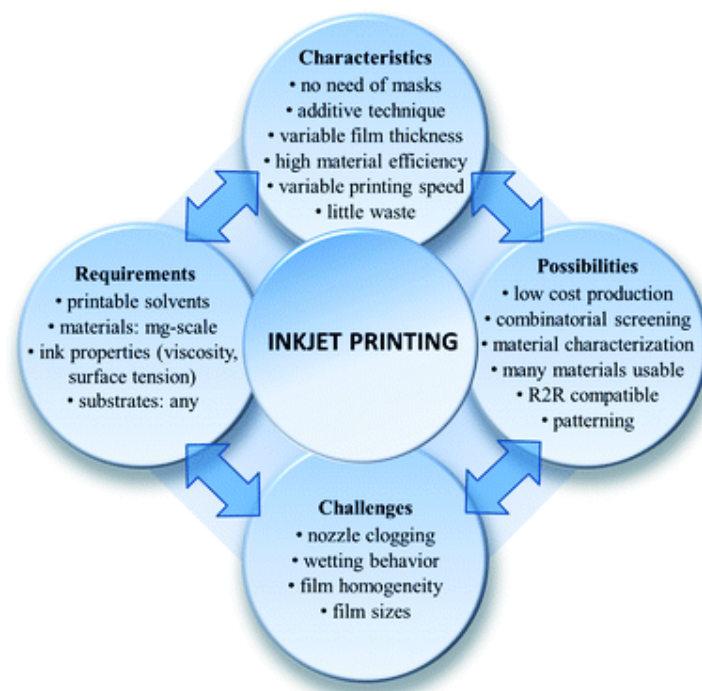


Fig. 2.2. Main characteristics, requirements, possibilities and challenges of the inkjet printing technology. Retrieved from (Teichler et al. 2012).

In this PhD project, desktop printed (Canon PIXMA IP4500) was used for fabrication of the  $\text{TiO}_2$  photodetector prototype (section 3.3.1) and a lab-scale printer (LP50 PixDRO) was used in the  $\text{TiO}_2$  optimization study (section 3.3.4), see Fig. 2.3.

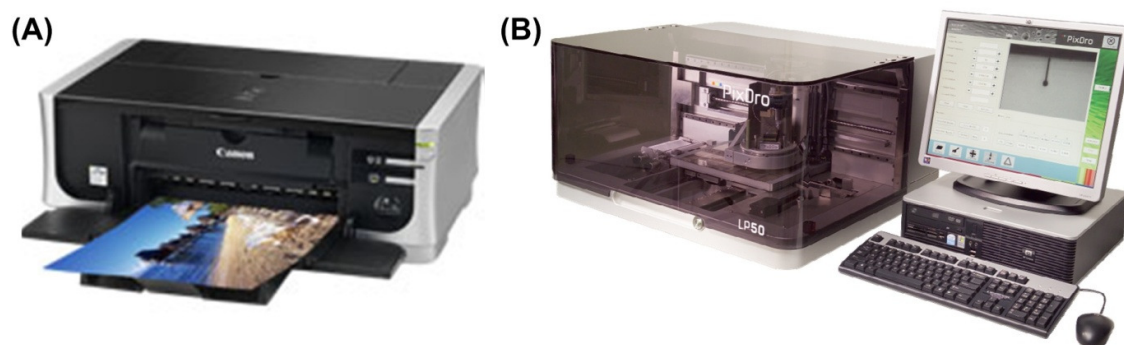


Fig. 2.3. Photographs of inkjet printers used in this work: (A) desktop printed (Canon PIXMA IP4500) used for fabrication of the  $\text{TiO}_2$  photodetector prototype and (B) lab-scale printer (LP50 PixDRO) used in the  $\text{TiO}_2$  optimization.

### 2.1.3. Spin coating

One of the simplest and most common methods of fabricating thin films is spin coating. Liquid material is dispensed onto the centre of a substrate and rotated at high velocities (typically between 1000 rpm and 10000 rpm) spreading the materials and forming a thin film layer (Fig. 2.4A). The final film thickness depends on the material properties such as viscosity, evaporation rate, surface tension and spinning parameters. During rotation, the fluid flows gradually outward to edges, however this flow is not enough strong to instantaneously make the resist to fly off the edges. Therefore, resist layer on the edges is thicker forming so called edge bead (Fig. 2.4B), that is inversely proportional to the spinning speed (Nima 2013).

The main limitation of spin coating is related with the fact that only one substrate can be coated at a time and large amount of waste (90% of applied material) (Teichler et al. 2012).

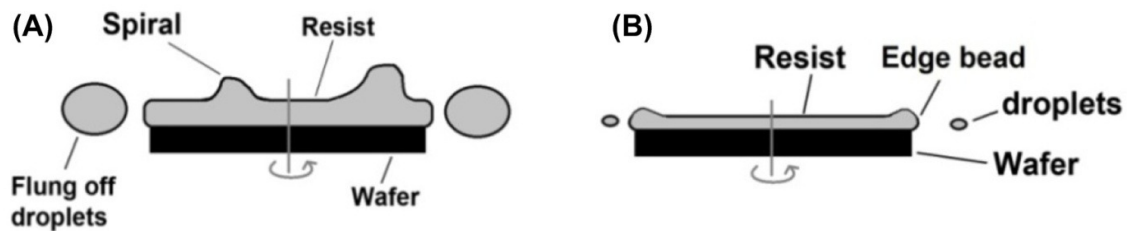


Fig. 2.4. (A) Schematic representation of spin coating process: the sample is rotated at high speed spreading the material and forming thin film layer. (B) The thickness distribution of spin coated layer showing the edge bead formed along wafer borders. Retrieved from (Nima 2013).

In this work, spin coating (spinner Karl Suss CT62, Suss MicroTec, Germany) was used to determine thickness of SU-8 (section 2.2.2) and PDMS slab for sealing of macro-machined containers (section 4.2.1).

### 2.1.4. Photolithography

Photolithography, probably the most important process in microfabrication, is a patterning method that uses irradiation to transfer a pattern to a substrate. The irradiation through a mask a photoresist layer initiates physico-chemical reactions, which enable selective removal of resist in the development. In positive resists, the exposed areas become more soluble in the developer, and in negative resists, the exposed parts become insoluble (Franssila 2010). The resolution is determined by mask dimensions, diffraction at mask edges and energy source (X-ray, UV light or electron beam). A shorter wavelength radiation enables to obtain higher lateral resolution features, however the most common is the UV photolithography (300–450 nm) due to its lower cost (Tabeling 2006).

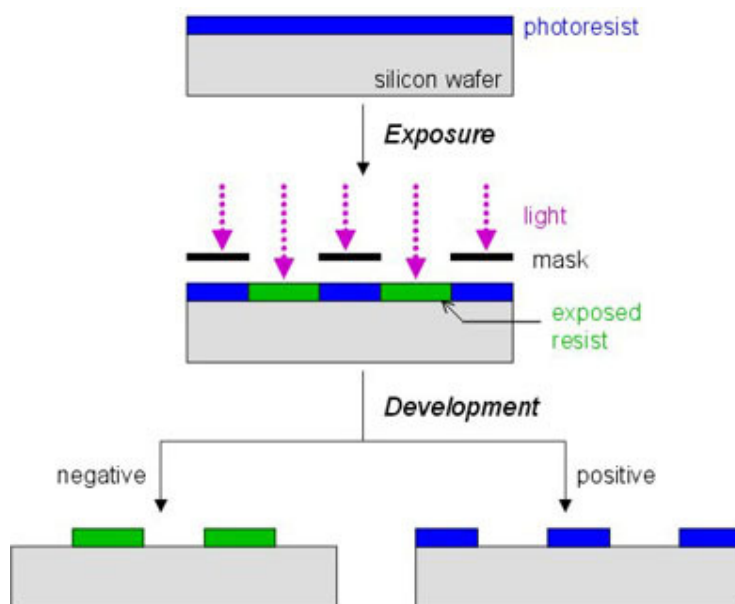


Fig. 2.5. Principle of the photolithography process: irradiation through a mask a photosensitive resist layer. The irradiation initiates physico-chemical reactions in the polymer, which enable selective removal of resist in the development. In positive resists, the exposed areas become more soluble in the developer, and in negative resists, the exposed parts become insoluble (<http://www.objective.com/metaldeposition> retrieved in 2014.03).

In this work, photolithography was performed using mask aligner MA6 (Suss, Germany) with UV 400 optics for SU-8 patterning. The details of the SU-8 photolithography procedure and its optimization are given in section 2.2.4.

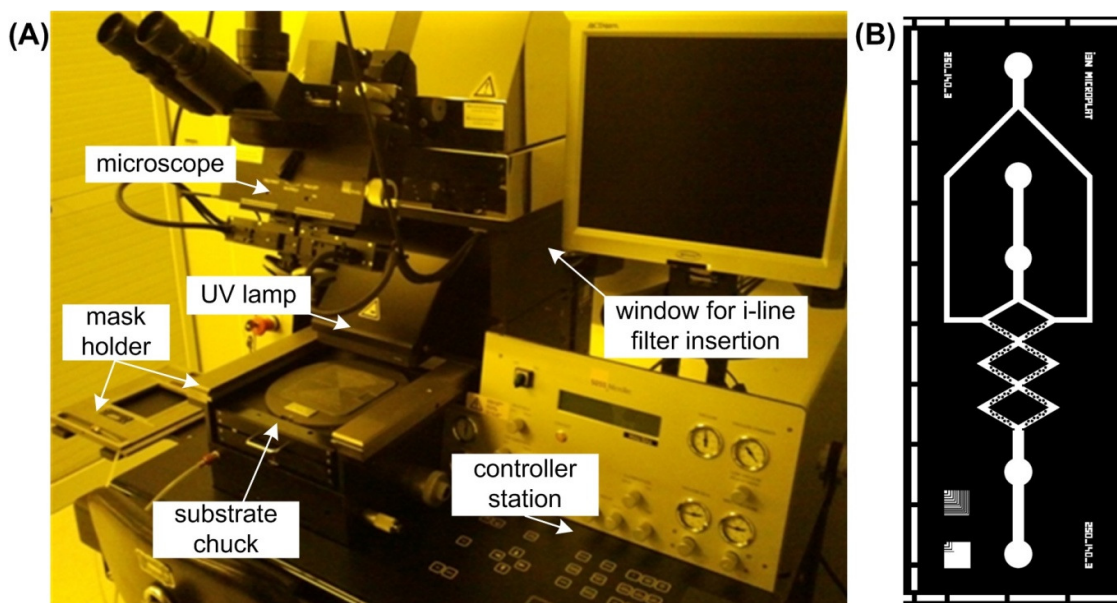


Fig. 2.6. (A) Mask aligner MA6 used for the SU-8 photolithography: the sample is placed on the substrate chuck, while the mask is placed in the mask holder and i-line filter is inserted into the UV400 optics to cut off radiation below 365 nm. After alignment process, the sample is UV exposed. (B) Layout of the photolithographic mask used for micromixers fabrication: dark mask regions define SU-8 regions that are dissolved in the developer.

### 2.1.5. Replica moulding soft-lithography

Soft-lithography, a low cost production method based on elastomeric stamps, allows for the creation of three-dimensional patterns at room temperatures and pressures. One of the most common soft lithography methods is replica moulding (casting)—the transfer of a pattern from a master into replica by solidifying a liquid precursor against the master (Elhadj et al. 2010). Because of its low investment cost, no need for specific tooling and high resolution, it has become one of the main techniques in microfluidics prototyping.

The replica moulding process starts with the fabrication of a master, usually by etching of silicon or by photolithography in SU-8. To facilitate the peeling of the replica, the master is covered with anti-stiction chemical, e.g. silane-derivative. A liquid mixture of pre-polymer (e.g. PDMS or fluorosilicone) and curing agent is then poured on top of the master and then cured. After cross-linking, the replica is peeled off the mould. The stripping is easy due to material elasticity. Fig. 2.7 shows photographs of the replica moulding procedure performed in this PhD project.

The replica can be used as a mould for the casting of subsequent chips to avoid damage of the master (see details in section 4.2.2) or can be used directly to fabricate chips. The replica is then cut into



individual chips and access holes for inlet and outlet are made using a sharp tip. After ultrasound cleaning, the chips are sealed.

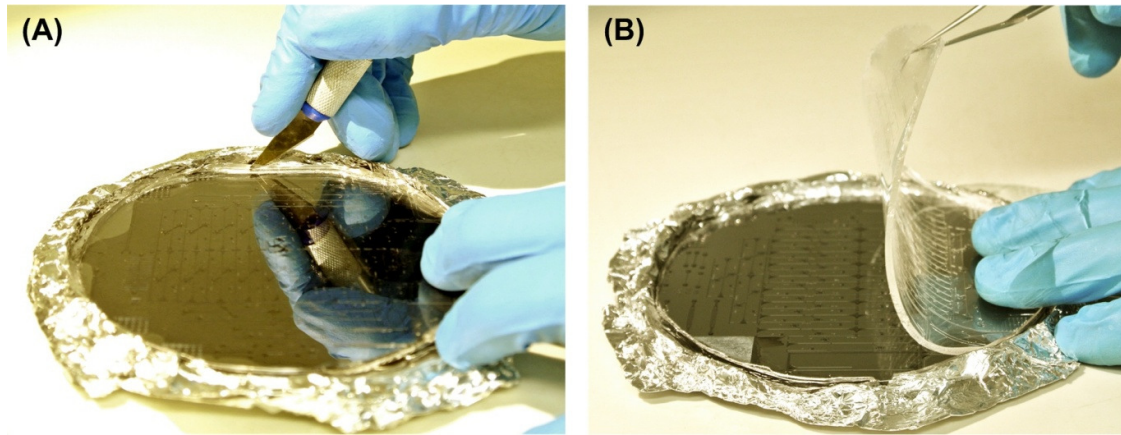


Fig. 2.7. Photographs of fabrication of PDMS microfluidic chip by replica moulding technique. A liquid mixture of PDMS pre-polymer and curing agent is poured on top of the SU-8 master and then cured. After cross-linking, the replica is peeled off the mould.

## 2.2. Chip fabrication

The most critical step in the chip microfabrication process is the production of the SU-8 mould. PDMS replicates with nano-precision in easy and fast way all the features presented in mould, therefore any mould defects will affect the PDMS chip structure. The presence of eight epoxy groups per monomer leads to the good chemical, mechanical and thermal properties of SU-8, however as a side effect of this strength, SU-8 is usually difficult to process and its properties are greatly affected by the parameters variations (del Campo and Greiner 2007). The processing of SU-8 is a time-consuming procedure that consists in 5 steps: spinning, soft bake, exposure, post bake and development (Fig. 2.8). The majority of these steps require optimization for the specific SU-8 thicknesses. Besides, the optimal parameters may change between SU-8 lots due to compositional variations of the basic material itself as well as by gravimetric decomposition of the polymer components during aging (Hammacher et al. 2008). Therefore, the fabrication of features in SU-8 should be optimized not only for a specific thickness, but also may need to be slightly tuned when working with a different lot.

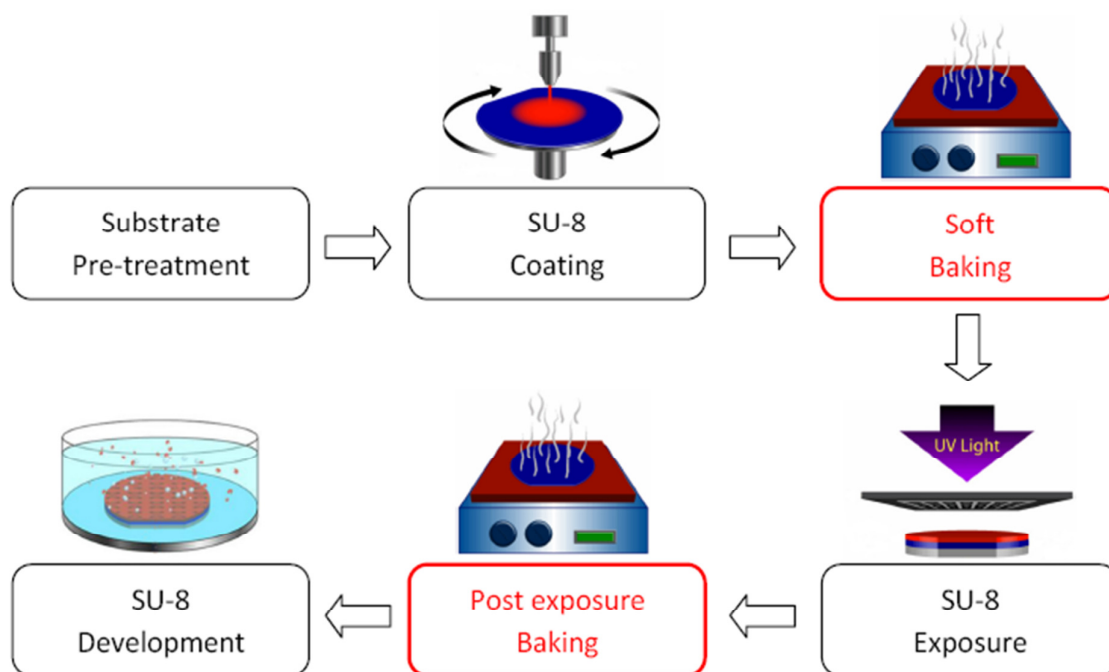


Fig. 2.8. Schematic representation of the SU-8 master fabrication: after SU-8 spin coating, the samples are soft-baked to evaporate solvent and then UV irradiated to initiate the cross-linking process that is thermally accelerated during the post bake. The unexposed SU-8 regions are removed in the developer bath and on the end, the samples are isopropanol rinsed and dried (<http://www.elveflow.com/microfluidic-reviews-and-tutorials/su-8-baking> retrieved in 2014.03).

The aimed PDMS channel depth is  $\sim 125 \mu\text{m}$  to enable the self-alignment of optical fibres of  $125 \mu\text{m}$  diameter (due to the PDMS elasticity, the grooves can be bit smaller than the fibres). To pattern such high features, SU-8 2050 (Microchem) was chosen as a mould material because as it contains more volatile solvent (cyclopentanone), the fabrication time can be reduced 8 times when comparing to the conventional SU-8 series.

The main issue of SU-8 is the large internal stress due to the polymerization process resulting in a dense structure, which can be reduced by use of a suitable substrate (similar values of thermal expansion coefficient, e.g. crystalline silicon) and proper chip geometry (avoiding large cross-linked areas), to prevent SU-8 from peeling (Conradie and Moore 2002a; Conradie and Moore 2002b). Besides, SU-8 adheres much better to silicon or gold substrates than to glass or other oxides. Indeed, we have observed that to obtain high features on glass substrate, more modifications of the manufacturer's protocol are needed than when working with a silicon wafer. Therefore, in all experiments with high SU-8 features ( $\sim 125 \mu\text{m}$ ), silicon wafers were used (glass substrates were used only in the initial SU-8 tests performed with short features ( $\sim 20 \mu\text{m}$ )).



### 2.2.1. Before the SU-8 processing

SU-8 processing is a long procedure with many variables, so all the fabrication steps should be done in the same day to not introduce additional variables. The most critical is to post bake and develop samples directly after exposing, otherwise acid cross-linking catalysts that were generated during UV exposure may migrate to un-exposed region affecting the features contrast.

Before the SU-8 processing, one should:

- a. prepare a protocol with the aimed parameters (see Annex)
- b. verify the laboratory ambient temperature. We observed that the laboratory ambient temperature is critical, as it affects SU-8 viscosity and also thermal curing. Our results show that in the ambient temperature window from 17 °C to 21 °C, reproducible results can be obtained if the spinning speed would be properly corrected being a function of ambient temperature. If the clean room ambient temperature is below 17 °C or above 21 °C, it may affect not only the viscosity, but also the SU-8 thermal curing therefore in such conditions it is hard to obtain reproducible results.
- c. confirm that the hot plates are well levelled and prepare a levelled place where the samples can be placed after baking.
- d. set the hot plates temperature at 180 °C; 65 °C and 95 °C and confirm by thermocouple whether the temperature is set properly.

### 2.2.2. SU-8 spin coating

Firstly, silicon wafers (10 cm diameter, orientation 100 cz, MEMC Electronic Materials, Inc., USA) were baked for 10 min at 180 °C to remove the adsorbed water molecules and were left to cool down for ~10 min.

The SU-8 layer height is defined by spin coating speed that should be determined basing on the datasheet taking into account that it considers the ambient temperature of 21 °C (Fig. 2.9). Our results show that for SU-8 2050 to obtain the same features height, for every 1 °C of temperature difference, the spinning speed should be tuned of ~25 rpm, i.e. if the ambient temperature is 1 °C lower, the spinning speed should be increased of 25 rpm, as the SU-8 viscosity decreases with temperature. Basing on the datasheet, to obtain 125 µm high SU-8 features, the spinning speed should be 1500 rpm (at 21 °C). As the resulting height may depend on specific spinner model, in the first tests the spinning speed should be screened to increase probability that one of the three processed samples will have aimed thickness, e.g. 1500 rpm  $\pm$  100 rpm corresponding to  $\pm$  10 µm. On the end, this speed should be tuned taking into account the ambient temperature (e.g. at 20 °C, the spinning speed would be 1425 rpm, 1525 rpm and 1625 rpm for three wafers).

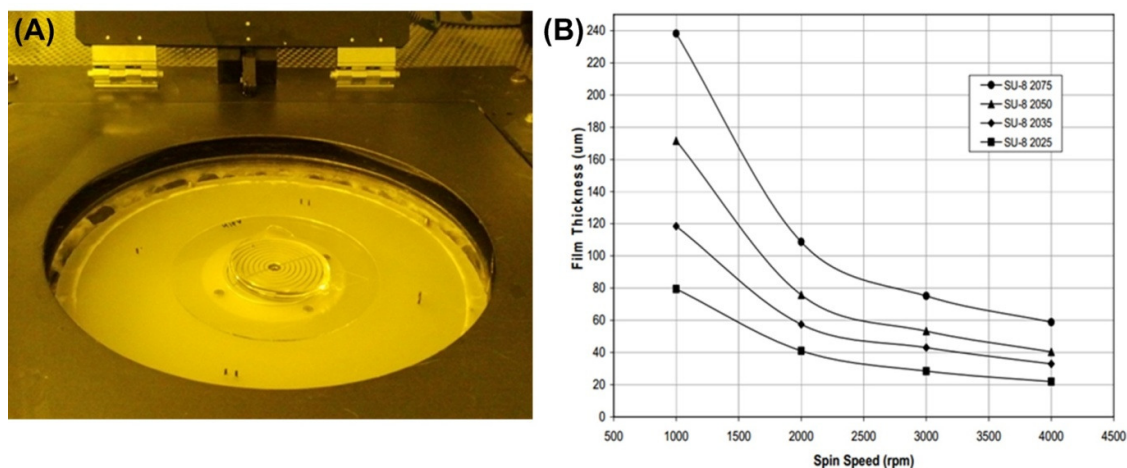


Fig. 2.9. (A) SU-8 2050 dispensed on a substrate prior to spin coating process. (B) Film thickness as a function of spin speed at ambient temperature of 21 °C (<http://www.microchem.com> retrieved in 2014.03). To obtain a desired spin speed, the values suggested in the manufacturer datasheet should be experimentally optimized.

SU-8 was dispensed on silicon wafer (around 4 ml per wafer of 10 cm diameter; the resist should be dispensed from close proximity to prevent air bubbles generation), pre-spun at 500 rpm for 7 s with acceleration of 100 rpm/s to spread over whole wafer and then spun for 30 s with acceleration of 300 rpm/s at speeds determined above (program nr 4 in the used spinner Karl Suss CT62, Suss MicroTec, Germany). In these tests, the 115–125 μm thick SU-8 layer was obtained for the spin speed of 1530 rpm at ambient temperature of 20.8 °C.

The spinner door should be carefully opened because due to high SU-8 viscosity, its spinning leftovers may stick to the door forming long fibres that may fall on the spin-coated wafer. In such case, the door should be carefully cleaned keeping the doors half-opened. Then, the wafers with SU-8 layer were placed on a plane surface until all the wafers would be covered with SU-8.

### 2.2.3. Soft bake

After the coating process, the samples are soft baked to evaporate the solvent keeping the gas exhaustion turned on. The wafers were placed on levelled hot plate (HS40A-2, Torrey Pines Scientific, Inc., USA) at 65 °C for 5 min (counting from the moment when the last wafer was placed) and then placed on the other hot plate at 95 °C for 25 min. Afterwards, wafer were left to cool down at levelled surface. To optimize the baking time, wafers were placed again at 95 °C to see if wrinkles would appear. If so, it indicates that longer baking time is needed, so the wafers should be kept for

few additional minutes at 95 °C and once again we should verify whether wrinkles would appear after cooling down and placing again at 95 °C. If so, repeat this procedure until no wrinkles appear.

#### **2.2.4. Exposure**

UV exposure of SU-8 generates a photoacid that catalyses the cross-linking of epoxy molecules. The SU-8 samples were initially exposed using an acetate mask (JD Photo-tools, UK) and mask aligner MA6 (Suss MicroTec, Germany) with UV400 lamp. SU-8 absorbs light of wavelength below 350 nm (Fig. 2.10A), therefore the top part of the layer would be more cross-linked than the bottom part causing a T-shape profile: a broader top and a narrower base. The used UV lamp (UV400 optics) has very low emission below 350 nm (Fig. 2.10B), however our results show that even such low irradiation causes the T-shape profile of SU-8 features (Fig. 2.11). The exposure through an i-line filter (G180336, Suss MicroTec, Germany; Fig. 2.10C) cuts off the light of wavelength below 350 nm allowing to cross-link homogenously the whole SU-8 layer resulting in vertical side walls.

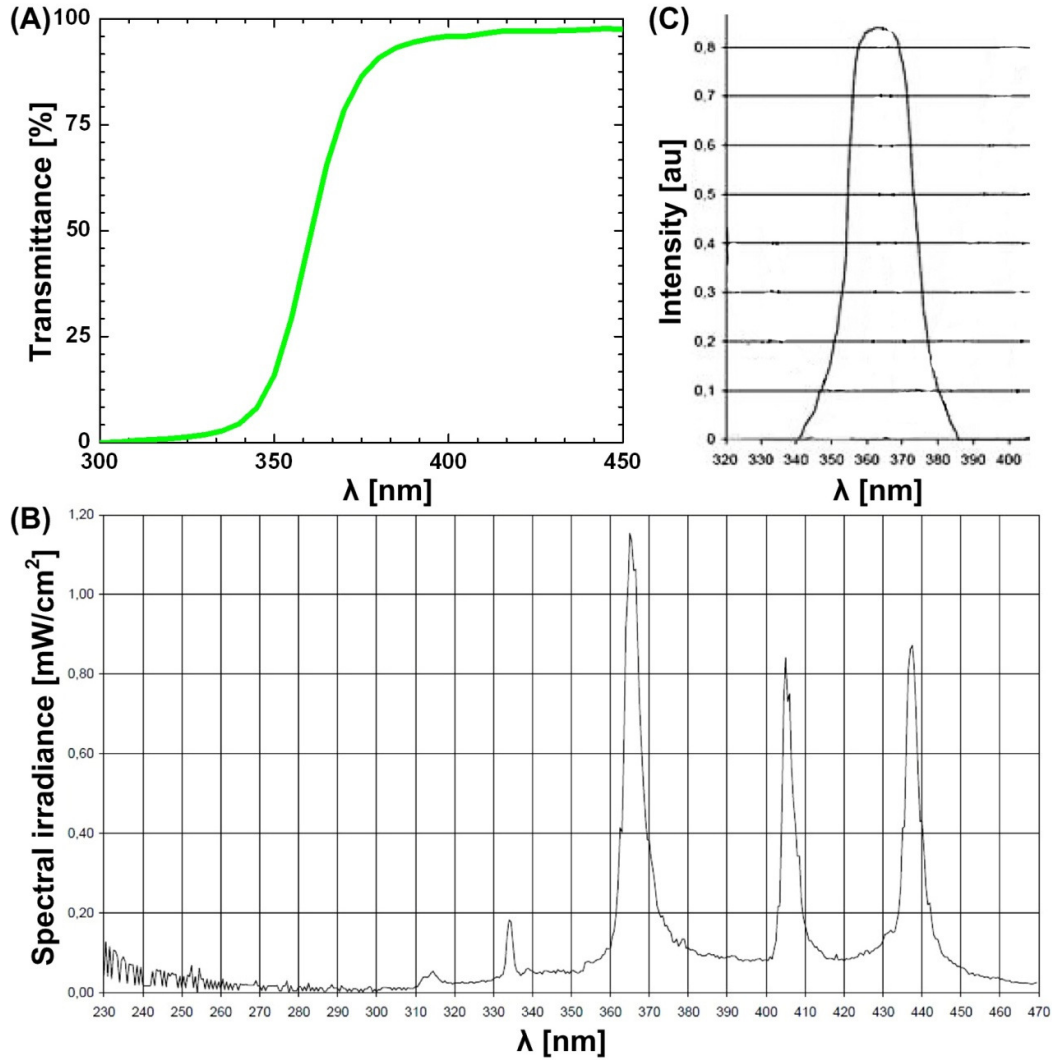


Fig. 2.10. (A) Transmission spectrum of 1 mm thick unexposed SU-8 (Gersteltec's courtesy); (B) spectral irradiance of MA6 mask aligner with UV400 optics and (C) transmission curve of i-line filter. SU-8 absorbs light of wavelength below 350 nm, therefore for homogenous exposure of the whole SU-8 layer, a filter should be used to eliminate the light of wavelength below 350 nm emitted by the UV400 optics. Adapted from the mask aligner and filter datasheets.

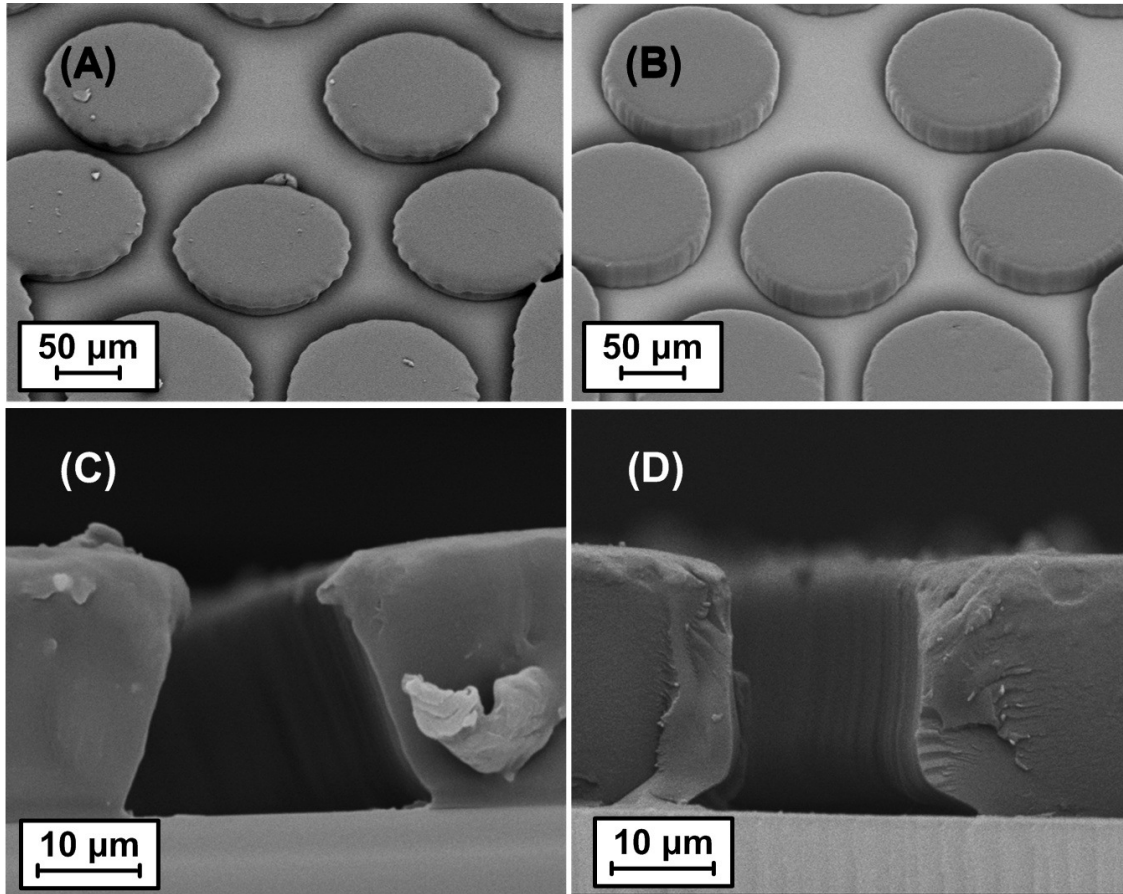
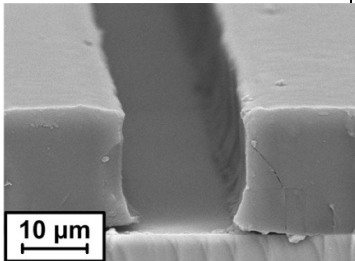
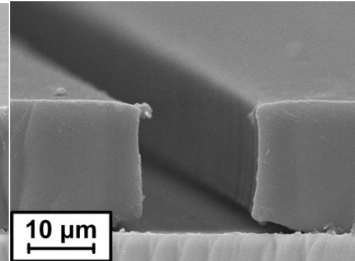
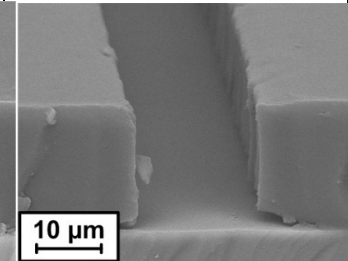
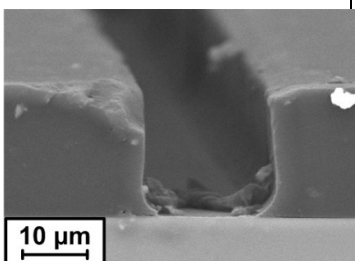
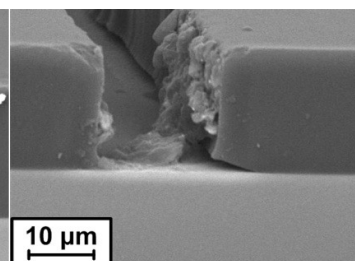
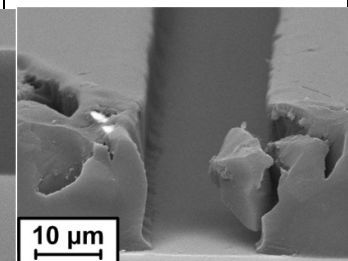


Fig. 2.11. Scanning electron micrographs of SU-8 features (20  $\mu\text{m}$  high on glass substrates): top view of samples exposed (A) without filter (7 s) and (B) with i-line filter (18 s) and cross-section of SU-8 channel exposed (C) without filter indicating the negative side walls and (D) through the i-line filter indicating nearly vertical side walls (89 degrees).

The samples exposed through the i-line filter have well defined structures and vertical side walls, however these chips were still not satisfactory due to irregularities on the bottom of the channel (visible at Fig. 2.11D). Several approaches were tested to resolve this problem: use of different substrates (glass and silicon) and use of different post-development treatment: no hard bake; hard bake in oven (as suggested by the manufacturer); hard bake on hot plate (to improve hardening of the bottom part of channel); hard bake after 2<sup>nd</sup> exposure (to cross-link remaining monomers). The results presented in Table 2.1 show that none of tested approaches has enabled to resolve the irregularities problem.

Table 2.1. The scanning electron micrographs of microchannels ( $20 \times 20 \mu\text{m}^2$ ) fabricated in SU-8 on glass or silicon wafer exposed through the i-line filter for 18 s. Various post-development treatments were applied to eliminate the irregularities of bottom part of channels.

	no hard bake	20 min at hot plate at 100 °C	2 <sup>nd</sup> exposure and 20 min at hot plate at 100 °C
on glass			
on silicon			

Further, we have tested the influence of the type of photolithographic mask. The results (Fig. 2.12) show that these irregularities could be eliminated if instead of an acetate mask, a higher quality mask would be used: the chromium pattern on glass (super high resolution chrome patterns of soda lime glass, JD Photo-tools, UK). This was probably caused by the fact that SU-8 is very sensitive to the light due to the presence of eight epoxy group per molecule; therefore a mask of high contrast between transparent and visible regions is required.

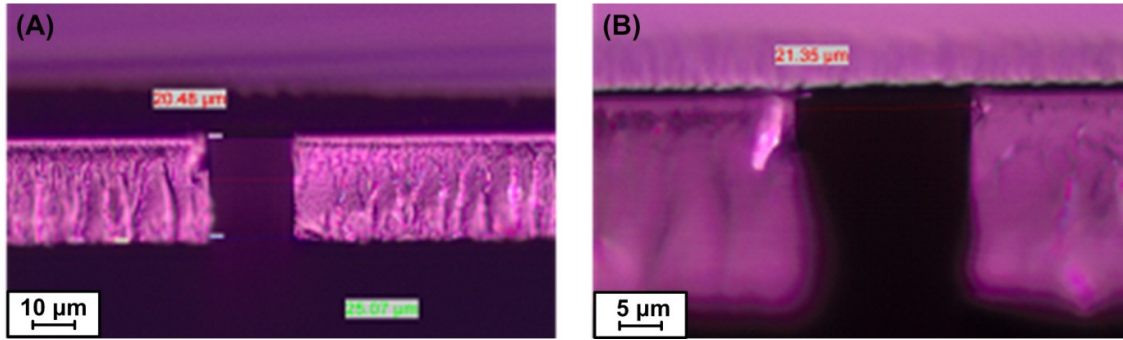


Fig. 2.12. The microscopic images of SU-8 microchannels cross section ( $20 \times 20 \mu\text{m}^2$  on silicon wafer) fabricated using chromium mask: (A) 100 $\times$  magnification and (B) 200 $\times$  magnification. The microchannels were fabricated on silicon wafers exposing through the i-line filter. The use of the high resolution and high contrast mask enabled to eliminate the irregularities on the channels bottom visible in Fig. 2.11 and Table 2.1.

Resuming, presented results show that for fabrication of SU-8 microchannels of vertical and smooth side walls, it is necessary to use a chromium mask and a 360 nm cut off filter even for UV400 optics. Before inserting the filter in the mask aligner, this should be set to constant power mode. If constant intensity mode would be kept while working with filter, the sensor would not be able to receive enough intensity and would show an aligner error. The mask should be placed in the holder in the way that the chromium side of the mask is in contact with SU-8 layer. Soft contact mode should be used. The samples should be exposed after 30 min of the lamp warming up (at least).

In the first SU-8 series (when spinning speed is being optimized), the exposure dose should be the same for all three wafers, to not increase number of variables. The initial exposure dose suggested for aimed thickness can be determined basing on the datasheet. The flood exposure should be done to verify lamp intensity in this specific day, as it may vary due to the use of constant power mode. To determine the exposure time, the aimed exposure dose should be divided by the lamp intensity. Although in the datasheet it is suggested to increase the dose of 40% when working with i-line filter, in our experiments the exposure intensity was measured when exposing through filter, so its presence was already taken into account.

In the next series (when spinning speed is optimized and fixed for all wafers), the exposure dose should be properly optimized to obtain features of high aspect ratio and good adhesion. To determine optimal exposure dose, various exposure doses should be tested around the doses suggested in the datasheet, e.g.  $\pm 10 \text{ mJ/cm}^2$ .

Microscopic images presented in Table 2.2 present the results of the exposure dose optimization for SU-8 layer of thickness of about  $140 \mu\text{m}$  (exposure dose suggested in the manufacturer datasheet:  $254$

mJ/cm<sup>2</sup>). All tested exposure doses (from 209 to 330 mJ/cm<sup>2</sup>) give features of smooth and vertical side walls. However, for higher exposure doses, the aspect ratio is higher: the minimum feature size is 30 µm for exposure of 209 mJ/cm<sup>2</sup> (aspect ratio: 4) and 15 µm for exposure of 330 mJ/cm<sup>2</sup> (aspect ratio: 8, see Table 2.3). Besides, the SU-8 structure is more homogenous (see cross-section images in Table 2.2) for the samples exposed with 330 mJ/cm<sup>2</sup>. On top view images of samples exposed with 209 and 241 mJ/cm<sup>2</sup>, double feature borders can be observed, perhaps due to the inhomogeneous structure of the layer revealed on the cross-section images: the top part of the layer is more cross-linked than the bottom. Most probably, the difference in the cross-linking degree between upper and down part of the SU-8 layer was not strong enough to cause the T-shape profile, but sufficient to reduce adhesion causing that the smallest features peeled out from the surface. The presence of 'double borders' on the top view SU-8 images can be an indicator that the exposure dose was too low. Therefore, to obtain high aspect ratio and homogenous SU-8 features, the exposure dose suggested in the datasheet should be increased of 30%. Indeed, for 125 µm thick SU-8 layer, the exposure dose of 309 mJ/cm<sup>2</sup> resulted in homogenous structure and high aspect ratio (13). Wrinkles visible on SU-8 surface are most probably caused by the SU-8 large internal stress. The number and size of wrinkles can be minimized, but most probably they cannot be eliminated due to dense cross-linking of SU-8, significant particularly when working with high features. In spite of these wrinkles, there was no leakage in the resulting PDMS chips.



Table 2.2. Microscopic images of 140  $\mu\text{m}$  thick SU-8 layer fabricated using various exposure doses on silicon wafers. The exposure dose of 330  $\text{mJ}/\text{cm}^2$  gives a higher aspect ratio and more homogenous SU-8 structure.

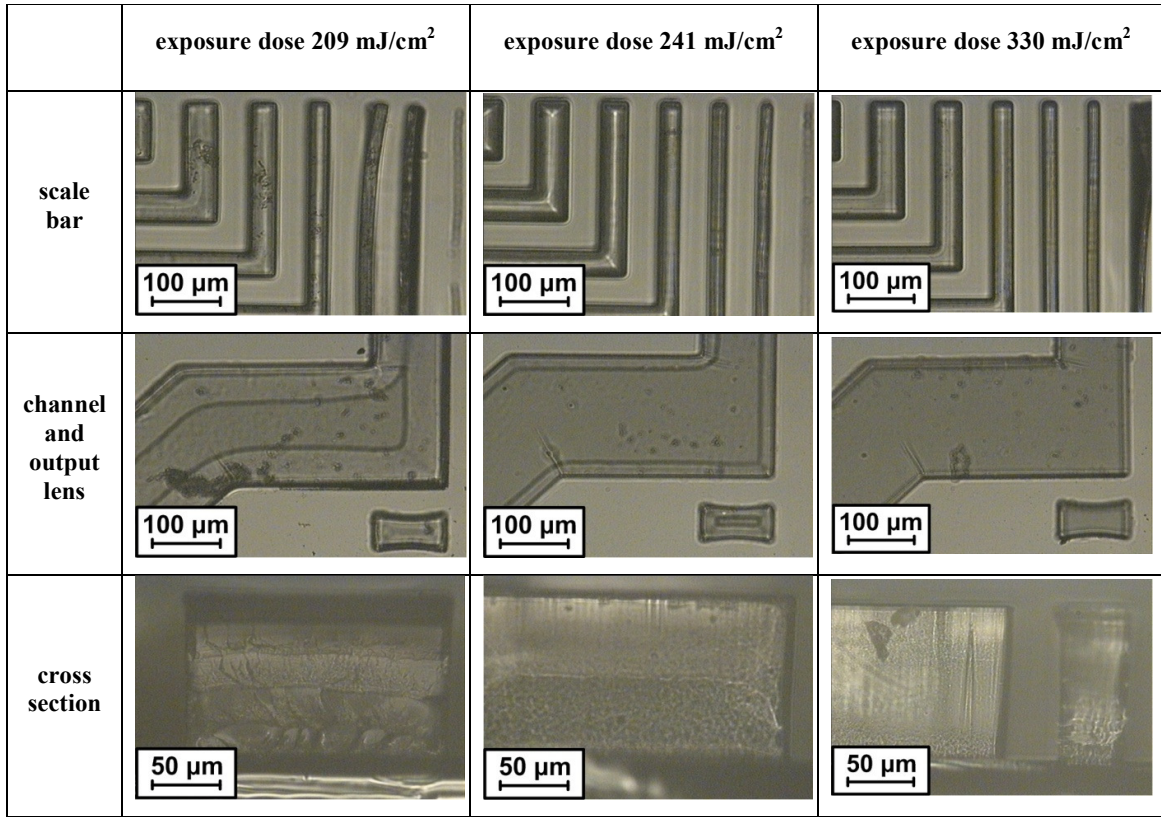


Table 2.3. Minimum size of features and channel for various exposure doses based on scale bar results presented on Table 2.2.

	minimum feature size	minimum channel size
exposure 209 $\text{mJ}/\text{cm}^2$	30	10
exposure 241 $\text{mJ}/\text{cm}^2$	20	10
exposure 330 $\text{mJ}/\text{cm}^2$	15	10

For the quality control, these samples have been analysed by scanning electron microscopy (Fig. 2.13). The obtained SU-8 features are well defined and have smooth edges (Fig. 2.13A), plane and nearly vertical side walls (87.8 degrees, Fig. 2.13B) and adhere well to the silicon wafer (Fig. 2.13C). The features corners are slightly rounded (Fig. 2.13A), most probably due to the presence of an air gap between mask and SU-8 during UV exposure related with the edge bead (Fig. 2.4). Due to the presence of the edge bead, the sample cannot be in hard contact with mask during exposure (soft contact mode was used). There is an air gap between central part of the layer and mask causing

Fresnel diffraction. The features' edges receive higher exposure doses and may become larger forming a T-shape structure (Won-Jong et al. 2006). Furthermore, due to diffraction, the fabrication of narrow SU-8 features is challenging. This effect might be reduced by removing the edge bead or placing a soft cushion below the wafer (Zhang et al. 2005). In our tests, in spite of the edge bead presence, we obtained vertical side walls and satisfactory aspect ratio (125:10). The rounded corners are not problematic in our application. In tests requiring higher resolution or sharp feature corners, the air gap should be eliminated.

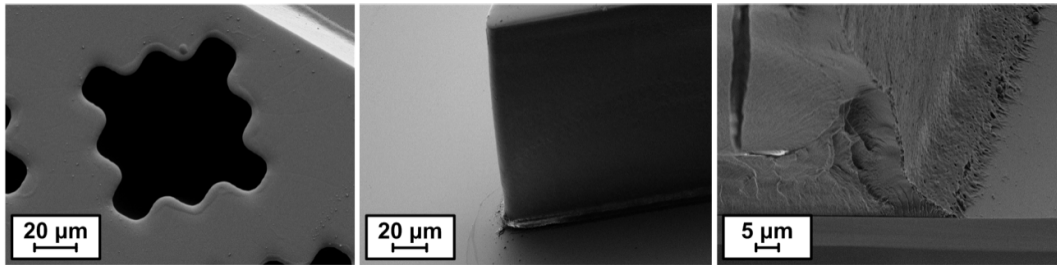


Fig. 2.13. SEM images of  $\sim 125\ \mu\text{m}$  high SU-8 features fabricated with exposure dose of  $309\ \text{mJ}/\text{cm}^2$  on silicon wafer: (A) top view indicating good features definition; (B) profile indicating smooth and nearly vertical side walls ( $87.8^\circ$ ) and (C) zoom on the interface SU-8 / wafer indicating good adhesion.

#### 2.2.5. Post bake

The UV exposure only initiates chemical amplification (photoacid generation), however the cross-linking process is too slow to be completed at ambient temperature; therefore the samples should be post baked. Indeed, during the baking, the pattern should become visible by naked eye due to the cross-linking of exposed SU-8 regions. It is important to observe when the pattern becomes visible: it should appear after 5–15 s of baking at  $95^\circ\text{C}$ . If it appears after shorter or longer time, it may indicate that the exposure dose was too high and too low, respectively. The samples should be post baked as soon as possible after exposure to prevent migration of the photoacid to unexposed SU-8 regions. The post bake was done in the same way as the soft bake, but for shorter time, i.e. 5 min at  $65^\circ\text{C}$  and 11 min at  $95^\circ\text{C}$ .

#### 2.2.6. Development

Then, the development in propylene glycol methyl ether acetate, PGMEA (Microchem) is done to chemically dissolve the unexposed SU-8. The samples should be developed as soon as possible after post bake to avoid photoacid migration. When working with high features, the development should be

done with a magnetic agitation to facilitate the dissolving of the bottom part of the layer, in particular from narrow cavities. The samples were developed for 18 min a magnetic agitation of 500 rpm. Subsequently, the samples were rinsed in clean developer for ~10 s and then in a mixture of isopropanol for ~10 s with strong manual agitation to remove the developer and finally gently dried with compressed nitrogen. Formation of white traces in the isopropanol bath indicates that the development time was too short: isopropanol and unexposed SU-8 create a white complex. If so, the sample should be developed during additional 1 min and then rinsed again. This procedure should be repeated until no white traces appear, while it is important to not place the samples in the developer bath that got contaminated with the white complex, because it might be difficult to remove.

Then, samples should be evaluated by optical microscopy to see if there is a need for additional development or rinsing. Too long development time may cause SU-8 peeling, therefore when adding development time it is a good practise to capture the microscopic images of the scale bar for comparison.

#### **2.2.7. Casting of PDMS mould**

Due to the SU-8 large internal stress and mould heterogeneous structure, SU-8 has tendency to peel out from the wafer, especially in the case of high aspect ratio features. Therefore, here instead of casting PDMS chips from SU-8 mould, we have fabricated an mediating epoxy mould that is much more robust due to its monolithic structure. Firstly, the PDMS was casted from the SU-8 mould. The SU-8 mould was placed in a Petri dish covered with an acetate foil to prevent gluing the wafer to the glass during the casting process. The samples were placed in a dessicator and 2 drops of tridecafluoro-1,1,2,2-tetrahydrooctyl trichlorosilane (Microchem, USA) were pipetted on a small glass piece and placed near the mould to facilitate the peeling of the cured PDMS. The samples were desiccated for 1 h.

PDMS (Sylgard 184, Dow Corning, Spain) was prepared by mixing a base and a curing agent in a 10:1 ratio of weight (about 35 g per wafer). The mixture was stirred and degassed in a vacuum desiccator for about 1 h. Afterwards, the PDMS was poured over the SU-8 mould, degassed again to remove bubbles and thermally cured on a levelled hot plate. The curing conditions depend on the desired dimensions: higher temperature causes stronger PDMS shrinking which is beneficial when desired features are smaller than defined by the SU-8 and/or mask resolution (Lee and Lee 2008b). In our tests, samples were cured at 100 °C for 3 h, as due to the PDMS elasticity the shrinkage was not problematic for insertion of optical fibres. The cured PDMS was peeled from the SU-8 mould by disconnecting from the wafers borders using a knife and then pulling gently.

### **2.2.8. Casting of epoxy mould**

The PDMS mould was placed on top of a Petri dish with the negative relief features up. When working with big area samples, the PDMS mould should be immobilized on a Petri dish (e.g. using a double side tape) to avoid lifting during the subsequent baking. An epoxy resin (ES562, Permabond) was poured upon it to form a ~2 mm thick layer. After ~72 h of degassing in a desiccator to remove bubbles, the epoxy glue was cured in a levelled oven at 120 °C for ~40 min, however the baking time may vary, so the samples should be observed: when epoxy cross-links, it changes colour from white to light yellow. It is important to not move samples during the curing, because at higher temperature the epoxy is more liquid, so it may easily spill. Then, the cured epoxy was peeled from the PDMS.

### **2.2.9. Casting of PDMS chips**

The epoxy mould was used for PDMS soft lithography using the same procedure as described in section 2.2.7. Fig. 2.14 summaries the chip microfabrication process showing the photographs of the samples produced at each step. The inlet of the PDMS chips was done by punching using a blunt tip of 1.7 mm outer diameter, while for the outlet a blunt needle of 1.07 mm outer diameter (19 gauge, Dotest, Spain) was used.

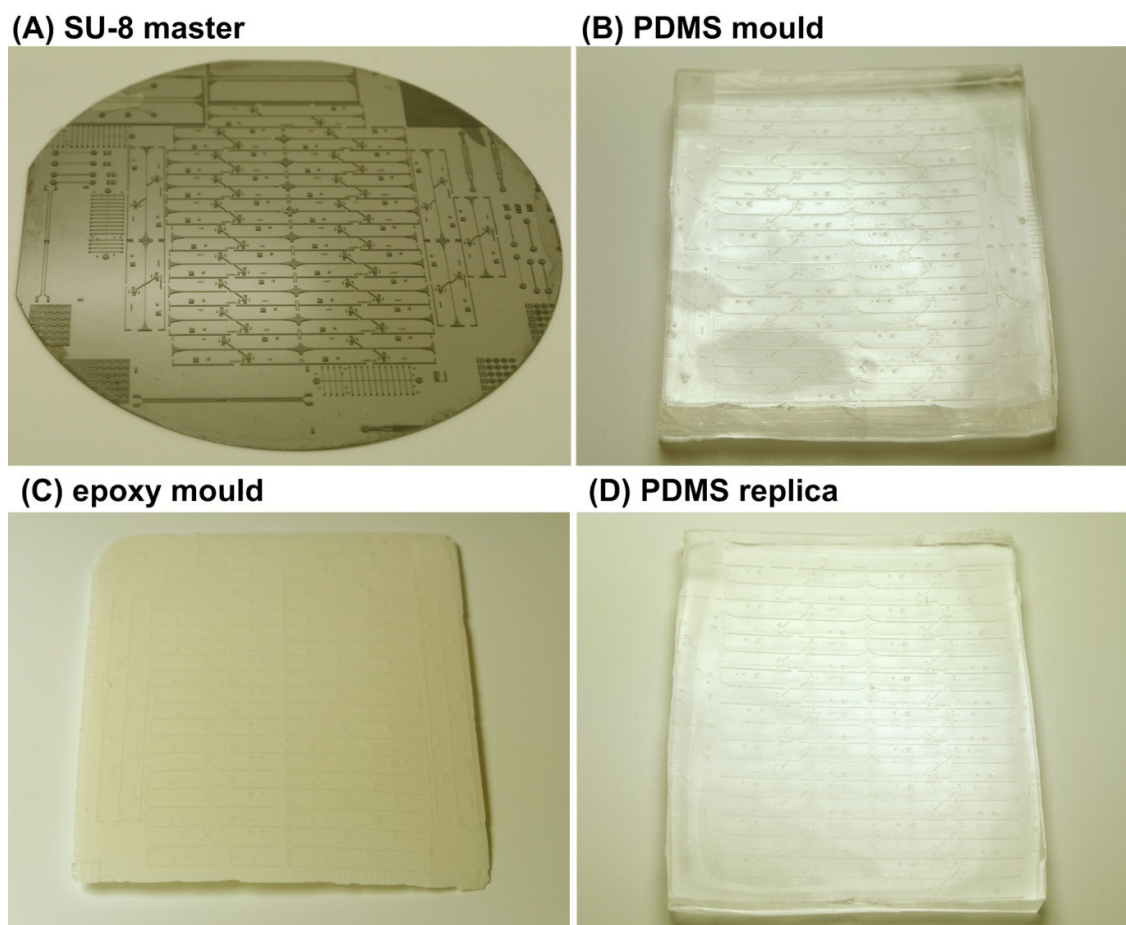


Fig. 2.14. The process of the chip microfabrication: the moulding process starts with the fabrication of the SU-8 master mould (A), then instead of casting PDMS repeatedly from this mould, PDMS is casted once (B) and used as mould for the patterning of an epoxy mould (C), which can then be used to produce many PDMS replicas (D) without suffering delamination problems.

#### 2.2.10. Sealing of PDMS chips

Due to the elasticity, PDMS chips can be reversibly sealed by forming conformal contact through adhesion forces with almost any surface that is sufficiently smooth (Sun and Rogers 2007). However, the reversible PDMS sealing is weak, so in many applications (e.g. high flow rates) the irreversible bonding is required to prevent fluid leakage. The irreversible sealing of PDMS with glass, silicon or another PDMS slab can be obtained by oxidation: generated highly active oxygen species remove the methyl groups from the PDMS surface forming polar silanol groups. When plasma treated surfaces are brought into contact, the condensation reaction occurs forming covalent bonds between those surfaces, sealing them irreversibly (Fig. 2.15). Besides, the oxidation process alters PDMS surface properties making it temporally hydrophilic. The most used methods for PDMS oxidation is oxygen plasma and UV light exposure due to high efficiency of the generation of active oxygen species.

The quality of the bonding strongly depends on the oxidation conditions. Too strong oxidation (i.e. too long oxidation times or too high concentration of oxygen species) causes formation of stable  $\text{SiO}_2$  structures on the PDMS surface decreasing density of silanol groups, while too low pressure results in anisotropic bombardment that may break the backbone of PDMS. In general, to obtain strong irreversible PDMS sealing, the oxidation should be performed at low plasma power, short treatment time and high reactor pressures. Furthermore, the samples should be brought into contact as soon as possible after the oxidation process (no later than 15 min after).

The conformal reversible PDMS sealing and the irreversible sealing based on PDMS oxidation can be applied only for sufficiently smooth surfaces. In the case of rough surfaces, PDMS can be irreversibly sealed using a pre-polymerization method (section 4.2.1).

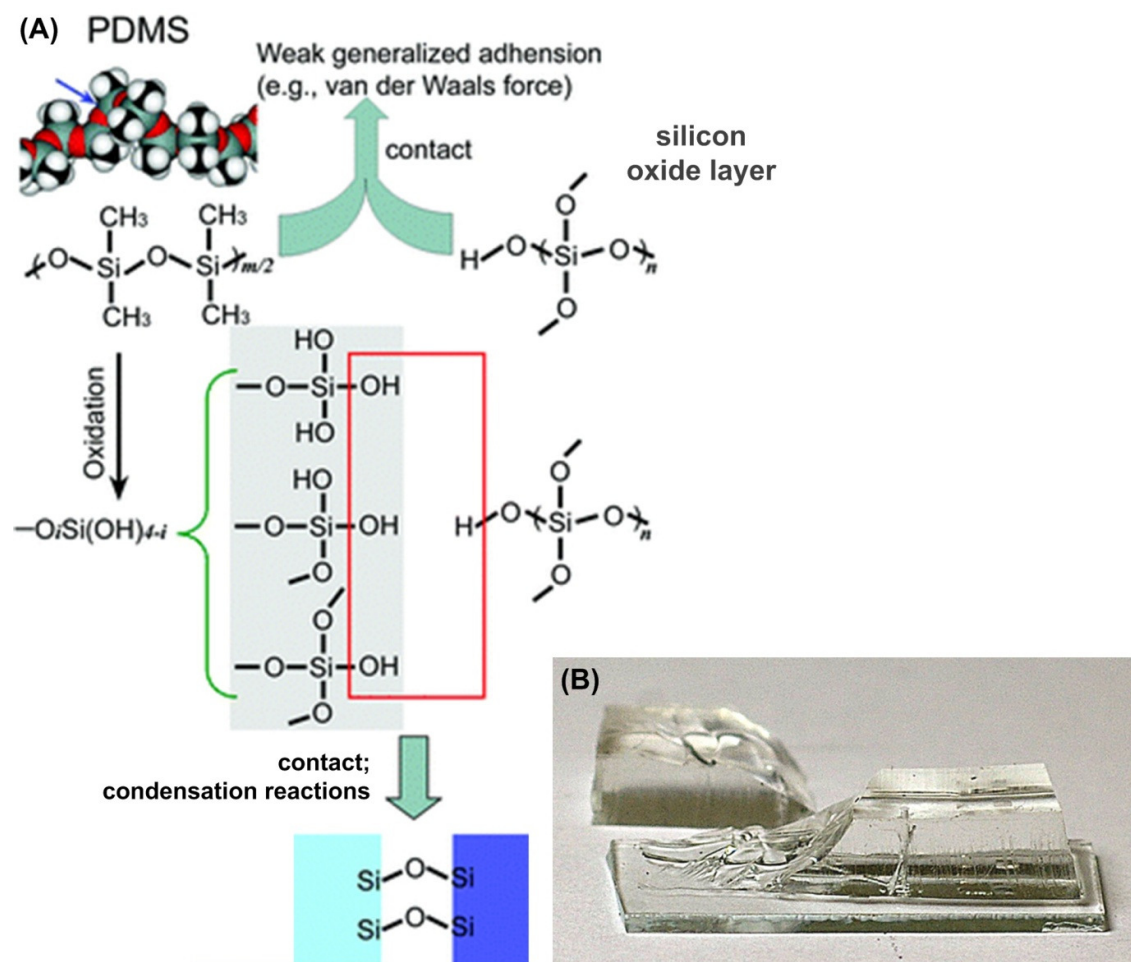


Fig. 2.15. (A) Schematic illustration of sealing of PDMS chips. The reversible sealing can be obtained basing on PDMS elasticity, while proper PDMS oxidation enables its irreversible sealing: generated highly active oxygen species remove the methyl groups from the PDMS surface forming polar silanol groups. When plasma treated surfaces are brought into contact, the condensation reaction occurs forming covalent bonds between those surfaces, sealing them irreversibly. Adapted from (Sun and Rogers 2007). (B) Photograph showing the strength of the PDMS sealing based on the oxidation process: it is easier to break PDMS than separate it from glass.

The chips were bonded to glass slides (soda lime glass) by oxygen plasma (60 s in 13 Pa, 100 W, Plasma electronic Buck Technologien, Germany) or UVO (16 min, 5 cm away from the UV lamp),. Directly after the treatment, PDMS chips were put into contact with the glass and the samples were baked for 5 min at 100 °C or for 20 min at 70 °C in a hot plate to increase the bond strength. The bond obtained by UVO treatment was weaker than in the case of plasma, so the samples should be rested overnight at room temperature to increase the strength.



### **2.3. Characterisation techniques**

Table 2.4 summaries all characterisation methods that were used for analysis of the tested materials and devices. The characterisation was performed mainly in the CEMOP and CENIMAT laboratory facilities with exception of microplate reader analysis performed in CIGHM (Life Science Department of FCT-UNL) and tests of micromixing performance (mixing efficiency and pressure drop) that were carried in Institute for Polymers and Composites of University of Minho.

All used characterisation techniques are commonly known, thus the description of their working principles will be omitted. Main characterisation methods will be shortly described providing a general description, applications in this work and characterisation conditions. Less commonly used techniques: determination of features' thickness using optical microscopy and acquisition the absorption spectra of solutions in microfluidic chips will be depicted with more details.



Table 2.4. Characterisation techniques used in this PhD work.

material/device	property	characterisation method
TiO <sub>2</sub> photodetector	nanoparticles' size and distribution	scanning electron microscopy (SEM): Auriga SEM-FIB, Zeiss, Germany
	spectral response	homemade set-up coupled to a Keithley Multimeter 238 Keithley Instruments, Inc., Cleveland, USA
	dye absorption	spectrophotometer: UV-3101PC UV/visible/NIR double beam, Shimadzu, Japan
SU-8 mould	features' definition	optical microscopy: Leitz Laborlux 12 ME ST, Germany integrated with a measurement tool
		SEM: Auriga SEM-FIB, Zeiss, Germany
		Confocal scanning microscopy: LSM 700, Carl Zeiss, Germany
	features' height	stylus profilometry: XP-200, Ambios Technology, Inc., Santa Cruz, USA
epoxy mould	features' definition	optical microscopy: Leitz Laborlux 12 ME ST, Germany integrated with a measurement tool
		confocal scanning microscopy: LSM 700, Carl Zeiss, Germany
		optical microscopy: Leitz Laborlux 12 ME ST, Germany integrated with a measurement tool
PDMS chip	features' definition	optical microscopy: Leitz Laborlux 12 ME ST, Germany integrated with a measurement tool
		SEM: Auriga SEM-FIB, Zeiss, Germany
		confocal scanning microscopy: LSM 700, Carl Zeiss, Germany
	features' height	optical microscopy: Leitz Laborlux 12 ME ST, Germany integrated with a measurement tool
	optical transmission	spectrophotometer: UV-3101PC UV/visible/NIR double beam, Shimadzu, Japan
fluid	optical absorption	spectrophotometer (used for AuNPs spectra): UV-3101PC UV/visible/NIR double beam, Shimadzu, Japan
		microplate reader (used for Au-nanoprobes spectra): Tecan Infinite M200, Switzerland
		spectra in chips: miniature fibre optic spectrometer USB4000, Ocean Optics, USA
bio-microfluidic platform	response linearity	output voltage as a function of LED current; detection response as a function of AuNPs concentration
	signal-to-losses ratio	stereo microscope Leica Zoom 2000, Germany and Pentax K100 camera; images analysed by ImageJ
micromixer	mixing efficiency	inverted microscope: Leica DMI 5000M, Leica Microsystems, Germany connected to light sensitive CCD camera: Lu160, Lumenera Corporation, USA
	pressure drop	differential pressure transducer: 26PC, Honeywell, USA

### 2.3.1. Scanning electron microscopy

Scanning electron microscopy (SEM) enables to obtain high magnification images (nanometre range) and also chemical composition of the sample. SEM image is formed by detection of secondary electrons emitted by sample upon interaction with highly energetic electron beam in vacuum environment. A thorough description of SEM principles can be found in (Egerton 2005).

In this work, SEM was used to analyse TiO<sub>2</sub> nanoparticles' size and distribution in developed photodetectors and to evaluate quality of microfluidic features. The observations were carried out using a Carl Zeiss AURIGA CrossBeam (FIB-SEM) workstation coupled with energy dispersive X-ray spectroscopy (EDS). The materials have been previously coated with a 15 nm thick Au/Pd conductive film to avoid charge effects.

### 2.3.2. Spectrophotometry

Spectrophotometry allows determination of absorption and reflection properties of a material or a solution by analysis of transmitted light intensity as a function of light source wavelength (functional principle can be found at <http://www.chemguide.co.uk/analysis/uvvisible/beerlambert.html>). In this work, the spectrophotometry was used to determine transmittance (and related absorbance) of PDMS slabs and various AuNP solutions to evaluate colorimetric changes and also to determine their concentrations via the Lambert-Beer law (eq. 1.6).

All absorption and transmission spectra from UV-3101PC UV/visible/NIR double beam, Shimadzu, Japan were acquired using medium scan speed, 1 nm slit width and 1 nm sampling interval in the range 400 – 800 nm using cuvette with solvent as a baseline and air as a reference.

The spectra of the solutions in chips were acquired using miniature fibre optic spectrometer (USB4000, Ocean Optics, US) using a halogen lamp for absorption spectra and green and red LEDs for transmission spectra. Firstly, the automatic measurement mode (absorbance wizard) was used to determine the optimum integration time (in presented tests: 610 ms for halogen lamp and 8 ms for LEDs; Fig. 2.16A). Then, a manual measurement mode was used, because it gives more freedom during tests (Fig. 2.16B). The spectra were acquired in the range of 400–800 nm averaging 10 scans and to smooth the signal a boxcar width of 20 was used (i.e. an averaging of a single data point with the values surrounding it). To reduce noise, these experiments were performed in the dark. Halogen lamp was warmed up at least for 1 h, while LEDs for 1 min. The LEDs transmission spectra were acquired in the intensity mode using empty channel as the reference, while both dark and light reference spectra were taken in dark conditions.

In the case of absorption analysis, the signal-to-noise ratio was low because of low power of the used halogen lamp. After each set of measurements, the software was restarted and new reference spectrum

was acquired, as due to the low signal-to-noise ratio, the signal may become unstable with time. Therefore, the reference spectra were taken for empty channel, so they could be acquired directly before sample injection. After the dark and light reference spectra were stored in the intensity mode, the solvent (water or buffer, for AuNPs and Au-nanoprobes, respectively) and sample absorption spectra were acquired. From the sample absorption spectrum, the solvent absorption spectrum was manually subtracted for normalization. Instructions for the spectra acquisition using the USB4000 spectrophotometer can be found at <http://www.oceanoptics.com/Applications.asp>.

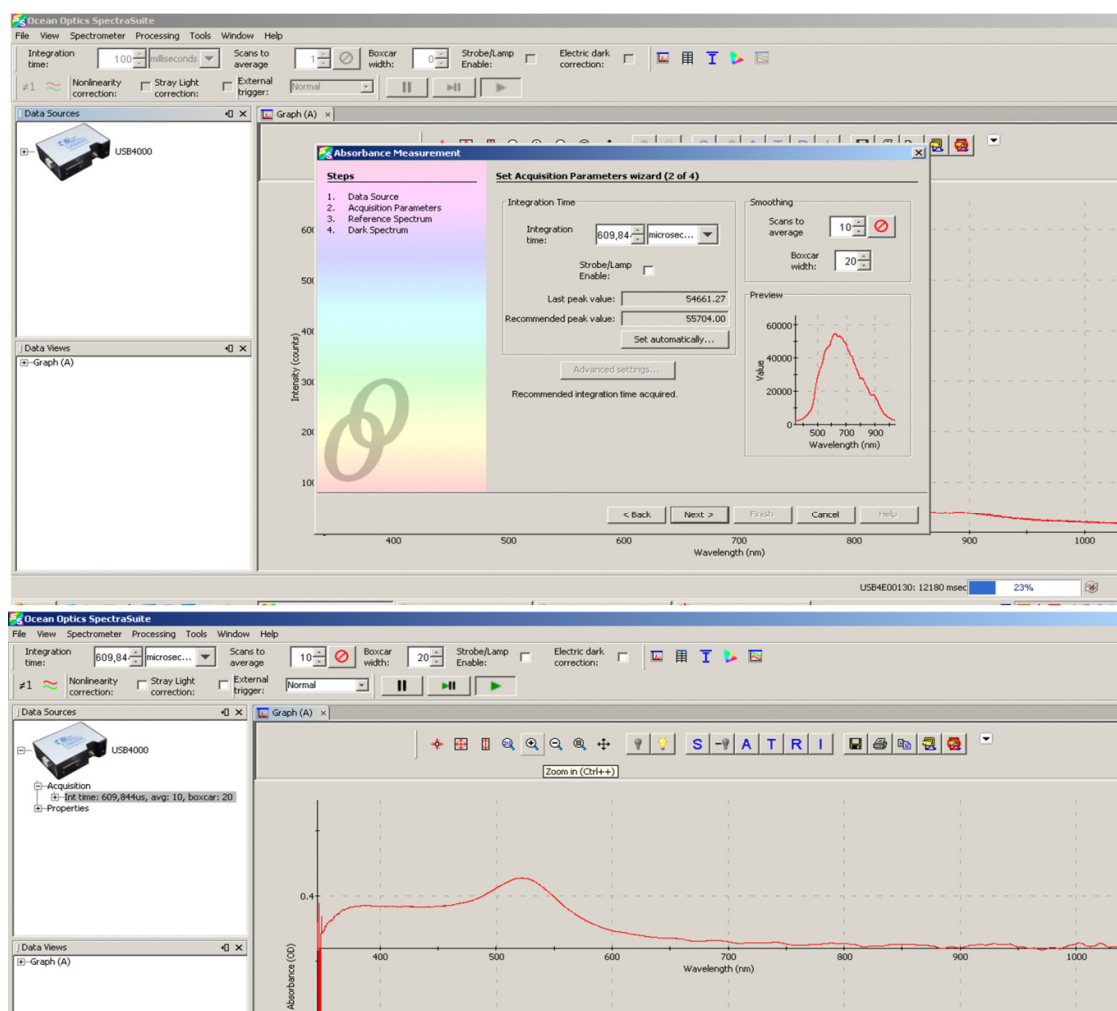


Fig. 2.16. Acquisition of solution spectra by miniature fibre optic spectrometer integrated with microfluidic chip. (A) The automatic measurement mode (absorbance wizard) was used to determine the optimum integration time. (B) Spectra were acquired using a manual measurement mode to enable more freedom during tests. After the dark and light reference spectra were stored in the intensity mode, the solvent and sample absorption spectra were acquired.

### 2.3.3. Stylus profilometry

Stylus profilometry is one of the most common techniques to measure features' height: a stylus is moved across the feature with a specific contact force and the vertical displacement is converted to the height. Details on profilometry principle can be found in (Sayers and Karamihas 1998).

In the development of presented microfluidic chips, the channel depth is critical for proper alignment of optical fibres and also for results reproducibility. When evaluating the SU-8 layer thickness, it is important to keep in mind that due to the spinning process, the SU-8 layer in the wafer centre is thinner than in other regions, in particular on the edge bead—a residual ridge in resist at edge of wafer, see Fig. 2.4 (Campo and Greiner 2007). In these tests, the layer thickness at half of the wafer radius (2.5 cm away from the wafer centre) was measured (otherwise specified) in various wafer sides to access the uniformity. In the case of the SU-8 mould that was used for patterning of chips for optical detection (sample P3A), the SU-8 thickness in the wafer centre was 110  $\mu\text{m}$ , while in the half of wafer radius 114  $\mu\text{m}$  and 118  $\mu\text{m}$  at two different sides of the wafer.

The SU-8 profiles were taken using XP-200 (Ambios Technology, Inc., Santa Cruz, USA) with 0.1 mm/s speed for the range of 550  $\mu\text{m}$  with filter level 8. For thickness range above 100  $\mu\text{m}$ , the stylus force cannot be changed and is fixed as the maximum value (10 mg), therefore the stylus may scratch the layer giving incorrect thickness value (in particular, when the SU-8 exposure time was too short) as it can be observed in Fig. 2.17. Furthermore, profilometry may give inaccurate profile results in characterisation of the high aspect ratio features due to high width of the measuring stylus: the radius of the stylus on the tip end is only 2.5  $\mu\text{m}$ , but then it increases with height. Therefore, instead of conventionally used profilometry, in this work, the features' height was determined mainly using optical microscopy with integrated measurement tool.

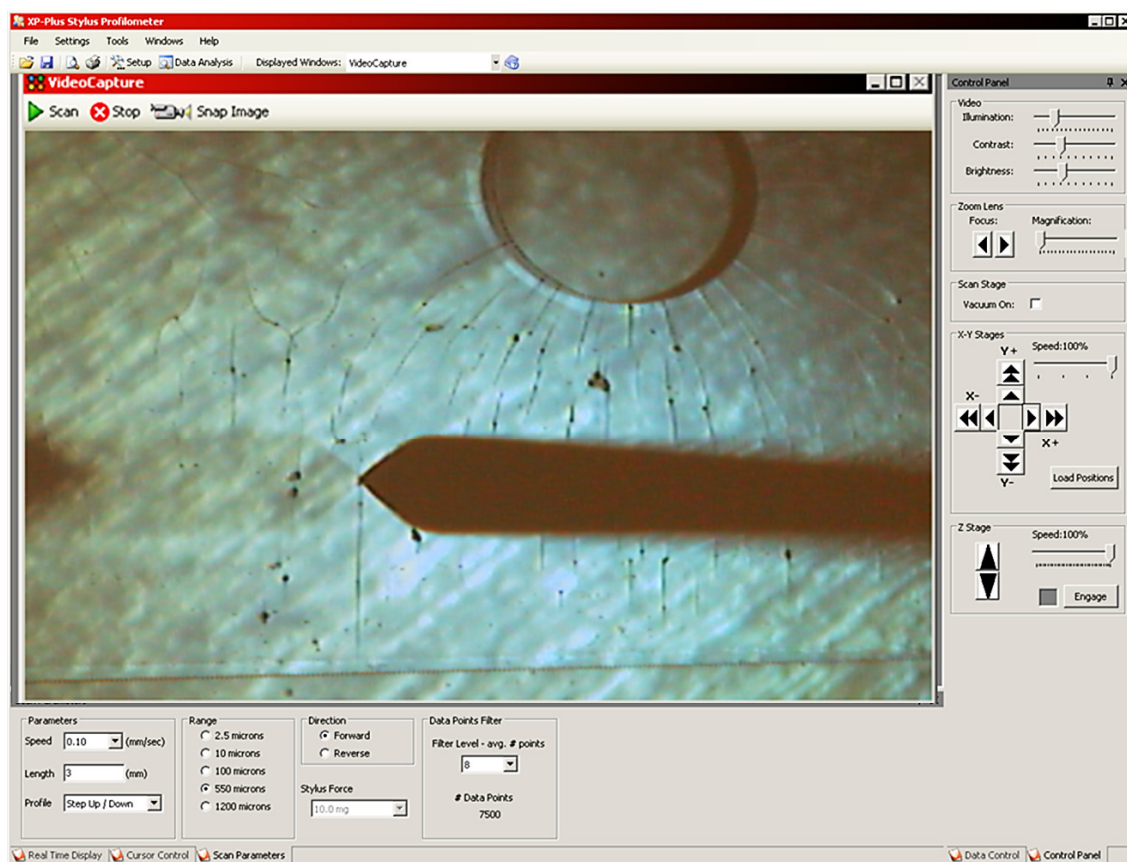


Fig. 2.17. Characterisation of the SU-8 feature by stylus profilometry. For such high thickness range (550  $\mu\text{m}$ ), the stylus force is fixed at the maximum value, so stylus may scratch the SU-8 layer surface.

### 2.3.4. Determination of features' thickness using optical microscopy

In this work, the features' thickness was usually measured by analysing the features cross-section by optical microscopy (Leitz Laborlux 12 ME ST, Germany) integrated with a measurement tool. It is difficult to cut SU-8 features, because of its tendency to peel out. It is much easier to cut PDMS due to its elasticity, so we casted the PDMS and then measured the features' height evaluating its cross-section. It is important to cut the features perpendicularly to the features walls; otherwise it might be difficult to focus well all the features' edges. To not spend much PDMS, few drops of PDMS pre-polymer and curing agent were placed on mould trying to avoid the regions containing high aspect ratio SU-8 features, because they may peel out during the demoulding process. After PDMS curing, the resulting thin PDMS membrane was immobilized perpendicularly under microscope using a bigger block of PDMS and the feature height and sidewall angle were measured (Fig. 2.18).

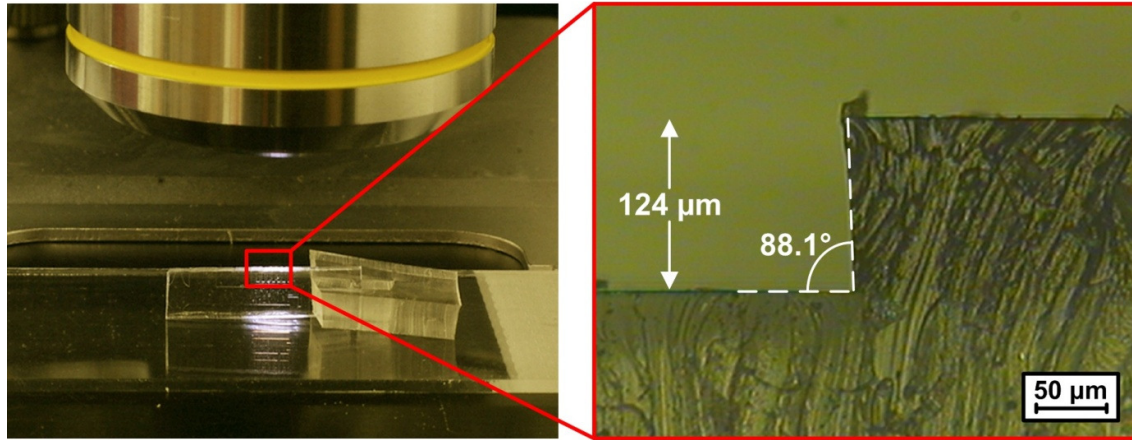


Fig. 2.18. Determination of features' thickness using optical microscopy: PDMS slab was immobilized perpendicularly under microscope using a bigger block of PDMS and the feature height and sidewall angle were measured.

### 2.3.5. Confocal scanning microscopy

Confocal scanning microscopy enables to obtain sharply defined optical micrographs and three-dimensional rendering using scanning point illumination and a spatial pinhole to eliminate out-of-focus light. Confocal imaging does not require use of vacuum neither any additional sample preparation. Principle of confocal microscopy imaging can be found at <http://zeiss-campus.magnet.fsu.edu/referencelibrary/pdfs/ZeissConfocalPrinciples.pdf>.

In this work, confocal scanning microscopy was used to analyse the definition and precision of the microfabricated features and also to evaluate the fidelity of the replica moulding process. The confocal analysis was carried out using LSM 700 (Carl Zeiss, Germany) with laser of 405 nm wavelength with scanning step of 300 nm.

## **Chapter 3**

Inkjet printed and “doctor blade” TiO<sub>2</sub>  
photodetectors for DNA biosensors

*This chapter is written basing on:*

Bernacka-Wojcik, I., Senadeera, R., Wojcik, P.J., Silva, L.B., Doria, G., Baptista, P.V., Aguas, H., Fortunato, E., Martins, R., 2010. Inkjet printed and “doctor blade” TiO<sub>2</sub> photodetectors for DNA biosensors. *Biosensors and Bioelectronics*, pp. 1229–1234. DOI: 10.1016/j.bios.2009.09.027

*This chapter differs from the article in:*

- the results and discussion section has been divided into subsections;
- the working principle of the dye sensitized photodetector has been described;
- the results have been updated by incorporation of the section 3.3.4. Optimization of inkjet printed TiO<sub>2</sub> photodetector;
- experimental details and conclusions have been modified taking into account the new results;
- the images have been edited for the uniformity of thesis formatting.

The author of the thesis was involved in the fabrication of the “doctor-blade” photodetector, characterisation of the photodetectors, AuNPs and Au-nanoprobe colorimetric analysis and was responsible for the design of the study, results analysis and writing of the paper.



<b>Chapter 3. Inkjet printed and “doctor blade” TiO<sub>2</sub> photodetectors for DNA biosensors</b>	<b>71</b>
<b>Summary</b>	<b>71</b>
<b>3.1. Introduction</b>	<b>71</b>
<b>3.2. Experimental section</b>	<b>74</b>
3.2.1. Fabrication of photodetectors	74
3.2.2. Characterisation of photodetectors	77
3.2.3. Preparation of DNA-functionalized gold nanoparticles	77
3.2.4. Detection procedure	77
<b>3.3. Results and discussion</b>	<b>78</b>
3.3.1. Photodetectors’ fabrication and characterisation	78
3.3.2. Colorimetric AuNPs analysis	80
3.3.3. Detection of DNA from <i>M. tuberculosis</i>	81
3.3.4. Optimization of inkjet printed TiO <sub>2</sub> photodetector	82
<b>3.4. Conclusions</b>	<b>87</b>



## Chapter 3. Inkjet printed and “doctor blade” TiO<sub>2</sub> photodetectors for DNA biosensors

### Summary

A dye sensitized TiO<sub>2</sub> photodetector has been integrated with a DNA detection method based on non-cross-linking hybridisation of DNA-functionalized gold nanoparticles, resulting in a disposable colorimetric biosensor. We present a new approach for the fabrication of dye sensitized TiO<sub>2</sub> photodetectors by an inkjet printing technique— a non-contact digital, additive, no mask and no vacuum patterning method, ideal for cost efficient mass production. The developed biosensor was compared against a dye sensitized photodetector fabricated by the traditional “doctor blade” method. Detection of gold nanoparticles aggregation was possible for concentrations as low as 1.0 nM for the “doctor blade” system, and 1.5 nM for the inkjet printed photodetector. The demonstrated sensitivity limits of developed biosensors are comparable to those of spectrophotometric techniques (1.0 nM). Our results show that a difference higher than 17% by traditional photodetector and 6% by inkjet printed in the photoresponses for the complementary and non-complementary gold nanoprobe assays could be attained for a specific DNA sequence from *Mycobacterium tuberculosis*, the etiologic agent of human tuberculosis. The decrease of costs associated with molecular diagnostic provided by a platform such as the one presented here may prove of paramount importance in developing countries.

### 3.1. Introduction

There is an increasing need to develop simple, rapid, and inexpensive detection platforms for diagnostic applications, monitoring food and water contamination by pathogens, environmental analysis, among others (Pejcic et al. 2006). Currently, the majority of available assays is performed under laboratory conditions, frequently with the assistance of expensive instruments and trained personnel. To circumvent these issues, we have combined three emerging technologies—dye sensitized TiO<sub>2</sub> photodetection (Oregon and Gratzel 1991), inkjet printing technology (Le 1998) and colorimetric DNA detection method based on DNA-functionalized gold nanoparticles (Storhoff et al. 1998). This combination is of utmost relevance for the fabrication of a biosensing platform that leads to significant cost and time reduction in detection assays.

The increasing control over the unique size-dependent properties of nanoscale materials has paved the way for integration of such materials into many and/or improved technologies. One such technology has been a range of colorimetric assays for DNA detection based on the distance-dependant optical properties of oligonucleotide functionalized gold nanoparticles. These nanoparticle based systems have been extensively used for the labelling of DNA/protein such that the specific nanoparticle tag allows for the detection of target molecules based on the properties of the material (Baptista et al.

2008). The surface plasmon resonance (SPR) of gold nanoparticles is responsible for their intense colours. In solution, monodispersed gold nanoparticles (AuNPs) appear red and exhibit a relatively narrow SPR band centred around 520 nm in the UV/vis spectrum. In contrast, a solution containing aggregated AuNPs appears blue in colour, corresponding to a characteristic red shift of the SPR. DNA or protein can be used as a linking molecule to aggregate the AuNPs and thus taking advantage of the optical properties of disperse versus aggregated gold particles for biodetection assays (Mirkin et al. 1996). A non-cross-linking hybridisation method has been presented, where aggregation of the DNA-functionalized gold nanoparticles (Au-nanoprobes) is induced by an increasing ionic strength of the solution—the presence of a complementary target to the Au-nanoprobe prevents aggregation and the solution remains red; whereas the presence of non-complementary/mismatched targets does not prevent aggregation, resulting in a visible colour change from red to blue (Baptista et al. 2006; Doria et al. 2007). We have integrated this system with an optoelectronic platform, using a high intensity light source and a colour sensitive amorphous/nanocrystalline silicon photodetector, so as to create a high efficiency biosensor that can be used for the detection of specific DNA sequences (Fortunato et al. 2006; Martins et al. 2007a; Silva et al. 2008).

Here, we report a new approach for the fabrication of dye sensitized nanocrystalline TiO<sub>2</sub> photodetectors (known also as Grätzel cell (Oregan and Gratzel 1991)) by an inkjet printing technique. This inkjet printed photodetector was optimized for use in conjunction with the Au-nanoprobe assay towards utilization as biosensor. This low cost and user-friendly biosensor may lead to significant cost reduction in more than one order of magnitude by minimizing the costs related to the high technology associated with fabrication of silicon-based photodetectors without losing the required sensitivity.

The working principle of the dye sensitized photodetector/solar cell is illustrated in Fig. 3.1A. A wide band gap semiconductor (usually TiO<sub>2</sub> due to its low cost, chemical stability and being non-toxic) is composed of nanoparticles which have been sintered enabling electronic conduction. The nanocrystalline structure of the semiconductor enabled to increase the surface area by three orders of magnitude significantly improving light absorption and resulting efficiency. The semiconductor nanoparticles are covered with a monolayer of charge transfer dye to broaden the light absorption. The light is absorbed by the sensitizing dye causing the electron transfer to higher energy level and then travels to semiconductor conduction band and afterwards to transparent conductive oxide. Through the external load, the electron travels to the counter electrode and subsequently to an organic solvent containing redox system, such as the iodide/triiodide couple. Then, the redox system reduces the dye to its original state.

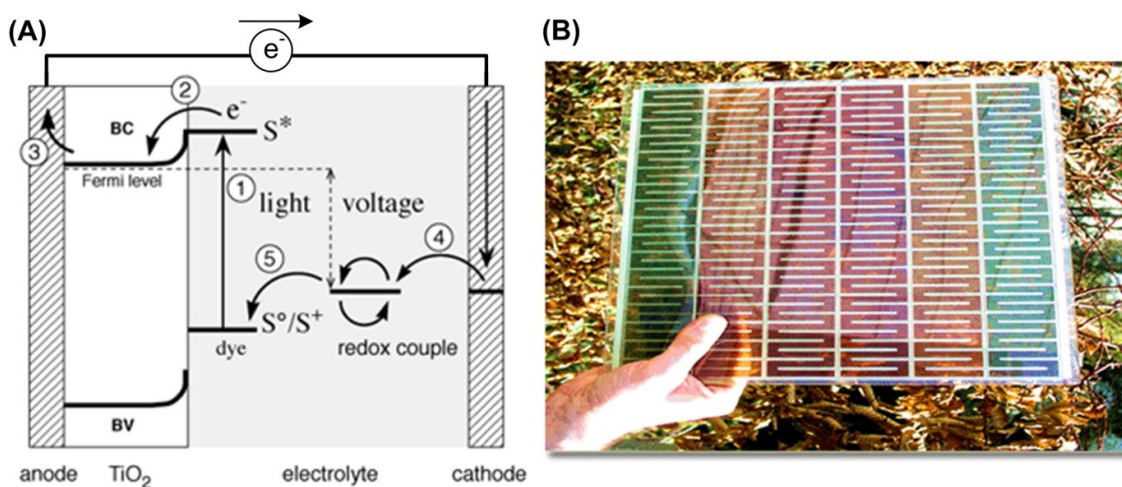


Fig. 3.1. (A) Working principle of dye sensitized photodetector/solar cell: 1. dye photo-oxidation; 2. injection of the excited electron to the semiconductor conduction band; 3. percolation of the electron through porous semiconductor layer towards transparent conductive oxide layer and to counter electrode through external load; 4. injection of electron to a redox system of electrolyte; 5. reduction of the dye to its original state by the electrolyte (<http://www.solaronix.com/technology/dyesolarcells> retrieved in 2014.03). (B) Photograph of dye sensitized solar cells module fabricated using sensitizing dyes of various colours (<http://www.solarisnano.com> retrieved in 2014.03).

The photocurrent generation of these dye sensitized  $\text{TiO}_2$  photodetectors depends on the incident photon energy and the highest spectral response occurs around the 530 nm region (the SPR peak of monodisperse Au-nanoprobes), thus enhancing the already high potential of this biosensing platform. Moreover, the sensitivity of this device can easily be tuned and adjusted by changing the dyes used in the sensitization, see Fig. 3.1B (Oregan and Gratzel 1991). The main limitation of dye sensitized photodetectors over their silicon-based counterparts is the fact that the liquid electrolyte causes significant problems associated with the device sealing and stability that affect the commercialization of these devices. This problem can be overcome by employing solid state dye sensitized photodetectors that contain no volatile electrolytes (Senadeera et al. 2002). The other disadvantage of these photodetectors, when comparing with their Si counterparts, is the lower light to electricity conversion efficiency. Nevertheless, for application of photodetectors in a colorimetric biosensor, conversion efficiency does not play a very important role.

The main development is the introduction of adequate and low cost processing technique for the fabrication of dye sensitized photodetectors—the inkjet printing technology. The use of inkjet printing technique, not only simplifies a patterning process, but also reduces the consumption of materials and energy, allowing the scaling-up from lab prototype device to industrial production. It is a non-contact, no mask and no vacuum patterning method, ideal for cost efficient mass production (Calvert 2001),

being a very attractive and powerful technology for the development of biosensors (Hart et al. 1996) and DNA arrays (Scheda et al. 1998). The decrease of costs associated with molecular diagnostic provided by a platform such as the one presented here may prove of paramount importance in developing countries. The use of inkjet printing in mass production of dye sensitized photodetectors reduces strongly their prices and opens up the possibility of easy fabrication of disposable photodetectors to be used in these biosensors, thus effective for broad application without compromising the device's reliability.

## **3.2. Experimental section**

### **3.2.1. Fabrication of photodetectors**

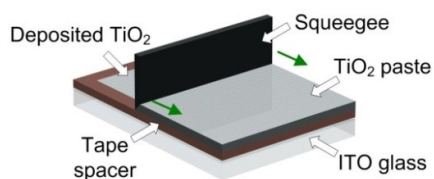
In the fabrication of the photodetectors by inkjet printing technique, viscosity and surface tension controlled aqueous TiO<sub>2</sub> dispersion (ink) were prepared using appropriate amounts of TiO<sub>2</sub> (Solaronix SA, Aubonne, Switzerland and Dye Sol 18NR-T) and Triton X-100 (JT Baker Chemical, Phillipsburg, USA). The dispersion was filtered through a 1.2  $\mu\text{m}$  pore size filter (Chromofil PET-120/25; Macherey-Nagel GmbH & Co. KG, Düren, Germany) and ultrasonically mixed with the appropriate amount of ethanol. A modified commercially available Canon PIXMA IP4500 desktop printer (Canon Virginia, Inc., Newport News, USA) with a resolution of 9600  $\times$  2400 dpi was used as the “device printer”. With this printing unit we can achieve the deposition of the material as a digital printing process, where the ink/material is ejected directly onto a glass substrate from 1536 nozzles driven by an electronic signal. The fabrication of the active layer of TiO<sub>2</sub> with a thickness of  $\sim$ 4–5  $\mu\text{m}$  by inkjet printing was performed at room temperature and atmosphere pressure. In the photodetector optimization study (section 3.3.4), a lab-scale inkjet printer (LP50 PixDRO) was used with heating of the printing stage at 70 °C with varying the number of the printing passes.

The films were deposited on pre-cleaned, indium doped tin oxide conducting glass substrates (ITO, 10–12  $\Omega\text{ sq}^{-1}$ ; Nippon Sheet Glass, Tokyo, Japan) and then sintered at 450 °C for 30 minutes in oven (Nabertherm, Lilienthal/Bremen, Germany). Improved electrical contacts from the ITO substrates were then printed with a commercial solvent-based silver nanoparticle formulation (SunTronic Jettable Silver-U5741; Sun Chemical Corporation, Parsippany, USA) using the Cannon printer and afterwards sintered at 120 °C for 30 minutes. Substrates were then stained in an absolute ethanol solution of Ruthenium dye (N3, cisdi(thiocyanato)bis(2,2-bipyridyl-4,4-dicarboxylate) ruthenium(II); Solaronix SA, Aubonne, Switzerland) for 24 hours. Photodetectors were then fabricated by sandwiching these photoelectrodes with a Pt-coated fluorine doped conducting glass (FTO; Nippon Sheet Glass, Tokyo, Japan). The redox electrolyte containing lithium iodide (0.5 M; Sigma–Aldrich, Steinheim, Germany) and iodine (0.05 M; Sigma–Aldrich, Steinheim, Germany) in a 6:4 v/v mixture of acetonitrile (Sigma–Aldrich, Steinheim, Germany) and propylene carbonate (Sigma–Aldrich,

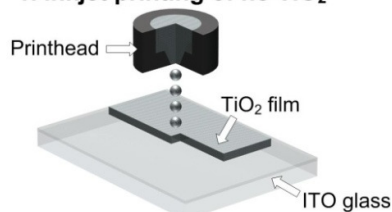
Steinheim, Germany) was introduced between the dye coated TiO<sub>2</sub> electrode and the Pt-counter electrode. Photodetectors with a TiO<sub>2</sub> thickness  $\sim 7\ \mu\text{m}$  (otherwise specified) were fabricated using the same TiO<sub>2</sub> paste by “doctor blade” method, as described by (Senadeera et al. 2005a).

Fig. 3.2 presents a schematic of the production of both photodetectors. The inset shows a scanning electron micrograph of the surface morphology of the TiO<sub>2</sub> film prepared by inkjet printing technology after sintering at 450 °C. No cracks on the surface are observed which indicates a very high inter-particle connectivity. The average diameter of TiO<sub>2</sub> particles is 25 nm.

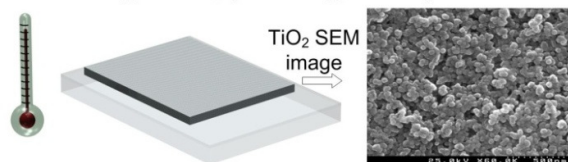
### 1. Deposition of nc-TiO<sub>2</sub> (Doctor Blade)



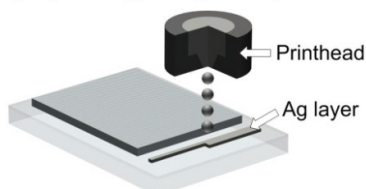
### 1. Inkjet printing of nc-TiO<sub>2</sub>



### 2. Sintering of TiO<sub>2</sub> (30 min @ 450 °C)



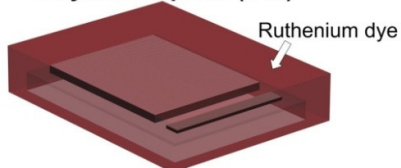
### 3. Inkjet printing of Ag nanoparticles



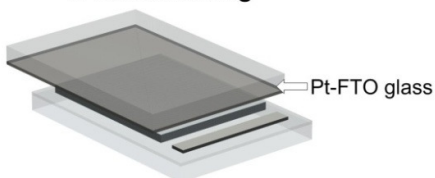
### 4. Sintering of Ag film (30 min @ 120 °C)



### 5. Dye adsorption (24h)



### 6. Sandwiching



### 7. Electrolyte filling

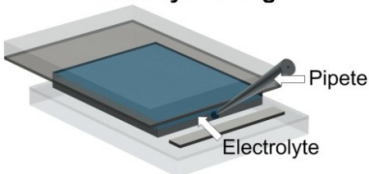


Fig. 3.2. Schematic of the TiO<sub>2</sub> photodetector fabrication by “doctor blade” and inkjet printing technique. The scanning electron micrograph presented the surface morphology of the TiO<sub>2</sub> film prepared by inkjet printing technology after sintering at 450 °C. The film is about 4 μm thick, no cracks on the surface are observed which indicates a very high inter-particle connectivity. The average diameter of TiO<sub>2</sub> particles is 25 nm.



### 3.2.2. Characterisation of photodetectors

The effectiveness of the photosensor to convert light of various wavelengths into electrical current was measured as the incident photon to current conversion efficiency (*IPCE*). *IPCE* (%) is defined as the number of electrons generated by light per number of photons incident on the photodetector, formulated by the simplified equation:

$$IPCE = \frac{1240 \times J_{sc}}{\lambda \times W_i} \quad \text{eq. (3.1)}$$

where  $J_{sc}$  is the short-circuit current density ( $\mu\text{A cm}^{-2}$ ),  $\lambda$  the excitation wavelength (nm) and  $W_i$  is the photon flux ( $\text{W m}^{-2}$ ). The *IPCE* was measured using a homemade set-up coupled to a Keithley Multimeter 238 (Keithley Instruments, Inc., Cleveland, USA) via a computer.

Thickness of  $\text{TiO}_2$  layers was determined by a profilometer Ambios Technology XP-200 (Ambios Technology, Inc., Santa Cruz, USA). Scanning electron micrograph of inkjet printed  $\text{TiO}_2$  layer was done using Hitachi S4100 (Hitachi, Tokyo, Japan). Absorption spectrum of ethanolic solution of the Ruthenium dye was measured using a UV/visible/NIR scanning spectrophotometer UV-3101PC (Shimadzu, Kyoto, Japan).

### 3.2.3. Preparation of DNA-functionalized gold nanoparticles

All oligonucleotides were purchased from STAB Vida, Portugal. The Au-nanoprobes were synthesized by derivatizing an aqueous solution of AuNPs with a thiolated oligonucleotide (5'-thiol-GGACGTGGAGGCGATC-3') recognizing a specific sequence within the *rpo-beta* gene of *Mycobacterium tuberculosis* (GenBank accession no. BX842574) and used as described by (Baptista et al. 2006), with either a complementary DNA oligonucleotide harboring part of the *rpo-beta* gene of *M. tuberculosis* (5'-GATCGCCTCCACGTCCGTTGGTATCAAGGTT-3') or a non-complementary DNA oligonucleotide (5'-GGTCGTCAGACTGTCGATGAAGCC-3'), both at a final concentration of 1.33  $\mu\text{M}$ .

### 3.2.4. Detection procedure

In the prototype biosensor, plastic cuvettes (10 mm path length; Plastibrand, Wertheim, Germany), filled with 75  $\mu\text{l}$  of AuNPs or Au-nanoprobes solution, were placed between the light source (a high power LED, 530 nm light, 35 nm spectral half-width, Luxeon K2 Emitter; Quadica Developments Inc., Brantford, Canada) and the photodetector. The entire platform is placed within a black environment, in order to eliminate ambient light interference. Photocurrents generated by photodetectors were measured by a digital electrometer (Keithley 238; Keithley Instruments, Inc.,

Cleveland, USA) connected to a computer via USB/GPIB interface card (Agilent 82357A; Agilent Technologies, Santa Clara, USA) with developed software (MatLab).

Measurements were performed after 15 minutes of salt addition to AuNPs or Au-nanoprobes solution (0.02 M NaCl or MgCl<sub>2</sub>, respectively). The measurements were repeated 6 times for each sample with a time interval of 150 seconds. Ultra-pure water (Millipore, Billerica, USA) and 10 mM phosphate buffer (pH 8), 0.1 M NaCl were used as reference solutions for AuNPs and Au-nanoprobes, respectively. For validation of the prototype, UV-3101PC and UVmini-1240 UV/visible/NIR scanning spectrophotometers (Shimadzu, Kyoto, Japan) were used for AuNPs and Au-nanoprobes measurements, respectively. DNA detection reactions were carried out with the appropriate target and Au-nanoprobes at a final concentration of 2.5 nM, in 10 mM phosphate buffer (pH 8). After 10 min of denaturation at 95 °C, the mixtures were allowed to slowly cool down to 20 °C until salt addition.

The reported expanded uncertainties are based on a standard uncertainty multiplied by a coverage factor  $k = 2.65$ , providing a coverage probability of approximately 95%. The uncertainty evaluation has been carried out in accordance with International Organization for Standardization requirements.

### **3.3. Results and discussion**

#### **3.3.1. Photodetectors' fabrication and characterisation**

We developed a disposable biosensor integrating a dye sensitized TiO<sub>2</sub> photodetector obtained by standard “doctor blade” method (from now on referred as “doctor blade” photodetector, DBP; (Smestad 1998)) and by inkjet printing technology (described as inkjet printed photodetector, IPP) to be used in conjunction with the Au-nanoprobes based method. In the case of fabrication of the IPP, through an improved formulation of specific water-based Solaronix inks (Section 3.2.1), we attained a TiO<sub>2</sub> photodetector by thermal inkjet printing technology. The inks must meet strict physicochemical properties (viscosity, surface tension, etc.) to achieve optimal performance of printed device. The optimum composition of TiO<sub>2</sub> water-based ink was 20 wt% of ethanol and 0.12 wt% of TiO<sub>2</sub>. Such composition resulted in a viscosity that was acceptable for conventional office printers (1–10 cP). Additionally, Triton X-100 (5%) was added to the ink, which resulted in more effective jetting while maintaining a well-defined and uniform film layer. The dispersion of TiO<sub>2</sub> does not undergo a sedimentation process (particles with diameter smaller than 1.2 µm). Long term viscosity measurements showed that this dispersion is also free of aggregation and demonstrated a greater chemical stability of crystal over solution in comparison with sol–gel ink. Highly conductive contact tracks from inkjet printed silver nanoparticle further helped in the stability and performance of this photodetector. This inkjet printing technique may circumvent the existing time-consuming and expensive microfabrication of conductive tracks by lithography or electrolysis.

Fig. 3.3 depicts the incident photon to current conversion efficiencies (*IPCE*) of the traditional DBP and novel IPP. The inset of the figure shows the absorption spectrum of the ethanol solution of Ruthenium (N3) dye. While the absorption spectrum of the N3 in ethanol showed an intense absorption at ~539 nm, the *IPCE* peaks of DBP and IPP were at 537 nm and 525 nm, respectively. As it is generally observed with the dye sensitized photodevices, the close relationship and shifts of the *IPCE* peaks with the optical absorption spectra indicate that the photo-electrochemical conversion is achieved through photosensitization, namely that N3 molecules absorbed photons and generated excited electrons, and the excited electrons were subsequently transferred to the conduction band of the TiO<sub>2</sub> electrode. These shifts mainly depend on the strength of the chelation of the dye molecules to the semiconducting surface and the surface morphology of the semiconductor. For both photodetectors, the maximum *IPCE* was observed around 530 nm, which is in the vicinity of the SPR peak of the monodisperse Au-nanoprobles, confirming the compatibility of the detector and Au-nanoprobles integration in a biosensor. The IPP showed lower *IPCE* than the DBP, probably due to the higher film thickness of the active layer of the DBP, which absorbs more dye molecules, hence creates higher photocurrent density and the *IPCE* (Junghanel and Tributsch 2005; Kang et al. 2004).

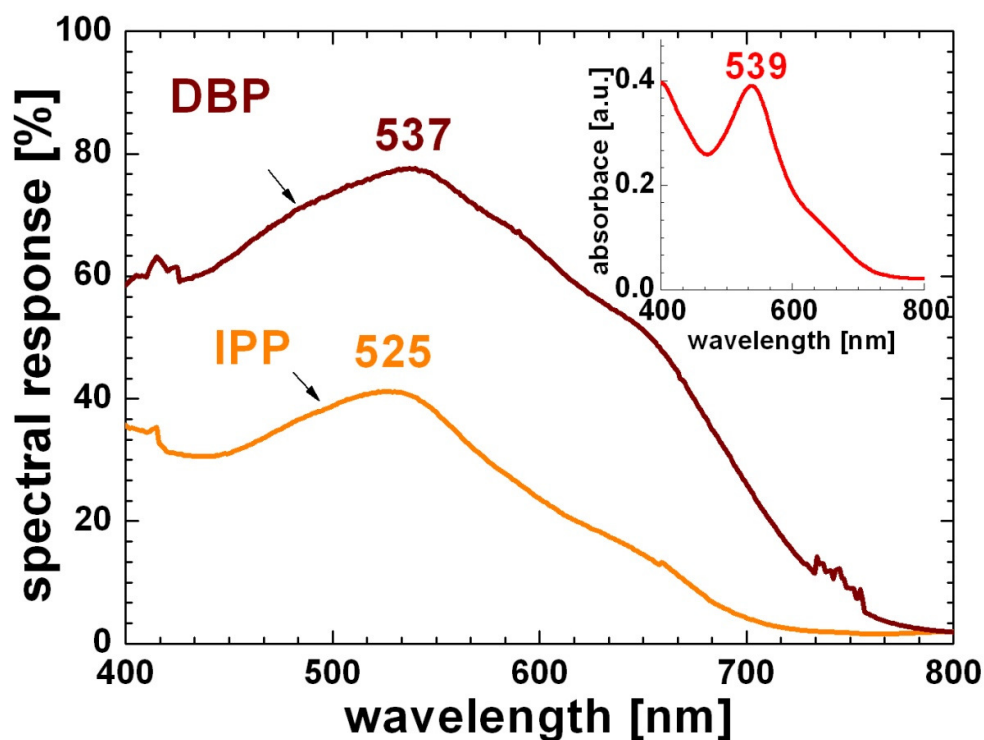


Fig. 3.3. Incident photon to current conversion efficiency (*IPCE*) of the photodetector obtained by “doctor blade” method (DBP) and by inkjet printing (IPP). The TiO<sub>2</sub> layer of DBP is about 1.75 times thicker than in the case of the IPP, which may explain the observed difference at the *IPCE*. Inset: Absorption spectrum of the ethanol solution of Ruthenium N3 dye.

### 3.3.2. Colorimetric AuNPs analysis

The fabricated photodetectors were individually mounted on a platform inside a black box to cut-off incident background light. Plastic cuvettes filled with each solution were then placed between the light source (green LED) and the photodetector. The photocurrent generated by the photodetector due to the non-absorbed light coming out from the cuvette was measured by an electrometer and relayed to the computer.

Several non-aggregated AuNPs solutions (red) of known concentrations were used to assess the response and the sensitivity of the sensors, and compared with data attained by conventional UV/vis spectrophotometry. Fig. 3.4A and B shows the results obtained using the novel platforms with either DBP or IPP, respectively. The inset shows the corresponding spectrophotometry results. The detection responses ( $R_{det}$ ) were calculated by measuring the differences in the photocurrent densities obtained for the reference (ultra-pure water and phosphate buffer for AuNPs and Au-nanoprobes, respectively) and the sample solution. Again, the sensor with the IPP showed lower photoresponses probably due to the lower thickness of the active layer compared to the device with DBP. To compare the responses of the developed sensors with those of the spectrophotometer, the integral of the absorption peak over the wavelength range between 520 and 540 nm (spanning the emission spectra of the LED) was used. The output signals of both the sensors and the spectrophotometer show a linear variation for the non-aggregated particles (red colour solution) with high accuracy ( $R^2 > 0.98$ ). In the case of the aggregated particles (blue colour solution), a non-linear variation is observed for both methodologies. This can be explained by the several different events occurring (e.g. aggregation, flocculation, precipitation and possible adsorption to the plastic surface of the cuvette), which lead to light scattering and decrease the amount of light being transmitted through the solution. Nevertheless, in terms of application as biosensor what is relevant is the capability of discrimination between the aggregated and non-aggregated forms of the AuNPs, and not the linearity of these responses. Very clear differences in the responses of the sensors were observed for the AuNPs solution concentrations routinely used in the Au-nanoprobe based DNA detection method (from 1.5 to 2.5 nM; (Baptista et al. 2006; Doria et al. 2007)). For low concentrations, below 1.0 nM for DBP and 1.5 nM for IPP, the generated photocurrent densities were nearly the same for both solutions indicating the sensitivity limit of the sensor. The detection limit of the spectrophotometer is superior to 0.5 nM. The measurements were consistent and reproducible, and comparable to those attained for spectrophotometry, showing that the developed sensors may be a low cost and effective alternative for use with the AuNPs based assay. We observe larger fluctuations of the acquired data in the comparison with spectrophotometry, because we are using a LED, which does not have a single wavelength emission but an emission profile of 30 nm half-width peak. This together with the considerable noise introduced by the system, e.g. photodetector, cables, power supply and electrometer is responsible for the larger uncertainty bars. All

these factors causing fluctuations during data acquisition need to be dealt upon at a later stage of prototype optimization.

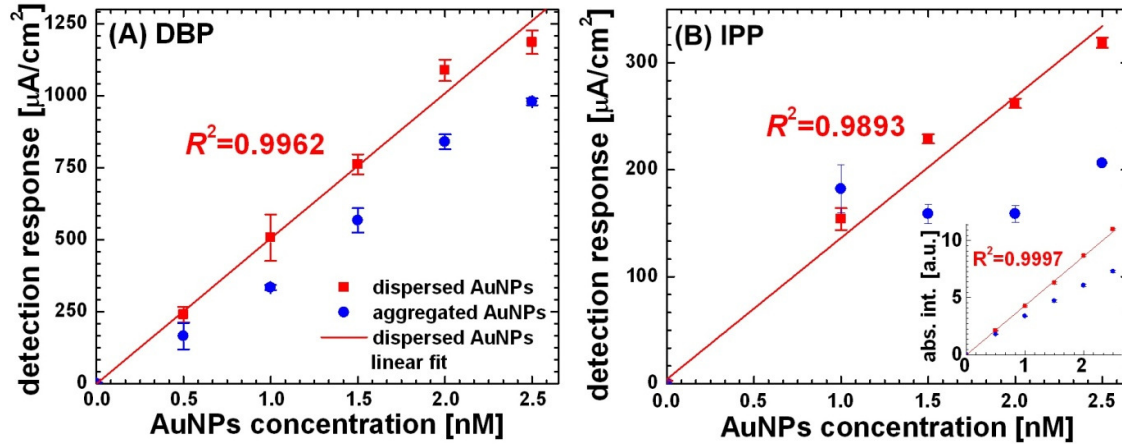


Fig. 3.4. Responses of the sensor with (A) “doctor blade” photodetector and (B) inkjet printed photodetector for different AuNP concentrations. Non-aggregated (red squares) and aggregated by salt addition (blue circles). The detection response ( $R_{det}$ )—difference in the photocurrent densities generated by photodetector when illuminating through the reference solution and through the sample solution. Measurements using a high power LED with 530 nm and 35 nm spectral half-width. *Inset*: Corresponding spectrophotometric measurements: absorption peak area integral from 520 to 540 nm as a function of AuNP concentration. Standard deviation bars were determined from 6 independent measurements.

### 3.3.3. Detection of DNA from *M. tuberculosis*

Finally, as a proof-of-concept, the sensors were applied in conjunction with the Au-nanoprobe assay to detect a specific DNA sequence from *M. tuberculosis* (Baptista et al. 2006), the etiologic agent of human tuberculosis. Mixtures containing the Au-nanoprobe and complementary oligonucleotide target (positive, POS—red) or non-complementary target (negative, NEG—blue), were screened by both the developed sensors and the spectrophotometer. The Au-nanoprobe aggregation (non-complementary assay) induced by salt addition resulted in the shift of the SPR maximum of 26 nm compared to the complementary assay, Fig. 3.5 inset). A clear difference in the detection response of the sensors between complementary (POS) and non-complementary (NEG) assays is observable in the  $\mu\text{A}$  range. The percentage difference between detection response for complementary and non-complementary assays was 17.5% for the DBP and 6.7% for the IPP (Fig. 3.5B). Even though the inkjet printed photodetectors gave lower difference of detection responses than photodetectors fabricated by the traditional method, it should be noted that the inkjet printing is employed for the first

time in the dye sensitized  $\text{TiO}_2$  technology, and the properties of IPPs still need to be fully optimized. Nevertheless, the IPP based platform was able to clearly detect the presence or the absence of a specific DNA target.

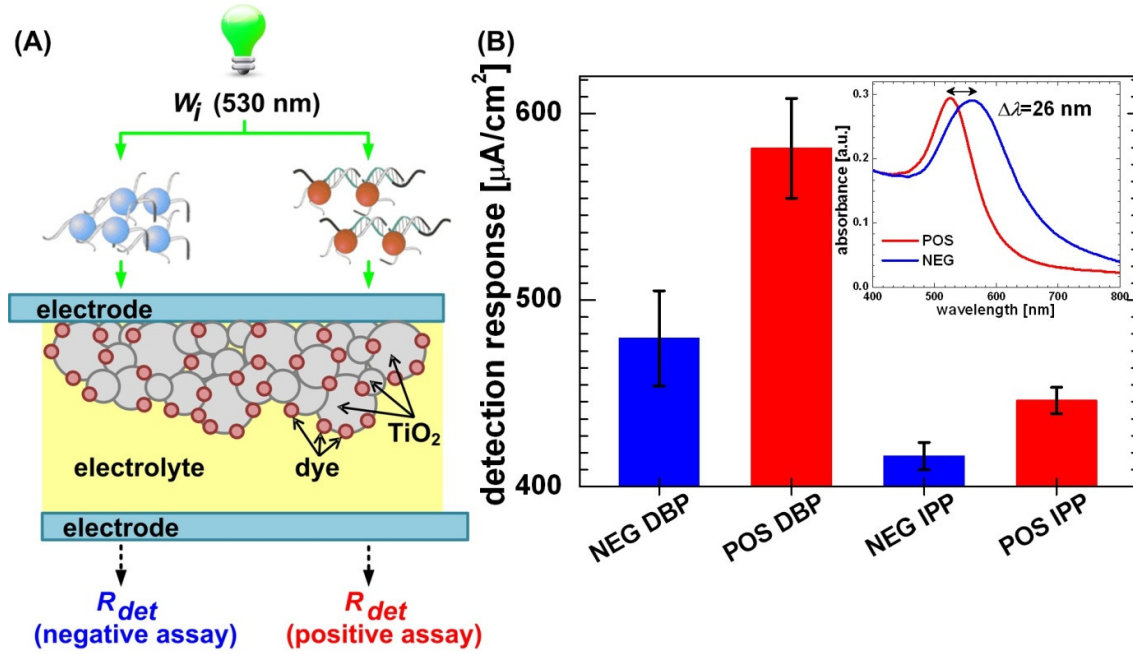


Fig. 3.5. (A) Schematic representation of DNA detection of the developed biosensor ( $W_f$ —the photon flux and  $R_{det}$ —detection responses). (B) The Au-nanoprobe based assays for *M. tuberculosis* DNA with the novel sensors with DBP and IPP: POS—complementary DNA target; NEG—non-complementary DNA target;  $R_{det}$ —difference in the photocurrent densities generated by photodetector when illuminating through the reference solution and through the sample solution. Inset: Absorption spectra of DNA solutions (in arbitrary units). The absorption spectrum of NEG was shifted for the same absorbance value at  $\lambda = 400$  nm as POS (shift =  $-0.0067$  a.u.) so as to allow better colour change visualization. DNA detection was carried out with the appropriate oligonucleotide target at a final concentration of  $1.33 \mu\text{M}$  and Au-nanoprobes at a final concentration of  $2.5$  nM. Standard deviation bars were determined from 6 independent measurements.

### 3.3.4. Optimization of inkjet printed $\text{TiO}_2$ photodetector

To improve the performance of the inkjet printed  $\text{TiO}_2$  photodetector, the thickness of  $\text{TiO}_2$  layer was varied to assess its optimum value.  $\text{TiO}_2$  layer of various thicknesses was fabricated also by “doctor blade” for the comparison purpose. In order to allow a better control of the printed film thickness,

instead a previously used desktop printed, a lab-scale inkjet printer (LP50 PixDRO) was used in these tests enabling to program number of printing passes and stage heating. In this study, the stage was heated at 70 °C to enhance the solvent evaporation during the deposition process. Afterwards, all the produced films were sintered at 450 °C for 30 min.

Commercial TiO<sub>2</sub> pastes that were developed for the screen printing (Solaronix and Dye Sol) were used in these tests. In the case of the Dye Sol paste, for higher film thickness (above 7.2 µm), the inkjet printed TiO<sub>2</sub> layer was peeling out from the substrate. The obtained thickness range was too low to give satisfactory device performance.

The Solaronix paste was more compatible with inkjet printing and it enabled to obtain a 12.6 µm thick TiO<sub>2</sub> layer when sintering with the temperature ramp of 10 °C/min. Fig. 3.6 presents profiles and optical micrographs of TiO<sub>2</sub> layers of various thicknesses fabricated using the Solaronix paste by “doctor blade” (Fig. 3.6A) and inkjet printing technique (Fig. 3.6B and C). In the inkjet printing, the thickness is defined by number of printing passes, while in the “doctor blade” method, the thickness is controlled only by the thickness of the used patterning mask, so only specific thickness values can be obtained. In Fig. 3.6, the TiO<sub>2</sub> films that resulted in functioning devices were labelled in green, while the malfunctioning—in red. Using the “doctor blade” method, TiO<sub>2</sub> films of thickness from 4.7 to 12.5 µm were obtained and 92% of these films gave functioning devices. For inkjet printing for the sintering temperature ramp of 10 °C/min, the thickness range of 1.7 to 12.6 µm was obtained and 90% of these samples resulted in working devices.

Then, to reduce the device production time, the inkjet printed TiO<sub>2</sub> films were sintered with 5 times higher temperature ramp (50 °C/min). With this approach, TiO<sub>2</sub> films of thickness from 1.3 to 8.5 µm were fabricated (above this range, TiO<sub>2</sub> layer was peeling out) and only 40% of them gave functioning devices due to the presence of cracks. Therefore, we conclude that the slow temperature increase during the sintering process is an important factor for the quality of the inkjet printed TiO<sub>2</sub>. In the further experiments, all the samples were sintered with the temperature ramp of 10 °C.

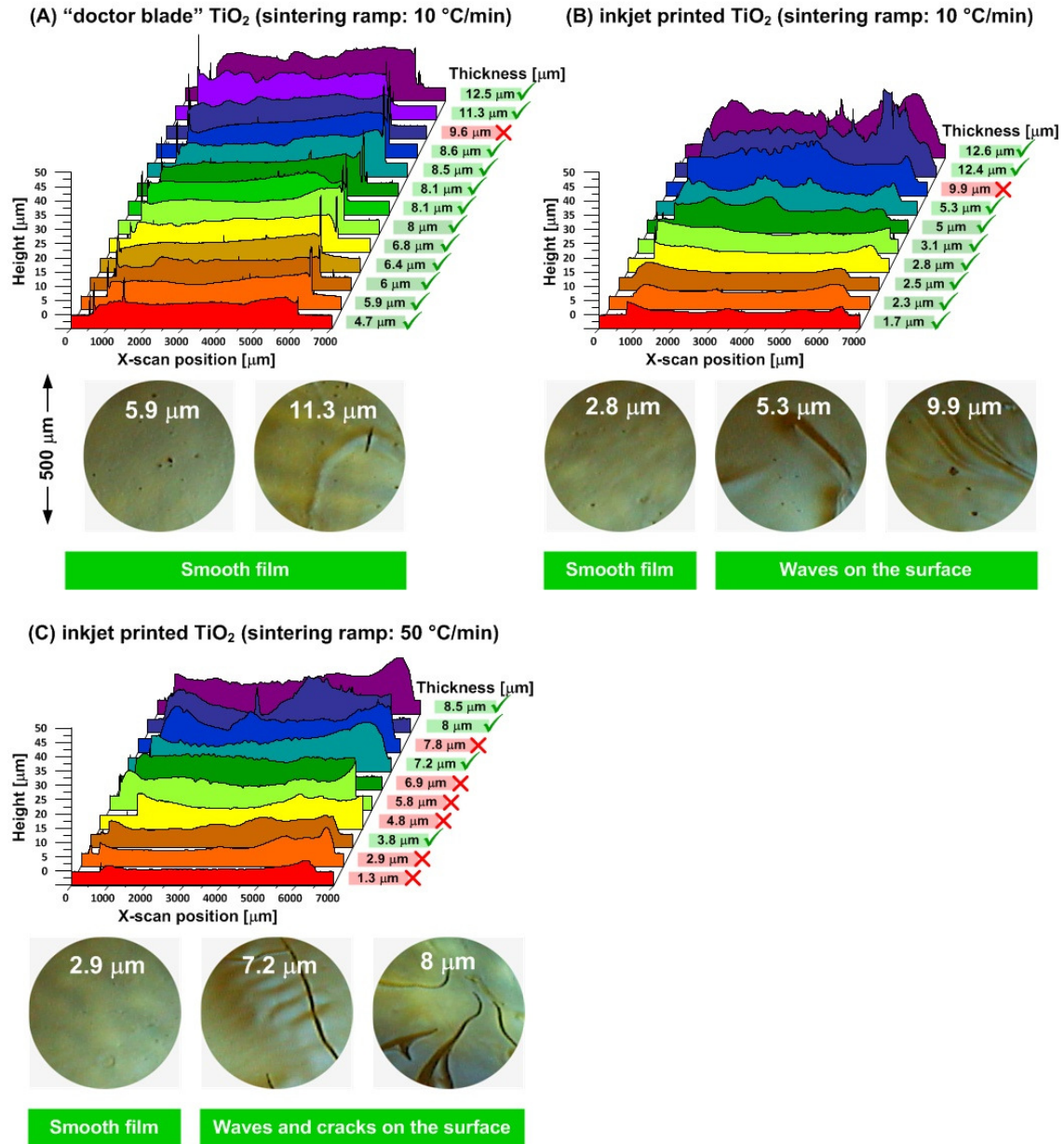


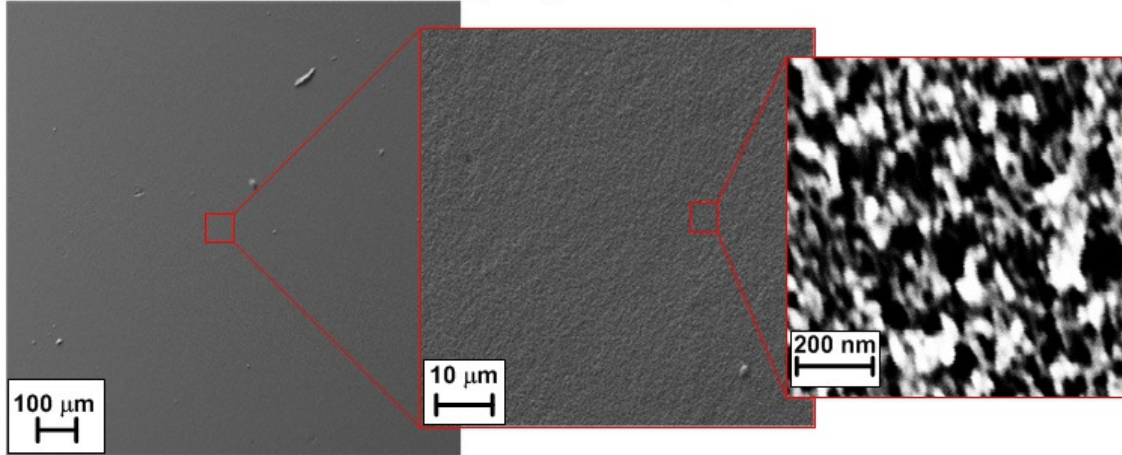
Fig. 3.6. Profiles and optical micrographs of TiO<sub>2</sub> layers of various thicknesses fabricated using the Solaronix paste by (A) “doctor blade” and (B) inkjet printing technique with sintering ramp of 10 °C/min and (C) 50 °C/min. During the inkjet printing process, the stage was heated to 70 °C. The TiO<sub>2</sub> films that resulted in functioning devices were labelled in green, while the malfunctioning—in red.

The obtained samples were characterised by scanning electron microscope to evaluate their morphology. As it can be seen in Fig. 3.7, the TiO<sub>2</sub> film fabricated by inkjet printing is much more porous and less compact than in the case of the “doctor blade”. Most probably it is related with the



fact that in the inkjet printing, the solvent evaporates during the droplet fly from the nozzle to the substrate due to its picoliter volume. Here, the solvent evaporation was additionally enhanced by the applied heating of printing stage (70 °C).

**(A) “doctor blade” TiO<sub>2</sub> (sintering ramp: 10 °C/min)**



**(B) inkjet printed TiO<sub>2</sub> (sintering ramp: 10 °C/min)**

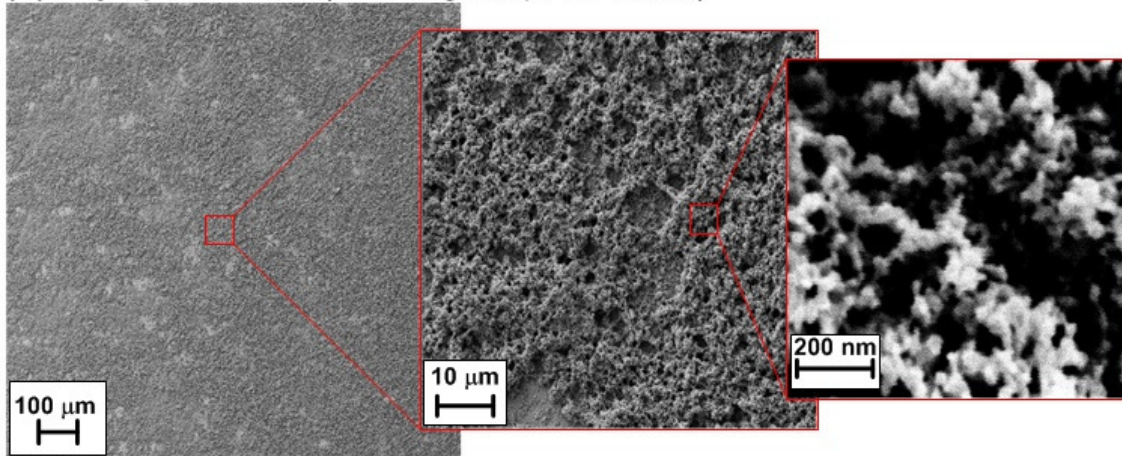


Fig. 3.7. SEM images of TiO<sub>2</sub> films fabricated using the Solaronix paste by (A) “doctor blade” (3.4 μm thick) and (B) inkjet printing technique (1.6 μm thick) with sintering ramp of 10 °C/min. The higher porosity of the inkjet printed TiO<sub>2</sub> films is most probably caused by the solvent evaporation during the droplet fly from the nozzle to the substrate that is additionally enhanced by the applied heating of printing stage (70 °C).

The resulting TiO<sub>2</sub> films were then used for fabrication of photodetectors and their performance was evaluated indirectly basing on their current-voltage characteristics under sun illumination. The energy conversion efficiency is not the most suitable parameter for the photodetector characterisation, but it

enables to compare the performance of various devices and also to evaluate their potential for the application in dye sensitized solar cells. Fig. 3.8 presents the energy conversion efficiency of the photodetectors incorporating “doctor blade” and inkjet printed TiO<sub>2</sub> films. In the case of the devices with “doctor blade” TiO<sub>2</sub>, the efficiency increases with thickness up to 8.6 μm ( $\eta_{\max} \approx 2.56\%$ ), but then it decreases at 12.5 μm. This dependence is in agreement with the experimental results (Huang et al. 2006) and simulation results reported elsewhere (Oktiawati et al. 2013) showing that the optimum TiO<sub>2</sub> layer thickness is around 10 μm. When the thickness of TiO<sub>2</sub> increases, more photons from solar energy can be adsorbed but the transport resistance increases and recombination resistance decreases, affecting the energy conversion efficiency. The optimal compromise of these effects occurs around film thickness of 10 μm, which results in the best device performance.

The incorporation of the inkjet printed TiO<sub>2</sub> film enabled to obtain a 20% higher efficiency: the device with 12.6 μm thick layer gave the efficiency of 3.06%. Most probably, this improvement is related with the higher porosity of the inkjet printed film (see Fig. 3.7) that allows better electrolyte penetration. To determine the optimal layer thickness, further tests should be performed screening around the thickness recommended in literature, i.e. 10 μm (in these tests, the 9.9 μm thick layer was not working properly, probably due to some defects, see Fig. 3.6).

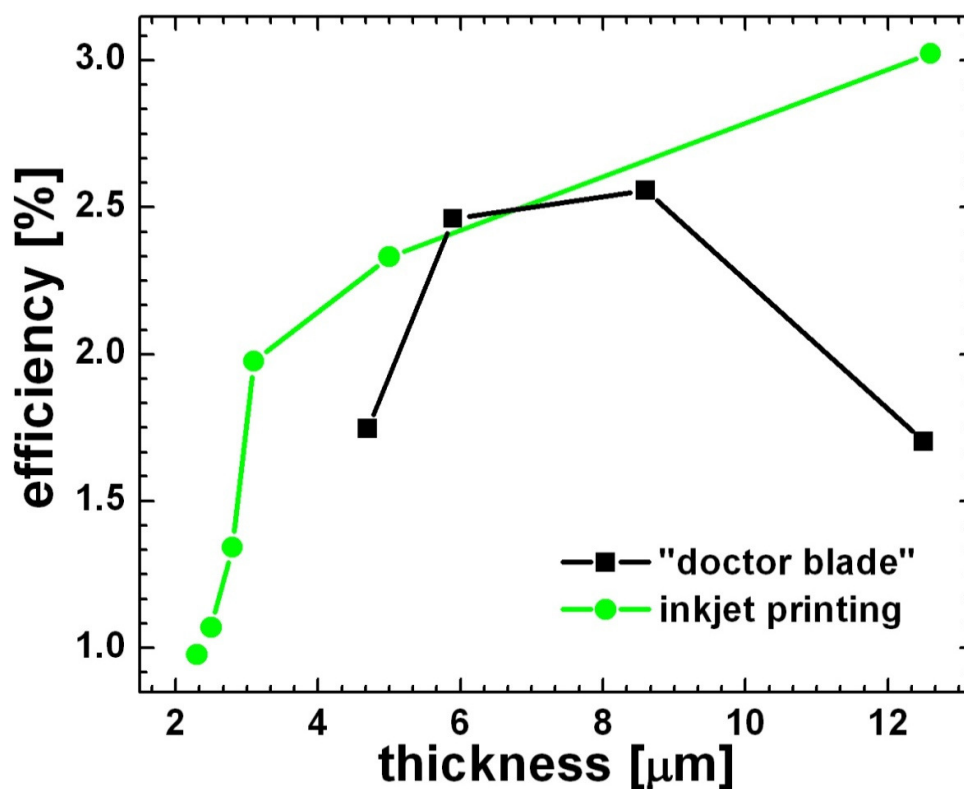


Fig. 3.8. Energy conversion efficiency of photodetectors incorporating  $\text{TiO}_2$  films fabricated using the Solaronix paste by (A) “doctor blade” and (B) inkjet printing technique (the connecting lines are for eyes guidance only).

### 3.4. Conclusions

To our knowledge the use of dye sensitized  $\text{TiO}_2$  sensors for DNA detection by means of Au-nanoprobes has been demonstrated for the first time. Moreover, we describe here pioneer results of inkjet printing technology application to the fabrication of the active layers of photodetectors. The developed biosensor including dye sensitized photodetector fabricated by traditional “doctor blade” method detected the aggregation of AuNPs concentrations as low as 1.0 nM, while for the inkjet printed photodetector the limit was set at 1.5 nM. The sensitivity limits of the developed biosensors are comparable to the sensitivity limit of the spectrophotometry based techniques (1.0 nM). Both photodetectors gave clear and distinct differences in the detection responses for the complementary and non-complementary DNA assays. Our results show that a difference of 17.5% by traditional photodetector and 6.7% by inkjet printed in photoresponses for the complementary and non-complementary Au-nanoprobe assays could be attained. The DBP gives nearly as good results as spectrophotometry, while usability and reliability of the established IPP used in DNA sequence identification still requires further experimental development. The photodetectors’ sensitivity for the

colorimetric changes can be further increased by enhancing the spectral responses of the detector through the use of different dyes.

To improve the performance of the inkjet printed photodetector, the printing procedure was optimized enabling to fabricated thick (up to 12.5  $\mu\text{m}$ ), smooth films of highly porous structure. Then, the thickness of inkjet printed  $\text{TiO}_2$  was adjusted allowing to obtain a 20% higher efficiency than in the case of the “doctor blade” devices. Due to its low cost and possibility to fabricate more porous structures, the inkjet printing is a promising patterning technology also for other  $\text{TiO}_2$  applications, such as dye sensitized solar cells, semiconductor devices, gas sensors, photochromic devices etc.

Once the photodetectors have been fully optimized, the same methodology should be applied to other relevant DNA target sequences and with increased complexity. Further research is being also carried out to evaluate the possible association within a fully integrated, portable biosensor by means of microfluidic technology. The combination of three emerging technologies: (i) dye sensitized  $\text{TiO}_2$  photodetection, (ii) inkjet printing technology and (iii) colorimetric DNA detection based on DNA-functionalized gold nanoparticles may lead to significant cost and time reduction in DNA detection.

## **Chapter 4**

Bio-microfluidic platform for gold nanoprobe  
based DNA detection—application to  
*Mycobacterium tuberculosis*

*This chapter is written basing on:*

Bernacka-Wojcik, I., Lopes, P., Vaz, A.C., Veigas, B., Wojcik, P.J., Simões, P., Barata., D., Fortunato, E., Baptista, P.V., Águas, H., Martins, R., 2013. Bio-microfluidic platform for gold nanoprobe based DNA detection—application to *Mycobacterium tuberculosis*. Biosensors and Bioelectronics 48(0), 87-93. DOI: 10.1016/j.bios.2013.03.079

*This chapter differs from the article in:*

- Supplementary information has been merged into the article text for the reading flow;
- in the chapter introduction, additional information has been provided to give the broader view; i.e. indication of the relation between work described in this chapter and in chapter 3 and description of the development of macro-machined PDMS containers);
- instead of using term “sensitivity”, the  $\Delta R_s$  was named “colorimetric discrimination”;
- the images have been edited for the uniformity of thesis formatting.

The author of the thesis was involved in design of the opto-electronic platform, Au-nanoprobe colorimetric analysis and was responsible for the design and integration of the bio-microfluidic platform, development of the macro-machined PDMS containers, optimisation of the microfabrication process, characterisation of the microchips, optical sensing tests and results analysis and writing of the paper.

<b>Chapter 4. Bio-microfluidic platform for gold nanoprobe based DNA detection— application to <i>Mycobacterium tuberculosis</i></b>	<b>93</b>
<b>Summary</b>	<b>93</b>
<b>4.1. Introduction</b>	<b>93</b>
<b>4.2. Experimental details</b>	<b>99</b>
4.2.1. Fabrication of macro-machined PDMS containers	99
4.2.2. Fabrication of microfluidic chip	99
4.2.3. Opto-electronic set-up	100
4.2.4. Sample DNA preparation	101
4.2.5. Au-nanoprobe synthesis and characterisation	102
4.2.6. Au-nanoprobe colorimetric assay	102
4.2.7. Detection procedure and analysis	103
<b>4.3. Results and discussion</b>	<b>103</b>
4.3.1. Development of macro-machined PDMS containers	103
4.3.2. Microfluidic chip development	108
4.3.3. Optical performance	113
4.3.4. <i>M. tuberculosis</i> detection via the microfluidic platform	115
<b>4.4. Conclusions</b>	<b>118</b>





## **Chapter 4. Bio-microfluidic platform for gold nanoprobe based DNA detection—application to *Mycobacterium tuberculosis***

### **Summary**

We have projected and fabricated a microfluidic platform for DNA sensing that makes use of an optical colorimetric detection method based on gold nanoparticles. The platform was fabricated using replica moulding technology in PDMS patterned by high aspect ratio SU-8 moulds. Biochips of various geometries were tested and evaluated in order to find out the most efficient architecture, and the rationale for design, microfabrication and detection performance is presented. The best biochip configuration has been successfully applied to the DNA detection of *Mycobacterium tuberculosis* using only 3  $\mu$ l on DNA solution (i.e. 90 ng of target DNA), therefore a 20-fold reduction of reagents volume is obtained when compared with the actual state-of-the-art.

### **4.1. Introduction**

Microfluidics has grown exponentially in recent years, providing efficient lab-on-chip platforms for drug discovery, studies of cell and molecular interactions and, above all, molecular diagnostics. Microfluidic devices allow the use of small amounts of reagents and sample in fast high throughput portable platforms that have the potential for automation and high-level integration that are associated with decreased cost (Mark et al. 2010). These devices can also be designed for multi-parallel operation, making the system more reliable as several control assays can be performed simultaneously with multiple samples (Abgrall 2007; Ben-Yoav et al. 2012; Khoshmanesh et al. 2011; Soe et al. 2012). Recently, many microfluidic devices for DNA analysis have been developed allowing for the miniaturisation of DNA amplification (Zhang et al. 2006), detection of picograms of DNA (Xiang et al. 2012a), fast DNA hybridisation (Henry and O'Sullivan 2012) and even integrated DNA analysis including sample pretreatment, DNA amplification and the detection (Burns et al. 1998). However, so far a complete lab on chip device for DNA analysis has not been successfully commercialised mainly due to high cost of the fabrication and/or manipulation (Choi et al. 2011).

Nanodiagnostics, i.e. the use of nanotechnology platforms for nanosensing applications based on the amazing optical properties of gold nanoparticles (Doria et al. 2012) have revolutionised the molecular field of analysis. In solution, disperse AuNPs appear red and exhibit a relatively narrow surface plasmon absorption band centred around 520 nm in the visible spectrum. In contrast, a solution containing aggregated AuNPs appears blue in colour, corresponding to a characteristic red shift of the surface plasmon resonance. AuNPs can be easily functionalized with relevant biomolecular moieties for bio-recognition, e.g. antibodies or ssDNA oligonucleotides and therefore can be used for biodetection assays (Storhoff et al. 2004; Taton et al. 2000). The use of thiol-ssDNA functionalised

gold nanoparticles (gold nanoprobess, Au-nanoprobess) for DNA detection has paved the way for simple yet sensitive and specific molecular diagnostic strategies. Amongst these, a detection scheme based on the differential colorimetric behaviour of Au-nanoprobess after salt induced aggregation mediated by the presence of a complementary target sequence has been widely explored—the presence of a complementary target prevents aggregation and the solution retains its original red colour; while absence of this specific sequence results in aggregation and the solution turns blue (Baptista et al. 2008), see Fig. 4.1 and Fig. 4.2. This DNA analysis method based on non-cross-linking DNA hybridisation has proved to be selective, sensitive, easy-to-perform, inexpensive and reliable in single-nucleotide polymorphism identification.

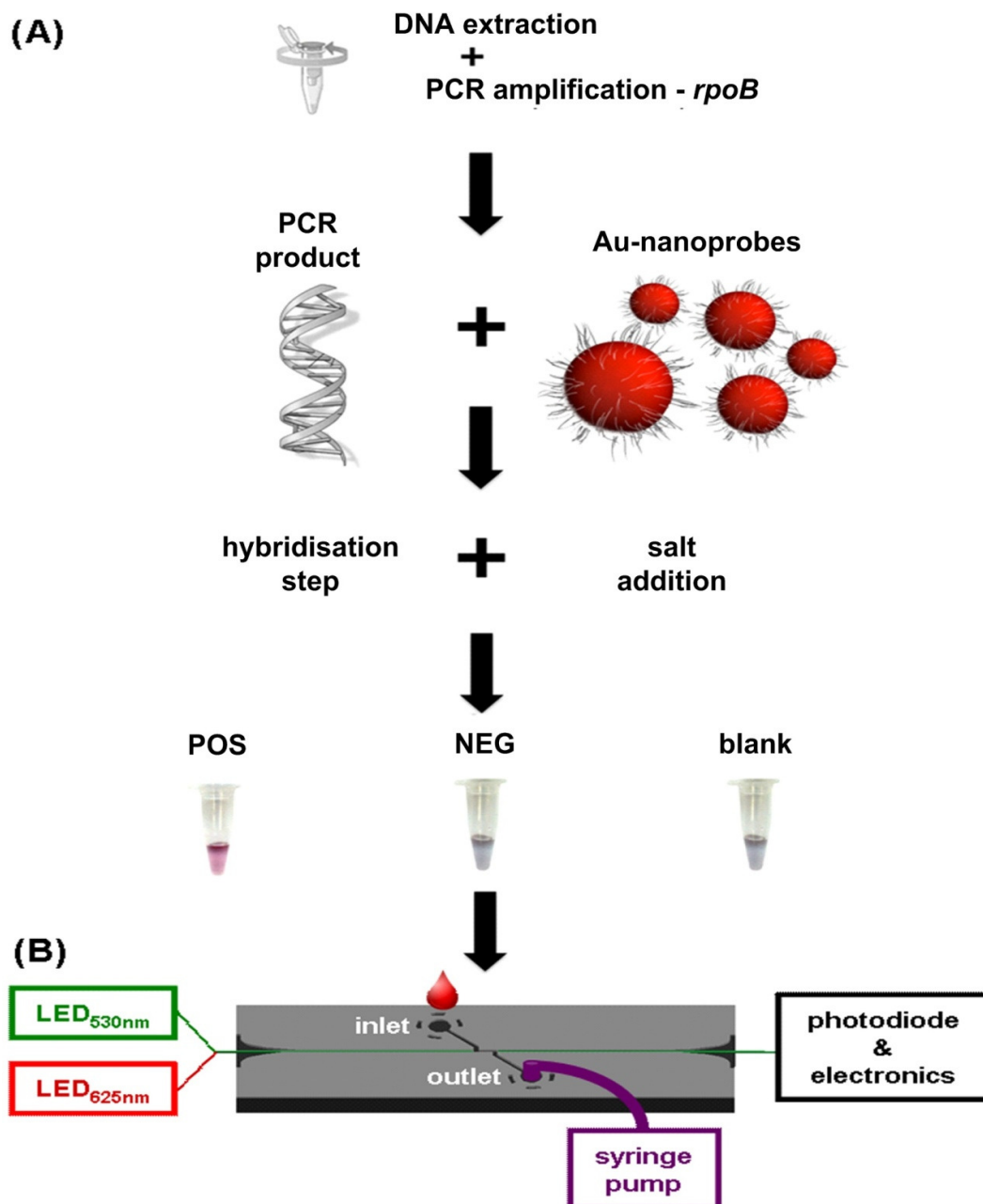


Fig. 4.1. (A) Schematic representation of the DNA detection method based on non-cross-linking DNA hybridisation of Au-nanoprobes. (B) Diagram of the developed microfluidic platform. Solution to be analysed is dispensed into the inlet well and injected to the channel by the withdrawing from the outlet using a syringe pump. Optical fibres guide the light from the LEDs to the microfluidic detection channel and then to the photodiode. The bulk part of the PDMS is not shown to not darken the image.

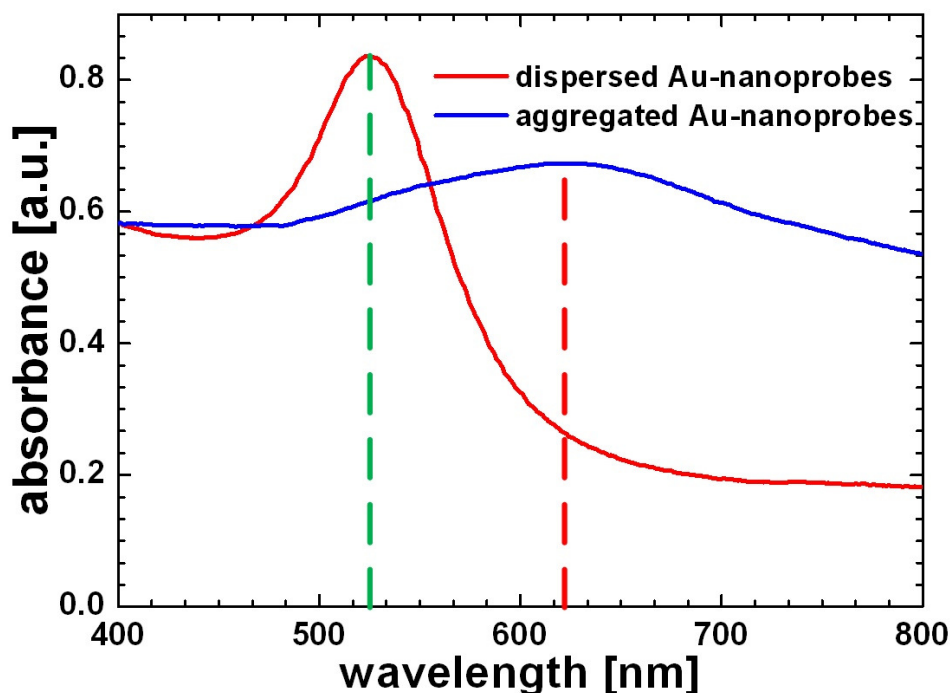


Fig. 4.2. Absorption spectra of disperse and aggregated MTBC Au-nanoprobes solution (2.5 nM Au-nanoprobe in 10 mM phosphate buffer (pH 8)) attained via standard 384 well micro-plate. The aggregation was induced by salt addition  $[MgCl_2] = 0.04$  M. Spectra values are normalised, i.e. spectrum of aggregated solution was shifted for the same absorbance value at  $\lambda = 400$  nm as disperse solution. The dashed lines correspond to the dominant wavelengths [530 nm (green) and 625 nm (red)] of the LEDs used in the detection and for determination of  $R_S$  ratio.

This colorimetric detection scheme was successfully applied to the molecular identification of *Mycobacterium tuberculosis*, the main etiological agent of human tuberculosis that affects more than 8.3 million people worldwide (Baptista et al. 2006; Costa et al. 2010; Veigas 2012). This system has been further optimised for the detection and characterisation of mutations associated with drug resistance (Veigas 2010) and identification of members of the *M. tuberculosis* Complex (MTBC) without the need of target amplification (Liandris et al. 2009). This molecular detection strategies have also been successfully integrated into an easy-to-operate, inexpensive and reliable optoelectronic platform using green and red light sources and a thin p-i-n silicon (Martins et al. 2007b; Silva et al. 2007; Silva et al. 2011) or  $TiO_2$ -based inkjet printed photodetectors (Bernacka-Wojcik et al. 2010) and more recently with paper-based microfluidics (Veigas et al. 2012).

The cost per tests could be reduced by lowering the needed volume of solution to minimize the reagents consumption. Initially, we have developed macro-machined PDMS containers to be integrated in chip carrier for vertical colorimetric detection. Nevertheless, it was challenging to

significantly reduce the volume using macro-machining techniques (lowest achieved solution volume: 50  $\mu$ l; 2 mm long optical path) and also the biosensor sensitivity was not sufficient to detect the colorimetric changes in these containers, most probably due to high optical losses. Therefore, to significantly reduce the solution volume without compromising the biosensor sensitivity, a microfluidic device should be incorporated taking advantage of the microfabrication tools.

Here, we describe the development of a bio-microfluidic platform for the colorimetric DNA analysis based on Au-nanoprobes as the first step towards integrated lab-on-chip device for the point of care use. The implementation of colorimetric measurements in microfluidic systems is challenging as the reduction in the optical path length (OPL) within the microchannel system could decrease the sensitivity, especially when the depth of the channel is used for detection (Viskari and Landers 2006). For that, we extended the OPL by detecting along a microchannel using optical fibres to transport light from the source to the microchannel and afterwards to the photodetector. The optical fibres are self-aligned with each other and with the detection channel by the insertion grooves defined in the microfluidic chip (Fig. 4.3). The microfluidic chip with the optical fibres can be disposable after each measurement to avoid risk of cross contamination, while the green and red light emitting diodes (LEDs), detector and electrical set-up constitute the fixed components of the biosensor system. The chip is fabricated in polydimethylsiloxane (PDMS), a silicon rubber, chosen due to its low price, biocompatibility, good optical properties and the ability to reproduce features on the micrometre scale with very high fidelity by replica moulding (McDonald et al. 2000). For the described design, PDMS needs to be patterned by a mould that allows fabrication of (i) high aspect ratio features to define high grooves for fibres insertion and (ii) features of smooth, vertical side walls to reduce optical losses within the system. SU-8, an epoxy-based negative photoresist (del Campo and Greiner 2007), satisfies these condition, but SU-8 moulds suffer delamination at the photoresist-substrate interface after fabrication of a few PDMS replicas, making it necessary to perform again the time consuming and expensive SU-8 photolithography. Besides that, SU-8 is highly sensitive to processing parameters (due to the presence of 8 epoxy groups per molecule), making it hard to produce two SU-8 samples exactly with the same characteristics (Hammacher et al. 2008). To achieve high reproducibility between multiple PDMS chips, it is desirable that they are all fabricated from the same mould. To solve this, we applied an intermediate epoxy mould that has been previously used for processing 20  $\mu$ m tall features, described by (Desai et al. 2009) to our 125  $\mu$ m features and experimentally verified the applicability of this process for the production of higher structures.

Although various research groups (Černá et al. 2013; Lawrie et al. 2013; Morozova et al. 2011; Yang et al. 2010) have followed the TiO<sub>2</sub> patterning approach that we had developed (Bernacka-Wojcik et al. 2010), in the microfluidic platform prototype, a silicon photodetector will be applied due to the commercial availability of silicon photodiode integrated with optical fibres.

Once this microfluidic platform was constructed, characterised and optimised, it was used for the detection of a specific DNA target sequence capable of unequivocal identification of MTBC members. Using the proposed microfluidic platform, we were capable of performing a specific identification of DNA from *M. tuberculosis* using only 3  $\mu$ l of solution, which represents a 20-fold reduction of volume when compared to the actual state-of-the-art (Silva et al. 2011).

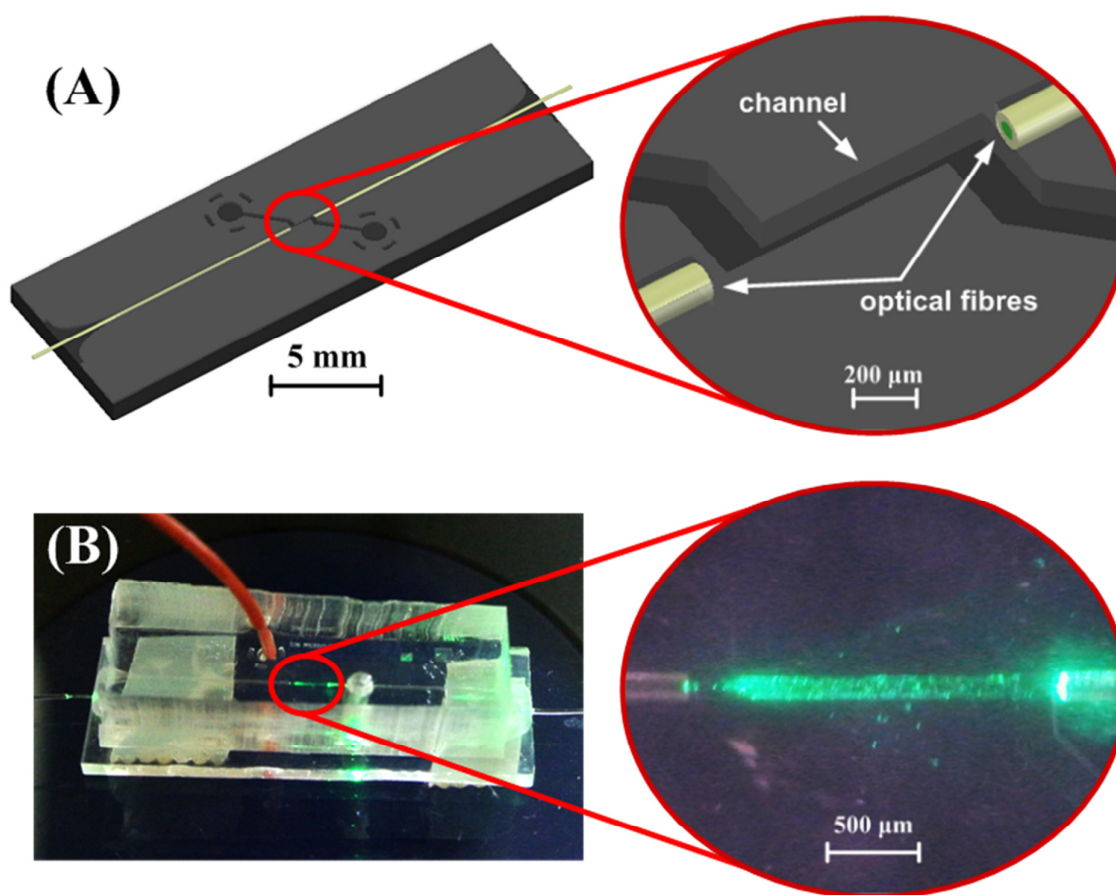


Fig. 4.3. Microfluidic chip. (A) 3D schematic representation of the microfluidic chip design and zoom in on the detection area (the bulk part of the PDMS is not shown to not darken the images). The light is guided to the microchannel by the optical fibres that are self-aligned by the insertion grooves in the chip. (B) Photograph and microscopic image of the channel filled with gold nanoparticles solution and illuminated by the green LED.

## 4.2. Experimental details

### 4.2.1. Fabrication of macro-machined PDMS containers

The mould was fabricated by Tita, Portugal in polyacetal using milling method. PDMS (Sylgard 184, Dow Corning, Spain) was prepared by mixing a base and a curing agent in a 10:1 ratio of weight. The mixture was stirred and degassed in a vacuum desiccator. Afterwards, the PDMS was poured over the polyacetal mould and cured at 100 °C on a levelled hot plate for 3 h, and the PDMS was peeled from the mould. The containers were sealed with a 0.8 mm thick PDMS slab obtained by spin coating on silicon wafer at 80 rpm for 90 s with acceleration of 100 rpm/s (Karl Suss CT62, Germany). The sealing was performed by a pre-polymerization method: PDMS pre-polymer slab was partially cured on a hot plate for 13 min at 65 °C (temperature ramp: 450 °C/h) forming a “jelly-like” structure. PDMS containers were brought in contact with the PDMS slab and immediately the forming bubbles were burst using sharp tip. The samples were kept overnight at room temperature. Then, the curing of the PDMS lid was completed by baking in oven at 80 °C for 1 h.

The absorption spectra were acquired using UV-3101PC UV/visible/NIR double beam spectrophotometer (Shimadzu, Japan).

### 4.2.2. Fabrication of microfluidic chip

The mould for PDMS patterning was fabricated by the ultraviolet photolithography in SU-8. SU-8 2050 (Microchem) was spin-coated on silicon wafers at 1530 rpm to form a ~125 µm thick layer (Karl Suss CT62, Germany). Soft baking was done on a levelled hot plate for 5 min at 65 °C and then for 28 min at 95 °C. After cooling, the samples were exposed on a mask aligner (MA6, Suss MicroTec, Germany) for 21 s with an exposure dose of 309 mJ/cm<sup>2</sup> through an i-line filter (G180336, Suss MicroTec, Germany) and a photolithographic mask. The mask was designed in AutoCAD 2011 (Autodesk, US) and made in chrome on soda lime glass (JD Photo-tools, UK). The samples were post-baked during 5 min at 65 °C and subsequently for 11 min at 95 °C. The samples were developed by submersing them in propylene glycol methyl ether acetate, PGMEA (Microchem) during 18 min with a magnetic agitation of 500 rpm, rinsing with isopropanol, and drying gently with compressed nitrogen. The mould was silanized with tridecafluoro-1,1,2,2-tetrahydrooctyl trichlorosilane (Microchem, USA).

PDMS was prepared as described above (section 4.2.1). The resulting PDMS structures were placed on top of a Petri dish with the negative relief features up, upon which an epoxy resin (ES562, Permabond) was poured to form a ~2 mm thick layer. After ~72 h degassing in desiccator to remove bubbles, the epoxy glue was cured in an oven at 120 °C for ~40 min. Then, the cured epoxy was peeled from the PDMS and used as a master mould for PDMS soft lithography using the same

procedure as described above. The inlets and outlets of the PDMS chips were done using a blunt needle. The chips were irreversibly bonded to glass slides by oxygen plasma (60 s in 13 Pa, 100 W, Plasma electronic Buck Technologien, Germany). After the plasma treatment, the PDMS–glass sandwich was baked at 100 °C for 5 min to increase the bond strength.

The samples were characterised by optical microscopy (Leitz Laborlux 12 ME ST) with a measurement tool, confocal scanning microscopy (LSM 700, Carl Zeiss, Germany), profilometry (XP-200, Ambios Technology, Inc., Santa Cruz, USA), UV-3101PC UV/visible/NIR double beam spectrophotometer (Shimadzu, Japan) and scanning electron microscopy (SEM-FIB, Zeiss Auriga, Germany).

#### **4.2.3. Opto-electronic set-up**

The fabricated microfluidic chips were integrated with an optoelectronic set-up. Firstly, the graded-index multimode optical fibres of 62.5  $\mu\text{m}$  core diameter, 125  $\mu\text{m}$  cladding diameter and NA of 0.275 (GIF625, Thorlabs, Germany) were stripped, cleaved and inserted into the input and output grooves of the chip with a drop of isopropanol for easier insertion. The other ends of the fibres were inserted into bare fibre terminator (BFTU, Thorlabs, Germany) and mating sleeves: (i) the input fibre was connected with SMA-ended GIF625 patch cable (Thorlabs, Germany) coupled to high-power green LED (M530F1, dominant wavelength: 530 nm, half width: 33 nm, typical output power: 5.1 mW, Thorlabs, Germany) or red LED (M625F1, dominant wavelength: 625 nm, half width: 18 nm, typical output power: 10.1 mW, Thorlabs, Germany). The LEDs were powered with values of 300 mA and 920 mA; (ii) the output fibre (62.5  $\mu\text{m}$  core multimode fibre) was connected to a pigtailed silicon photodiode (FDSP625, Thorlabs, Germany). The electrical signal from the photodiode was provided to the input of operation amplifier circuit with a feedback loop resistance of 20 M $\Omega$  and supplied by  $\pm 15$  V (see Fig. 4.4).



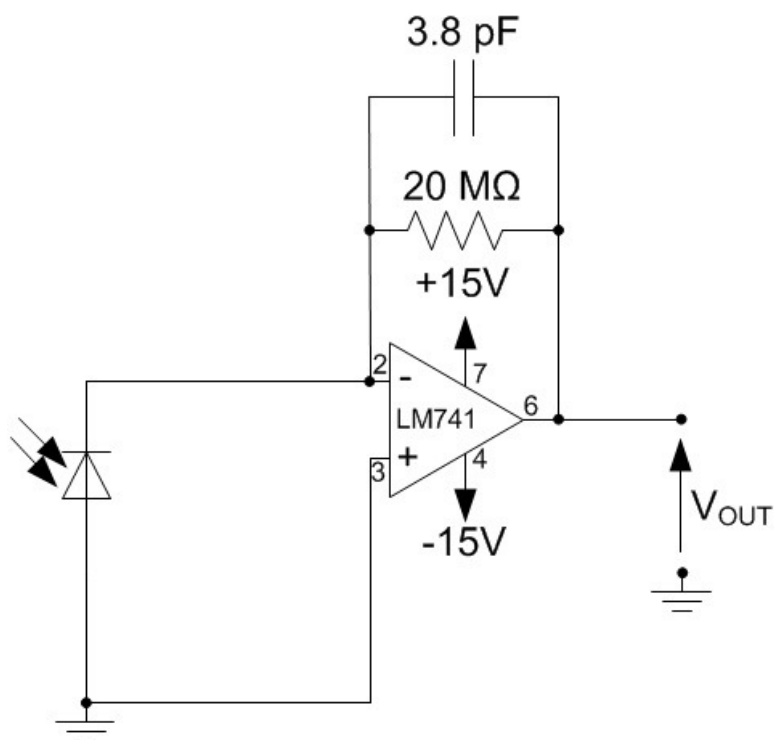


Fig. 4.4. Circuit diagram used for optical-to-electrical signal conversion and amplification. The electrical signal from the photodiode was provided to the input of operation amplifier circuit with a feedback loop resistance of 20 MΩ and supplied by  $\pm 15$  V.

#### 4.2.4. Sample DNA preparation

A specific PCR-amplified 395 bp fragment recognizing a specific sequence within the *rpo-beta* gene of *Mycobacterium tuberculosis* (GenBank accession no. L27989) was used as target for the Aunanoprobe detection assay (Baptista et al. 2008). PCR amplification was performed in a final volume of 50  $\mu$ l containing 50 mM KCl, 10 mM Tris-HCl (pH 8.3), 2.2 mM MgCl<sub>2</sub>, 200 mM of each dNTP, and 1 U of Taq DNA polymerase (Amersham Biosciences, GE Health-care, Europe, GmbH), 10 pmol of each primer (P1 5'-GAG AAT TCG GTC GGC GAG CTG ATC C-3'; P2 5'-CGA AGC TTG ACC CGC GCG TAC ACC-3') (De Beenhouwer et al.; Soo et al. 2009) involving 35 cycles of 45 s denaturation at 94 °C, 45 s annealing at 58 °C followed by 45 s extension at 72 °C. Amplification was observed by 1 % Agarose gel electrophoresis and further confirmed by direct sequencing using big dye v3.1 terminator technology (STABVIDA, Portugal). DNA samples isolated from *M. tuberculosis* and non-MTBC Mycobacteria cultures were used as positive MTBC (complementary) and non-MTBC (non-complementary) samples, respectively. The non-MTBC sample is derived from a clinical isolate from *Mycobacterium kansasii*, whose sequence differs from that of *M. tuberculosis* the *rpo-beta* target region by a single nucleotide.

#### 4.2.5. Au-nanoprobe synthesis and characterisation

Gold nanoparticles (AuNP), with an average diameter of ~14 nm, were synthesised by the citrate reduction method described by (Lee and Meisel 1982). Briefly, 250 ml of 1 mM HAuCl<sub>4</sub> were heated while stirring, 25 ml of 28.8 mM sodium citrate were added, and the solution was refluxed for 15 min. Afterwards, the solution was left at room temperature to cool down. The gold nanoprobe was prepared by incubating the thiol-modified oligonucleotides with the AuNPs during 16 h. The solution was washed with 10 mM phosphate buffer (pH 8), and increasing salt concentration, in order to reduce non-specific binding between the thiol-modified oligonucleotides and the AuNPs. The solution was centrifuged, the resulting pellet resuspended in 10 mM phosphate buffer (pH 8), 0.1 M NaCl and stored in the dark at 4 °C till further use (Storhoff et al. 1998).

Comparative analysis of *rpoB* gene sequences from mycobacteria was performed through sequence alignment using the Geneious v.4.7.6 software. Probe specificity was tested *in silico* using the BLAST tools from GenBank. The MTBC probe 5'-thiol-GAT CGC CTC CAC GTC C-3' (STABVIDA, Portugal) was then used to functionalise AuNPs as previously described (Baptista et al. 2006; Veigas 2010). For target discrimination assessment and assay calibration, non-modified synthetic oligonucleotides were used, MTBC complex sequence 5'-GGA GAT TGG TTT TGA CGT TTA TGT GGA CGT GGA GGC GAT C-3'; and non-MTB 5'-GGA GAT TGG TTT TGA CGT TTA TGT GGA TCG CCT CCA CGT C-3') positive (complementary) and negative (non-complementary), respectively. These calibration data were used to assess the probe specificity in presence of DNA sample.

#### 4.2.6. Au-nanoprobe colorimetric assay

The 395 bp PCR products were ethanol precipitated, resuspended in deionised water and used for the Au-nanoprobe assay. Each colorimetric assay was performed in a total volume of 30 µl, with Au-nanoprobes at a final concentration of 2.5 nM in 10 mM phosphate buffer (pH 8), 0.1 M NaCl and target DNA at a final concentration of 10 µg/ml, as previously described (Baptista et al. 2006; Veigas 2010). The assay consisted on the spectrophotometric comparison of a “Blank” (without DNA), 10 mM phosphate buffer (pH 8), 0.1 M NaCl; “Probe”, 10 mM phosphate buffer (pH 8); and the samples. After 10 min at 95 °C for target DNA denaturation, the mixtures were allowed to stand for 30 min at room temperature and MgCl<sub>2</sub> was added—[MgCl<sub>2</sub>] = 0.04 M for MTBC probe. After 30 min at room temperature, for colour development, the mixtures and the blank were assayed by UV/visible spectroscopy in a microplate reader (Tecan Infinite M200).

For assaying with the microfluidic platform, a total assay volume of 3 µl was used with 2.5 nM Au-nanoprobes in 10 mM phosphate buffer (pH 8), 0.1 M NaCl and target DNA at a final concentration of 30 ng/µl. After 10 min at 95 °C for target DNA denaturation, the mixtures were allowed to stand

for 30 min at room temperature and  $\text{MgCl}_2$  was added— $[\text{MgCl}_2] = 0.04 \text{ M}$  for MTBC probe. After 30 min at room temperature for colour development, the mixtures and the blank were tested.

#### 4.2.7. Detection procedure and analysis

Measurements were performed after 10 min or 30 min of salt addition to AuNPs or Au-nanoprobes ( $0.04 \text{ M MgCl}_2$ ), respectively, for the colour development. The microfluidic chip was first rinsed with isopropanol. Then,  $3 \mu\text{l}$  of each solution to be analysed was dispensed into the inlet well and injected to the channel by the withdrawing from the outlet using a syringe pump (flow rate:  $5 \mu\text{l}/\text{min}$ , Legato 210P, KD Scientific, USA). This procedure helped to suppress the formation of bubbles and to reduce the dead volume. Then, the output voltage was measured for two light intensities (input red LED powered with  $300 \text{ mA}$  and  $920 \text{ mA}$ ) and with three times sampling and then repeated for the green LED.

The detection response ( $R_s$ ) was calculated as the ratio between the output voltage for red LED (dominant wavelength:  $625 \text{ nm}$ ) and green LED (dominant wavelength:  $530 \text{ nm}$ ) normalised to the baseline solution (ultra-pure water, eq. (1)), thus making the signal acquisition independent from the LEDs' intensity,

$$R_s = \frac{U_{\text{sample}(625\text{nm})}/U_{\text{sample}(530\text{nm})}}{U_{\text{baseline}(625\text{nm})}/U_{\text{baseline}(530\text{nm})}} \quad \text{eq. (4.1)}$$

where  $R_s$  is the ratio calculated,  $\text{Sample}_X$  is the reading of the platform for the sample solution for the light source X (LED of dominant wavelength  $625 \text{ nm}$  or  $530 \text{ nm}$ ) and  $\text{Baseline}_X$  is the equivalent for the baseline solution. The colorimetric discrimination ( $\Delta R_s$ ) is defined as the difference between the detection responses for the positive and negative assay.

For validation of the prototype, a microplate reader (Tecan Infinite M200) was used for absorbance measurements.

A one-way ANOVA analysis with Tukey's Multiple Comparison test using Prism GraphPad (San Diego, CA) was used to validate results. One-way analysis of variance was used to test for differences between four groups of data (Probe, Blank, MTBC sample and non-MTBC sample). Additional statistical analysis of the differences was carried out using Tukey's multiple comparison procedures.

### 4.3. Results and discussion

#### 4.3.1. Development of macro-machined PDMS containers

Towards the miniaturization of the DNA biosensor for colorimetric detection, macro-machined containers were developed. These containers would be placed in a chip carrier below a light source

and above a photodetector (vertical detection scheme; see Fig. 4.5) and should satisfy following requirements: (i) high transmittance in visible range; (ii) allow vertical colorimetric measurements (containers should be closed from top, to guarantee that optical path length would not be affected by the meniscus shape); (iii) compatibility with the DNA detection by means of Au-nanoprobes and (iv) reduce significantly the needed volume of solution.

The containers have been fabricated using replica moulding technology of PDMS using macro-machined polyacetal moulds (Fig. 4.6A). In order to determine minimum optical path that allows colorimetric DNA detection, containers of various optical path length were fabricated (Fig. 4.6B and Table 4.1).

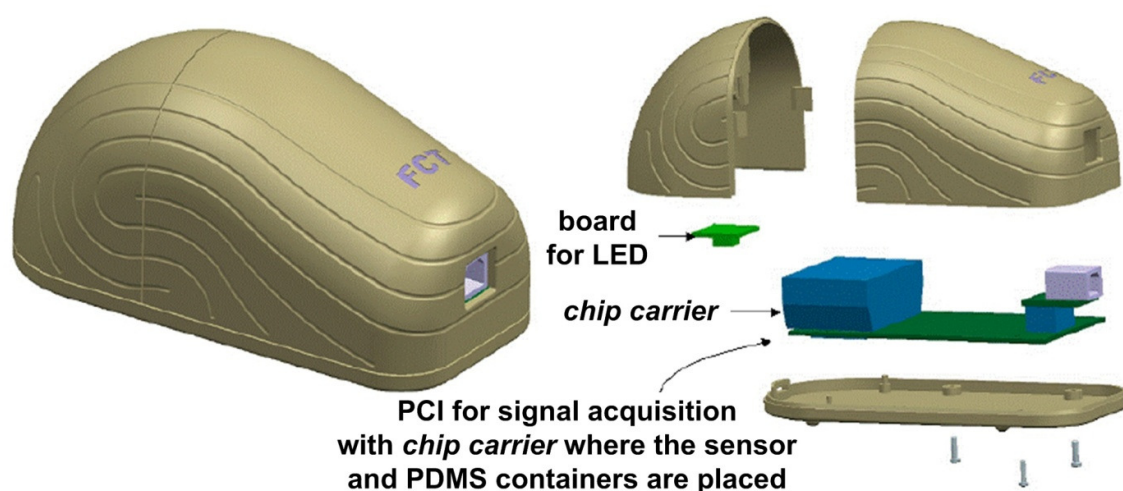


Fig. 4.5. Portable, integrated colorimetric DNA biosensor with *chip carrier* for insertion of photodetector and macro-machined PDMS containers. The light from RGB LED is transmitted vertically through the solution placed in PDMS container and afterwards is detected by photodetector placed underneath the container. The photocurrent generated by photodetector is filtered, amplified, converted to a digital signal and transmitted to a computer via a serial communication protocol. Adapted from (Silva 2010).

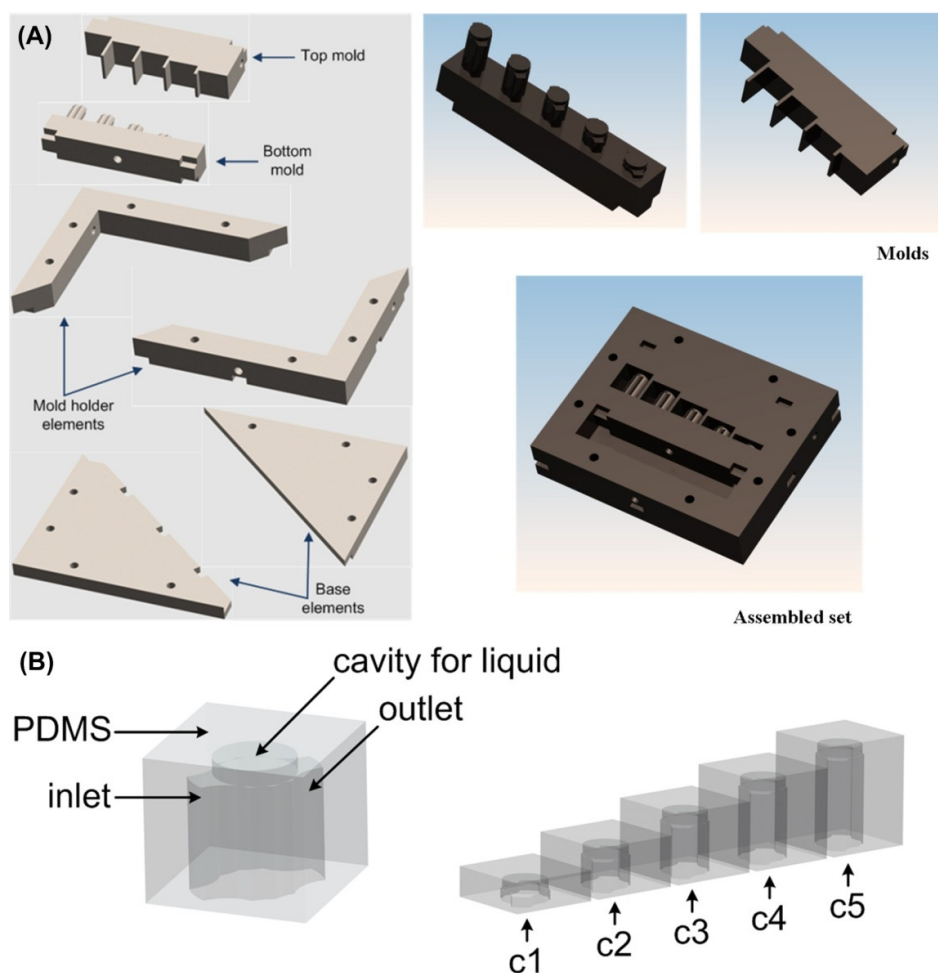


Fig. 4.6. Design of (A) the macro-machined polyacetal mould and (B) the resulting PDMS containers to be used in the colorimetric DNA biosensor.

Table 4.1. Dimensions of developed PDMS containers (\*total volume of container = volume of cylinder + volume of inlet and outlet).

container symbol	cylinder height [mm]	cylinder top area [mm <sup>2</sup> ]	volume of cylinder* [mm <sup>3</sup> ]
c1	2	20	39 (total $\approx$ 50)
c2	4	20	79
c3	6	20	118
c4	8	20	157
c5	10	20	196

The attempts to seal the casted containers with PDMS lids by the conventional oxygen plasma treatment were not successful, most probably due to high surface roughness of the mould that affects

the surface of the resulting containers. Therefore, we have applied a unconventional sealing technology based on PDMS pre-polymerization (Schrott et al. 2010), a method that has been developed for sealing of rough surfaces. The PDMS containers were placed on the pre-polymerized PDMS lid and afterwards the polymerization was completed, resulting in irreversible bonding.

The volume of the cylinders is relatively high due to their high radius (2.5 mm), however with this design, 4 photodetectors for each measurement can be used enabling the cross-checking and simultaneous use of photodetectors of different spectral response for the colorimetric analysis with a white light.

The fabricated containers were evaluated in terms of the optical transparency by spectrophotometry. Absorption spectrum of a container filled with water (2 mm long optical path; reference: air) indicates its high transparency (i.e.  $A \approx 0.1$ ) in the whole visible light range (Fig. 4.7). Subsequently, the containers were applied for the detection of the AuNPs colorimetric changes by means of spectrophotometry. Fig. 4.7 presents absorption spectra of dispersed and aggregated AuNPs in various containers of optical path length from 2 to 10 mm. As a reference, a corresponding container filled with water was used. The concentration of AuNPs in all described tests is around 2.5 nM. The results show that all developed PDMS containers enable detection of AuNPs colorimetric changes by spectrophotometry.

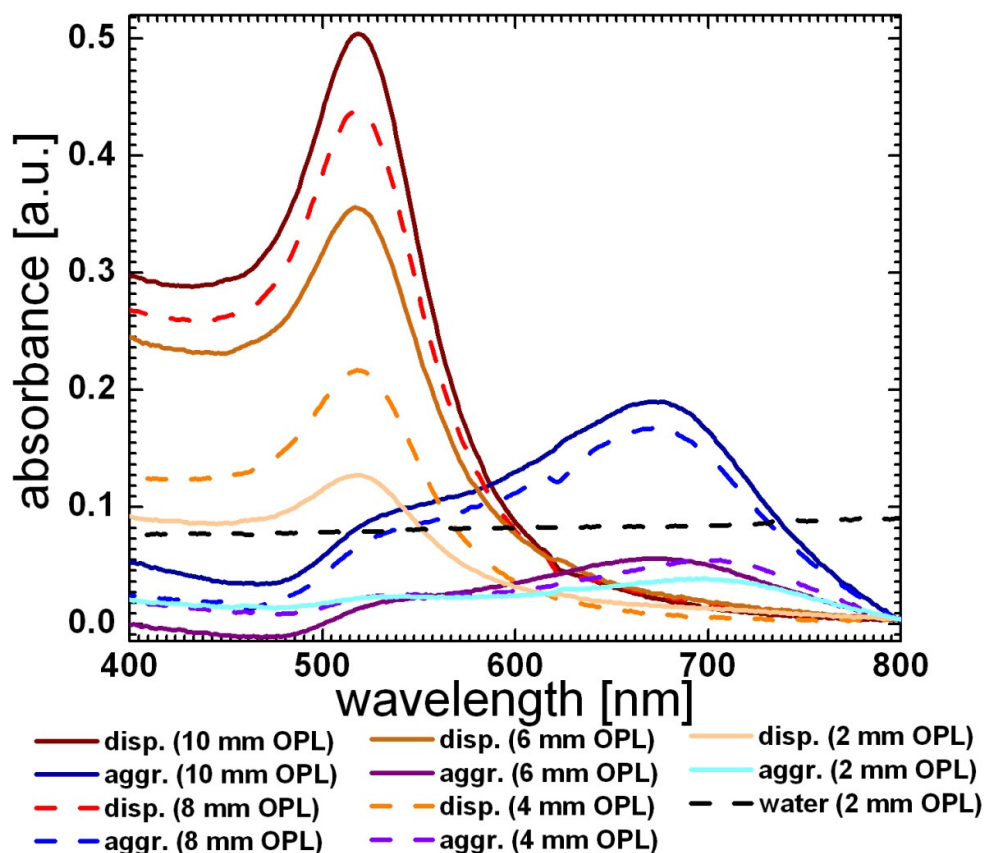


Fig. 4.7. Absorption spectra of dispersed and aggregated AuNPs ( $\sim 2.5$  nM) in various containers. Reference: air in the water spectrum and respective container filled with water for AuNPs spectra.

Subsequently, the container of the shortest optical path (2 mm) was used to evaluate the compatibility between PDMS and the DNA detection method based on non-crosslinking hybridisation of Au-nanoprobes. Fig. 4.8 shows that the colorimetric changes of Au-nanoprobes take place in the developed macro-machined PDMS containers, indicating the compatibility between PDMS and this detection method. However, the biosensor sensitivity was not sufficient to enable proper colorimetric Au-nanoprobe analysis when using the developed containers, most probably due to large optical losses.

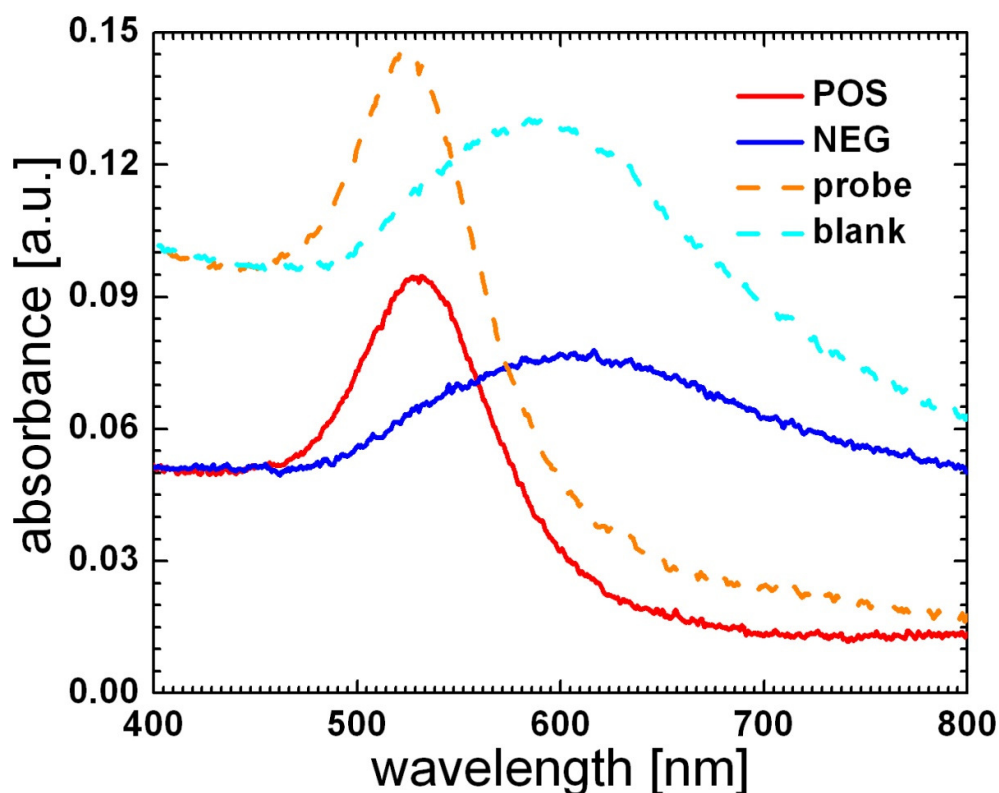


Fig. 4.8. Absorption spectra of the Au-nanoprobe assay for *M. tuberculosis* detection in the macro-machined PDMS container (optical path: 2 mm, volume of the solution: 50  $\mu$ l): probe; blank (without DNA), POS—complementary DNA target; NEG—non-complementary DNA target. The spectra were taken 30 min after salt addition using a container filled with phosphate buffer (pH 8, 10 mM) as a reference. [Au-nanoprobe] = 2.5 nM; [MgCl<sub>2</sub>] = 0.04 M; [oligonucleotide target] = 1.33  $\mu$ M.

Although the developed macro-machined PDMS containers sealed by pre-polymerization method enabled observation of the Au-nanoprobe colorimetric changes by spectrophotometry, the needed solution volume is still high (10  $\mu$ l lower than in the case of quartz cuvette). It is challenging to significantly reduce the solution volume using macro-machining techniques for the mould fabrication, therefore in the next step, microfluidic device will be developed taking advantage of the microfabrication tools.

#### 4.3.2. Microfluidic chip development

Due to the decrease of the optical path in microfluidic systems, most platforms show decreased optical detection capabilities when compared to standard UV/visible spectrophotometers. We tackled this issue by means of a simple yet functional design—the path length for light absorption was increased by allowing light acquisition, i.e. detection to occur along the whole channel. The



difficulties in coupling the light in and out of the channel was resolved by incorporating optical fibres to convey the light source directly into the microfluidic chamber and then to the photodiode. Perpendicular to the microchannel, there are grooves for insertion of the fibres (Fig. 4.3A). The width and depth of the fibre insertion groove was around 125  $\mu\text{m}$  allowing optical fibres of 125  $\mu\text{m}$  diameter to be accurately fixed and easily aligned with each other and the channel. Besides, in this approach, light can be guided very close to the solution, so the light dispersion is reduced. There is only a 50  $\mu\text{m}$  wide PDMS wall between fluid and fibres, so no direct contact with the liquid occurs. The optimised chip presents a microfluidic channel of 110  $\mu\text{m} \times 125 \mu\text{m}$  (width  $\times$  height) so as to enable the fabrication of the SU-8 mould in a single photolithography step. Chips of channel length from 0.5 mm to 4.0 mm were fabricated in order to test the influence of the OPL on the system sensitivity. The microchannel is connected to an inlet and outlet of 1.0 mm diameter for sample delivery—see Fig. 4.3A and B.

The mould for microfluidic chip fabrication was produced in SU-8 by UV photolithography. In order to obtain vertical side walls, the exposure was done through an i-line filter to prevent the T-shape cross section. Without the filter, most of the light with wavelengths shorter than 360 nm is absorbed near the surface of a SU-8 layer, which results in features with a broader top and a narrower base. SEM images (Fig. 4.9) confirm nearly vertical side walls (87.8°) of the SU-8 features and the good definition of the PDMS channels produced by replica moulding from the SU-8 mould.

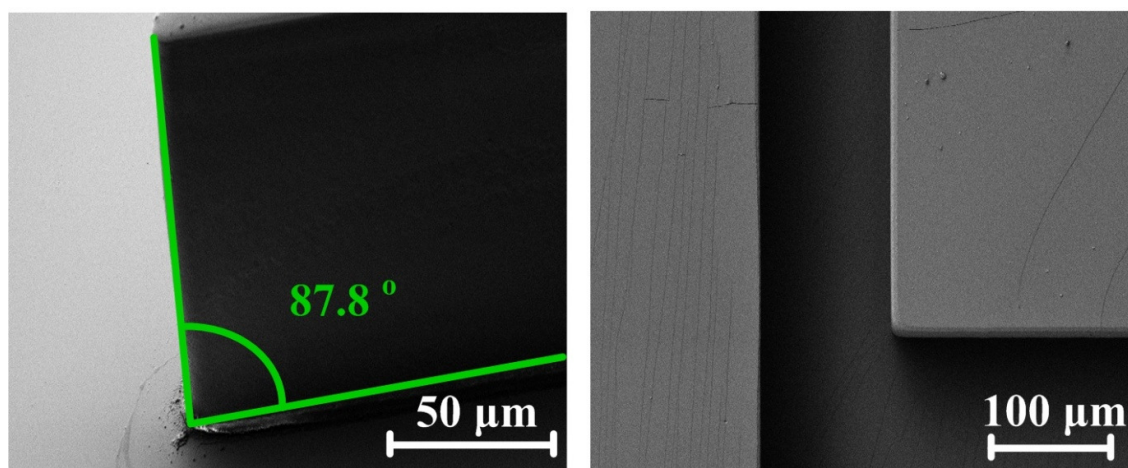


Fig. 4.9. SEM characterisation of microfluidic chip. SEM images showing: (A) side wall angle of the SU-8 feature (achieved aspect ratio: 12) and (B) microchannel in PDMS patterned by the SU-8 mould. Perfectly flat and smooth walls are clearly visualised.

The SU-8 mould was characterised by the stylus profiler in order access surface smoothness and to measure features thickness. The profile shown in Fig. 4.10A indicates that the SU-8 feature is 126  $\mu\text{m}$

thick and the surface is smooth, however the side walls are tilted, although scanning electron microscopy (Fig. 4.9) and the optical microscopy results (Fig. 4.11 and Fig. 4.12) indicate nearly vertical side walls of these features. It is most probably caused by the profiler limitation related with high width of the measuring stylus, because the radius of the stylus on the tip end is only 2.5  $\mu\text{m}$ , but then it increases with height, so the profiler may give inaccurate results in characterisation of the high aspect ratio features.

Optical specular transmittance of PDMS slabs of various thicknesses (0.8–5.0 mm) was measured by the spectrophotometry. Results show high transmittance (above 80%) in the whole visible range of all characterised PDMS slabs (Fig. 4.10B). For thicker slabs, the transmittance for the green light range is lower than for red light range (86% vs. 91%), while for thinner slabs it is nearly constant. In the developed device the light passes PDMS walls of only 50  $\mu\text{m}$  thickness, so most probably the transmittance in whole visible light is about 93%.

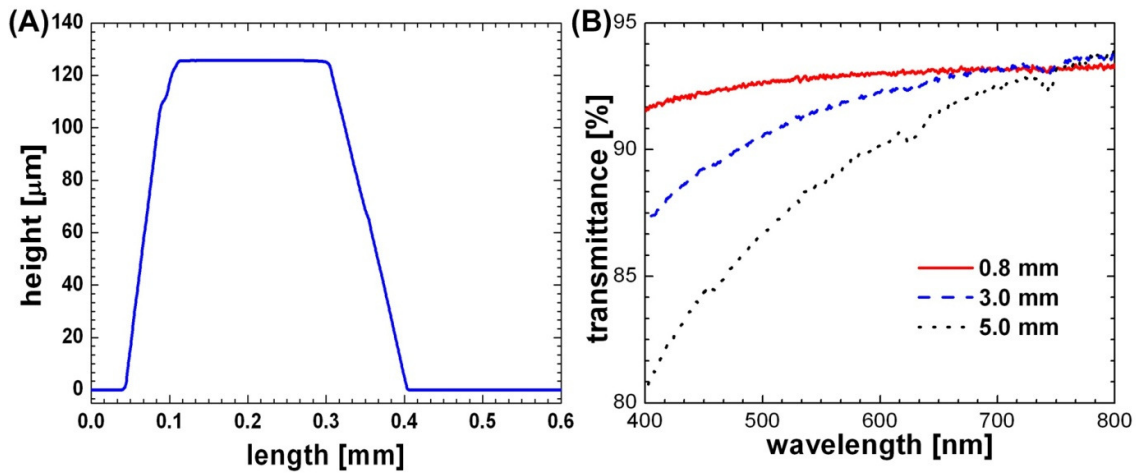


Fig. 4.10. (A) Profilometer measurement of a SU-8 mould feature with 126  $\mu\text{m}$  of height. (B) Optical specular transmittance of PDMS slabs of various thicknesses.

The main issue of SU-8 is the large internal stress, which can be reduced by use of a suitable substrate with similar values of thermal expansion coefficient (e.g. crystalline silicon) and proper chip geometry, avoiding large cross-linked areas. The internal stress of SU-8 can be minimised, however cannot be eliminated. Therefore, SU-8 features have the tendency to peel off from the substrate after a few PDMS replica procedures, making it necessary to perform again the time consuming and expensive SU-8 photolithography process. Additionally, SU-8 is very sensitive to processing parameters making it hard to reproduce SU-8 structures of exactly the same properties, as optimal parameters may change between SU-8 lots due to compositional variations of the material and by

gravimetric decomposition of the polymer components during aging (Hammacher et al. 2008). To overcome these issues, we applied a mediating epoxy mould that forms a monolithic structure (i.e. without fragile material interfaces). The moulding process starts with the fabrication of the SU-8 master mould, then instead of casting PDMS repeatedly from this mould, PDMS is casted once and used as mould for the patterning of an epoxy mould, which can then be used to produce many PDMS replicas without suffering delamination problems. Fig. 4.11 shows the optical microscope images, while Fig. 4.12—confocal scanning microscope images of  $\sim 124\ \mu\text{m}$  tall features obtained at each fabrication step. The results demonstrate that the shape, profile and the thickness of the features are precisely replicated at each step. The width of smallest fabricated feature is  $10\ \mu\text{m}$  giving an aspect ratio of 12. The ends of the fibre insertion grooves made in the PDMS replicas have flat and smooth walls (see Fig. 4.9; Fig. 4.11 and Fig. 4.12), allowing for insertion of the optical fibres to the ends of the channels without any gap, thus generating much less optical distortion and scattering when comparing to the curved walls (Liang et al. 1996). The surface of the epoxy mould is rougher than the SU-8 mould, but in spite of this, there was not leaks after sealing the PDMS chips produced from the epoxy master (Fig. 1B). This strategy allows the production of numerous PDMS chips with high aspect ratio features of the same characteristics, so the tests can be done in a reproducible way.

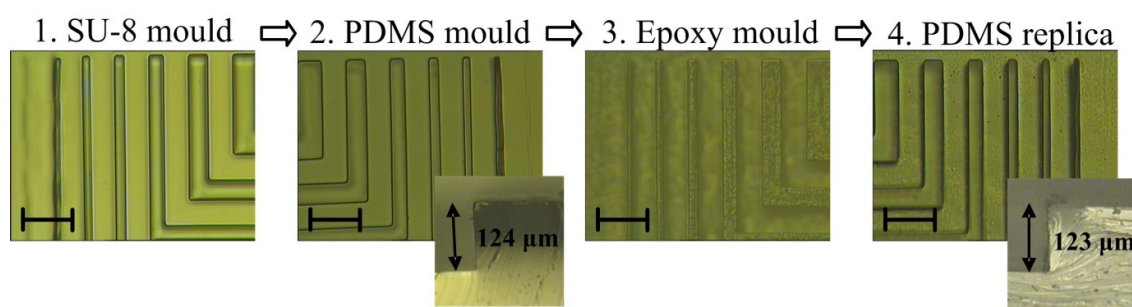


Fig. 4.11. Fabrication process. Microscopic images of top views and cross sections of the test features fabricated in each fabrication step (scale bar length:  $100\ \mu\text{m}$ ). The smallest feature is  $10\ \mu\text{m}$  wide with aspect ratio of 12.

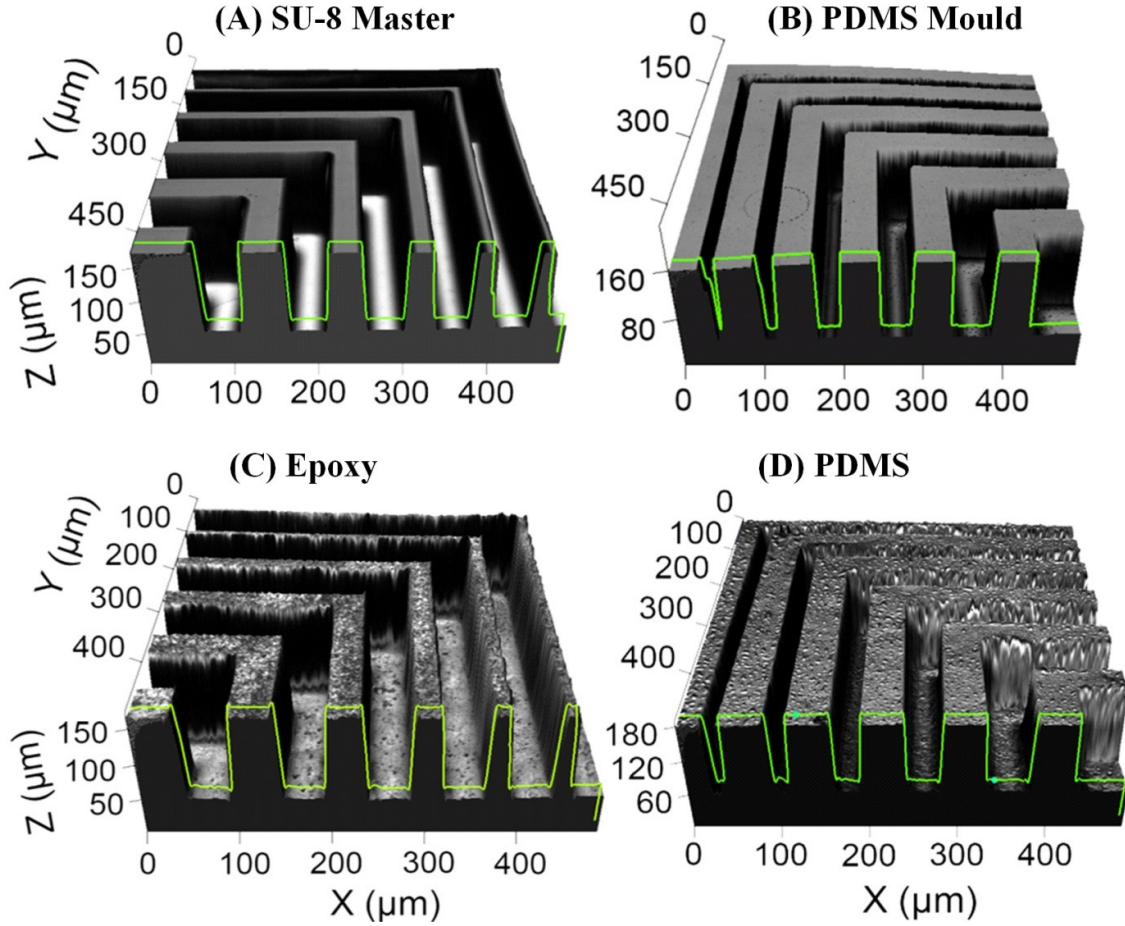


Fig. 4.12. Fabrication process. Confocal scanning microscope images, showing the definition obtained in each fabrication step: (A) SU-8 master; (B) first PDMS mould cast from the SU-8 master; (C) epoxy mould cast from the first PDMS mould and (D) final PDMS replica cast from the epoxy mould clearly replicating the features of the original SU-8 master.

Fig. 4.13 shows an optical microscopic image of the insertion groove with the optical fibre immobilized in it. The proper dimensions of the groove allow tight immobilization of the fibres and consequently their alignment with each other and with the detection channel. Optical fibres become very fragile after stripping of the buffer layer, so the funnel shape of the entrance in the groove greatly facilitates the insertion and reduces probability of fibre breaking.

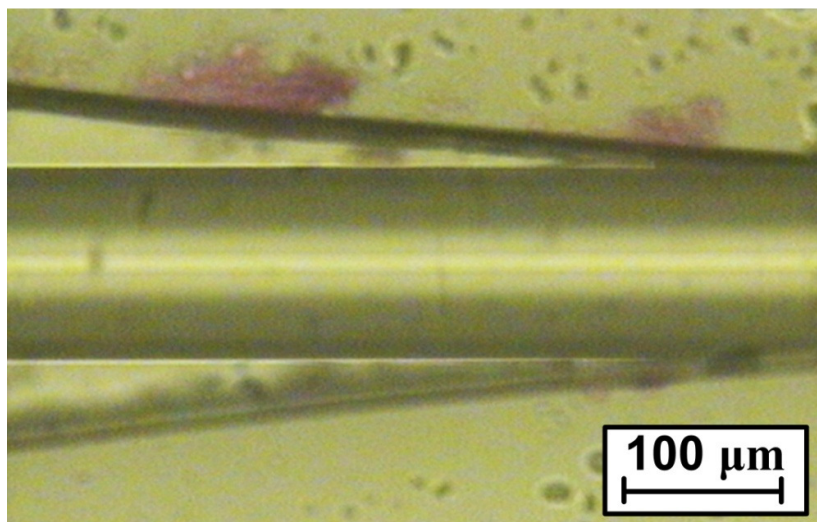


Fig. 4.13. Microscopic image of an optical fibre immobilized in a PDMS groove. The proper dimensions of the groove allow thigh immobilization of the fibres and consequently their alignment with each other and with the detection channel. The funnel shape of the entrance facilitates the insertion and reduces probability of fibre breaking.

#### 4.3.3. Optical performance

Firstly, the system output was measured for the 2 mm long microchannel filled with deionized water, as a function of the LED current, which is proportional to the light intensity. Results indicate the good linearity of the system response for both 530 nm and 625 nm LEDs in the whole intensity range—see Fig. 4.14A. Then, 2.5 nM gold nanoparticle solutions, both non-aggregated (red colour solution) and aggregated (blue colour solution), were used for optimisation. Chips of various detection channel lengths (0.5–4 mm) were tested to assess the sensitivity of the developed microfluidic platform as a function of the optical path length (OPL)—Fig. 4.14B. For all tested OPLs, the microfluidic platform could distinguish the non-aggregated and aggregated AuNPs solutions ( $\Delta R_s > 0$ ). Generally, the sensitivity increases with the OPL, but also the noise becomes higher due to the divergence of the light radiated from the excitation fibre (Mogensen et al. 2004). For evaluation of the optical path length effect on the losses, the power loss was estimated having into account the numerical aperture of the fibres (0.275), channel length and fluid refractive index ( $\sim 1.33$ ). Fig. 4.15A and B illustrate how severe the channel length is to the power. We considered that light in a diverging beam spreads uniformly along a spherical surface—the wave front—so the same power will be spread over an increasing area with distance. That area increases with ( $distance^2$ ), so the fraction of available power will decrease with ( $distance^{-2}$ ). The slight difference between the refractive index for the PDMS walls and the solution filled channel was ignored. Dispersion events and interface reflections were also



discarded. The optical losses could be minimized by proper light converging, e.g. by the use of microlenses taking advantage of the differences in refractive index between air and PDMS.

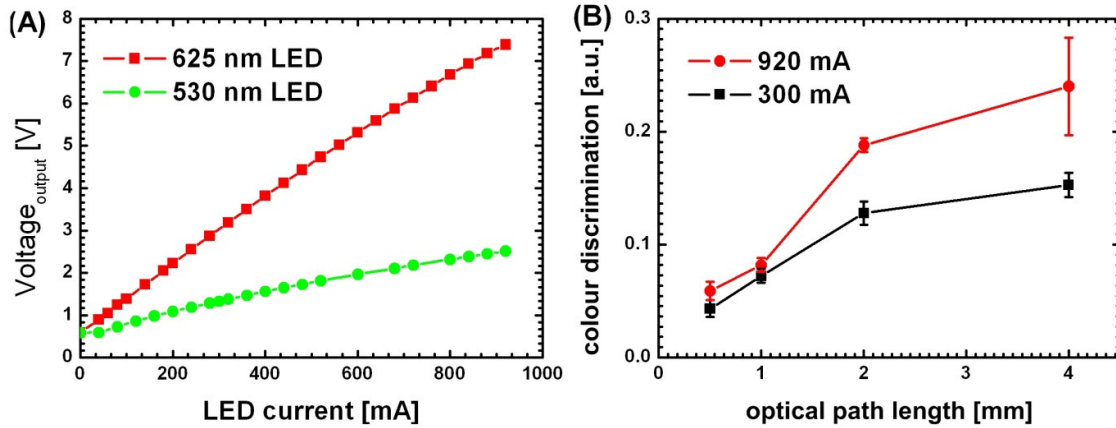


Fig. 4.14. Optical sensing with the microfluidic platform. (A) Output voltage generated by the platform for the chip of 2 mm long microchannel filled with water as a function of LEDs current; (B) sensitivity of the developed microfluidic platform defined as a difference between the detection responses (calculated from equation (4.1)) for the non-aggregated and aggregated AuNPs solutions. The tests were done for various optical path lengths (OPL) with LEDs powered with 300 mA and 920 mA. The data points represent the average of three readout measurements and the error bars indicate the standard deviation (the connecting lines are for eyes guidance only).

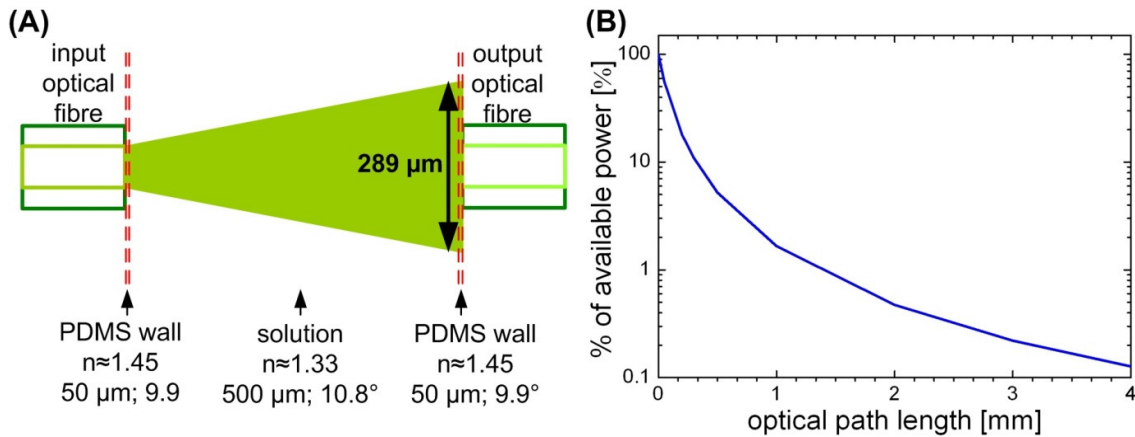


Fig. 4.15. (A) Estimation of the beam width at the end of the chamber containing the microfluidic channel of a length of 0.5 mm. This estimation is intended for power loss evaluation. (B) Percentage of available power reaching the collecting optical fibre as a function of the optical path length in the developed microfluidic chips (for NA = 0.275 and  $n = 1.33$ ).

As it can be seen in Fig. 4.14B, for the OPL up to 1 mm, the sensitivity shows almost no dependence with light intensity, but for longer OPLs the sensitivity increases around 50% when higher light intensity increases (LED current from 300 to 920 mA), however due to less stable readouts, the standard deviation also increases. It has been shown that for absorbance based measurements, the best signal to noise ratio is obtained for 1 mm long OPL (Snakenborg et al. 2003). Nevertheless, it should be taken into account that in this detection method the colorimetric changes are a result of surface plasmon resonance band shifts, which introduce variations to the readout. Considering the need for clear discrimination between positive and negative results, a 2 mm OPL was chosen for the DNA tests as the best trade-off between sensitivity and noise.

To fill up a detection channel of 0.5 mm length, only 7 nl of the solution is needed, while for 2 mm and 4 mm long channel, 14 nl and 57 nl are needed, respectively. Currently, 3  $\mu$ l of solution were used per test for all tested chips due to the dead volume needed to fill up the inlet and outlet channels (308 nl) and the fluidic connections. This volume may be reduced in the further steps of the platform development.

#### **4.3.4. *M. tuberculosis* detection via the microfluidic platform**

As a proof-of-concept, the developed microfluidic platform was applied in conjunction with the Au-nanoprobe assay to detect a specific DNA sequence from *M. tuberculosis*, the main etiologic agent of human tuberculosis. A clear difference of response from the platform between complementary (POS) and non-complementary (NEG) assays is observable (Fig. 4.16) for all tested assay pairs: i) colloidal (POS) and aggregated gold nanoparticles (NEG); ii) control samples: Au-nanoprobe (POS) and blank (MTBC Au-nanoprobe alone with salt; NEG); iii) MTBC Au-nanoprobe with complementary and non-complementary synthetic oligonucleotides with salt; iv) MTBC Au-nanoprobe with complementary and non-complementary PCR products with salt. Although the detection response values are slightly different for each assay, the developed microfluidic platform yielded statistically different results for all the positive assays when compared to negatives. Again, the sensitivity is higher when light of higher intensity is used (920 mA LED current), but less intense light could also clearly differentiate between all positive and all negative assays. The same samples were assayed via a standard microplate reader platform showing comparable detection and discrimination capability (see Fig. 4.17). Despite successful detection of *M. tuberculosis*, and statistically significant discrimination between positive and negative samples, the data acquired using the microfluidic platform present a slight wider standard variation than those originating from the microplate reader. This is due to the fact that the presented system does not use monochromatic light but a LED light source with an emission profile of 20–30 nm half-width peak instead of a single wavelength with a band-width below 9 nm with an accuracy of  $\pm 0.5$  nm. Additionally, the introduction of noise can also

be associated with the system design, e.g. photodiode, cables, power supply and electrometer. Further system optimization will have to tackle all these factors causing fluctuations during data acquisition.

Concerning the time needed for the DNA detection using the developed system, following PCR amplification (Fig. 4.1), the colorimetric detection takes approximately 30 minutes for colour development. Then, the detection within the platform is almost instantaneous: as soon as the fluid fills up completely the detection channel (flow rate: 5  $\mu\text{l}/\text{min}$ ), the measurement can be done within few seconds.

Different technologies (for example, droplet-based microfluidic systems (Xiang et al. 2012a; Xiang et al. 2012b) have shown more sensitivity, however our approach's simplicity could be of a great advantage at low cost.

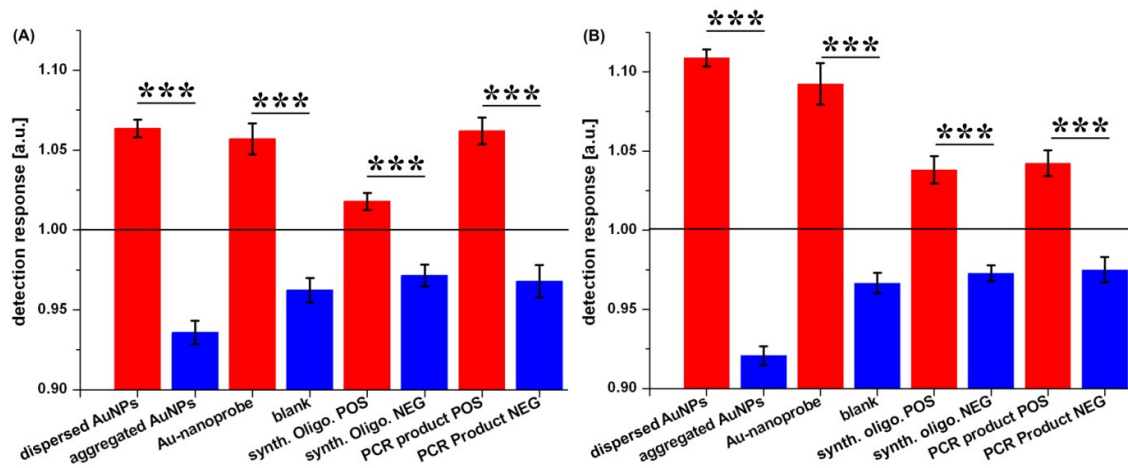


Fig. 4.16. *M. tuberculosis* detection via proposed bio-microfluidic platform. Au-nanoprobe assay mixtures (2.5 nM Au-nanoprobe 30 ng/ $\mu\text{l}$  of sample DNA in 10 mM phosphate buffer (pH 8)) after 15 min of incubation following salt addition  $[\text{MgCl}_2] = 0.04$  M. Results obtained using: (A) PDMS microfluidic platform with LEDs powered with 300 mA and (B) with 920 mA (see eq. 4.1). The bars represent the average of independent measurements and the error bars indicate standard deviation. The horizontal line represents the threshold of 1 considered for discrimination between positive and negative. Statistical analysis was performed using Prism 5 graph pad, using one-way ANOVA with Tukey's Multiple Comparison test; \*\*\*= $p < 0.0001$ ,  $n \geq 5$ .



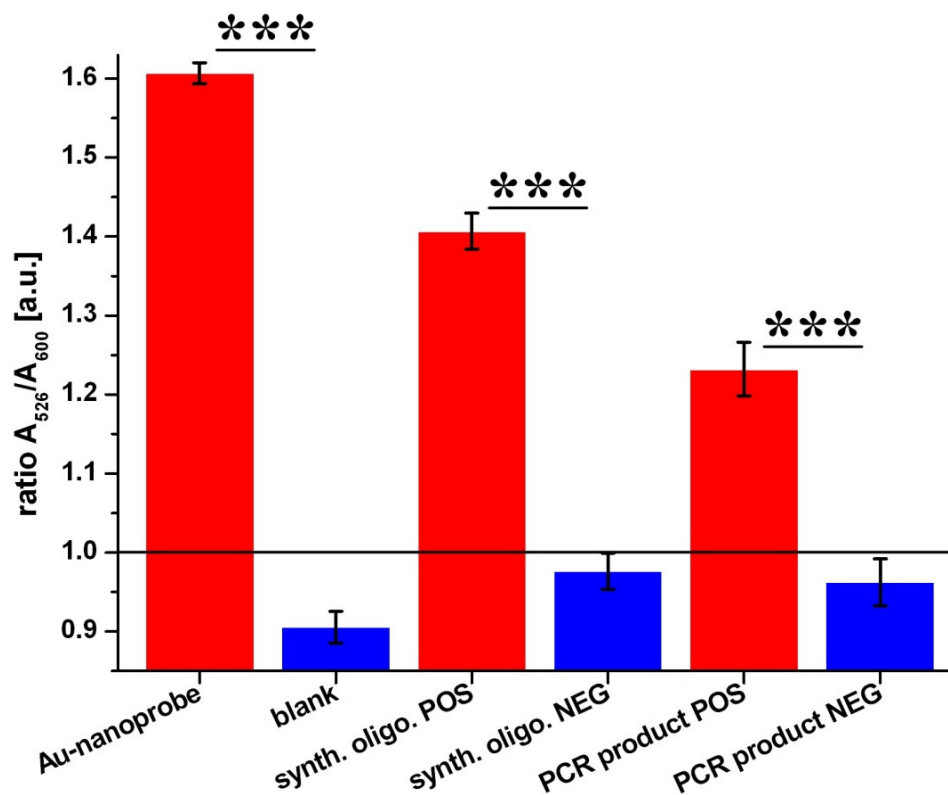


Fig. 4.17. Microplate reader results of Au-nanoprobe assay for MTBC detection: MTBC standard assay performed in a microplate reader. Au-nanoprobe aggregation as measured by ratio of aggregation for the assay mixtures [2.5 nM Au-nanoprobe, 10  $\mu$ g/ml of sample DNA in 10 mM phosphate buffer (pH 8)] after 15 min of incubation following salt addition [ $\text{MgCl}_2$ ] = 0.04 M. The bars represent the average of independent measurements and the error bars indicate standard deviation. The horizontal line represents the threshold of 1 considered for discrimination between positive and negative. Statistical analysis was performed using Prism 5 graph pad, using one-way ANOVA with Tukey's Multiple Comparison test; \*\*\*= $p < 0.0001$ ,  $n \geq 5$ .

In order to access the linear range of the detection platform, the detection response as a function of the gold nanoparticles concentration was measured (Fig. 4.18). The results show nearly linear response with AuNPs concentration (adjusted  $R$ -square coefficient = 0.95937), and basing on our results, similar response is expected for Au-nanoprobes concentration.

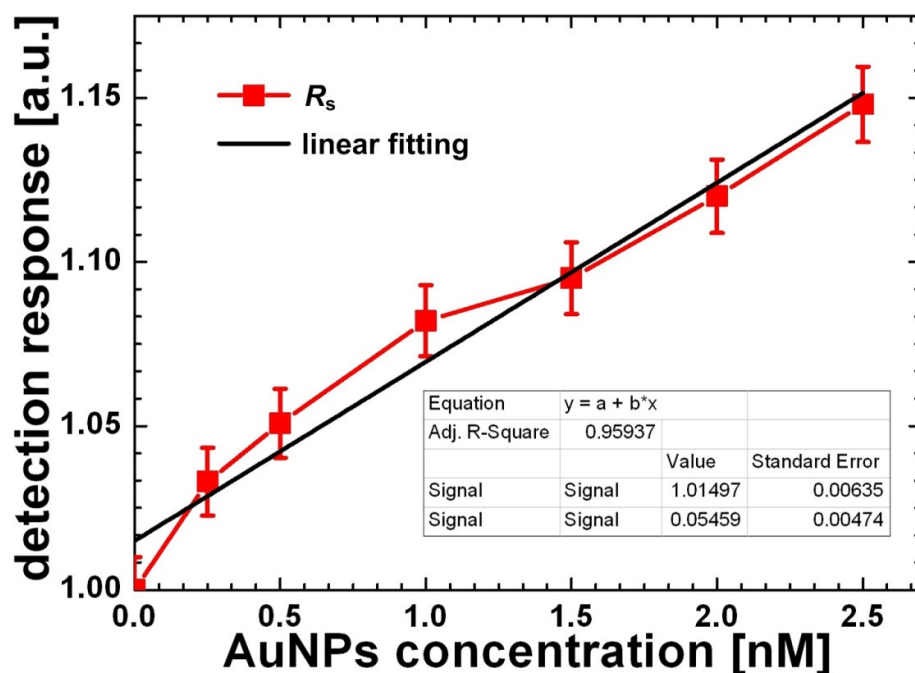


Fig. 4.18. The detection response ( $R_s$ ; eq. 4.1) as a function of the gold nanoparticles concentration. The detection response increases linearly with AuNPs concentration (adjusted  $R$ -square coefficient = 0.95937). The measurements were taken with the LEDs powered with 400 mA.

#### 4.4. Conclusions

We have miniaturised a colorimetric DNA biosensor based on non-crosslinking hybridisation of DNA-functionalised gold nanoparticles. The platform consists in a disposable low cost bio-microfluidic chip with optical fibres and a non-disposable host device, which integrates light sources, photodetectors and electronic equipment. The developed platform requires only 3  $\mu$ l of solution of DNA concentration of 30 ng/ $\mu$ l (90 ng), therefore the 20-fold reduction of the needed volume was obtained when comparing to the bulk version of this biosensor and 10-fold reduction when comparing with the reference method (microplate reader). The needed solution volume can be further reduced by minimising the dead volume since only 14 nl is needed to fill up completely the 2 mm long microchannel.

The platform was applied with Au-nanoprobes for colorimetric detection of specific DNA sequence from *M. tuberculosis*. The lower LED intensities (current of 300 mA) yields sufficient discrimination between positive and negative assays of all tested solutions, therefore it will be used in the future work as more suitable for the platform miniaturisation and integration, i.e. the LEDs could be powered directly from PC by USB interface. To improve performance, incorporation of 2D microlenses may be considered so as to converge light into the sample taking advantage of the

refractive indexes differences between air and PDMS. These 2D micro-optical components can be fabricated by a replica moulding method using a single layer SU-8 mould.



## **Chapter 5**

Single nucleotide polymorphism detection  
using gold nanoprobe and optimized bio-  
microfluidic platform with embedded  
microlenses

*This chapter is written basing on:*

Bernacka-Wojcik, I., Águas, H., Carlos, F.F., Lopes, P., Wojcik, P.J., Costa, M., Veigas, B., Igreja, R., Fortunato, E., Baptista, P.V., Martins, R., Single nucleotide polymorphism detection using gold nanoprobe and optimized bio-microfluidic platform with embedded microlenses. Under preparation (2014).

*This chapter differs from the article in:*

- Supplementary information has been merged into the article text for the reading flow.

The author of the thesis was involved in the set-up optimization, microlenses design, SNP detection and was responsible for the microchips fabrication and characterisation, optical sensing tests, results analysis and writing of the paper.

<b>Chapter 5. Single nucleotide polymorphism detection using gold nanoprobe and optimized bio-microfluidic platform with embedded microlenses.....</b>	<b>125</b>
<b>Summary.....</b>	<b>125</b>
<b>5.1. Introduction.....</b>	<b>125</b>
<b>5.2. Experimental details .....</b>	<b>127</b>
5.2.1. Fabrication of microfluidic chip .....	127
5.2.2. Opto-electronic set-up .....	128
5.2.3. Sample DNA preparation .....	129
5.2.4. Au-nanoprobe synthesis and characterisation.....	129
5.2.5. Au-nanoprobe colorimetric assay .....	129
5.2.6. Detection procedure and analysis .....	130
<b>5.3. Results and discussion .....</b>	<b>130</b>
5.3.1. Set-up optimization.....	130
5.3.2. Microlenses design and fabrication .....	132
5.3.3. Effect of microlenses on colorimetric AuNPs analysis .....	137
5.3.4. SNP detection using the optimized system.....	139
<b>5.4. Conclusions.....</b>	<b>144</b>





## **Chapter 5. Single nucleotide polymorphism detection using gold nanoprobe and optimized bio-microfluidic platform with embedded microlenses**

### **Summary**

The use of microfluidics platforms combined with the optimal optical properties of gold nanoparticles has found plenty of application in molecular biosensing. Here, we describe the optimization of our previously reported bio-microfluidic platform for colorimetric DNA detection using gold nanoprobe (Au-nanoprobe) that resulted in a 160% improvement of colorimetric analysis results. Incorporation of 2D microlenses allowed to converge light into the sample and then to the output fibre core taking advantage of the refractive index differences between air and PDMS. The proper light collimation resulted in a 6 times higher signal-to-loss ratio reaching the output optical fibre in comparison with the chip without lenses. We further optimized an optoelectronic acquisition system that yielded increased accuracy and reduced noise.

To demonstrate the full potential of this platform, the optimized bio-microfluidic platform was coupled to the non-cross-linking colorimetric assay to detect a single nucleotide polymorphism (SNP) associated with increased risk of obesity *fat-mass and obesity-associated (FTO)* rs9939609. This way, it was possible to screen a set of biological samples using target DNA concentration below the limit of detection of the conventionally used microplate reader (i.e. 15 ng/ $\mu$ l) with 10 times lower solution volume (3  $\mu$ l).

### **5.1. Introduction**

Due to the micro-scale dimensions and the resulting high surface-to-volume ratio, microfluidic systems offer numerous advantages including reduced reagent use, portability, faster sample analysis, higher throughput, potential of automation and high-level integration, all of which are associated with decreased cost (Mark et al. 2010). These devices can also be designed for multi-parallel operation, making the system more reliable as several control assays can be performed simultaneously with multiple samples (Abgrall 2007; Ben-Yoav et al. 2012; Khoshmanesh et al. 2011; Soe et al. 2012). Recently, several microfluidic devices have been developed to tag and characterize specific DNA sequences using for this purpose miniaturised approaches (Zhang et al. 2006) that only need a small amount of analyte (pictograms) (Xiang et al. 2012a) and even integrated DNA analysis including sample pre-treatment, DNA amplification and detection (Burns et al. 1998; Liu et al. 2004; Oblath et al. 2013). However, so far a complete lab-on-chip device for DNA analysis has not been successfully commercialized mainly due to high cost of the fabrication and/or manipulation (Choi et al. 2011).

The size-dependent colorimetric properties of gold nanoparticles (AuNPs) have been extensively used as a label for DNA and RNA analysis (Doria et al. 2012; Larginho and Baptista 2012). The use of DNA-functionalized AuNPs (Au-nanoprobes) is a very attractive alternative to fluorescence based assays due to their sensitivity, selectivity and possibility of using much simpler instrumentation. In the *non-cross-linking* DNA detection method developed by Baptista and co-workers, specific sequence detection is achieved by the colorimetric comparison of a solution before and after salt induced Au-nanoprobe aggregation: upon salt addition presence of complementary DNA prevents aggregation of Au-nanoprobes and the solution remains red; whereas, presence of a non-complementary/mismatch DNA sequences does not convey such protection and the solution turns blue (Conde et al. 2010; Doria et al. 2010; Doria et al. 2007), see Fig. 5.1. This molecular detection technique has been integrated into an inexpensive and reliable optoelectronic platform using green and red light sources and a thin p-i-n silicon (Martins et al. 2007b; Silva et al. 2007; Silva et al. 2011) or TiO<sub>2</sub>-based ink-jet printed photodetectors (Bernacka-Wojcik et al. 2010) and more recently with paper-based microfluidics (Veigas et al. 2012).

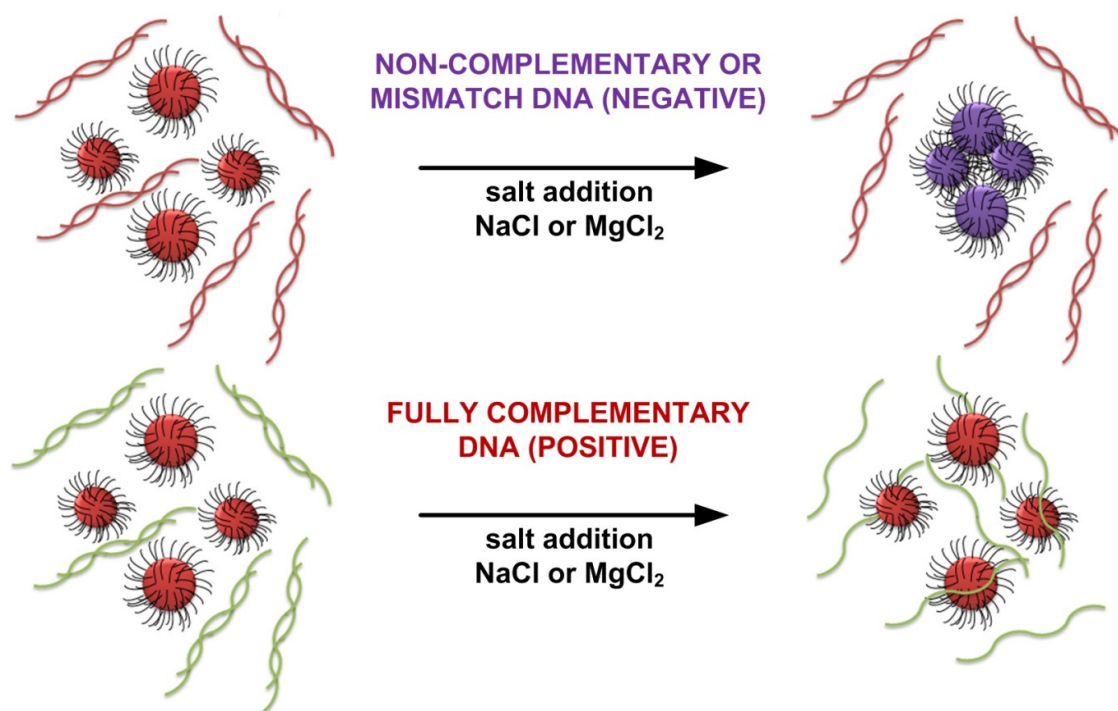


Fig. 5.1. Principle of colorimetric DNA detection method based on non-cross-linking hybridisation of Au-nanoprobes: at high salt concentration, only the presence of fully complementary DNA prevents aggregation and the solution remains red.

The use of colorimetric transduction for the Au-nanoprobes based DNA detection offers the advantage of involving only simple equipment such as a light-emitting diode for excitation and a photodiode for detection. However, implementation of colorimetric measurements in microfluidic systems is challenging as reduction of the optical path length (OPL) within the microchannel system can decrease the system sensitivity, especially when the depth of the channel is used for detection (Viskari and Landers 2006). Recently, our group has developed a bio-microfluidic platform for the colorimetric DNA analysis by extending the OPL by detection along a PDMS microchannel, using optical fibres to transmit the light (Bernacka-Wojcik et al. 2013).

In this paper, we describe the optimization of the bio-microfluidic platform for Au-nanoprobe based DNA detection that has resulted in a 160% improvement of colorimetric discrimination. The optimized bio-microfluidic platform in conjunction with Au-nanoprobes allowed to detect a single nucleotide gene polymorphisms related with *fat-mass and obesity-associated (FTO) rs9939609* (Carlos et al. 2013) using 10 times lower solution volume and 5 ng/ $\mu$ l lower DNA target concentration than required for a conventional microplate reader.

## 5.2. Experimental details

### 5.2.1. Fabrication of microfluidic chip

The mould for PDMS patterning was fabricated by ultraviolet photolithography in SU-8 as described in detail elsewhere (Bernacka-Wojcik et al. 2013). Briefly, SU-8 2050 (Microchem) was spin-coated to form a  $\sim 125$   $\mu$ m thick layer. Samples were then soft-baked, exposed on a mask aligner (MA6, Suss MicroTec, Germany) with an exposure dose of 309 mJ/cm<sup>2</sup> through an i-line filter (G180336, Suss MicroTec, Germany) and post-baked. Development was performed by submersing in propylene glycol methyl ether acetate, PGMEA (Microchem), during 18 min with magnetic agitation of 500 rpm. The mould was silanized with tridecafluoro-1,1,2,2-tetrahydrooctyl trichlorosilane (Microchem, USA).

PDMS (Sylgard 184, Dow Corning, Spain) was prepared by mixing a base and a curing agent in a 10:1 ratio of weight. Afterwards, the PDMS was poured over the SU-8 mould and cured at 100 °C on a levelled hot plate for 3 h, and the PDMS was peeled off from the SU-8 mould.

The PDMS structures were placed on top of a Petri dish with the negative relief features up, upon which an epoxy resin (ES562, Permabond) was poured to form a  $\sim 2$  mm thick layer. After  $\sim 72$  h degassing in desiccator to remove bubbles, the epoxy glue was cured in an oven at 120 °C for  $\sim 40$  min. Then, the cured epoxy was peeled from the PDMS and used as a master mould for PDMS soft lithography using the same procedure as described above. Chips were irreversibly bonded to glass slides by UVO cleaner. After the treatment, the PDMS-glass sandwich was baked at 100 °C for 5 min to increase the bond strength.

The microfluidic devices were characterised by confocal scanning microscopy (LSM 700, Carl Zeiss, Germany) and scanning electron microscopy (SEM-FIB, Zeiss Auriga, Germany). The microscopic images were taken using Stereo Microscope Leica Zoom 2000 (Germany) and Pentax K100 camera in dark conditions (ISO 800; exposure time 30 s; aperture 8).

### 5.2.2. Opto-electronic set-up

The fabricated microfluidic chips were integrated with an optoelectronic set-up. Firstly, the graded-index multimode optical fibres of 62.5  $\mu\text{m}$  core diameter, 125  $\mu\text{m}$  cladding diameter and NA of 0.275 (GIF625, Thorlabs, Germany) were stripped, cleaved and inserted into the input and output grooves of the chip with a drop of isopropanol for easier insertion (Fig. 1A and B). The other ends of the fibres were inserted into a bare fibre terminator (BFTU, Thorlabs, Germany) and mating sleeves: i) the input fibre was connected with a SMA-ended GIF625 patch cable (Thorlabs, Germany) coupled to green a SMD LED (LT W5SN, Osram, Germany) or a red SMD LED (LR W5SN, Osram, Germany); LEDs emission spectra are available in Fig. 5.2A. These SMD LEDs were placed in a box of M530F1 (Thorlabs, Germany) and powered with 400 mA; ii) an output fibre (62.5  $\mu\text{m}$  core multimode fibre) was connected to a pigtailed silicon photodiode (FDSP625, Thorlabs, Germany). The electrical signal from the photodiode was provided to the input of operation amplifier circuit with a feedback loop resistance of 20 M $\Omega$  and supplied by  $\pm 15$  V (see Fig. 5.2B).

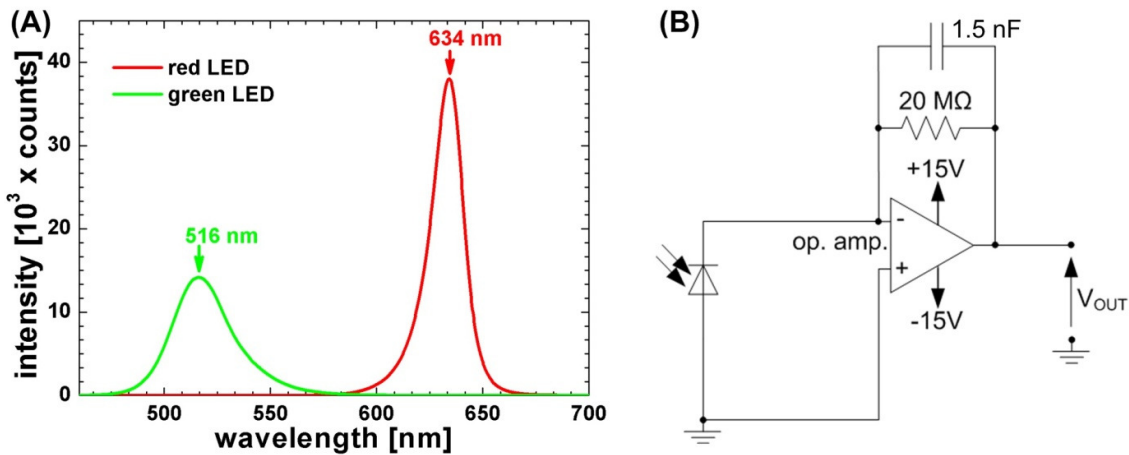


Fig. 5.2. (A) Emission spectra of SMD LEDs used for the colorimetric analysis. The spectra were acquired using miniature fiber optic spectrophotometer (Ocean Optics USB4000) integrated with an empty microfluidic chip (integration time: 8 ms; LEDs supplied with 0.4 A). (B) Circuit diagram used for optical-to-electrical signal conversion and amplification.

### 5.2.3. Sample DNA preparation

A specific fragment of 225 bp of the *FTO* gene was PCR amplified from genomic DNA. Samples were purified according to the manufacturer's protocol after collection from a finger prick using a lancet and preserved in FTA™ Indicated Micro Card (Whatman, UK). PCR reactions were performed in a final volume of 50 µl, containing 1.5X of PCR buffer, 2.5 mM of MgCl<sub>2</sub>, 0.2 mM of dNTPs, 0.2 U/µl of Surf HotTaq DNA polymerase and 0.2 µM of each primer (FTOForward 5'-TTCAAACTGGCTCTTGAATG-3' and FTORreverse 5'-CAGTCAGAAATGGAGTGGGAG-3'). All PCR reagents were provided by STABVIDA, Portugal. PCR amplification involved a first denaturation step at 95 °C for 15 min, followed by 35 cycles, of 94 °C for 1 min, annealing at 60 °C for 30 sec and extension at 70 °C for 30 sec, and one final extension step at 70 °C for 6 min. PCR amplicons were analysed on a 1.0% agarose electrophoresis gel stained with Red Gel and visualized under UV light followed by direct sequencing for sequence confirmation, carried out at STABVIDA with 100 ng / 100 bp of the PCR amplified product using the Big Dye V3.1 technology (Applied Biosystems, California, USA) in an Applied Biosystems 3730XL DNA Analyser.

### 5.2.4. Au-nanoprobe synthesis and characterisation

Gold nanoprobes were synthesised as previously described by our group (Veigas et al. 2012). Briefly, gold nanoparticles (AuNP), with an average diameter of ~14 nm, were synthesised by the citrate reduction method described by Lee and Meisel (Lee and Meisel 1982), where 250 ml of 1 mM HAuCl<sub>4</sub> was heated while stirring, 25 ml of 28.8 mM sodium citrate were added and the solution refluxed for 15 min. Afterwards, the solution was left at room temperature to cool down. The gold nanoprobes were prepared by incubating the thiol-modified oligonucleotides with the AuNPs during 16 h. The solution was washed with 10 mM phosphate buffer (pH 8), and increasing salt concentration, in order to reduce the non-specific binding between the thiol-modified oligonucleotides and the AuNPs. The solution was centrifuged, the resulting pellet resuspended in 10 mM phosphate buffer (pH 8), 0.1 M NaCl and stored in the dark at 4 °C till further use.

### 5.2.5. Au-nanoprobe colorimetric assay

For assays on the microfluidic platform, a total volume of 3 µl was used with 2.5 nM Au-nanoprobes in 10 mM phosphate buffer (pH 8), 0.1 M NaCl and target DNA at a final concentration of 30 ng/µl. After 2 min at 95 °C for target DNA denaturation, the mixtures were allowed to stand for 15 min at room temperature and MgCl<sub>2</sub> was added - [MgCl<sub>2</sub>] = 0.11 M for probe. After 30 min at room temperature for colour development, the mixtures and the blank (without target DNA) were measured.

### 5.2.6. Detection procedure and analysis

The microfluidic channel was first rinsed with isopropanol, then 3  $\mu\text{l}$  of each solution to be analysed was dispensed into the inlet well and injected to the channel by the withdrawing from the outlet using a syringe pump (flow rate: 5  $\mu\text{l}/\text{min}$ , Legato 210P, KD Scientific, USA). This procedure helped to suppress the formation of bubbles and to reduce the dead volume. Then, the output voltage was measured for the red LED powered with 400 mA acquiring 150 values every 0.2 s, then repeated for the green LED.

Salt (0.11 M  $\text{MgCl}_2$ ) was added to solutions in a test tube and then was injected to the microchannel 8 or 26 min after salt addition to AuNPs or Au-nanoprobes, respectively. Measurements were performed after 10 min or 30 min of salt addition to AuNPs or Au-nanoprobes, respectively, for the colour development.

For validation of the prototype, double beam spectrophotometer (UV-3101PC UV/visible/NIR, Shimadzu, Japan) was used for absorbance measurements of AuNPs solutions and microplate reader (Tecan Infinite M200, Switzerland) for Au-nanoprobes solutions. The spectra of the solutions in chips were acquired using miniature fibre optic spectrometer (USB4000, Ocean Optics, US).

The reported expanded uncertainties are based on the standard uncertainty multiplied by a coverage factor  $k = 3$ , providing a coverage probability of approximately 99.7%. The type A uncertainty evaluation has been carried out in accordance with the International Organization for Standardization requirements (Guide to Expression of Uncertainty in Measurements, ISO 1995, Switzerland). A one-way ANOVA analysis with Tukey's Multiple Comparison test using Prism GraphPad (San Diego, CA) was used to validate the results.

## 5.3. Results and discussion

### 5.3.1. Set-up optimization

We previously reported the coupling of a bio-microfluidic platform to Au-nanoprobe colorimetric DNA detection (Bernacka-Wojcik et al. 2013). Here, we optimized this platform in terms of cost, electrical signal processing and sensitivity to colour variation. To optimize the detection protocol and device performance, the citrate capped AuNPs were used. AuNPs solutions mimic well the optical properties of the colorimetric DNA assay solutions: a dispersed AuNPs solution (red colour) spectrum mimics a positive DNA assay, while aggregated AuNPs (blue colour) mimic a negative one. The colorimetric discrimination of the AuNP solutions was performed through a developed system that measures an output voltage ( $U$ ) obtained when the sample is illuminated with red light (from a LED source of dominating wavelength 634 nm) and a green light (from a LED source of dominating wavelength 516 nm; LEDs emission spectra available in Fig. 5.2A). Then, a ratio  $U_{634 \text{ nm}} / U_{516 \text{ nm}}$  is

calculated for each sample: the red colour solution gives a higher ratio than the blue colour solution. The detection response ( $R_s$ ) is determined by normalization of the sample ratio to the baseline ratio (measured with ultra-pure water for AuNPs or phosphate buffer for Au-nanoprobe) according to equation (5.1).

$$R_s = \frac{U_{sample(634nm)}/U_{sample(516nm)}}{U_{baseline(634nm)}/U_{baseline(516nm)}} \quad \text{eq. (5.1)}$$

The colorimetric discrimination ( $\Delta R_s$ ), i.e. the discrimination between red and blue colour solutions, is calculated for each set of tests according to equation (5.2).

$$\Delta R_s = R_s(\text{dispersed\_solution}) - R_s(\text{aggregated\_solution}) \quad \text{eq. (5.2)}$$

As the electrical signal generated by the photodiode is in nanoampere range, a monitor of such low current should present very low input impedance to respond with negligible voltage across the photodiode. A typical current-to-voltage converter with an op amp can provide almost zero impedance and high-amplifier loop gain, lowering voltage swing from the amplifier input. The electrical circuit for current-voltage conversion presented in the previously published work (Bernacka-Wojcik et al. 2013) was optimized to reduce noise and increase results accuracy (see Fig. 5.2B and Table 5.1). The op amp 741 (input bias current about 30 nA; input impedance about  $2 \times 10^6 \Omega$ ) was replaced by a JFET op amp TL081 that has almost 1000 times lower input bias current (30 pA) and much higher input impedance ( $10^{12} \Omega$ ) leading to an increased in the signal to noise ratio. Furthermore, a three orders of magnitude higher feedback capacitor (1.5 nF) was used to reduce the bandwidth and the noise (by means of the compensation for the photodiode capacitance). To increase the measurements' accuracy, a data acquisition system was implemented: National Instruments USB 6008 data acquisition board with a custom-made LabVIEW programme to register the data. For each measurement, 150 output voltage values are acquired every 0.2 second, then averaged and standard deviation calculated. With this optimized setup, the obtained standard deviation was always below 5% per measurement and the AuNPs colour discrimination was improved by 96% (previous state-of-the-art detection ratio  $\Delta R_s = 0.128 \pm 0.011$ ; the optimized  $\Delta R_s = 0.251 \pm 0.012$ ). For the DNA tests, the setup was further optimized by replacing the TL081 with the AD549 op amp with ultralow input bias current of 50 fA and very high input impedance ( $10^{13} \Omega$ ) and input enabling to reduce the standard deviation to values below 2% per measurement.

Table 5.1. Main characteristics of the operational amplifiers used in various system optimization stages.

	op amp 741	op amp TL081	op amp AD549
<b>input bias current [pA]</b>	30000	30	0.05
<b>input impedance [<math>\Omega</math>]</b>	$2 \times 10^6$	$10^{12}$	$10 \times 10^{12}$
<b>used in</b>	(Bernacka-Wojcik et al. 2013)	AuNPs (present work)	Au-nanoprobes (present work)

To reduce the device cost, the PDMS chips were sealed to glass using a UV ozone cleaner (UVO) instead of the oxygen plasma system previously utilized. The UVO treatment activates chemically both surfaces (glass and PDMS) making them reactive to physical contact. The irreversible sealing was obtained for the samples that were placed in the cleaner about 5 cm away from the UV lamp and treated during 16 min. After 1 min for the exhaustion of the ozone gas created during exposure, the samples were withdrawn from the cleaner and their surface put into contact. To increase the bonding strength, the samples were then kept for 20 min at 70 °C in a hot plate and let to rest overnight at room temperature before use. The resulting bonding resisted the manual peel test.

### 5.3.2. Microlenses design and fabrication

To further improve the setup performance, self-aligned planar microlenses were incorporated in the chip to properly collimate light into the detection channel and then to the output fibre core taking advantage of the refractive index differences between air and PDMS (Camou et al. 2003). These 2D micro-optical components were fabricated by a replica moulding method using a single layer SU-8 mould, so they did not require any additional steps in the fabrication process.

Various input microlenses configurations were designed using the ray-tracing paraxial approximation. The light emitted by the LEDs is guided to the microfluidic channel by an input optical fibre of 62.5  $\mu\text{m}$  core diameter and the numerical aperture of 0.25 (see Fig. 5.3 and Fig. 5.4A–B). To focus the light on the channel content (aimed beam width: 100  $\mu\text{m}$ ), various input lens configurations were designed and tested: bi-concave air microlens and bi-convex PDMS microlens. The depth of all the chip features was around 125  $\mu\text{m}$  allowing optical fibres of 125  $\mu\text{m}$  diameter to be accurately fixed and easily aligned with each other and the channel. The designing was done setting the smallest feature width around 50  $\mu\text{m}$  (aspect ratio: 2.5) to prevent fluid leakage or fabrication issues, although an aspect ratio of 10 could be achieved by the used fabrication process (see (Bernacka-Wojcik et al.



2013). Table 5.2 shows the parameters of the designed input lenses configurations and the characteristics of the resulting beam ( $y$ —half of the beam width;  $\theta$ —the beam propagation maximum angle).

After interacting with the fluid to be analysed, the out light should be collected by the output fibre (core diameter: 62.5  $\mu\text{m}$ ;  $NA$ : 0.25). The output lenses were designed using the thin lenses approximation. To shorten the focusing length taking into account the small acceptance angle, a pair of lenses was to be used: bi-concave and bi-convex air lenses with the characteristics presented in Table 5.3.

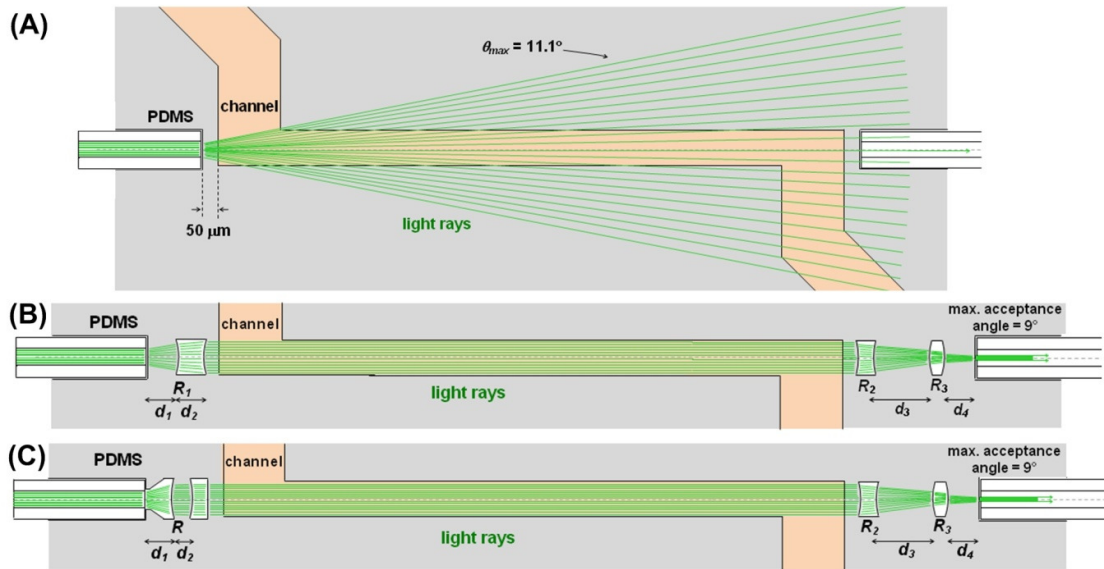


Fig. 5.3. 2D schema of light propagation in PDMS chip of 2 mm long optical path: (A) uncollimated; (B) with input and output air lenses and (C) with PDMS input lens and output air lenses (to scale).

Table 5.2. The curvatures ( $R$ ), distances ( $d$ ) and the characteristics of the resulting light beam ( $y$  and  $\theta$ ) for the input bi-concave air microlens and the input bi-convex PDMS microlens.

	air lens	PDMS lens
<b>R</b>	-175 $\mu\text{m}$	250 $\mu\text{m}$
<b>d<sub>1</sub></b>	100 $\mu\text{m}$	80 $\mu\text{m}$
<b>d<sub>2</sub></b>	80 $\mu\text{m}$	70 $\mu\text{m}$
<b>y</b>	50.160 $\mu\text{m}$	50.004 $\mu\text{m}$
<b><math>\theta</math></b>	-0.001200°	0.000146°

Table 5.3. The curvatures ( $R$ ), distances ( $d$ ) and the characteristics of the resulting light beam ( $y$  and  $\theta$ ) for the output bi-concave and bi-convex air microlens.

	output air lenses
$R_2$	-210 $\mu\text{m}$
$d_3$	180 $\mu\text{m}$
$R_3$	180 $\mu\text{m}$
$d_4$	50 $\mu\text{m}$
$y$	6.044 $\mu\text{m}$
$\theta$	-0.141970°

The chips incorporating the designed lenses were fabricated in PDMS by the replica moulding using SU-8 mould and an intermediate epoxy mould (the latter is used to increase the number of fabricated chip replica, see details elsewhere (Bernacka-Wojcik et al. 2013)). The fabricated lenses were characterized by optical microscopy in dark conditions with long exposure time (30 s; Fig. 1C and D), confocal microscopy (Fig. 5.4) and scanning electron microscopy (Fig. 5.5). Fig. 5.4C shows that in the chip without lenses, the light beam diverges and a big part of the light will not be transmitted into the output fibre core. Only a very small fraction of light will interact with the fluid and an even smaller fraction will be collected by the output fibre core. Furthermore, the light intensity will not be uniform along the channel thus endangering a good interaction. In the case of the chip with air lens (Fig. 5.4D), the light beam is well collimated on the channel content and afterwards converged into the output fibre core by the output lenses in accordance with the schema of the light propagation (Fig. 5.3 and Fig. 5.4A–B). It should be noted that those images show scattered light intensity, while for the detection, only the transmitted light is analysed; however, in those images the propagation of the light beam can be observed, as the scattered light intensity is proportional to the total light intensity.

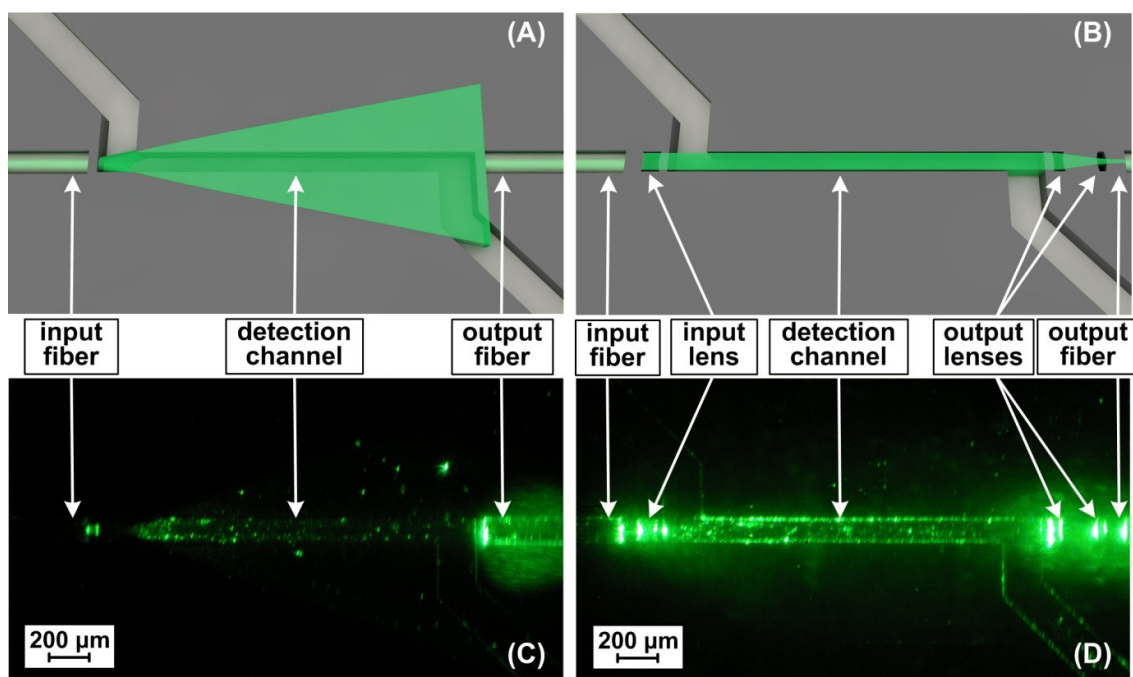


Fig. 5.4. (A) 3D schema of light propagation in chip of 2 mm long optical path without lenses and (B) with 2D air microlenses (the schema is drawn to scale; only the light propagation in the plane of the channel is considered as the light in vertical direction remains diverged). (C) Top view microscopic images of channel filled with water illuminated by green LED (0.9 A) in chip without lenses and (D) with 2D air microlenses.

The incorporation of microlenses increases significantly the number of interfaces on the optical pathway, while on each interface there is a light scattering and reflection causing optical losses (visible on Fig. 5.4D). Here, these losses were reduced by proper design of the microfabrication process. Firstly, a high resolution chrome mask was used to obtain low roughness features. Secondly, SU-8 was chosen as a mould material for PDMS patterning providing much smoother sidewalls than in the case of chemically etched moulds. Thirdly, SU-8 was UV exposed through i-line filter to prevent formation of T-shape features resulting in nearly vertical sidewalls (87.8 degrees). SEM images (Fig. 5.5) and confocal microscopy images (Fig. 5.6) reveal a good definition of the PDMS features and smooth sidewalls. The confocal microscopy images indicated some irregularities on the chip surface (visible also as reflecting spots in Fig. 5.4C and D) that are most probably related with the use of the epoxy mould that is much rougher than the SU-8 mould (see details elsewhere (Bernacka-Wojcik et al. 2013)). However, these irregularities do not cause any leaks and do not interfere with the detection system allowing proper analysis of the colorimetric changes of the AuNPs solutions. The cracks visible on the SEM images are associated with the thin gold layer that was

deposited to increase quality of SEM images (the confocal microscopy images of the same samples before the gold deposition show a crack-free surface, see Fig. 5.6).

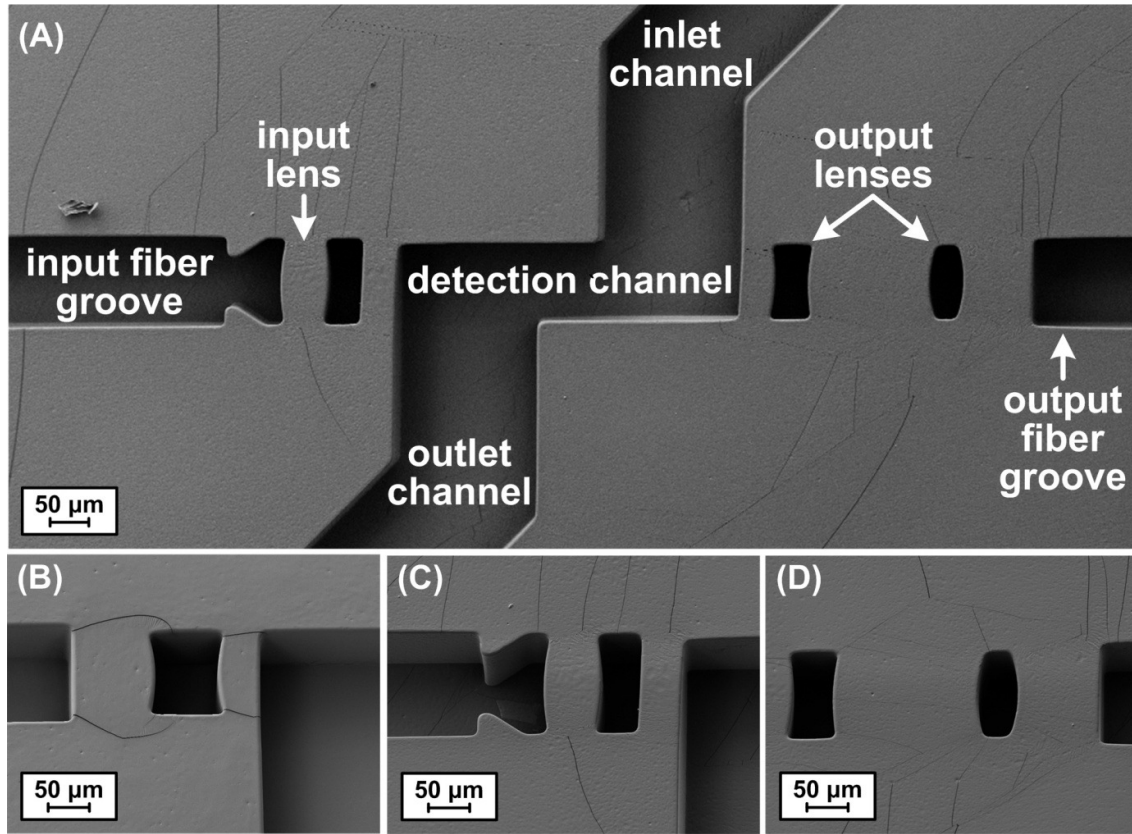


Fig. 5.5. Scanning electron micrographs of the PDMS chip: (A) main chip features; (B) input air microlens; (C) input PDMS microlens and (D) output air lenses. The images B – D were taken with the stage 20 degrees tilted to visualize better the aspect ratio.

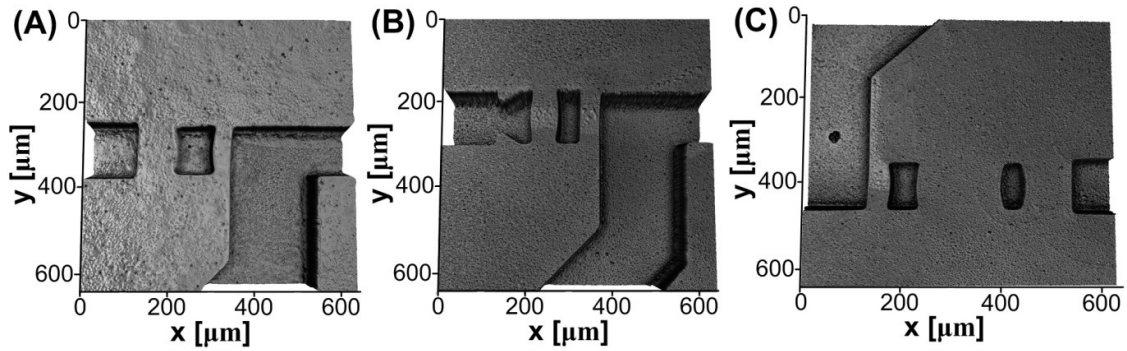


Fig. 5.6. Confocal microscope images of fabricated 2D microlenses: (A) input air lens; (B) input PDMS lens and (C) output air lenses.

### 5.3.3. Effect of microlenses on colorimetric AuNPs analysis

The performance of the microlenses was tested analysing the colour of AuNPs solution (Fig. 5.7A). The discrimination of the colour of the AuNPs solution (i.e. the difference between detection response for the dispersed and the aggregated AuNPs;  $\Delta R_s$ ) was  $0.251 \pm 0.012$  for the chip without lenses, while for the chip with the air lens it was  $0.335 \pm 0.007$  (34% of improvement) and  $0.337 \pm 0.009$  (34% of improvement) for chip with the PDMS lens. Both tested microlens configuration show the same detection improvement, however from the practical point of view, it is much easier to position the input fibre properly using the air lens configuration instead of the PDMS lens. In the latter, the fibre is stopped by the PDMS clips (see Fig. 5.5C and Fig. 5.3C) that due to the PDMS elasticity may not resist the fibre insertion movement. It is much more practical to use the air lens where the fibre is stopped by the 50  $\mu\text{m}$  thick PDMS wall. Therefore, in the following experiments only the configuration with air lenses was used.

Comparing with the previous state-of-the art ( $\Delta R_s = 0.128 \pm 0.011$ ), the optimized setup with the air lenses provides 160% higher discrimination of the AuNPs colour. The incorporated lenses not only increase the light intensity that reaches the output fibre, but also increase interaction fluid-beam: even setting the signal at the same value for the baseline solution for both configurations, the chip with lenses yields much better discrimination between red and blue colour AuNPs solutions. The 2D (Fig. 5.3) and 3D schema of light propagation (Fig. 5.4A and B) visualize well this mechanism: in the chip without lenses, the output fibre collects only the irradiation that passed the channel straight from the input fibre core to the output core (max. acceptance angle: 9 degree), therefore only a small portion of the total fluid will interact with propagating light. The incorporation of the output microlenses allows the interaction of all the available fluid with propagating light, yielding a much higher discrimination between signals obtained from the solutions of different colours.

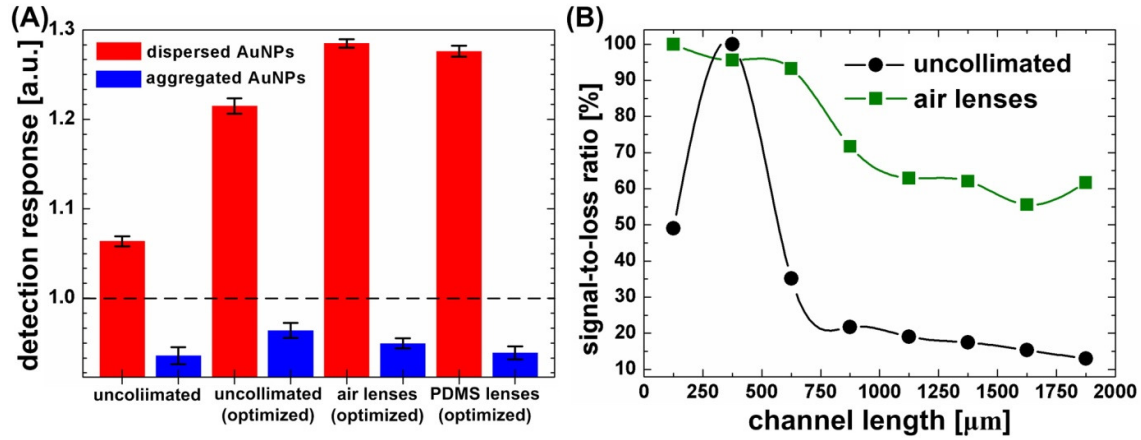


Fig. 5.7. (A) The detection response ( $R_s$ , eq. (5.1)) of the microfluidic platform for dispersed (in red) and aggregated (in blue) AuNPs solutions using microfluidics chips without lenses (before and after system optimization described in section 3.1), with air microlenses and with PDMS microlenses (LEDs powered with 0.4 A). The horizontal dashed line represents the threshold of 1 considered for discrimination between red and blue colour solutions. (B) The propagation of the signal-to-loss ratio along the channel in chip without lenses and chip with the air microlenses based on the analysis of the pixels intensity in Fig. 5.4C and D.

To quantitatively estimate the propagation of the light signal-to-loss ratio along the channel in the chips with and without air lens, the pixels intensity of the images presented in Fig. 1C and D was analysed by the ImageJ software. The channel was divided into 8 segments of 250 μm length and for each channel segment the integrated density (i.e. the sum of the values of the pixels intensity in the region) was measured. This value was then divided by the region area. The obtained value was defined as the signal, while the integrated density on the regions outside of the channel was defined as loss. Fig. 5.7B presents the propagation of the signal-to-loss ratio along the channel in the chip without lens and chip with air lens as a percentage of the maximum signal-to-loss ratio. In the chip without lens, the highest signal-to-loss ratio is on the channel segment from 250 μm to 500 μm, because on the beginning on the channel, the light illuminates only a part of the channel content (see Fig. 5.4A and C and Fig. 5.3A). Then, the signal-to-loss ratio decreases along the channel due to the beam divergence and only about 10% reaches the channel end. In the case of the chip with air lens, the signal-to-loss ratio is more constant along the channel and about 60% is transmitted to the channel end.

### 5.3.4. SNP detection using the optimized system

Subsequently, the microfluidic chip with air lenses was used in conjunction with specific Au-nanoprobe for the characterisation of an SNP in *FTO* (Carlos et al. 2013). Firstly, the chip was integrated with a miniature fibre optic spectrometer to analyse the assays' colorimetric changes and their variation with time elapsing after salt addition. Comparing the spectra acquired using the fibre optic spectrometer and chip with the spectra acquired by a microplate reader (see Fig. 5.8), a higher noise is attained since the light source in the miniature spectrometer is much weaker, thus the signal-to-noise ratio is low. Absorbance values on chip are about 5 times lower than those from the microplate reader that correlated directly to the difference in optical path length: in chip the optical path is 5 times shorter (2 mm) than in the microplate (10 mm). Nevertheless, the obtained absorption spectra are very similar for these two strategies but the microfluidic chip requires 10 times less volume.

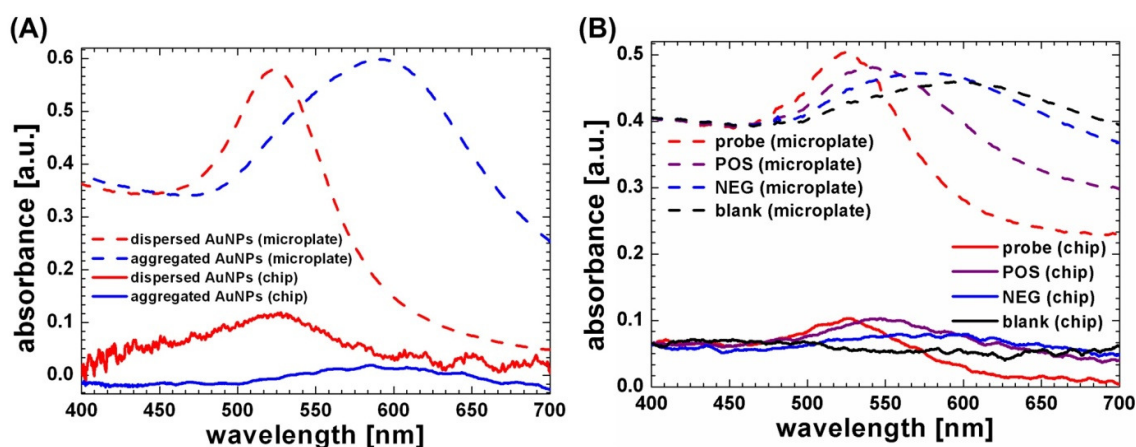


Fig. 5.8. Absorption spectra acquired using miniature fibre optic spectrophotometer integrated with a microfluidic chip ('chip'; 3  $\mu$ l; 2 mm long optical path; integration time: 610 ms) and using conventional microplate reader (30  $\mu$ l; 10 mm long optical path). (A) Spectra of the dispersed and aggregated AuNPs (3 min after salt addition). (B) Spectra of the Au-nanoprobe assay for the *FTO* single nucleotide polymorphism detection: blank (without DNA), positive (POS) and negative (NEG) assay (30 ng/ $\mu$ l of target DNA). The spectra were taken 30 min after salt addition. The absorption spectra of blank, POS and NEG were shifted for the same absorbance value at  $\lambda = 400$  nm as probe, so as to allow better visualisation.

The LEDs transmission spectra were acquired using the miniature fibre optic spectrometer integrated with the chip for the channel filled with water, the Au-nanoprobe and blank (8 min; 15 min and 30 min after salt addition; see Fig. 5.9) to analyse how the colour of the solutions affected the LEDs light

reaching the photodetector. The obtained spectra were much smoother due to the higher light intensity of the LEDs used when comparing to the halogen lamp. As expected, the red colour solution reduces the transmitted intensity of the green LED, while the blue colour solutions reduce the red light intensity. A longer time after salt addition (i.e. 15 and 30 min), the transmitted intensity of the LEDs increases because the colour of the blank solution becomes weaker with time due to precipitation of the aggregates.



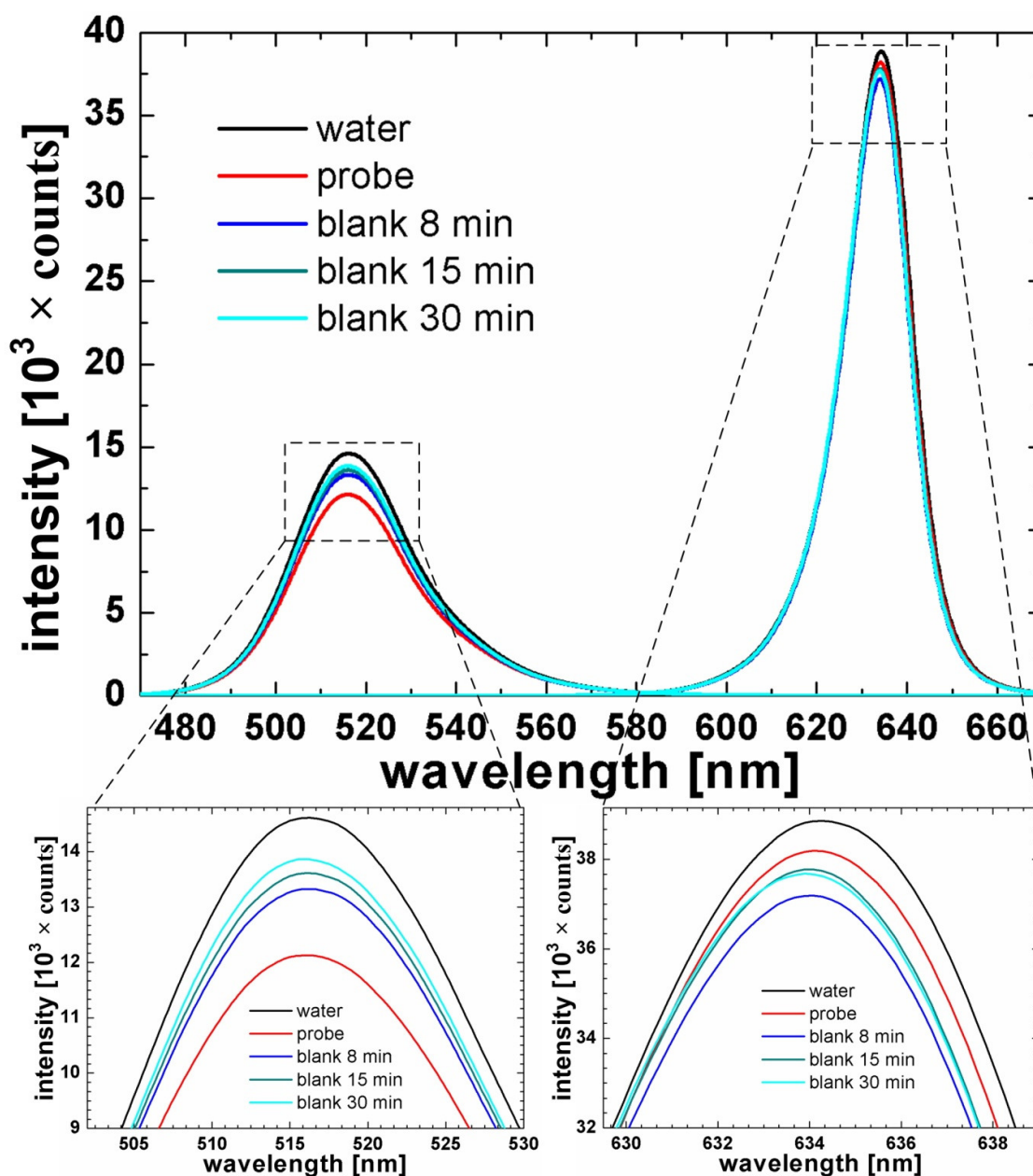


Fig. 5.9. Transmission spectra of green and red LEDs acquired using miniature fiber optic spectrophotometer integrated with microfluidic chip with air lenses filled with water, the Au-nanoprobe and blank (8 min; 15 min and 30 min after salt addition; the samples were injected into the channel directly after salt addition). LEDs powered with 0.4 A; reference: empty chip; integration time: 8 ms.

The microfluidic platform gave statistically significant discrimination between positive and negative samples using 30 ng/ $\mu\text{l}$  with 10 times less volume than for the microplate reader (Fig. 5.10). Furthermore, the microfluidic platform could discriminate between samples below the microplate

reader's limit of detection (LOD). While the microplate could only give a discriminatory response at concentrations equal or higher than 20 ng/ $\mu$ l, the microfluidic platform begins to discriminate at 15 ng/ $\mu$ l. The use of 15 ng/ $\mu$ l of sample DNA on the microfluidic platform yields a much weaker response between positive and negative sample, but a statistical analysis using a paired t-test shows these responses are significantly different from each other ( $p$ -value<0.001) with 99.9% confidence interval.

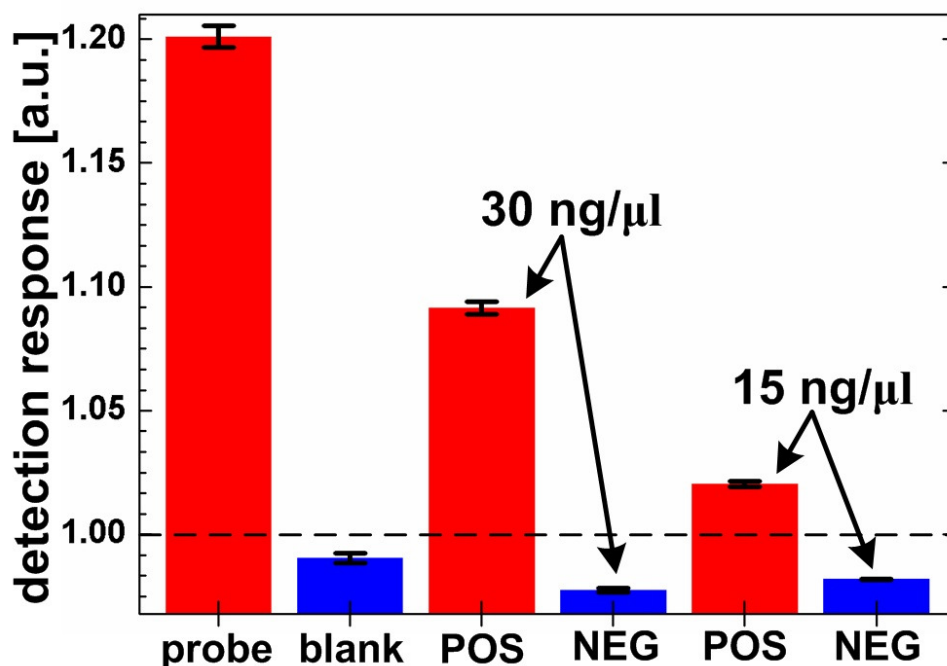


Fig. 5.10. Results of the colorimetric DNA detection (eq. 5.1) of the *FTO* single nucleotide polymorphism using Au-nanoprobes and the optimized bio-microfluidic platform with chip with air lenses using 3  $\mu$ l of solution with 15 and 30 ng/ $\mu$ l of target DNA. The horizontal dashed line represents the threshold of 1 considered for discrimination between positive and negative.

Images of channels using an optical microscope coupled to a digital camera and with a long exposure time (30 s) allowed to visualise different scatter intensities of AuNPs within channels. Following salt addition, aggregation may be inferred from the higher intensity scattering punctuation in the channel that increases with time—see Fig. 5.11. These intensities correlate to expected difference in aggregation between positive (small aggregates) and negative samples (larger aggregates).

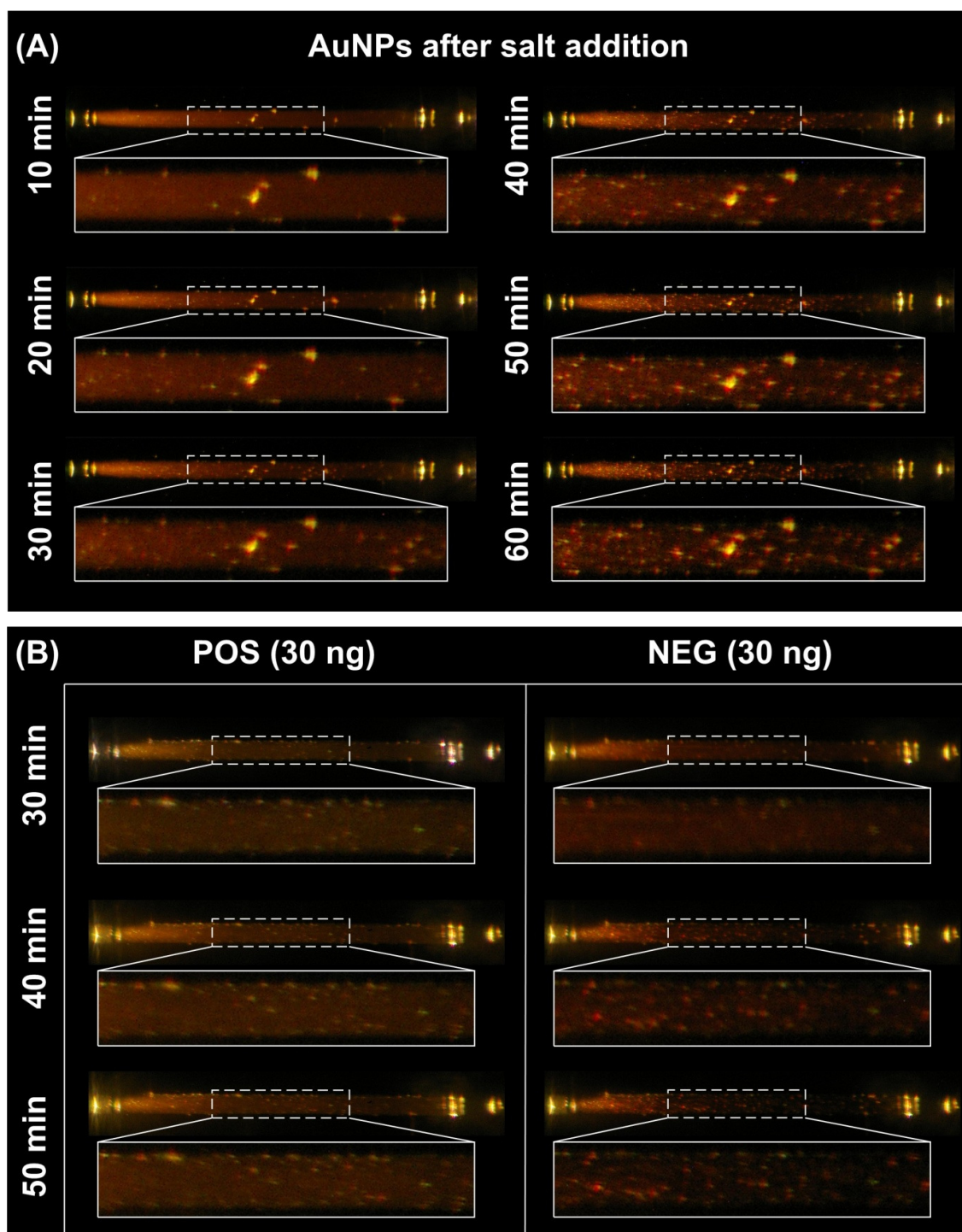


Fig. 5.11. Microscopic images of chip with air microlenses illuminated by halogen lamp taken in dark conditions using Stereo Microscope and Pentax K100 camera with long exposure time (30 s). (A) AuNPs 10 to 60 min after salt addition (the solutions were injected into the channel directly after salt addition). (B) The positive and negative colorimetric Au-nanoprobe assays for *FTO* single mismatch detection (target DNA concentration: 30 ng/ $\mu$ l) taken 30; 40 and 50 min after salt addition (the solutions were injected to the channel 26 min after salt addition).

## 5.4. Conclusions

The combination of the unique optical properties of gold nanoprobe with microfluidic platform resulted in sensitive and accurate sensor for single nucleotide polymorphism detection operating using small volumes of solutions and without the need for substrate functionalization or sophisticated instrumentation. The optimized bio-microfluidic platform clearly distinguishes between positive and negative samples using 10 times lower solution volume and target DNA concentration below the limit of the detection attained with a conventional microplate reader (i.e. 15 ng/ $\mu$ l). The thoroughly described optimization of the microfluidic platform (concerning electrical signal processing; design, fabrication and performance of various microlenses) has significantly improved the results of AuNPs colorimetric analysis and can also be applied to other absorbance-based microfluidic devices as a simple and cheap mean to compensate for reduction of optical path length.

In the next step of the setup optimization, the mixing of reagents should be performed in the microfluidic chip to reduce the risk of sample contamination. Furthermore, waveguides should be incorporated to facilitate the chip exchange towards the point of care use.

## **Chapter 6**

Experimental optimization of a passive planar  
rhombic micromixer with obstacles for  
effective mixing in a short channel length

*This chapter is written basing on:*

Bernacka-Wojcik, I., Ribeiro, S., Wojcik, P.J., Alves, P., Busani, T., Fortunato, E., Baptista, P.V., Águas, H., Hilliou, L., Martins, R. 2014. Experimental optimization of a passive planar rhombic micromixer with obstacles for effective mixing in a short channel length.. RSC Advances. DOI: 10.1039/C4RA10160J

*This chapter differs from the article in:*

- Supplementary information has been merged into the article text for the reading flow.

The author of the thesis was involved in design of the micromixers, results analysis and was responsible for the microchip fabrication and characterisation, and writing of the paper.

<b>Chapter 6. Experimental optimization of a passive planar rhombic micromixer with obstacles for effective mixing in a short channel length .....</b>	<b>149</b>
<b>Summary.....</b>	<b>149</b>
<b>6.1. Introduction.....</b>	<b>149</b>
<b>6.2. Experimental details .....</b>	<b>153</b>
6.2.1. Fabrication of microfluidic device.....	153
6.2.2. Assessment of mixing efficiency.....	154
6.2.3. Pressure drop measurements.....	155
6.2.4. Statistical analysis.....	155
<b>6.3. Results and discussion .....</b>	<b>156</b>
6.3.1. Mixer design and fabrication.....	156
6.3.2. Mixing efficiency and mechanism.....	158
6.3.3. Pressure drop .....	162
6.3.4. Statistical analysis of the results.....	165
<b>6.4. Conclusions.....</b>	<b>171</b>





## **Chapter 6. Experimental optimization of a passive planar rhombic micromixer with obstacles for effective mixing in a short channel length**

### **Summary**

This paper presents the performance of a passive planar rhombic micromixer with diamond-shaped obstacles and a rectangular contraction between the rhombi. The device was experimentally optimized using water for high mixing efficiency and low pressure drop over a wide range of Reynolds numbers ( $Re = 0.1\text{--}117.6$ ) by varying geometrical parameters, such as number of rhombi, distance between obstacles and contraction width. Due to the large amount of data generated, statistical methods were used to facilitate and improve the results of the analysis. The results revealed a rank of factors influencing mixing efficiency: Reynolds number > number of rhombi > contraction width > inter-obstacles distance. The pressure drop measured after three rhombi depends mainly on  $Re$  and inter-obstacles distance. The resulting optimum geometry for low  $Re$  regime has a contraction width of 101  $\mu\text{m}$  and inter-obstacles distance of 93  $\mu\text{m}$ , while for high  $Re$  regime, a contraction width of 400  $\mu\text{m}$  and inter-obstacles distance of 121  $\mu\text{m}$ ) are more appropriate. These mixers enabled 80% mixing efficiency creating a pressure drop of 6.0 Pa at  $Re = 0.1$  and  $5.1 \times 10^4$  Pa at  $Re = 117.6$ , with a mixer length of 2.5 mm. To the authors' knowledge, the developed mixer is one of the shortest planar passive micromixers reported to date.









### **6.1. Introduction**

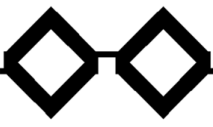



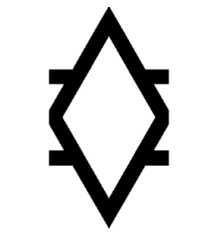
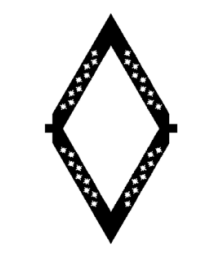
Miniaturisation is a recent trend in analytical chemistry and life sciences due to the possibility of performing sophisticated analysis within a hand hold size, faster sample analysis, higher throughput, portability, reduced reagent use, all of which are associated with decreased cost. However, physical and chemical surface effects such as capillary forces, surface roughness and chemical interactions of construction materials with reaction processes, become more dominant at the micro-scale (Whitesides 2006), thus impeding a simple scaling down approach of existing mixing systems. For microfluidic systems, the Reynolds number ( $Re$ ) is typically smaller than 100 and the flow is considered essentially laminar, which critically limits mixing efficiency (Capretto et al. 2011). Convective mass transfer occurs only in the fluid flow direction and mixing is achieved merely by molecular diffusion. However, diffusion alone is inefficient and imposes the need of long microchannels, meaning that mixing at the micro-scale should be artificially enhanced. Accordingly, two basic principles are exploited to enhance mixing at the micro-scale: active or passive (Capretto et al. 2011). Active mixers depend on an external energy source to achieve mixing, whereas passive mixers solely rely on fluid

pumping energy and use special channel designs to restructure the flow, reduce the diffusion length and maximize the contact surface area between fluids (Lee et al. 2011).

In contrast to active micromixers or three-dimensional passive micromixers, planar passive micromixers are more cost efficient, can be easily integrated with other microfluidic components and can be fabricated using conventional single layer photolithography techniques. As such, research for achieving best mixing efficiency in the shortest time and smallest pressure drop using planar passive micromixers has thrived during the last decade. The field is often reviewed, see for instance (Capretto et al. 2011; Kuo and Chiu 2011; Lee et al. 2011; Wang et al. 2002). Table 6.1 summarizes the main types of existing passive planar micromixers, with the corresponding best mixing efficiencies reported to date, relying essentially on chaotic advection to mix water-based fluids with Newtonian behaviour. This table is certainly not a comprehensive review of designs and performance, but its content can serve to appraise mixing efficiencies, pressure drops and mixing distances achieved with innovative micromixer designs. All microchannel designs summarized in Table 6.1 rely on the split and recombine concept and/or on chaotic advection where obstacles or baffles are inserted along the channel to promote converging and diverging flows. Interestingly, only four out of fourteen designs use curvilinear channels to enhance secondary flows in the curves. Such flows usually result from the elasticity of the fluid rather than from inertial effects; thus, they should be promising in enhancing mixing when viscoelastic fluids such as polymer solutions are used (Burghilea et al. 2004).

Table 6.1. Summary of planar passive micromixer designs with respective performance reported in the literature (\* data obtained through simulations).

chip design (ref.)	mixing length (mm)	channel width ( $\mu\text{m}$ )	channel depth ( $\mu\text{m}$ )	$Re$ range	best mixing performance (corresponding $Re$ )	pressure drop in Pa (corresponding $Re$ )	schematic
Y-rectangular mixer (Kashid et al. 2011)	40.0	250	292	10–1000 (1 ml/min–18 ml/min)	$\sim 100\%$ (not available; 8 ml/min)	$\sim 9.0 \times 10^4$ (not available; 8 ml/min)	
rectangular channel with triangle-shaped mixing elements (Conlisk and O'Connor 2012)	32.0	150	50	0.1–20.0	90% (0.1 and 20)	not available	
rhombic (angle $90^\circ$ ) with a converging-diverging element (Chung and Shih 2008)	13.3	250	130	5–200	80% (5) 94% (200)	$1.6 \times 10^2$ (10)* $5.7 \times 10^3$ (200)*	
rectangular channel with diamond-shaped obstacles (Bhagat et al. 2007)	11.0	200	55	0.02–10.00	90% (0.1)	$1.5 \times 10^2$ (0.1)*	
curved channels with unbalanced splits and collisions of streams (Ansari et al. 2010)	8.0	300 (sum of sub-channels' width)	120	10–80	64% (80)	not available	
rectangular channel with baffles (Chung et al. 2008b)	8.0	400 (50–150 for baffle)	130	40–80	$> 90\%$ (80)	$3.1 \times 10^4$ (80)*	
labyrinth: "S-shaped" mixers with $180^\circ$ turns (Li et al. 2012a)	7.3	220	267	2.5–30.0	80% (5)	not available	
rhombic (angle $60^\circ$ ) with a converging-diverging element (Chung et al. 2008a)	6.8	250 (100 for converging-diverging element)	130	0.1–110.0	86% (0.1) 85% (110)	$1.2 \times 10^1$ (0.1)* $2.1 \times 10^4$ (110)*	

rhombic (angle 90°) with asymmetrical constriction between rhombi (Chung and Shih 2007)	4.8	250 (88–700 for constrictions)	120	1–50	90% (20)	$3.6 \times 10^3$ (20)*	
C-shape channel with baffles (Tsai and Wu 2011)	3.6	130 (40 for baffles)	130	1–100	85% (81)	$3.4 \times 10^4$ (81)*	
rectangular channel with baffles and gaps (Shih and Chung 2008)	2.4	400 (50–150 for gaps)	120	0.1–30.0	91% (0.1) 94% (30)	$1.5 \times 10^1$ (0.1)* $1.5 \times 10^2$ (1)* $1.3 \times 10^4$ (40)*	
modified square wave mixer with by-passes (Goovaerts et al. 2012)	1.9 per repeating unit	200–400	200	not available (0.1 ml/min–14 ml/min)	87% (not available; 0.2 ml/min)	$7.0 \times 10^3$ per repeating unit (not available; 4.0 ml/min)	
rhombic (angle 60°) with branch channels (Chang et al. 2011)	not available	250 (100 for branch channels)	120	10–120	98% (120)	$9.0 \times 10^3$ (120)*	
rhombic (angle 60°) with diamond-shaped obstacles and rectangular contractions (this paper)	2.5	200	130	0.1–117.6	80% (0.1 and 117.6)	6.0 (0.1) $5.1 \times 10^4$ (117.6)	

Ubiquitous to all studies reported in Table 6.1 is the occurrence of a minimum in mixing efficiency for Reynolds numbers in the range of 1 to 10. This is related to the transition from diffusion to advection driven mixing. Also, all these mixers were optimized using computational fluid dynamics simulations, only the best designs having been fabricated and experimentally tested for mixing efficiency. Only (Kashid et al. 2011) and (Goovaerts et al. 2012) have measured experimentally the pressure drop, while the others reported data obtained exclusively from simulations. Although simulations can provide valuable qualitative and quantitative predictions significantly reducing time and cost, it is difficult to access their uncertainty, as the results are affected by the accuracy of modelling, discretization and iteration. For instance, (Matsunaga et al. 2013) have shown that for a T-shaped micromixer operating in the *Re* range of 140–250, grid-based simulations may overestimate mixing efficiency by up to 30%. Therefore, this paper is based exclusively on the experimental

characterisation of micromixers. We present a passive planar rhombic micromixer (Chung and Shih 2008) with obstructions in the microchannel (Bhagat et al. 2007) and a contraction placed after each rhombus to further increase interface generation between fluid elements. All these mixing elements (i.e. rhombic channel; obstructions and contractions) enhance mixing through stretching, folding, and break-up processes caused by transverse flows. Rhombic channels induce recirculation at each angle and should also promote curved fluid streams in the rhombus tips. Such curved streams should enhance elastic instabilities and turbulences, and will be further used in a future study focusing on the mixing efficiency and pressure drop optimization for viscoelastic fluids. In addition, a rectangular contraction (called elsewhere “gap” (Bhagat et al. 2007)) is placed after each rhombus to enhance extensional flows which are known for significantly improving the mixing in viscoelastic fluids (Utracki 2002). The aim of this study is to experimentally optimize the micromixer design by varying geometrical parameters and to identify the most relevant ones for obtaining the best mixing efficiency and shortest mixing length with minimal pressure drop for Newtonian fluids. We investigate the influence of the diamonds distance ( $d$ ) and contraction width ( $w_c$ ) on mixing efficiency and pressure drop over a wide range of flow conditions. For each chip, the total pressure drop and mixing efficiencies at three locations along the channel were measured for twelve  $Re$  values ranging from 0.1 to 117.6. Due to the complexity of the study and the number of studied responses, statistical methods were used to facilitate and improve the data analysis.

## 6.2. Experimental details

### 6.2.1. Fabrication of microfluidic device

The mould for PDMS patterning was fabricated by ultraviolet photolithography in SU-8 2050 (Microchem, USA). The material was spin-coated on silicon wafers at 1530 rpm to form a  $\sim 130$   $\mu\text{m}$  thick layer, then soft baked on a levelled hot plate for 5 min at 65 °C and then for 24 min at 95 °C. After cooling (10 min), the samples were UV exposed on a mask aligner (MA6, Suss MicroTec, Germany) for 21 s with an exposure dose of  $\sim 309$   $\text{mJ}/\text{cm}^2$  through an i-line filter (G180336, Suss MicroTec, Germany). Then, the samples were post-baked during 5 min at 65 °C and subsequently for 11 min at 95 °C. Patterns were developed by submersing them in PGMEA (Microchem, USA) during 18 min with magnetic agitation of 500 rpm, rinsing them with IPA and gently drying with compressed nitrogen. The mould was silanized with tridecafluoro-1,1,2,2-tetrahydrooctyl trichlorosilane (Microchem, USA).

PDMS (Sylgard 184, Dow Corning, Spain) was prepared by mixing a base and a curing agent in a 10:1 weight ratio. The mixture was stirred and degassed in a vacuum desiccator. Afterwards, the PDMS was poured over the SU-8 mould and cured at 100 °C on a levelled hot plate for 3 hours. Then, the PDMS was peeled off from the SU-8 mould.

The PDMS structures were placed on top of a Petri dish with the negative relief features up. On top of the features of the PDMS structure, an epoxy glue (ES562, Permabond) was poured to form a ~2 mm thick layer. After ~72 h degassing in a desiccator, the epoxy glue was cured in an oven at 120 °C for ~40 min. Then, the cured epoxy was peeled from the PDMS and utilized as a master mould for PDMS soft lithography using the same procedure as described above. The inlets and outlets of the PDMS chips were made using a blunt needle. The chips were irreversibly bonded to glass slides by plasma oxygen (60 s in 13 Pa, 100 W, Plasma electronic Buck Technologien, Germany). After the plasma treatment, the PDMS-glass sandwich was baked at 100 °C for 5 min to increase the bond strength. The chips were characterized by optical microscopy (Leitz Laborlux 12 ME ST), profilometry (XP-200, Ambios Technology, Inc., Santa Cruz, USA) and scanning electron microscopy (SEM, Zeiss Auriga, Germany).

### 6.2.2. Assessment of mixing efficiency

Two fluids were supplied to the microchannels using a syringe pump (Harvard Apparatus PHD 22/200) with two syringes (Hamilton 1005LTN, USA) with 5.0 ml and 2.5 ml capacity. During the experiments, the first syringe was filled with a blue dye (food grade dye, E133) at a 20 times dilution in deionized water and the 2.5 ml syringe was filled with deionized water only. The two syringes were driven at flow rates ranging from 0.06 ml/h ( $Re = 0.1$ ) to 56.00 ml/h ( $Re = 117.6$ ), measured in separated calibration runs where volumetric flow rates were recorded using gravimetric balances at the micromixers' outlet. The image capturing system consists of an inverted microscope (Leica DMI 5000M, Leica Microsystems, Germany) connected to a light sensitive CCD camera (Lu160, Lumenera Corporation, USA). Images were processed using ImageJ software to quantify the mixing index and mixing efficiency. The concentration  $c_i$  at an image point is represented by the pixel intensity value  $I_i$ , with the limiting values of concentration  $c_{max}$  and  $c_{min}$  corresponding to  $I_{max}$  and  $I_{min}$ , respectively. Pixel intensity values were normalized according to eq. 1.

$$\bar{I}_i = \frac{I_i - I_{min}}{I_{max} - I_{min}} \quad \text{eq. (6.1)}$$

The mixing index ( $\sigma$ ) is defined as the standard deviation of the pixel intensity distribution along a line (see Fig. 1C) across the micromixer channel (Stroock et al. 2002):

$$\sigma = \sqrt{\langle (\bar{I}_i - \langle \bar{I} \rangle)^2 \rangle} \quad \text{eq. (6.2)}$$

where  $\bar{I}_i$  is the normalized grey-scale pixel intensity given by eq. 1 (between 0 and 1) and  $\langle \bar{I} \rangle$  is the normalized average greyscale intensity. The value of  $\sigma$  is 0.5 for completely segregated (unmixed) streams at micromixer entrance and 0 for perfectly mixed streams. The mixing efficiencies ( $M$ ) were then calculated from  $\sigma$  using (Shih and Chung 2008):

$$M = 100 \times (1 - \frac{\sigma}{\langle \bar{I} \rangle}) \quad \text{eq. (6.3)}$$

where  $\langle \bar{I} \rangle \approx 0.40 \pm 0.05$ , due to asymmetric inlets' configuration. The uncertainty of  $M$  determination comes mainly from accuracy of image analysis (pixels noise), reproducibility of image analysis (2 snapshots were taken at 2 different instants, thus averaging possible fluid fluctuations) and chip construction reproducibility (some measurements were repeated in a second chip with the same configuration). The combined  $M$  determination uncertainty is 6.6% originating largely from pixels noise.

The  $Re$  number was calculated with the following expression:

$$Re = \frac{2\rho Q}{(W_c+h)\eta_o} \quad \text{eq. (6.4)}$$

in which  $\rho$  is the density of water (998 kg/m<sup>3</sup>),  $Q$  is the volumetric flow (m<sup>3</sup>/s),  $w_c$  is the width ( $2 \times 10^{-4}$  m) of the equivalent rectangular channel and  $h$  is the height ( $1.3 \times 10^{-4}$  m), and  $\eta_o$  is the viscosity of the dyed water ( $8 \times 10^{-4}$  Pa  $\times$  s) measured at 28 °C (the temperature at which both mixing efficiency and pressure drop were measured) using a stress controlled rotational rheometer (MCR300, Paar Physica) equipped with concentric cylinders (CC27, Paar Physica). Within the detection limit of the rheometer and the shearing geometry used, we noted no difference between the viscosity of the dyed fluid and the viscosity of the deionized water.

### 6.2.3. Pressure drop measurements

Pressure drop was measured using a differential pressure transducer (26PC, Honeywell, USA) connected to the pressure taps of the micromixer with flexible Tygon tube (internal diameter 0.8 mm). The transducer voltage output was digitized (NI 9215, National Instruments, USA) and further processed using a home-written LabVIEW routine enabling the on-the-fly oversampling of data, resulting in an increased sensitivity of the transducer (Hilliou et al. 2004). The transducer (with tubing) was calibrated using a pressure pump (MFCS-100, Fluigent, France) in the range  $7 \times 10^2$ – $1 \times 10^5$  Pa.

### 6.2.4. Statistical analysis

Statistical data analysis was performed using JMP 8.01 software (S.A.S. Institute Inc., Cary, NC, USA). Graphical presentations of the models were generated in JMP 8.01 and processed graphically in OriginPRO 8.5 2010 (OriginLab Corporation, Northampton, MA, USA) diagramming tool.

## 6.3. Results and discussion

### 6.3.1. Mixer design and fabrication

The proposed mixer enhances mixing by three means: (i) obstacles within the microchannel; (ii) rhombic channel structure and (iii) contraction in between rhombi (Fig. 6.1A). The inlet channel of fluid A is split into 2 channels with a width of 200  $\mu\text{m}$ , while the inlet and outlet channels of fluid B are 2000  $\mu\text{m}$  long and 400  $\mu\text{m}$  wide. The diameter of inlets and outlet is 1000  $\mu\text{m}$ . Additionally, 2 mm away from the inlet B and outlet, pressure taps (diameter: 1000  $\mu\text{m}$ ) were placed for measurement of pressure drop.

The presence of obstacles alters the flow direction, inducing recirculation that causes transversal mass transport. Large recirculation is beneficial for increased interfacial contact area between two species improving diffusion-based and convective mixing. Proper configuration of obstacles is critical, e.g. symmetric obstacles reduce the contact surface leading to lower mixing efficiency than in the absence of obstacles (Lee and Lee 2008a). Generally, obstacles are efficient mainly for fast flows (usually at  $Re$  above 10) and only optimized geometries (i.e. diamond-shaped (Bhagat et al. 2007) or asymmetric rectangles (Bhagat and Papautsky 2008)) enable satisfactory mixing at  $Re$  below 1. Diamond-shaped obstacles provide better mixing performance than circular- or triangular-shaped obstructions because they split the flow without introducing stagnation areas inside the channel. Furthermore, stepping of the walls of the diamond-shaped obstructions improves mixing efficiencies (Bhagat et al. 2007). Therefore, diamond-shaped obstacles (100  $\mu\text{m} \times 100 \mu\text{m}$ ; width  $\times$  length) with 20  $\mu\text{m}$  steps were positioned inside a microchannel (200  $\mu\text{m} \times 125 \mu\text{m}$ ; width  $\times$  height) with an offset of 30  $\mu\text{m}$ . Since the obstacles occupy the whole depth of the channel, the chip mould can be processed in a single photolithography step. This is of extreme relevance when prototyping and scale up production are concerned.

At very low  $Re$  (below 1), micromixers based on diamond-stepped obstacles require a long mixing channel (about 11 mm). A rhombic channel structure was therefore adapted to induce recirculation at rhombus corners (Chung et al. 2008a). When  $Re$  is high enough, vortices may be created at the rhombus turns, increasing the advective transport. The average velocity in the rhombic mixer is only half of that in the zigzag mixer, yielding a lower pressure drop. A turning angle of the rhombic mixer of  $60^\circ$  was chosen, as it is the best compromise between mixer footprint, induced dead volume and mixing efficiency (Chung et al. 2008a). The length of the rhombic period is fixed at 1500  $\mu\text{m}$ , while the length of the contraction between rhombi is 100  $\mu\text{m}$ .

Once the fluid flows out of the rhombic channel, two streams merge into a single one by means of a contraction and accelerate due to smaller cross-sectional area. After passing the contraction, flow is decelerated and separated into two streams. The added contraction can provide better mixing efficiency at lower  $Re$  by increase of the interfacial area due to stretching and at higher  $Re$  by



recirculation and vortices (Chung et al. 2008a). Here, a rectangular contraction was used as this configuration resulted in the shortest mixer length and one of the highest mixing efficiencies reported so far for planar passive mixers (Shih and Chung 2008) (see Table 6.1).

To optimize the mixer performance (in terms of lower pressure drop and shorter length), various mixer configurations were tested, where the controlled variables are the number of rhombi (1, 2 and 3), the width of the contraction between rhombi ( $w_t = 100\text{--}400\text{ }\mu\text{m}$ ) and the distance between stepped diamond-shaped obstacles ( $d = 60\text{--}140\text{ }\mu\text{m}$ ). There were 9 chips configurations of various combinations of  $w_t$  and  $d$ . The mixing efficiency was analysed after each rhombus to evaluate the influence of the number of rhombi.

The micromixers were fabricated in PDMS by a replica moulding technique using a mould produced in SU-8 by UV photolithography (Bernacka-Wojcik et al. 2013). SU-8 moulds suffer delamination at the photoresist-substrate interface after fabrication of few PDMS replicas, therefore we have used an intermediate monolithic epoxy mould to increase the number of possible PDMS replicas from the same SU-8 mould. The moulding process starts with the fabrication of an SU-8 mould, then instead of casting PDMS repeatedly from this mould, PDMS is casted once and used as mould for patterning of an epoxy mould, which can then be used to produce many PDMS replicas without suffering from the delamination problem. The SEM image (Fig. 6.1B) confirms the good definition of the PDMS features. The PDMS replicas obtained by this process are about 5% smaller than the designed dimensions due to PDMS shrinkage (Lee and Lee 2008b), i.e. the obstacles width is  $95\text{ }\mu\text{m}$  instead of the intended  $100\text{ }\mu\text{m}$ . Fig. 6.1B presents also a photograph of the microfluidic mixer filled with dyes for better visualization.

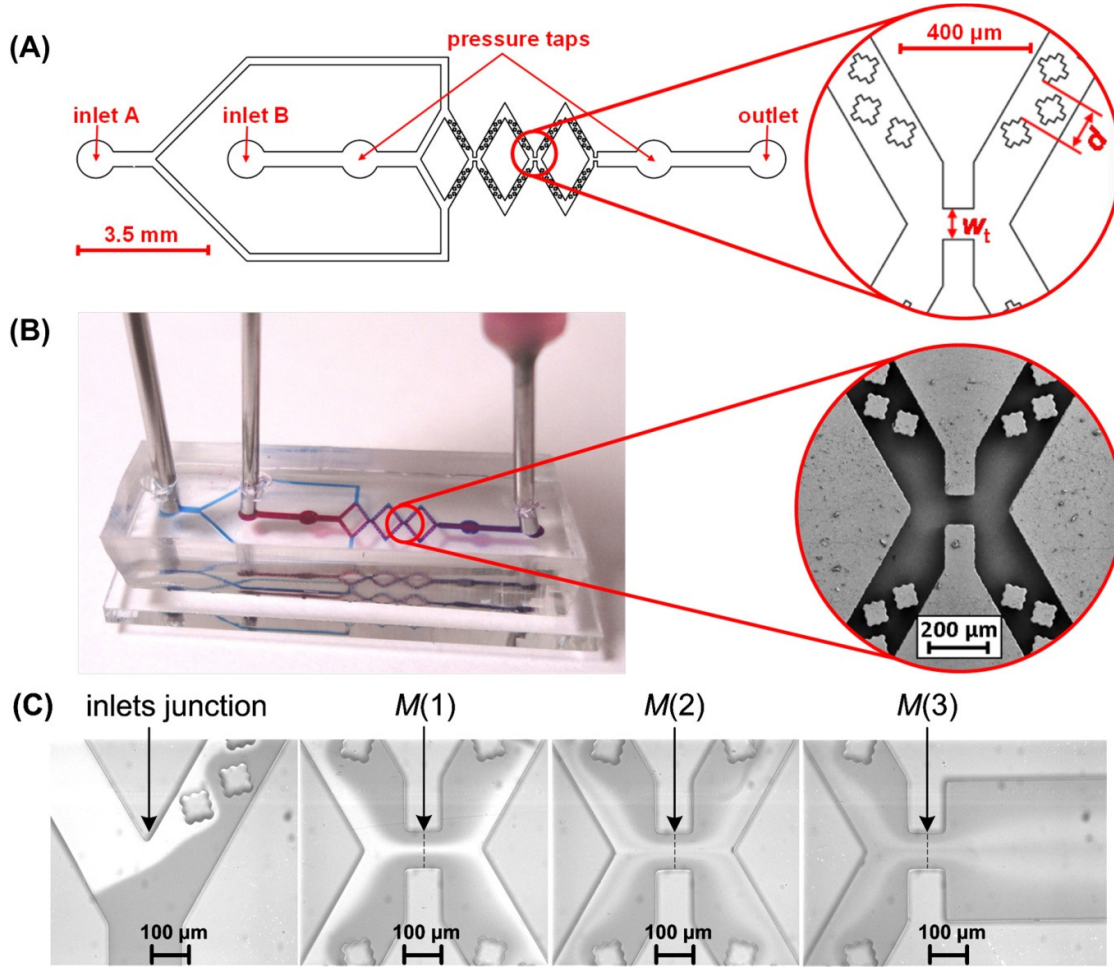


Fig. 6.1(A) Schematic diagram of the designed rhombic micromixer with stepped diamond-shaped obstacles and rectangular contractions between rhombi. (B) PDMS micromixer fabricated using SU-8 mould and epoxy mediating mould. (C) Optical microscopy images taken at different locations along a micromixer with  $w_t = 100 \mu\text{m}$  and  $d = 140 \mu\text{m}$  at  $Re = 8.2$ . Mixing efficiency was analysed along the channel in the middle of the first contraction,  $M(1)$ , second contraction,  $M(2)$  and third contraction,  $M(3)$ , as indicated by the vertical dotted lines.

### 6.3.2. Mixing efficiency and mechanism

Fig. 6.1C displays representative snapshots captured for a micromixer ( $w_t = 250 \mu\text{m}$  and  $d = 140 \mu\text{m}$ ) operated at  $Re = 8.2$ . At the entrance of the first rhomb, the light grey corresponds to pure water, while the darker grey corresponds to the dyed water. As the two fluids flow along the channel, increased mixing is apparent. For each chip, the mixing efficiency in the middle of the first contraction,  $M(1)$ , second contraction,  $M(2)$  and third contraction,  $M(3)$  were measured for various  $Re$ . Furthermore,  $M$  at the outlet channel was measured, but no increase was observed, probably due to a short distance ( $100 \mu\text{m}$ ) from the  $M(3)$  access line. To assess the mixing mechanism, images of

the micromixers with  $w_t$  from 100 to 400  $\mu\text{m}$  were compared at various  $Re$ .  $Re$  of 1.2; 5.9 and 88.2 were chosen to better visualize the fluid behaviour. At  $Re = 0.1$  and  $Re = 117.6$ , the fluids at the first contraction are already significantly mixed by means of the obstacles, so the grey-scale contrast between fluids is much lower. Fig. 6.2A presents optical microscopy images taken at the first contraction of a micromixer of  $d = 140 \mu\text{m}$ , revealing the effect of  $w_t$  on the flow for various  $Re$ . Passing through the contraction, the flow is accelerated and decelerated afterwards. At  $Re = 1.2$  and  $Re = 5.9$ , the flow is laminar and mixing is enhanced only by the increased contact between fluids. At the lowest  $Re$  (1.2), mixing is better than in the case of  $Re = 5.9$  due to increased residence time. At higher  $Re$  (88.2), there is stronger fluid agitation and the flow is greatly affected by the contraction width. At the lowest contraction width ( $w_t = 100 \mu\text{m}$ ), after flowing through the contraction, the water stream is transferred from the inner channel walls towards the outer walls, improving mixing. The flow features were observed for the rectangular contraction by (Bhagat et al. 2007) and can be explained by the formation of vortices. The size of the contraction is critical for the vortices formation at the exit of the contraction: in mixers of  $d = 140 \mu\text{m}$ , for  $w_t = 100 \mu\text{m}$ , vortices are generated starting from  $Re = 29.4$ ; for  $w_t = 250 \mu\text{m}$ , vortices are formed only at  $Re = 117.6$ , while for  $w_t = 400 \mu\text{m}$ , vortices are not observed in any of the tested flow conditions. Fig. 6.2B shows a comparison of the vortices generated at  $Re = 28.4$ ;  $Re = 58.8$  and  $Re = 117.6$  in the mixer with  $w_t = 100 \mu\text{m}$  and  $d = 140 \mu\text{m}$ . The size and intensity of the generated vortices increase significantly with  $Re$  enhancing mixing.

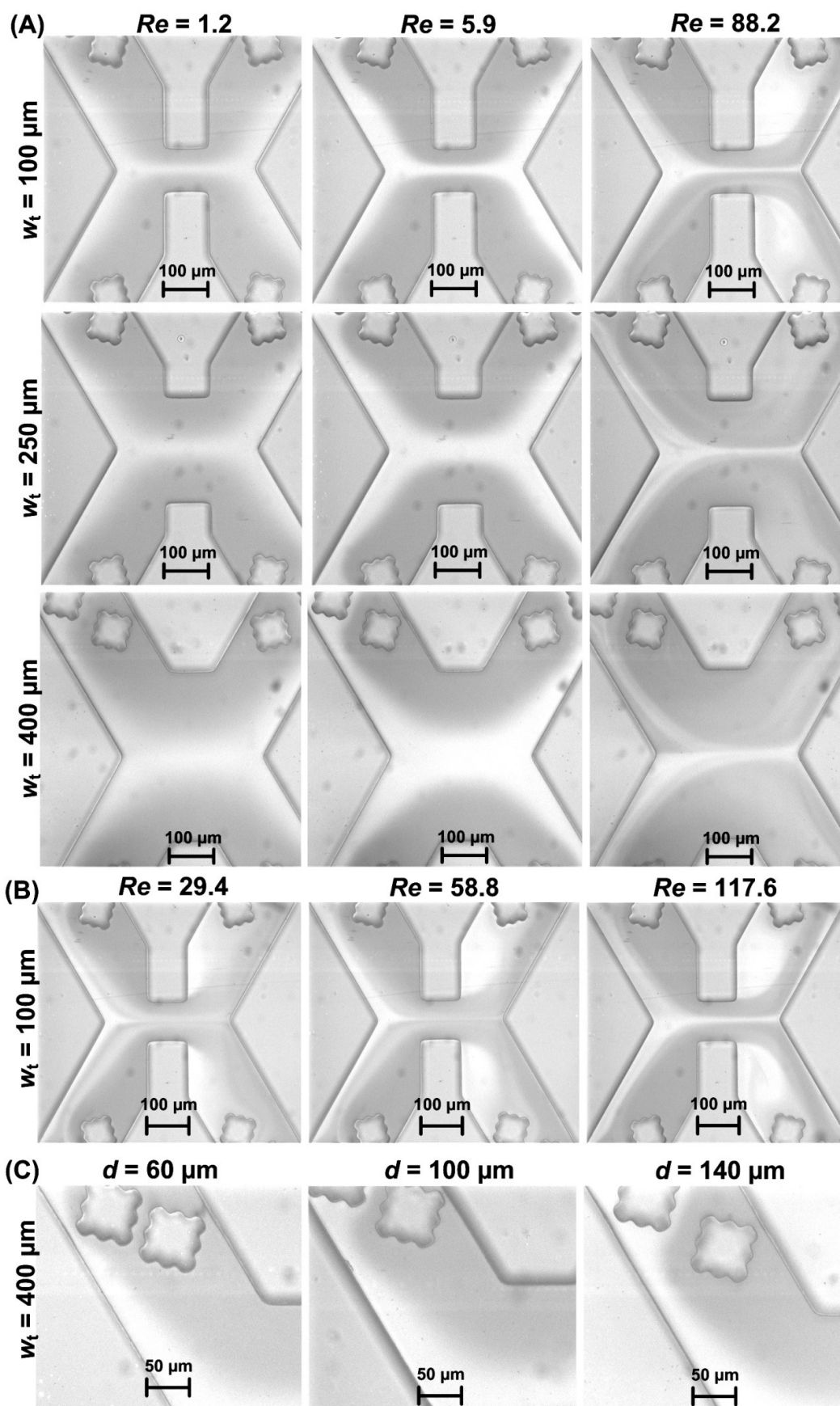


Fig. 6.2. Optical microscopy images taken at the first contraction for various flow conditions. (A) Influence of the contraction width ( $w_t$ ) on fluid mixing at  $Re = 1.2$ ;  $Re = 5.9$  and  $Re = 88.2$ , in mixers with inter-obstacles distance  $d = 140 \mu\text{m}$ . At lower  $w_t$  and higher  $Re$ , strong acceleration and subsequent deceleration of flows leads to formation of vortices. (B) Comparison of vortices generated at  $Re = 28.4$ ;  $Re = 58.8$  and  $Re = 117.6$  in mixer with  $w_t = 100 \mu\text{m}$ . (C) Influence of the inter-obstacles distance ( $d$  varying from  $60 \mu\text{m}$  to  $140 \mu\text{m}$ ) for micromixers with  $w_t = 400 \mu\text{m}$  at  $Re = 5.9$ . For  $d = 60 \mu\text{m}$ , the fluids flow mainly next to the channel walls due to low inter-obstacles channel width.

The effect of  $d$  on mixing at  $Re = 5.9$  in mixers with  $w_t = 400 \mu\text{m}$  is visualized in Fig. 6.2C. The images indicate that for the mixer with  $d = 60 \mu\text{m}$ , water flows mainly next to the channel walls due to small inter-obstacles channel width (i.e.  $20 \mu\text{m}$ ; equal to the distance obstacle-channel wall). For  $d$  above  $100 \mu\text{m}$ , the inter-obstacles channel width is much larger enabling water to flow in between the obstacles, splitting and recombining the streams with dyed water.

Fig. 6.3 presents the mixing efficiency ( $M$ ) of chips of various configurations. In all cases, the dependence between  $M$  and  $Re$  shows a minimum at  $Re = 5.9$ . Below this value, the lower the  $Re$  the longer the residence time and the better the mixing by pure diffusion (Bhagat et al. 2007) (see Fig. 6.2A for comparison of mixing state at  $Re = 1.2$  and  $Re = 5.9$ ). Above  $Re = 5.9$ , the mixing efficiency increases with  $Re$  due to the stronger fluid agitation and higher advection. The chip with  $w_t = 400 \mu\text{m}$  and  $d = 100 \mu\text{m}$  shows non-consistent mixing efficiency results, possibly due to fabrication or mixing measurement issues, thus this chip was not taken into account when conducting data analysis.

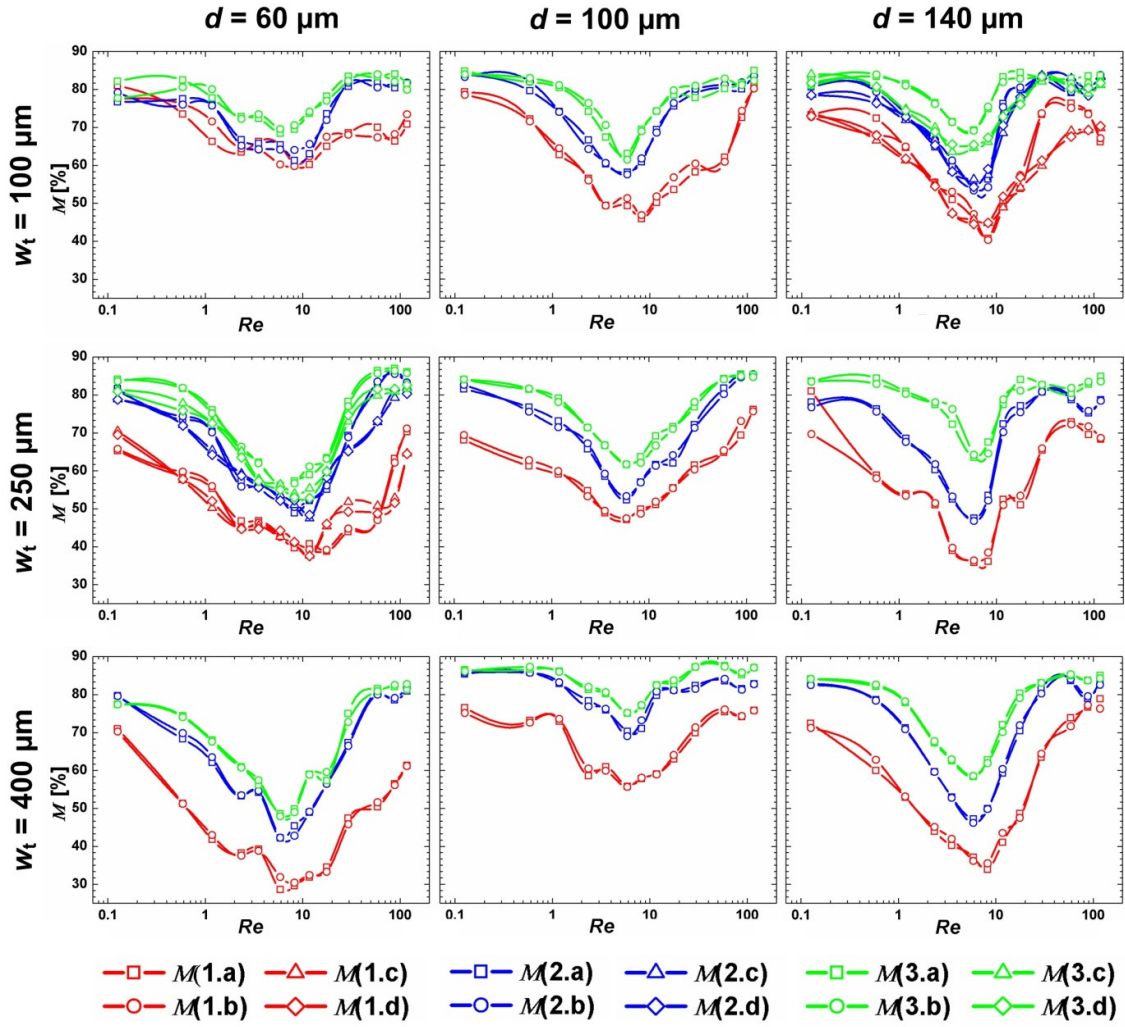


Fig. 6.3. Experimental mixing efficiency ( $M$ ; given in %) of mixers with various configurations at the middle of the first contraction ( $M(1)$ ; red line), second contraction ( $M(2)$ ; blue line) and third contraction ( $M(3)$ ; green line). Data points labelled  $a$  and  $b$  were determined from two different images taken from the first chip, while data points labelled  $c$  and  $d$  were determined from two different images taken from the second chip. Connecting lines are for eye guidance only.

In order to better understand the mixing mechanism and the role of  $d$ ,  $w_t$  and number of rhombi, an efficient mathematical methodology based on statistical techniques was applied for the analysis of the large amount of data displayed in Fig. 6.3 (see section 3.4).

### 6.3.3. Pressure drop

Firstly, the experimental protocol of the pressure drop ( $dP$ ) measurements was validated by estimating the viscosity of water computed from the pressure drop measured at 28  $^{\circ}\text{C}$  for different flow rates,

using the mixer that should develop larger pressures ( $w_t = 100 \text{ } \mu\text{m}$ ;  $d = 60 \text{ } \mu\text{m}$ ). This is needed to better match the pressure range that can be measured with the differential pressure transducer. The complex geometry of the developed mixer was simplified into a rectangular channel with length  $l$ , height  $h$  and width  $w$ . The wall shear stress ( $\tau$ ) was computed from  $dP$  using the following equation:

$$\tau = \frac{hdP}{2l\left(1+\frac{h}{w}\right)} \quad \text{eq. (6.5)}$$

where,  $l$  is the distance between the two pressure taps ( $l = 6800 \text{ } \mu\text{m}$ ) and  $h$  is  $120 \text{ } \mu\text{m}$  (as determined by stylus profilometry and optical microscopy).

The apparent shear rate ( $\dot{\gamma}_{app}$ ) was computed from the measured volumetric flow  $Q$  using the following equation (Newtonian flow):

$$\dot{\gamma}_{app} = \frac{6Q}{wh^2} \quad \text{eq. (6.6)}$$

The inset in Fig. 6.4A shows the log-log plot of the apparent shear rate as a function of the stress. A power law fitting to the data gives an exponent  $1.08 \pm 0.07$ , which indicates a Newtonian behavior (Balmforth et al. 2001), confirming that no additional stress build up occurs in the micromixer in spite of the presence of converging and diverging flows. Similar conclusions were reached from  $dP$  measurements of water passing in a micron-sized contraction (Rodd et al. 2005). Thus, the approximation of the complex microchannel to a rectangular channel as proposed by equation 5 does not bring any error to the  $dP$  for the range of flow rates studied here. Accordingly, the stress computed in eq. (5) is error free as long as a correct effective channel width  $w$  is used (see below). The true shear rate ( $\dot{\gamma}$ ) is obtained by correcting the apparent shear rate using the following equation:

$$\dot{\gamma} = \frac{\dot{\gamma}_{app}}{3} \left( 2 + \frac{d \ln \dot{\gamma}_{app}}{d \ln \tau} \right) \quad \text{eq. (6.7)}$$

The viscosity ( $\eta$ ) is then obtained from the Newton relationship:

$$\tau = \eta \dot{\gamma} \quad \text{eq. (6.8)}$$

Essentially, viscosity data shown in Fig. 6.4A for the larger shear rates matches the viscosity values measured in separate measurements at  $28 \text{ } ^\circ\text{C}$  with a stress-controlled rotational rheometer. At lower shear rates, the shear viscosity shows some scattering due to the limit of sensitivity of the differential pressure transducer. We note that viscosity matching is achieved when an effective channel width of  $w = 32 \text{ } \mu\text{m}$  is used in eq. 5 and 6. Thus, data in Fig. 6.4A indicate that the micromixer of dimensions  $w_t = 100 \text{ } \mu\text{m}$ ;  $d = 60 \text{ } \mu\text{m}$  can be used as a large shear rate rheometer for low viscosity liquids, since shear rates as large as  $2 \times 10^5 \text{ s}^{-1}$  can be achieved with no inertia instabilities, in contrast to conventional rotational rheometers.

Fig. 6.4B presents experimental  $dP$  results measured after three rhombi for all tested mixer configurations. Generally,  $dP$  increases linearly with  $Re$ , however for low  $Re$  (usually below 12), the



pressure drop values were very close to the detection limit of the pressure sensor. Below  $2.0 \times 10^3$  Pa,  $dP$  values are affected by the limit in pressure sensor sensitivity. Thus, a linear regression (intercept 0) of the  $dP$  data points measured at larger  $Re$  was used to extrapolate the  $dP$  for lower  $Re$ .

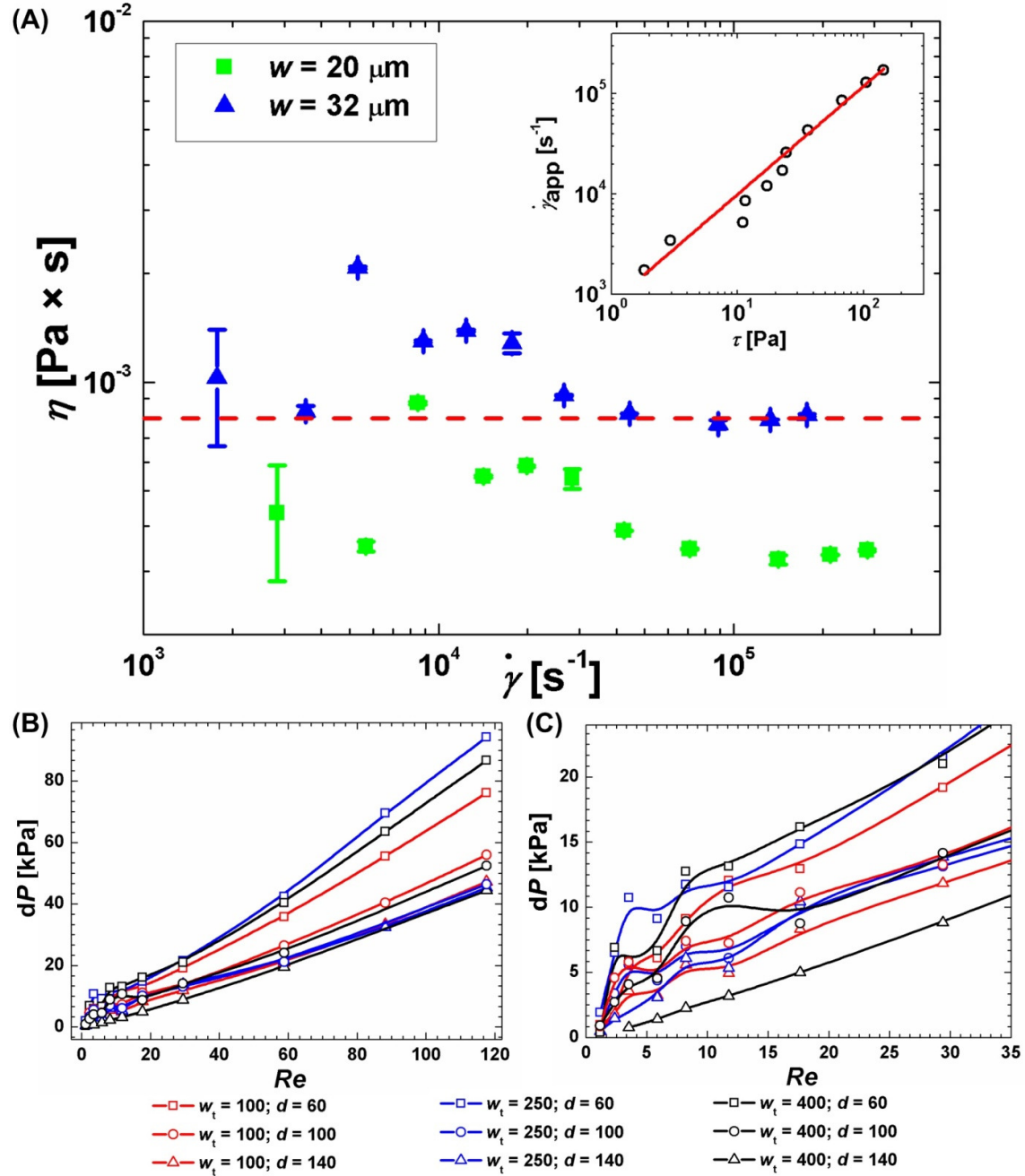


Fig. 6.4(A) Shear rate dependence of the shear viscosity computed from the pressure drop ( $dP$ ) and the volumetric flow rate ( $Q$ ) measured with chip of  $w_t = 100$   $\mu$ m;  $d = 60$   $\mu$ m for two values of the effective channel width ( $w$ ): 20  $\mu$ m (squares) and 32  $\mu$ m (triangles). The red dashed horizontal line indicates the viscosity ( $8 \times 10^{-3}$  Pa  $\times$  s) of water at 28  $^{\circ}$ C measured with a rotational rheometer. Inset:



stress dependence of the apparent shear rate. The red line is a linear fit to the data with slope of  $1.08 \pm 0.07$  indicating a Newtonian behavior. (B) Experimental pressure drop ( $dP$ ) for micromixers of various configurations ( $w_t$  and  $d$  are given in  $\mu\text{m}$ ). (C) Zoom in on the low  $Re$  region. For low  $dP$  values (usually below 12), there is no linear dependence between  $dP$  and  $Re$  due to the detection limit of the pressure sensor.

#### 6.3.4. Statistical analysis of the results

As it can be seen in Fig. 6.3 and Fig. 6.4, a large amount of data has been generated in this study, therefore to evaluate influence of the geometric parameters on the device performance for various flow regimes, statistical data treatment was used for the analysis of the results. The  $Re$  space was divided in two regions that can be approximated reasonably well by two independent Response Surface Methodology (RSM) models: low  $Re$  regime (from 0.1 to 5.9) and high  $Re$  regime (from 5.9 to 117.6). The analysis was focused on  $Re = 0.1$ , which is representative of typical micro-flow conditions (Bhagat et al. 2007) and also  $Re = 117.6$  for higher throughput applications. The model is fitted using RSM in order to:

- screen for the most important factors influencing the mixing efficiencies and pressure drop.
- build a mathematical model for all responses under consideration.
- develop a procedure to identify the most desirable conditions for mixer performance.

Fitting model,  $\log_{10}(Re)$  was used for  $M$  results and  $Re$  for  $dP$  data. The  $Re$  space was divided in two regions that can be approximated reasonably well by two independent RSM models: low  $Re$  regime (from 0.1 to 5.9) and high  $Re$  regime (from 5.9 to 117.6). The regimes intentionally overlap with each other.

When considering all known mathematical models in which the response surface is continuous over the region being studied, the most suitable in this case seems to be a second-order (quadratic) ( $M(1)$ ;  $M(2)$ ;  $M(3)$  and  $dP$ ) model expressed in a canonical form:

$$Y_k = \sum_{i=1}^q \beta_i X_i + \sum_{i=1}^{q-1} \sum_{j=i+1}^q \beta_{ij} X_i X_j + \sum_{i=1}^q \beta_{ii} X_i^2 + \beta_0 \quad \text{eq. (6.9)}$$

This function connects each characteristic response ( $Y_k$ ) with defined  $q$  factors ( $X_i$ ) taking into account main effects ( $\beta_i$ ), 2<sup>nd</sup> order interactions ( $\beta_{ij}$ ), squared factors ( $\beta_{ii}$ ) and an intercept value ( $\beta_0$  for  $i = 0$ ).

Model improvement for each response was evaluated based on a summary of fit (*i.e.* the least square regression) parameters summarized in Table 6.2 .

The following parameters were considered:

$$R^2 = 1 - \frac{SS_{\text{residuals}}}{SS_{\text{total}}} \quad \text{eq. (6.10)}$$

$$R^2\text{-adj} = 1 - \frac{\frac{SS_{\text{residuals}}}{n-K}}{\frac{SS_{\text{total}}}{n-1}} \quad \text{eq. (6.11)}$$

where  $R^2$  is the coefficient of determination and  $R^2\text{-adj}$  is an adjusted coefficient of determination. An  $R^2$  parameter of 1 means that the prediction model represents actual data with no error, while the 0 value indicates that the prediction model serves no better than the overall response mean. The  $R^2\text{-adj}$  adapts the  $R^2$  and makes it more comparable within models with different number of parameters.

The experimental data points were sieved to eliminate those that do not follow the most pronounced trend, probably due to a gross error (see Table 6.2). About 5% of all  $M$  data points were eliminated in sieving, increasing the  $R^2$  and  $R^2\text{-adj}$  parameters in an average of 0.02. In the case of the  $dP$  analysis, the  $R^2$  and  $R^2\text{-adj}$  were very high (0.98), therefore no data points were eliminated.

Table 6.2. Summary of data sieving and corresponding model validation parameters based on least square regression.  $N$  is the number of observations.

regime	response	initial data			after data sieving			difference		
		$R^2$	$R^2\text{-adj}$	$N$	$R^2$	$R^2\text{-adj}$	$N$	$R^2$	$R^2\text{-adj}$	$N$ [%]
low $Re$	$M(1)$	0.93	0.93	120	0.96	0.95	113	0.03	0.02	6
	$M(2)$	0.96	0.95	120	0.96	0.96	118	0	0.01	2
	$M(3)$	0.93	0.92	120	0.96	0.95	112	0.03	0.03	7
	$dP$	0.98	0.98	120	data sieving not needed					
high $Re$	$M(1)$	0.87	0.87	160	0.91	0.90	149	0.04	0.03	7
	$M(2)$	0.89	0.88	160	0.91	0.91	152	0.02	0.03	5
	$M(3)$	0.89	0.89	160	0.91	0.91	156	0.02	0.02	3
	$dP$	0.98	0.98	156	data sieving not needed					

The second-order polynomial responses modelling (quadratic) offered by the RSM appeared to be sufficient for all responses under consideration due to the ability to supply a high coefficient of determination, i.e.  $R^2 = (0.96, 0.96, 0.96, 0.98)$  and  $R^2 = (0.91, 0.91, 0.91, 0.98)$  for  $M(1)$ ,  $M(2)$ ,  $M(3)$  and  $dP$  in low  $Re$  and high  $Re$  regime, respectively. Such high values of  $R^2$ , especially in a low  $Re$  regime, indicate good correspondence between the model prediction (fitting) and the experiments, while simultaneously minimizing the overall number of coefficients.

The model for each response was validated basing on analysis of  $F$ -ratio statistics ( $F$ -ratio) and the ANOVA probability ( $\text{Prob} > F$ ). The larger  $F$ -ratio value, the greater the likelihood that the

differences between the means are due to something other than chance alone ( $F$ -ratio  $> 1$ ). The  $\text{Prob} > F$  value is a probability of obtaining a  $F$ -ratio greater than 1 calculated if there is no difference in the population group means. Values smaller than 0.05 are considered evidence that the predicted model is statistically better than the overall response mean. The ANOVA significance probabilities ( $\text{Prob} > F$ ) for fitted models are lower than 0.0001 supporting the fitting accuracy. The obtained  $F$ -ratio values are much higher than 1 ( $F$  above 150) indicating that the models for all responses are much better than the overall response means. The  $F$ -ratio values for  $M(1)$ ,  $M(2)$  and  $M(3)$  are almost two times higher at low  $Re$  ( $F$ -ratio of 260; 296 and 258, respectively) than at high  $Re$  regime ( $F$ -ratio of 152; 166 and 168, respectively). Conversely, the  $F$ -ratio calculated for  $dP$  is significantly higher for high  $Re$  regime ( $F$ -ratio of 906) due to the lower accuracy of measurements of  $dP$  for low  $Re$  ( $F$ -ratio of 667, note that at low  $Re$ ,  $dP$  was obtained from linear extrapolation of data measured at larger  $Re$ , due to detector noise; see section 6.3.3). A higher order non-linear dependence was not detected for any of the responses under consideration. Therefore, a more-complex model is not required, and the lack of fit comes from difficulties associated with accurate measurements of those responses (i.e. method limitations).

Fig. 6.5 presents the results of mathematical fitting to the experimental data points of mixing efficiency (Fig. 6.5A–C) and pressure drop (Fig. 6.5D) for  $Re = 0.1$  and  $Re = 117.6$ . The mixing efficiency of 80% can be considered as full mixing (SadAbadi et al. 2013; Tran-Minh et al. 2013).

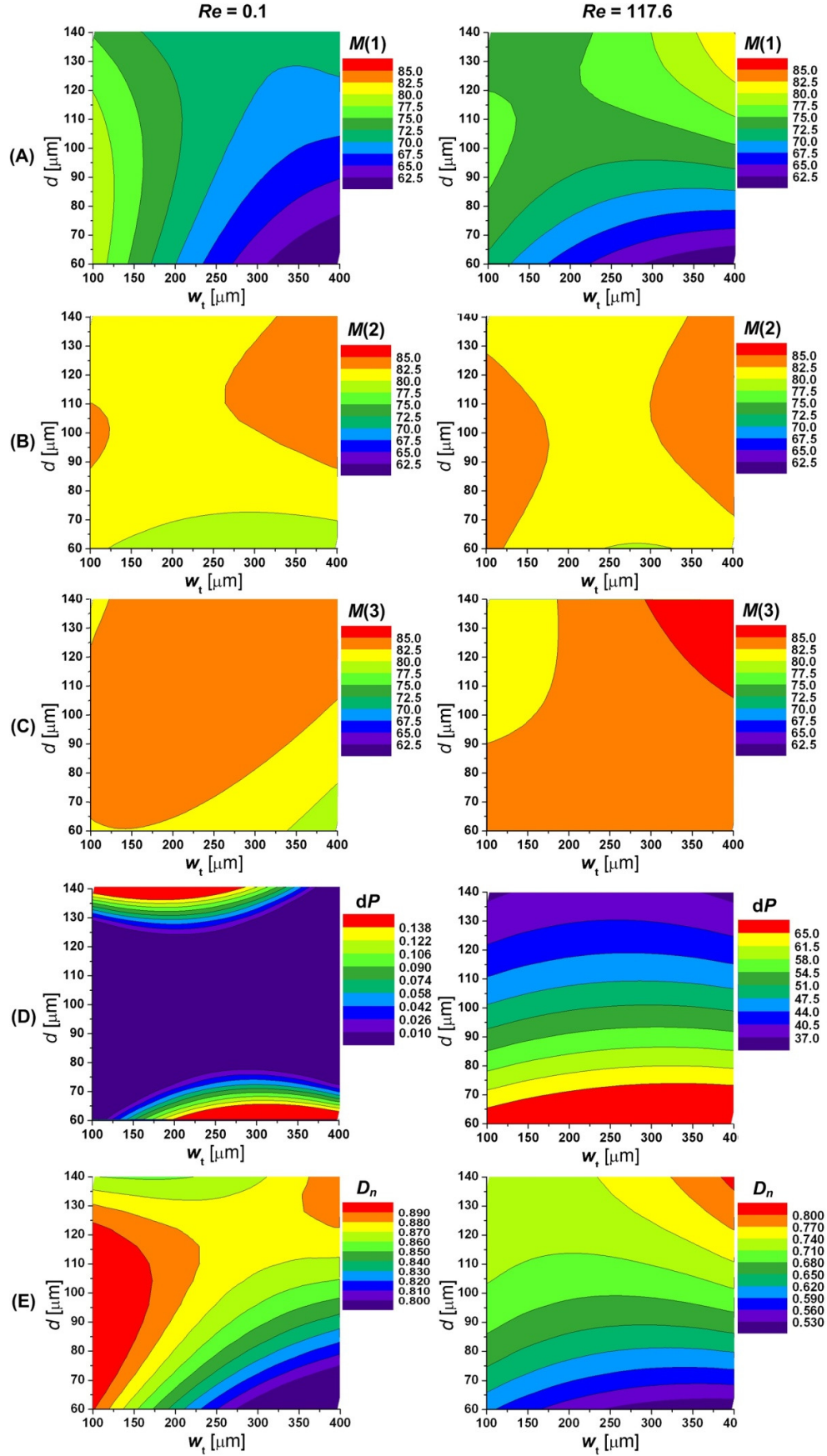


Fig. 6.5. Results obtained from mathematical fitting to the experimental data points (A) of mixing efficiency (given in %) measured at the middle of the first contraction ( $M(1)$ ); (B) at the second contraction ( $M(2)$ ); (C) at the third contraction ( $M(3)$ ) and (D) of pressure drop ( $dP$ ; given in kPa) measured after three rhombi. (E) Desirability results ( $D_n$ ) defined as maximum values of  $M(1)$ ;  $M(2)$  and  $M(3)$  and minimum of  $dP$ .

The results indicate that the number of rhombi has the strongest effect on the mixing index: generally,  $M$  increases with the number of rhombi, even if after the second rhombus the increase is much lower. After the first rhombus (mixer length: 0.9 mm), the mixing efficiency is below 80%, indicating that the fluids are not sufficiently mixed and that additional rhombi are needed (in fact, in the first rhombus the fluids are in contact only in a half of the rhomb, as the other half acts as inlet channel; see Fig. 6.1A). After the second rhombus (mixer length: 2.5 mm), the mixing efficiency is above 80% for all tested configurations. The third rhombus (mixer length: 4.1 mm) would further improve mixing (up to 85% for  $Re = 117.6$ ), however at the cost of a much longer channel (1.6 mm longer; i.e. 64% longer in the case of two rhombi mixer). Therefore a two rhombi mixer seems to give the best compromise between mixing efficiency and channel length.

At the first contraction, the mixing efficiency varies between 62.5% and 77.5% for the two analysed  $Re$ . At  $Re = 0.1$ ,  $M(1)$  is affected mainly by  $w_t$ : generally, smaller  $w_t$  gives better mixing, probably due to increased local Reynolds numbers and better contraction-expansion of stream lines.  $d$  is less significant for  $M(1)$  at  $Re = 0.1$ , as the obstacles have usually major effect on mixing for fast flows.  $d$  starts playing a more significant role for  $w_t$  above 250  $\mu\text{m}$ , where higher  $d$  values yield higher  $M(1)$ . In fact, the images shown in Fig. 6.2C indicate that in case of  $d = 60 \mu\text{m}$ , the hydraulic resistance between obstacles is too high, so the flow develops mainly close to the channel walls. Summarizing, at  $Re = 0.1$  the highest  $M(1)$  values are obtained for low  $w_t$  and low  $d$ , while the lowest  $M(1)$  occurs for high  $w_t$  and low  $d$ . At  $Re = 117.6$ , the lowest  $M(1)$  is also obtained for regions of high  $w_t$  and low  $d$ , whereas the highest  $M(1)$  is observed for high  $w_t$  and  $d$ .

For the same two  $Re$  values,  $M(2)$  and  $M(3)$  vary from 77.5 to 82.5%, therefore this variation range is very close to the range of uncertainty of the  $M$  determination ( $\pm 6.6\%$ ). Most probably, at the second and third contractions, all tested mixer configurations have yielded good mixing and the mixing efficiency saturates. In order to evaluate the effect of geometrical factors on  $M(2)$  and  $M(3)$ , a mixing analysis method of lower uncertainty of the  $M$  determination should be used, e.g. based on a fluorescent dye.

In Fig. 6.5A–C, the effect of the generation of vortices on the mixing state is not visible, as  $M(1)$  is measured in the middle of the first contraction (before the vortices are generated; see ), whereas for  $M(2)$  and  $M(3)$  the range of mixing efficiency variation is very close to the  $M$  uncertainty range. Thus,

to measure the effect of the vortices on the mixing state, the mixing efficiency should be measured in more locations along the chip.

The  $dP$  results obtained from the mathematical fitting (Fig. 6.5D) reveal that for  $Re = 0.1$  and  $Re = 117.6$ ,  $dP$  is mainly influenced by the inter-obstacles distance and the effect of  $w_t$  is barely visible. At  $Re = 0.1$ ,  $dP$  values are comparable with the values reported in literature (see Table 6.1): it varies from 10 to 138 Pa. The smallest  $dP$  are obtained for  $d$  between 77 and 125  $\mu\text{m}$ ; then, the  $dP$  values gradually increase for  $d$  values below and above this range. At  $Re = 117.6$ ,  $dP$  is much higher than at  $Re = 0.1$ : between  $4.6 \times 10^4$  Pa and  $8.6 \times 10^4$  Pa. As expected, the closer the obstacles, the higher  $dP$ . It should be noted that  $dP$  was measured for mixers with three rhombi (length: 4.1 mm), while our results indicate that two rhombi mixers (length: 2.5 mm) are sufficient to obtain satisfactory mixing for Newtonian fluids.

The tests of significance of all effects (i.e. factors and interactions) on mixing efficiencies and pressure drop were quantitatively performed using Student's  $t$ -test statistics. In general, the model predicts that mixing depends on  $Re$ , irrespectively of its value. However, only for  $M(1)$  this dependence seems to have a linear character. When considering geometrical factors,  $w_t$  affects mixing the most, while  $d$  seems to have a lower but still meaningful effect on the measured responses. Among all factors,  $Re$  was found to influence  $dP$  the most. This dependence seems to have a linear character. When considering geometrical factors,  $d$  nonlinearly affects  $dP$  significantly, while the role of  $w_t$  is negligible. The pattern of significance of all factors under consideration is similar for both  $Re$  regimes (i.e. significance pattern at low  $Re$  is a subset of the significance pattern at high  $Re$ ).

Response surface maps of experimental regions presented in Fig. 6.5 facilitate the decision-making process of determining the most appropriate geometry. However, a numerical multi-response optimization enables to find the specific point that maximizes the global desirability, and thus, the optimal performance of the mixer (Derringer and Suich 1980). The desirability (i.e. optimization goal,  $D_n$ ) was defined as maximum values of  $M(1)$ ;  $M(2)$  and  $M(3)$  and minimum of  $dP$ . The contour plots of  $D_n$  at low and high  $Re$  regimes are presented in Fig. 6.5. The resulting optimum geometry determined from desirability profiles is described by:  $w_t = 101 \mu\text{m}$ ,  $d = 93 \mu\text{m}$  at low  $Re$  regime and  $w_t = 400 \mu\text{m}$ ,  $d = 121 \mu\text{m}$  at high  $Re$  regime.

Above robust optimization deals with an optimization problem in which the set of feasible solutions are precisely provided for low and high  $Re$  regimes. However, as the factors may be uncertain, it is more practical to provide a feasible range of factors in which desirability is reasonably close to the optimal value. The desirability function for low  $Re$  exhibits a broad peak at low  $w_t$  values and low / medium  $d$  values. Therefore, it can be assumed that the uncertainty at the level of 10% in  $w_t$  and  $d$  will still result in robust solution (-1.1% change in  $D_n$ ). When considering high  $Re$  regime, the peak in

desirability function is much narrower. The uncertainty at the level of 5% in  $w_t$  and  $d$  results in -3.7% change in  $D_n$ .

## 6.4. Conclusions

To compare the developed micromixer with the state of the art passive planar micromixers reported in Table 6.1, the mixer length was evaluated, as all the reported mixers give  $M \geq 80\%$  which can be considered as a full mixing (SadAbadi et al. 2013; Tran-Minh et al. 2013). The developed mixer enables efficient fluid mixing for low ( $Re = 0.1$ ) and high  $Re$  ( $Re = 117.6$ ) using a channel much shorter (2.5 mm) than in majority of planar passive micromixer; only (Shih and Chung 2008) have reported a mixer of comparable length (see Table 6.1). The combination of rhombic channel geometry, diamond-shaped obstacles and rectangular contraction placed after each rhombus has enabled to significantly reduce the mixing length:  $\sim 4 \times$  lower than the rectangular mixer with diamond-shaped obstacles (mixing length: 11.0 mm) (Bhagat et al. 2007) and  $\sim 3 \times$  lower than the rhombic (angle  $60^\circ$ ) with a converging-diverging element placed after three-rhombi channel (mixing length: 6.8 mm) (Chung et al. 2008a).

To find a compromise, a mixer design should be optimized to obtain high mixing efficiency with pressure drop as low as possible. As such, in this work the statistical analysis was used to determine mixer configuration that gives the best compromise between those responses. The resulting optimum geometry is  $w_t = 101 \mu\text{m}$ ,  $d = 93 \mu\text{m}$  at low  $Re$  regime and  $w_t = 400 \mu\text{m}$ ,  $d = 121 \mu\text{m}$  at high  $Re$  regime. For low  $Re$  flows, the pressure drop is low enough (6.0 Pa) for the application in lab-on-chip devices, while for high  $Re$  the mixer imposed relatively large pressure drop ( $5.1 \times 10^4$  Pa). Although, the PDMS chips sealed to glass by oxygen plasma treatment can handle pressures up to  $3.4 \times 10^5$  Pa (McDonald et al. 2000), i.e.  $\sim 7$  times higher than the developed mixer requires at  $Re = 117.6$ , a lower pressure drop would be beneficial for the overall device performance and for integration of the mixer with other microfluidic components. Therefore, the developed device enables efficient mixing with low pressure drop within a very short channel at low  $Re$ , making it suitable for applications where several tasks of complex analysis are needed.

Besides, results presented in this paper show that the use of statistical methods can improve significantly the data analysis enabling determination of the most important factors influencing the mixing efficiencies and pressure drop, building a mathematical model for all responses under consideration and identification of the most desirable conditions for mixer performance. Providing details of the statistical analysis, we aim to make this efficient mathematical strategy more available to a broader community.

In many microfluidics applications (e.g. inkjet printing; biological analysis), aqueous fluids containing low concentrations of high molecular weight polymers are used (Rodd et al. 2005). Therefore in future work, effect of viscoelasticity on the mixer performance will be studied.



## **Chapter 7**

### General conclusions



<b>Chapter 7. General conclusions .....</b>	<b>177</b>
<b>Summary.....</b>	<b>177</b>
<b>7.1. Conclusions.....</b>	<b>177</b>
<b>7.2. Future work.....</b>	<b>179</b>
7.2.1. Integration of microfluidic waveguides to facilitate the chip exchange .....	179
7.2.2. Integration of the optical detection chip with the micromixer.....	180
7.2.3. Miniaturization of further laboratory tasks towards “bleed and read” device .....	180



## Chapter 7. General conclusions

### Summary

This chapter provides discussion on the results described in this PhD thesis in more general aspect and an analysis of their significance. Future perspectives for further development of this research area are also described.

### 7.1. Conclusions

The work described in this PhD thesis has enabled to significantly improve the colorimetric DNA biosensor based on non-cross-linking hybridization of Au-nanoprobes.

Table 7.1 presents the comparison between the previous state-of-the-art (Silva et al. 2011) and the final prototype developed in this PhD work, and also the evolution of the biosensor along this PhD work. To enable performance comparison, the colorimetric discrimination results ( $\Delta R_s$ ; i.e. the difference between the detection responses for dispersed and aggregated solutions) have been normalized to the detection response for the dispersed solution (eq. 7.1)

$$\Delta R_s(\text{normalized}) = \frac{R_s(\text{dispersed}) - R_s(\text{aggregated})}{R_s(\text{dispersed})} \quad \text{eq. (7.1)}$$

Due to the fact that in these tests different Au-nanoprobes were used yielding variations in the resulting solution colour, the colorimetric discrimination result are based on the analysis of non-functionalised AuNPs,

The biosensor with the inkjet printed photodetector shows 35% lower colorimetric AuNPs discrimination than the silicon counterpart. It is probably related with its lower photosensitivity and also with the fact that in this device, only one colour light source was used, while the two colour analysis enhance strongly the colorimetric discrimination. The main advantage of the biosensor incorporating inkjet printed TiO<sub>2</sub> photodetector is about 10 times cost reduction.

The incorporation of microfluidic technology and fibre optics has enabled to reduce significantly the volume of the solution: the developed microfluidic prototypes need only 5% of the solution volume that was needed for the macroscale biosensors (3  $\mu$ l vs 60  $\mu$ l). The first model of the bio-microfluidic platform is much less sensitive to the AuNPs colorimetric changes (78% lower value of the normalized colorimetric discrimination), probably due to a shorter optical path length, beam divergence and low electrical signal generated by the photodiode (in nanoampere range). Then, the platform has been optimized in terms of (i) the electrical signal processing to increase the output reliability and reduce noise and (ii) the light propagation by incorporation of microlenses. These modifications enabled to improve significantly the results of the AuNPs colorimetric analysis. The final microfluidic prototype shows 52% lower colorimetric discrimination when comparing to the

macroscale biosensor incorporating a silicon photodetector. The lower response of the microfluidic platform is probably related with the use of 80% shorted optical path that directly affects the sensitivity of the absorbance-based measurements. However, the optimized platform could clearly detect the colorimetric changes in the Au-nanoprobe assay for single base mismatch using only 3  $\mu\text{l}$  of solution. Furthermore, the use of bio-microfluidic platform enabled to reduce the limit of the detection of the method attained with a conventional microplate reader: the microplate could only give a discriminatory response at concentrations equal or higher than 20  $\text{ng}/\mu\text{l}$ , while the microfluidic platform begins to discriminate at 15  $\text{ng}/\mu\text{l}$ .

Table 7.1. Comparison of the biosensor performance along the optimization process. The normalized colorimetric discrimination, i.e.  $\Delta R_s(\text{normalized})$ , was defined as the AuNPs colorimetric discrimination (the difference between the detection response for dispersed AuNPs and aggregated AuNPs solutions) normalized to the detection response for the dispersed AuNPs (see eq. 7.1).

	<b>solution volume [<math>\mu\text{l}</math>]</b>	<b>colorimetric discrimination (normalized)</b>	<b>light source</b>	<b>target DNA</b>	<b>novelty vs (Silva et al. 2011)</b>
<b>previous state-of-the-art (Silva et al. 2011)</b>	60	0.54	RGBA LED	<i>M. tuberculosis</i> specific sequence	
<b>inkjet printed photodetector (chapter 3)</b>	60	0.35	green LED	<i>M. tuberculosis</i> specific sequence	use of $\text{TiO}_2$ photodetector patterned by a new cost-effective method—inkjet printing
<b>bio-microfluidic platform development (chapter 4)</b>	3	0.12	green and red fibre coupled LEDs	<i>M. tuberculosis</i> specific sequence	incorporation of microfluidics (20 $\times$ lower reagent use, integrated)
<b>optimized platform with microlenses (chapter 5)</b>	3	0.26	green and red fibre coupled LEDs	obesity related <i>FTO</i> single base mismatch	circuit optimization and use of microlenses (single base mismatch sensitivity)

As it can be seen in Table 7.1, the combination of the unique optical properties of gold nanoprobes with microfluidic platform resulted in sensitive and accurate sensor for single nucleotide polymorphism detection operating using small volumes of solutions and low target DNA concentrations. The detection of single nucleotide mismatches is of high importance, as they consist majority of all detected genetic changes (Weber et al. 2002) and are associated with several multifactorial diseases, such as cancer, diabetes, and to the individual response to therapeutics (Bell

2004). The thoroughly described here optimization of the microfluidic platform (concerning electrical signal processing; design, fabrication and performance of various microlenses) has significantly improved the results of AuNPs colorimetric analysis and can also be applied to other absorbance-based microfluidic devices as a simple and cheap mean to compensate for reduction of optical path length.

Furthermore, the integration of microfluidic technology opens up the possibility of further integration aiming to provide a POC “bleed and read” device. The developed micromixer consist a next “puzzle” towards reaching that goal, whereas the suggestions for the further developments are described below.

## **7.2. Future work**

To meet the POC use requirements, the developed biosensor needs further optimization. In author’s opinion, the following developments should be performed:

### **7.2.1. Integration of microfluidic waveguides to facilitate the chip exchange**

In the developed configuration, the optical fibres are used to guide the light from the light source to the detection channel and afterwards to the photodetector, however the use of the optical fibre require careful insertion of fragile fibres and their proper alignment with the PDMS wall to reduce optical losses. To facilitate chip exchange, microfluidic waveguides should be incorporated. The microfluidic chip with waveguides would be disposed after each test, to avoid cross-contaminations, while LEDs, photodetector and electronics would consist a non-disposable host device. The interface between chip and the host device has to be properly designed to enable self-alignment of the waveguides with LEDs and photodetector that would be independent from the operator, e.g. using a pitch-holes system. The design should enable sufficient alignment tolerances.

There are various strategies for microfluidic waveguide development (Baig et al. 2013; Missinne et al. 2014; Ram and Lee 2009). The approach based on a capillary filling technique (Fig. 7.1) seems to be the most appropriate for the implementation in the developed platform as it would require only minor mask modifications and simple additional fabrication steps (Missinne et al. 2014). To obtain the refractive index contrast between cladding and core, two different types of PDMS could be used, e.g. Sylgard 184 (Dow Corning,  $n = 1.41$ ) as cladding material and LS-6257 (Nusil,  $n = 1.57$ ) as core material. The channels patterned in the cladding material can be capillary filled with the core material pre-polymer that is cured afterwards, forming solid state, stretchable waveguides of numerical aperture of 0.69 (Missinne et al. 2014). In this configuration, PDMS Sylgard 184 should be used as the substrate material to provide bottom cladding.

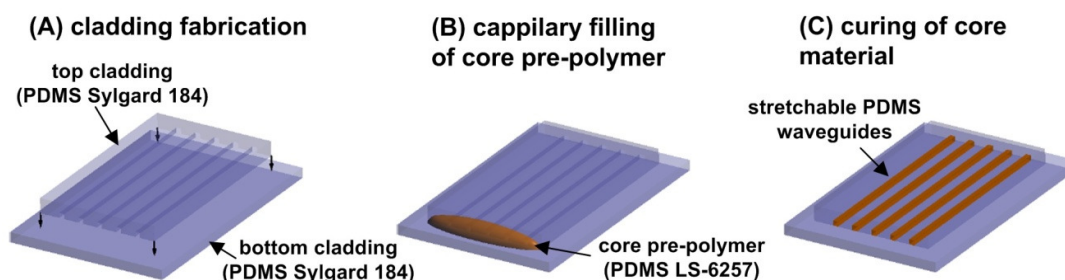


Fig. 7.1. Schematic representation of fabrication of the PDMS waveguides based on a capillary filling technique. The channels patterned in the cladding material can be capillary filled with the core material pre-polymer that is cured afterwards, forming solid state, stretchable waveguides. Adapted from (Missinne et al. 2014).

These waveguides have higher numerical aperture than the optical fibres used in this work (0.275), therefore the resulting beam divergence angle is much higher (31 degrees instead of 11 degrees). Thus, the incorporation of the developed lenses will be crucial in this configuration.

### 7.2.2. Integration of the optical detection chip with the micromixer

During this PhD work, two units of the device have been developed and optimized. In the next step, the chips of the best performance, i.e. the optical chip of 2 mm long optical path with air microlenses and micromixer with 2 rhombi, should be integrated enabling (i) mixing of the DNA solutions (Au-nanoprobe and target DNA) with salt to induce the aggregation process and afterwards (ii) optical analysis to determine the colour of the resulting solution. Long exposure time images should be acquired to visualize the aggregation process along the micromixer.

### 7.2.3. Miniaturization of further laboratory tasks towards “bleed and read” device

Towards a POC “bleed and read” device, further laboratory task should be performed on chip: (i) sample preparation to extract target DNA from blood sample; (ii) DNA amplification (subject of ongoing BSc. project); (iii) hybridisation reactions of target DNA with the Au-nanoprobes and (iv) mixing of the involved solutions. Eventually, simultaneous parallel control tests should be performed with positive, negative and blank solutions, to increase the results reliability. Fig. 7.2 presents a layout proposal of a lab-on-chip device for colorimetric DNA detection starting from unamplified target DNA and Au-nanoprobes.



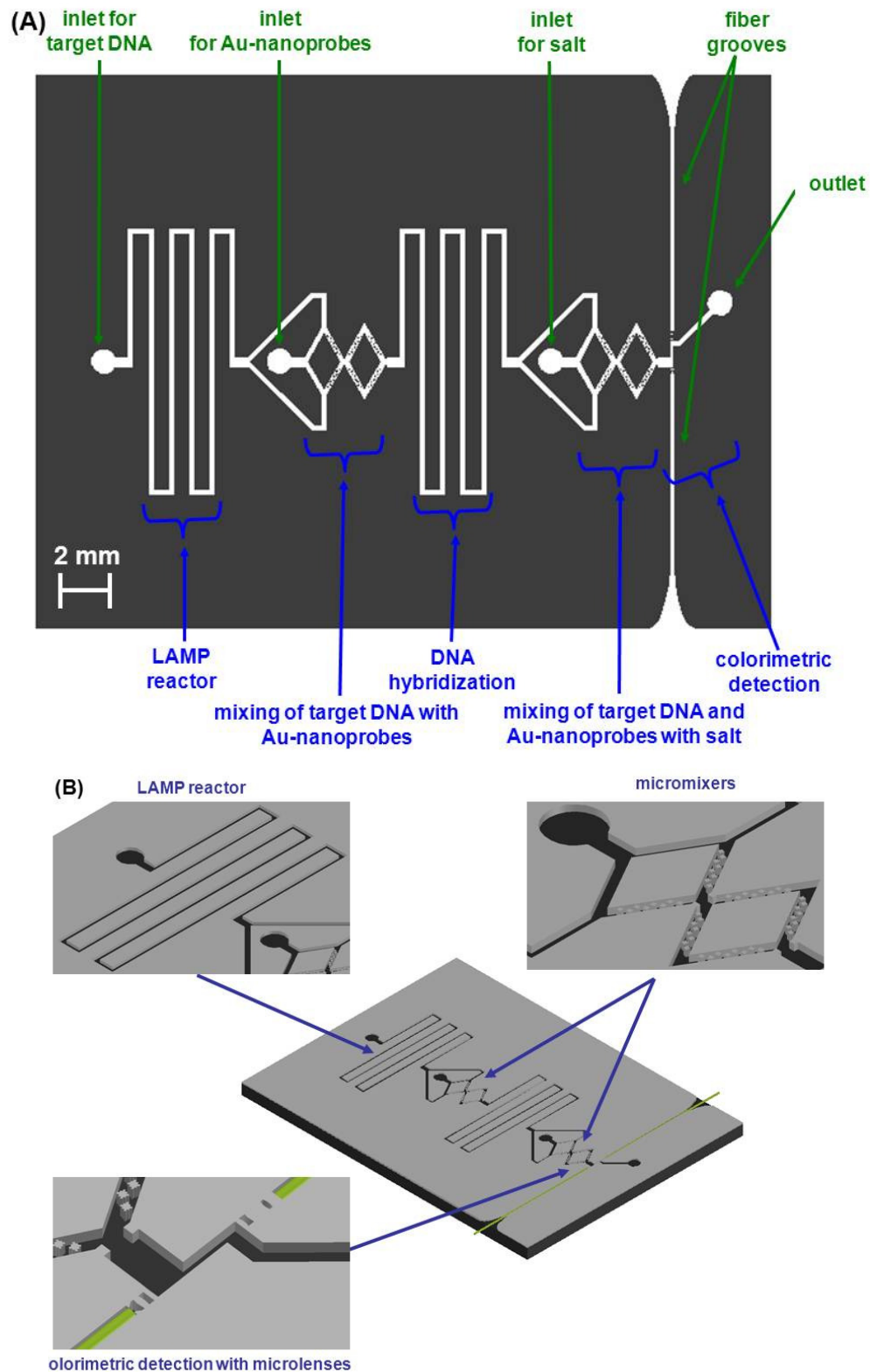


Fig. 7.2. Layout proposal of a lab-on-chip device for colorimetric DNA detection starting from unamplified target DNA and Au-nanoprobes: (A) top view; (B) three-dimensional representation.

As a final conclusion, the author believes that the work described in this PhD thesis will contribute significantly to the development of a low cost, fully integrated POC device for genetic analysis based on Au-nanoprobes.

## Appendix 1. SU-8 run sheet for 125 $\mu\text{m}$ thick layer

series ..... done on ..... by ..... (ambient temp. = .....  $^{\circ}\text{C}$ , humidity = .....%)

	sample .....A	sample .....B	sample .....C
<b>wafer preparation</b>	Si monitor wafers, 4in., baking 10 min @ 180 $^{\circ}\text{C}$ , cool down $\geq 10\text{min}$		
<b>aimed thickness [<math>\mu\text{m}</math>]</b>	110–125 in center	110–125 in center	110–125 in center
<b>spin coat</b>	SU-8 2050 500rpm/7s/100rpm/s, then ..... rpm/30s/300rpm/s. Most promising speed at 21 $^{\circ}\text{C}$ = 1530 rpm		
	..... rpm	..... rpm	..... rpm
<b>relax [min]</b>			
<b>soft bake</b>	5 min @ 65 $^{\circ}\text{C}$ , then 24 min @ 95 $^{\circ}\text{C}$ , cooling $\geq 10$ min		
<b>exposure</b>	CP mode, though i-filter, soft exp., most promising exposure dose = 309 $\text{mJ}/\text{cm}^2$		
	..... s, ..... mW (..... $\text{mJ}/\text{cm}^2$ )	..... s, ..... mW (..... $\text{mJ}/\text{cm}^2$ )	..... s, ..... mW (..... $\text{mJ}/\text{cm}^2$ )
<b>post bake</b>	5 min @ 65 $^{\circ}\text{C}$ , then 11 min @ 95 $^{\circ}\text{C}$		
<b>development [min]</b>	18 min @ 500 rpm (features facing up)		
<b>rinsing</b>	10 s in clean developer, 10 s in isopropanol with strong manual agitation, gently dried with nitrogen		
<b>thickness by microscope (PDMS)</b>	at wafer center: ..... $\mu\text{m}$	at wafer center: ..... $\mu\text{m}$	at wafer center: ..... $\mu\text{m}$
	at r = 2.5 cm: ..... $\mu\text{m}$	at r = 2.5 cm: ..... $\mu\text{m}$	at r = 2.5 cm: ..... $\mu\text{m}$
<b>notes</b>			



## References

- Abgrall, P., Gue, A.-M., 2007. Lab-on-chip technologies: making a microfluidic network and coupling it into a complete microsystems-a review. *J. Micromech. Microeng.* 17(5), R15.
- Adams, M.L., Enzelberger, M., Quake, S., Scherer, A., 2003. Microfluidic integration on detector arrays for absorption and fluorescence micro-spectrometers. *Sens. Actuator A-Phys.* 104(1), 25-31.
- Aegerter, M., Mennig, M., Berni, A., Mennig, M., Schmidt, H., 2004. Doctor Blade. *Sol-Gel Technologies for Glass Producers and Users*, pp. 89-92. Springer US.
- Al-Mumen, H., Dong, L., Li, W., 2013. SU-8 doped and encapsulated n-type graphene nanomesh with high air stability. *Appl. Phys. Lett.* 103(23), 232113.
- Ansari, M.A., Kim, K.-Y., Anwar, K., Kim, S.M., 2010. A novel passive micromixer based on unbalanced splits and collisions of fluid streams. *J. Micromech. Microeng.* 20(5), 055007.
- Baig, S., Jiang, G., Sun, Q., Wang, M.R., 2013. Fabrication of single-mode channel polymer waveguides using vacuum assisted microfluidic soft lithography. *J. Europ. Opt. Soc. Rap. Public.* 8, 13076.
- Balmforth, N.J., Provenzale, A., Balmforth, N.J., Craster, R.V., 2001. Geophysical Aspects of Non-Newtonian Fluid Mechanics. *Geomorphological Fluid Mechanics*, pp. 34-51. Springer Berlin Heidelberg.
- Balslev, S., Jorgensen, A.M., Bilenberg, B., Mogensen, K.B., Snakenborg, D., Geschke, O., Kutter, J.P., Kristensen, A., 2006. Lab-on-a-chip with integrated optical transducers. *Lab Chip* 6(2), 213-217.
- Baptista, P., Doria, G., Henriques, D., Pereira, E., Franco, R., 2005. Colorimetric detection of eukaryotic gene expression with DNA-derivatized gold nanoparticles. *Journal of Biotechnology* 119(2), 111-117.
- Baptista, P., Pereira, E., Eaton, P., Doria, G., Miranda, A., Gomes, I., Quaresma, P., Franco, R., 2008. Gold nanoparticles for the development of clinical diagnosis methods. *Anal. Bioanal. Chem.* 391(3), 943-950.
- Baptista, P.V., 2012. Could gold nanoprobe be an important tool in cancer diagnostics? *Expert Rev. Mol. Diagn.* 12(6), 541-543.
- Baptista, P.V., Koziol-Montewka, M., Paluch-Oles, J., Doria, G., Franco, R., 2006. Gold-nanoparticle-probe-based assay for rapid and direct detection of *Mycobacterium tuberculosis* DNA in clinical samples. *Clinical Chemistry* 52(7), 1433-1434.
- Bashir, R., 2004. BioMEMS: state-of-the-art in detection, opportunities and prospects. *Adv. Drug Deliv. Rev.* 56(11), 1565-1586.
- Becker, H., Gärtner, C., 2008. Polymer microfabrication technologies for microfluidic systems. *Anal. Bioanal. Chem.* 390(1), 89-111.
- Becker, H., Locascio, L.E., 2002. Polymer microfluidic devices. *Talanta* 56(2), 267-287.
- Bell, J., 2004. Predicting disease using genomics. *Nat. Biotechnol.* 22(6), 453-456.
- Ben-Yoav, H., Dykstra, P.H., Bentley, W.E., Ghodssi, R., 2012. A microfluidic-based electrochemical biochip for label-free diffusion-restricted DNA hybridization analysis. *Biosens Bioelectron* 38(1), 114-120.
- Bernacka-Wojcik, I., Lopes, P., Catarina Vaz, A., Veigas, B., Wojcik, P.J., Simoes, P., Barata, D., Fortunato, E., Viana Baptista, P., Aguas, H., Martins, R., 2013. Bio-microfluidic platform for gold nanoprobe based DNA detection—application to *Mycobacterium tuberculosis*. *Biosensors and Bioelectronics* 48(0), 87-93.
- Bernacka-Wojcik, I., Senadeera, R., Wojcik, P.J., Silva, L.B., Doria, G., Baptista, P., Aguas, H., Fortunato, E., Martins, R., 2010. Inkjet printed and "doctor blade" TiO<sub>2</sub> photodetectors for DNA biosensors. *Biosensors and Bioelectronics*, pp. 1229-1234.
- Bhagat, A.A.S., Papautsky, I., 2008. Enhancing particle dispersion in a passive planar micromixer using rectangular obstacles. *J. Micromech. Microeng.* 18(8), 085005.
- Bhagat, A.A.S., Peterson, E.T.K., Papautsky, I., 2007. A passive planar micromixer with obstructions for mixing at low Reynolds numbers. *J. Micromech. Microeng.* 17(5), 1017.
- Bora, U., Sett, A., Singh, D., 2013. Nucleic Acid Based Biosensors for Clinical Applications. *Biosens J* 1(104).

Bruzewicz, D., Reches, M., Whitesides, G., 2008. Low-Cost Printing of Poly(dimethylsiloxane) Barriers To Define Microchannels in Paper. *Anal. Chem.* 80(9), 3387-3392.

Burghlelea, T., Segre, E., Bar-Joseph, I., Groisman, A., Steinberg, V., 2004. Chaotic flow and efficient mixing in a microchannel with a polymer solution. *Physical Review E* 69(6), 066305.

Burns, M.A., Johnson, B.N., Brahmasandra, S.N., Handique, K., Webster, J.R., Krishnan, M., Sammarco, T.S., Man, P.M., Jones, D., Heldsinger, D., Mastrangelo, C.H., Burke, D.T., 1998. An integrated nanoliter DNA analysis device. *Science* 282(5388), 484-487.

Calvert, P., 2001. Inkjet printing for materials and devices. *Chemistry of Materials* 13(10), 3299-3305.

Camou, S., Fujita, H., Fujii, T., 2003. PDMS 2D optical lens integrated with microfluidic channels: principle and characterization. *Lab Chip* 3(1), 40-45.

Campo, A.d., Greiner, C., 2007. SU-8: a photoresist for high-aspect-ratio and 3D submicron lithography. *Journal of Micromechanics and Microengineering* 17(6), R81.

Capretto, L., Cheng, W., Hill, M., Zhang, X., Lin, B., 2011. Micromixing Within Microfluidic Devices. pp. 27-68. Springer Berlin / Heidelberg.

Carlos, F.F., Silva-Nunes, J., Flores, O., Brito, M., Doria, G., Veiga, L., Baptista, P.V., 2013. Association of FTO and PPAR $\gamma$  polymorphisms with obesity in Portuguese women. *Diabetes Metab Syndr Obes.* 6, 241-245.

Černá, M., Veselý, M., Dzik, P., Guillard, C., Puzenat, E., Lepičová, M., 2013. Fabrication, characterization and photocatalytic activity of TiO<sub>2</sub> layers prepared by inkjet printing of stabilized nanocrystalline suspensions. *Applied Catalysis B: Environmental* 138-139, 84-94.

Chang, C.K., Shih, T.R., Chung, C.K., 2011. Design and fabrication of an advanced rhombic micromixer with branch channels. *Nano/Micro Engineered and Molecular Systems (NEMS)*, 2011 IEEE International Conference on, pp. 245-248.

Chin, C.D., Linder, V., Sia, S.K., 2012. Commercialization of microfluidic point-of-care diagnostic devices. *Lab Chip* 12(12), 2118-2134.

Choi, S., Goryll, M., Sin, L.Y.M., Wong, P.K., Chae, J., 2011. Microfluidic-based biosensors toward point-of-care detection of nucleic acids and proteins. *Microfluid. Nanofluid.* 10(2), 231-247.

Chung, C., Shih, T., 2008. Effect of geometry on fluid mixing of the rhombic micromixers. *Microfluid. Nanofluid.* 4(5), 419-425.

Chung, C.K., Shih, T.R., 2007. A rhombic micromixer with asymmetrical flow for enhancing mixing. *J. Micromech. Microeng.* 17(12), 2495.

Chung, C.K., Shih, T.R., Chen, T.C., Wu, B.H., 2008a. Mixing behavior of the rhombic micromixers over a wide Reynolds number range using Taguchi method and 3D numerical simulations. *Biomed. Microdevices* 10, 739-748.

Chung, C.K., Wu, C.Y., Shih, T.R., 2008b. Effect of baffle height and Reynolds number on fluid mixing. *Microsyst. Technol.* 14(9-11), 1317-1323.

Cipriany, B.R., Murphy, P.J., Hagarman, J.A., Cerf, A., Latulippe, D., Levy, S.L., Benítez, J.J., Tan, C.P., Topolancik, J., Soloway, P.D., Craighead, H.G., 2012. Real-time analysis and selection of methylated DNA by fluorescence-activated single molecule sorting in a nanofluidic channel. *PNAS*.

Conde, J., de la Fuente, J.M., Baptista, P.V., 2010. RNA quantification using gold nanoprobe - application to cancer diagnostics. *J Nanobiotechnology* 8(5).

Conlisk, K., O'Connor, G., 2012. Analysis of passive microfluidic mixers incorporating 2D and 3D baffle geometries fabricated using an excimer laser. *Microfluid. Nanofluid.* 12(6), 941-951.

Conradie, E., H., Moore, D.F., 2002a. SU-8 thick photoresist processing as a functional material for MEMS applications. *J. Micromech. Microeng.* 12(4), 368.

Conradie, E.H., Moore, D.F., 2002b. SU-8 thick photoresist processing as a functional material for MEMS applications. *JOURNAL OF MICROMECHANICS AND MICROENGINEERING*, 368-374.

Costa, P., Amaro, A., Botelho, A., Inacio, J., Baptista, P.V., 2010. Gold nanoprobe assay for the identification of mycobacteria of the *Mycobacterium tuberculosis* complex. *Clinical Microbiology and Infection* 16(9), 1464-1469.

Costa, P., Amaro, A., Botelho, A., Inácio, J., Baptista, P.V., 2009. Gold nanoprobe assay for identification of mycobacteria from the *Mycobacterium tuberculosis* complex. *Clinical Microbiology and Infection* 16(9), 1464-1469.

Dang, M.C., Dang, T.M.D., Fribourg-Blanc, E., 2013. Inkjet printing technology and conductive inks synthesis for microfabrication techniques. *Advances in Natural Sciences: Nanoscience and Nanotechnology* 4(1), 015009.

De Beenhouwer, H., Lhiang, Z., Jannes, G., Mijs, W., Machtelinckx, L., Rossau, R., Traore, H., Portaels, F., Rapid detection of rifampicin resistance in sputum and biopsy specimens from tuberculosis patients by PCR and line probe assay. *Tuber Lung Dis.* 1995 Oct;76(5):425-30.

del Campo, A., Greiner, C., 2007. SU-8: a photoresist for high-aspect-ratio and 3D submicron lithography. *J. Micromech. Microeng.* 17(6), R81-R95.

deMello, A.J., French, P.M.W., Neil, M.A.A., Edel, J.B., Benninger, R.K.P., Bradley, D.D.C., Robinson, T., Srisa-Art, M., Hofmann, O., deMello, J.C., 2009. Optical detection in microfluidics: From the small to the large. *Solid-State Sensors, Actuators and Microsystems Conference, 2009. TRANSDUCERS 2009. International*, pp. 712-717.

Derringer, G., Suich, R., 1980. Simultaneous optimization of several response variables. *Journal of quality technology* 12(4), 214-219.

Desai, S.P., Freeman, D.M., Voldman, J., 2009. Plastic masters-rigid templates for soft lithography. *Lab Chip* 9(11), 1631-1637.

Deying, X., Juchao, Y., Shifeng, H., 2012. Fabrication of Nanofluidic Biochips with Nanochannels for Applications in DNA Analysis. *Small* 8(18), 2787-2801.

Di Carlo, D., 2009. Inertial microfluidics. *Lab Chip* 9(21), 3038-3046.

Doria, G., Baumgartner, B.G., Franco, R., Baptista, P.V., 2010. Optimizing Au-nanoprobes for specific sequence discrimination. *Colloids and Surfaces B: Biointerfaces* 77(1), 122-124.

Doria, G., Conde, J., Veigas, B., Giestas, L., Almeida, C., Assuncao, M., Rosa, J., Baptista, P.V., 2012. Noble Metal Nanoparticles for Biosensing Applications. *Sensors* 12(2), 1657-1687.

Doria, G., Franco, R., Baptista, P., 2007. Nanodiagnostics: fast colorimetric method for single nucleotide polymorphism/mutation detection. *IET Nanobiotechnology* 1(4), 53-57.

Duan, C.H., Wang, W., Xie, Q., 2013. Review article: Fabrication of nanofluidic devices. *Biomicrofluidics* 7(2).

Dutta, P., Morse, J., 2008. A review of nanofluidic patents. *Recent Pat Nanotechnol.* 2(3), 150-159.

Dykman, L., Khlebtsov, N., 2012. Gold nanoparticles in biomedical applications: recent advances and perspectives. *Chem. Soc. Rev.* 41(6), 2256-2282.

Egerton, R.F., 2005. *Physical Principles of Electron Microscopy. An Introduction to TEM, SEM, and AEM.* Springer.

Ehrmeyer, S.S., Laessig, R.H., 2007. Point-of-care testing, medical error, and patient safety: a 2007 assessment. *Clin. Chem. Lab. Med.* 45(6), 766-773.

Elhadj, S., Rioux, R.M., Dickey, M.D., DeYoreo, J.J., Whitesides, G.M., 2010. Subnanometer Replica Molding of Molecular Steps on Ionic Crystals. *Nano Lett.* 10(10), 4140-4145.

Erickson, D., Li, D.Q., 2004. Integrated microfluidic devices. *Anal. Chim. Acta* 507(1), 11-26.

Esteves, A.C.C., Brokken-Zijp, J., Laven, J., Huinink, H.P., Reuvers, N.J.W., Van, M.P., de With, G., 2009. Influence of cross-linker concentration on the cross-linking of PDMS and the network structures formed. *Polymer* 50(16), 3955-3966.

Feidenhans'l, N.A., Lafleur, J.P., Jensen, T.G., Kutter, J.P., 2014. Surface functionalized thiol-ene waveguides for fluorescence biosensing in microfluidic devices. *Electrophoresis* 35(2-3), 282-288.

Feng, H., Gaur, A., Sun, Y., Word, M., Niu, J., Adesida, I., Shim, M., Shim, A., Rogers, J.A., 2006. Processing dependent behavior of soft imprint lithography on the 1-10-nm scale. *Nanotechnology, IEEE Transactions on* 5(3), 301-308.

Fortunato, E., Martins, R., Baptista, P., 2006. Detection and quantification system of biological, matter constituted by one or more optical sensors and one or more light sources, associated process and related applications. In: *FCT-UNL (Ed.)*. 103561-PT.

Franssila, S., 2010. *Introduction to Microfabrication.* John Wiley & Sons, Ltd, Chichester, UK.

Garcia, D., Ghansah, I., LeBlanc, J., Butte, M.J., 2012. Counting cells with a low-cost integrated microfluidics-waveguide sensor. *Biomicrofluidics* 6(1), 014115.

Goovaerts, R., Smits, W., Desmet, G., Denayer, J., De Malsche, W., 2012. Combined improved mixing and reduced energy dissipation by combining convective effects and lamination. *Chemical Engineering Journal* 211(0), 260-269.

Gotz, S., Karst, U., 2007. Recent developments in optical detection methods for microchip separations. *Anal. Bioanal. Chem.* 387(1), 183-192.

Hahn, S., Mergenthaler, S., Zimmermann, B., Holzgreve, W., 2003. Nucleic acid based biosensors: The desires of the user. 1st Workshop on New Trends in Nucleic Acid Based Biosensors, pp. 151-154. Elsevier Science Sa, Florence, ITALY.

Hammacher, J., Fuehle, A., Flaemig, J., Saupe, J., Loechel, B., Grimm, J., 2008. Stress engineering and mechanical properties of SU-8-layers for mechanical applications. *Microsystem Technologies* 14(9), 1515-1523.

Han, K.N., Li, C.A., Seong, G.H., 2013. Microfluidic Chips for Immunoassays. *Annu. Rev. Anal. Chem.* 6(1), 119-141.

Hart, A.L., Turner, A.P.F., Hopcroft, D., 1996. On the use of screen- and ink-jet printing to produce amperometric enzyme electrodes for lactate. *Biosens. Bioelectron.* 11(3), 263-270.

Henry, O.Y.F., O'Sullivan, C.K., 2012. Rapid DNA hybridization in microfluidics. *Trac-Trend Anal Chem* 33, 9-22.

Hilliou, L., van Dusschoten, D., Wilhelm, M., Burhin, H., Rodger, E.R., 2004. Increasing the Force Torque Transducer Sensitivity of an RPA 2000 by a Factor 5 - 10 via Advanced Data Acquisition. *Rubber Chemistry and Technology* 77(1), 192-200.

<http://Lab-on-Chip.gene-quantification.info>, retrieved in 2014.03.

<http://www.elveflow.com/microfluidic-reviews-and-tutorials/su-8-baking>, retrieved in 2014.03.

<http://www.microchem.com>, retrieved in 2014.03. SU-8 2000 datasheet.

<http://www.objactive.com/metaldeposition>, retrieved in 2014.03.

<http://www.solarisnano.com>, retrieved in 2014.03.

<http://www.solaronix.com/technology/dyesolarcells>, retrieved in 2014.03.

Huang, C.-Y., Hsu, Y.-C., Chen, J.-G., Suryanarayanan, V., Lee, K.-M., Ho, K.-C., 2006. The effects of hydrothermal temperature and thickness of TiO<sub>2</sub> film on the performance of a dye-sensitized solar cell. *Solar Energy Materials and Solar Cells* 90(15), 2391-2397.

Huh, D., Hamilton, G.A., Ingber, D.E., 2011. From 3D cell culture to organs-on-chips. *Trends in Cell Biology* 21(12), 745-754.

Hunt, H.C., Wilkinson, J.S., 2008. Optofluidic integration for microanalysis. *Microfluid. Nanofluid.* 4(1-2), 53-79.

Janasek, D., Franzke, J., Manz, A., 2006. Scaling and the design of miniaturized chemical-analysis systems. *Nature* 442(7101), 374-380.

Junghanel, M., Tributsch, H., 2005. Role of nanochemical environments in porous TiO<sub>2</sub> in photocurrent efficiency and degradation in dye sensitized solar cells. *J. Phys. Chem. B* 109(48), 22876-22883.

Kang, M.G., Ryu, K.S., Chang, S.H., Park, N.G., Hong J.P., Kim, K.J., 2004. Dependence of TiO<sub>2</sub> Film Thickness on Photocurrent-Voltage Characteristics of Dye-Sensitized Solar Cells. *Bull. Korean Chem. Soc.* 25, 742-744.

Kashid, M., Renken, A., Kiwi-Minsker, L., 2011. Mixing efficiency and energy consumption for five generic microchannel designs. *Chemical Engineering Journal* 167(2-3), 436-443.

Khoshmanesh, K., Nahavandi, S., Baratchi, S., Mitchell, A., Kalantar-zadeh, K., 2011. Dielectrophoretic platforms for bio-microfluidic systems. *Biosens Bioelectron* 26(5), 1800-1814.

King, D., O'Sullivan, M., Ducree, J., 2014. Optical detection strategies for centrifugal microfluidic platforms. *Journal of Modern Optics* 61(2), 85-101.

Krishnaswamy, N., Srinivas, T., Rao, G.M., Varma, M.M., 2013. Analysis of Integrated Optofluidic Lab-on-a-Chip Sensor Based on Refractive Index and Absorbance Sensing. *IEEE Sens. J.* 13(5), 1730-1741.

Kuo, J.S., Chiu, D.T., 2011. Controlling mass transport in microfluidic devices. *Annual Review of Analytical Chemistry* 4, 275-296.

Kuswandi, B., Nuriman, Huskens, J., Verboom, W., 2007. Optical sensing systems for microfluidic devices: A review. *Anal. Chim. Acta* 601(2), 141-155.

Larguinho, M., Baptista, P.V., 2012. Gold and silver nanoparticles for clinical diagnostics-From genomics to proteomics. *Journal of Proteomics* 75(10), 2811-2823.

Lawrie, K., Mills, A., Hazafy, D., 2013. Simple inkjet-printed, UV-activated oxygen indicator. *Sensors and Actuators B: Chemical* 176(0), 1154-1159.



Le, H.P., 1998. Progress and trends in ink-jet printing technology. *Journal of Imaging Science and Technology* 42(1), 49-62.

Lee, C.-Y., Chang, C.-L., Wang, Y.-N., Fu, L.-M., 2011. Microfluidic Mixing: A Review. *Int. J. Mol. Sci.* 12(5), 3263-3287.

Lee, D., Lee, S.H., 2008a. Static micro-mixing analysis by using Sequential Quadratic Programming and a confocal microscope. *Journal of the Korean Physical Society* 52(3), 580-587.

Lee, P.C., Meisel, D., 1982. Adsorption and Surface-Enhanced Raman of Dyes on Silver and Gold Sols. *J. Phys. Chem.* 86(17), 3391-3395.

Lee, S., Lee, S., 2008b. Shrinkage ratio of PDMS and its alignment method for the wafer level process. *Microsyst. Technol.* 14(2), 205-208.

Lei, K.F., 2012. Microfluidic systems for diagnostic applications: a review. *J Lab Autom* 17(5), 330-347.

Levy, S.L., Craighead, H.G., 2010. DNA manipulation, sorting, and mapping in nanofluidic systems. *Chem Soc Rev* 39(3), 1133-1152.

Li, P., Cogswell, J., Faghri, M., 2012a. Design and test of a passive planar labyrinth micromixer for rapid fluid mixing. *Sensors and Actuators B* 174(0), 126-132.

Li, X., Ballerini, D.R., Shen, W., 2012b. A perspective on paper-based microfluidics: Current status and future trends. *Biomicrofluidics* 6(1), 11301-1130113.

Liandris, E., Gazouli, M., Andreadou, M., ĀEomor, M., Abazovic, N., Sechi, L.A., Ikonomopoulos, J., 2009. Direct detection of unamplified DNA from pathogenic mycobacteria using DNA-derivatized gold nanoparticles. *Journal of Microbiological Methods* 78(3), 260-264.

Liang, Z., Chiem, N., Ocvirk, G., Tang, T., Fluri, K., Harrison, D.J., 1996. Microfabrication of a Planar Absorbance and Fluorescence Cell for Integrated Capillary Electrophoresis Devices. *Anal. Chem.* 68(6), 1040-1046.

Lien, K.-Y., Chuang, Y.-H., Hung, L.-Y., Hsu, K.-F., Lai, W.-W., Ho, C.-L., Chou, C.-Y., Lee, G.-B., 2010. Rapid isolation and detection of cancer cells by utilizing integrated microfluidic systems. *Lab Chip* 10(21), 2875-2886.

Lin, B., 2011. *Microfluidics: Technologies and Applications*. Springer.

Lin, B., Gai, H., Li, Y., Yeung, E., 2011. Optical Detection Systems on Microfluidic Chips. *Microfluidics*, pp. 171-201. Springer Berlin Heidelberg.

Liu, R.H., Yang, J., Lenigk, R., Bonanno, J., Grodzinski, P., 2004. Self-Contained, Fully Integrated Biochip for Sample Preparation, Polymerase Chain Reaction Amplification, and DNA Microarray Detection. *Anal. Chem.* 76(7), 1824-1831.

Llobera, A., Demming, S., Wilke, R., Buttgenbach, S., 2007. Multiple internal reflection poly(dimethylsiloxane) systems for optical sensing. pp. 1560-1566.

Mark, D., Haeberle, S., Roth, G., Stetten, F., Zengerle, R., Kakaç, S., Kosoy, B., Li, D., Pramuanjaroenkij, A., 2010. Microfluidic Lab-on-a-Chip Platforms: Requirements, Characteristics and Applications. *Chem. Soc. Rev.* 39, 1153-1182.

Martins, R., Baptista, P., Raniero, L., Doria, G., Silva, L., Franco, R., Fortunato, E., 2007a. Amorphous/nanocrystalline silicon biosensor for the specific identification of unamplified nucleic acid sequences using gold nanoparticle probes. *Appl. Phys. Lett.* 90(2), 3.

Martins, R., Baptista, P., Raniero, L., Doria, G., Silva, L., Franco, R., Fortunato, E., 2007b. Amorphous/nanocrystalline silicon biosensor for the specific identification of unamplified nucleic acid sequences using gold nanoparticle probes. *Appl. Phys. Lett.* 90(2), 023903.

Martins, R., Baptista, P., Silva, L., Raniero, L., Doria, G., Franco, R., Fortunato, E., 2008. Identification of unamplified genomic DNA sequences using gold nanoparticle probes and a novel thin film photodetector. *Journal of Non-Crystalline Solids* 354(19-25), 2580-2584.

Martins, T.D., Ribeiro, A.C.C., de Camargo, H.S., Filho, P.A.d.C., Cavalcante, H.P.M., Dias, H.P.M., 2013. New Insights on Optical Biosensors: Techniques, Construction and Application.

Matsunaga, T., Lee, H.-J., Nishino, K., 2013. An approach for accurate simulation of liquid mixing in a T-shaped micromixer. *Lab Chip* 13(8), 1515-1521.

McDonald, J.C., Duffy, D.C., Anderson, J.R., Chiu, D.T., Wu, H.K., Schueller, O.J.A., Whitesides, G.M., 2000. Fabrication of microfluidic systems in poly(dimethylsiloxane). *Electrophoresis* 21(1), 27-40.

McNaught, A.D., Wilkinson, A., IUPAC. Compendium of Chemical Terminology, 2nd ed. (the "Gold Book"). WileyBlackwell; 2nd Revised edition edition.

Medina-Sanchez, M., Miserere, S., Merkoci, A., 2012. Nanomaterials and lab-on-a-chip technologies. *Lab Chip* 12(11), 1932-1943.

Michael Chen, C.Y., 2012. Patent review of novel nanostructured devices, nanofabrication methods and applications in nanofluidics and nanomedicine. *Recent Pat Nanotechnol.* 2012 Jun 1;6(2):114-23. 6(2), 114-123.

Mirkin, C.A., Letsinger, R.L., Mucic, R.C., Storhoff, J.J., 1996. A DNA-based method for rationally assembling nanoparticles into macroscopic materials. *Nature* 382(6592), 607-609.

Missinne, J., Kalathimekkad, S., Van Hoe, B., Bosman, E., Vanfleteren, J., Van Steenberge, G., 2014. Stretchable optical waveguides. *Optics Express* 22(4), 4168-4179.

Mogensen, K.B., Klank, H., Kutter, J.P., 2004. Recent developments in detection for microfluidic systems. *Electrophoresis* 25(21-22), 3498-3512.

Mogensen, K.B., Kutter, J.P., 2009. Optical detection in microfluidic systems. *Electrophoresis* 30(S1), S92-S100.

Mogensen, K.B., Petersen, N.J., Hubner, J., Kutter, J.P., 2001. Monolithic integration of optical waveguides for absorbance detection in microfabricated electrophoresis devices. *Electrophoresis* 22(18), 3930-3938.

Mohammed, M.-I., Desmulliez, M.P.Y., 2013. Planar lens integrated capillary action microfluidic immunoassay device for the optical detection of troponin I. *Biomicrofluidics* 7(6), 064112.

Morozova, M., Kluson, P., Krysa, J., Dzik, P., Vesely, M., Solcova, O., 2011. Thin TiO<sub>2</sub> films prepared by inkjet printing of the reverse micelles sol-gel composition. *Sensors and Actuators B: Chemical* 160(1), 371-378.

Myers, F.B., Lee, L.P., 2008. Innovations in optical microfluidic technologies for point-of-care diagnostics. *Lab Chip* 8(12), 2015-2031.

Nima, A., 2013. Resist Homogeneity.

Oblath, E.A., Henley, W.H., Alarie, J.P., Ramsey, J.M., 2013. A microfluidic chip integrating DNA extraction and real-time PCR for the detection of bacteria in saliva. *Lab Chip* 13(7), 1325-1332.

Oktawati, U.Y., Mohamed, N.M., Burhanudin, Z.A., 2013. Effects of TiO<sub>2</sub> electrode thickness on the performance of dye solar cell by simulation. *Micro and Nanoelectronics (RSM), 2013 IEEE Regional Symposium on*, pp. 406-409.

Oregan, B., Gratzel, M., 1991. A Low-Cost, High-Efficiency Solar-Cell Based on Dye-Sensitized Colloidal TiO<sub>2</sub> Films. *Nature* 353(6346), 737-740.

Pejcic, B., De Marco, R., Parkinson, G., 2006. The role of biosensors in the detection of emerging infectious diseases. *Analyst* 131(10), 1079-1090.

Petryayeva, E., Krull, U.J., 2011. Localized surface plasmon resonance: Nanostructures, bioassays and biosensing-a review. *Anal. Chim. Acta* 706(1), 8-24.

Price, C.W., Leslie, D.C., Landers, J.P., 2009. Nucleic acid extraction techniques and application to the microchip. *Lab Chip* 9(17), 2484-2494.

Ram, R.J., Lee, K., 2009. Optical Waveguides for Microfluidic Integration. *IEEE LEOS Annual Meeting Conference Proceedings 2009*, pp. 371-372, Leos.

Ren, K., Zhou, J., Wu, H., 2013. Materials for Microfluidic Chip Fabrication. *Accounts of Chemical Research* 46(11), 2396-2406.

Reynolds, O., 1883. An experimental investigation of the circumstances which determine whether the motion of water shall be direct or sinuous : and of the law of resistance in parallel channels. *Phil. Trans. R. Soc. Lond. A*.

Ro, K.W., Lim, K., Shim, B.C., Hahn, J.H., 2005. Integrated light collimating system for extended optical-path-length absorbance detection in microchip-based capillary electrophoresis. *Anal. Chem.* 77(16), 5160-5166.

Rodd, L.E., Scott, T.P., Boger, D.V., Cooper-White, J.J., McKinley, G.H., 2005. The inertio-elastic planar entry flow of low-viscosity elastic fluids in micro-fabricated geometries. *Journal of Non-Newtonian Fluid Mechanics* 129(1), 1.

SadAbadi, H., Packirisamy, M., Wuthrich, R., 2013. High performance cascaded PDMS micromixer based on split-and-recombination flows for lab-on-a-chip applications. *RSC Advances* 3(20), 7296-7305.

Sato, K., Hosokawa, K., Maeda, M., 2003. Rapid Aggregation of Gold Nanoparticles Induced by Non-Cross-Linking DNA Hybridization. *J. Am. Chem. Soc.* 125(27), 8102-8103.

Sayers, M.W., Karamihas, S.M., 1998. *The Little Book of Profiling*.

Schena, M., Heller, R.A., Theriault, T.P., Konrad, K., Lachenmeier, E., Davis, R.W., 1998. Microarrays: biotechnology's discovery platform for functional genomics. *Trends in Biotechnology* 16(7), 301-306.

Schofield, C.L., Field, R.A., Russell, D.A., 2007. Glyconanoparticles for the colorimetric detection of cholera toxin. *Anal Chem* 79(4), 1356-1361.

Schrott, W., Svoboda, M., Slouka, Z., Pribyl, M., Snita, D., 2010. PDMS microfluidic chips prepared by a novel casting and pre-polymerization method. *Microelectronic Engineering* 87(5-8), 1600-1602.

Schuenemann, M., Harvey, E.C., 2007. Polymer-Based Microsystem Techniques. In: Marks, R.S., Cullen, D.C., Karube, I., Lowe, C.R., Weetall, H.H. (Eds.), *Handbook of Biosensors and Biochips*, pp. 1(43)-16(43). John Wiley & Sons, Ltd., Chichester, England.

Senadeera, G.K.R., Jayaweera, P.V.V., Perera, V.P.S., Tennakone, K., 2002. Solid-state dye-sensitized photocell based on pentacene as a hole collector. *Solar Energy Materials and Solar Cells* 73(1), 103-108.

Senadeera, G.K.R., Kitamura, T., Wada, Y., Yanagida, S., 2005a. Photosensitization of nanocrystalline TiO<sub>2</sub> films by a polymer with two carboxylic groups, poly (3-thiophenemalononic acid). *Solar Energy Materials and Solar Cells* 88(3), 315-322.

Senadeera, G.K.R., Kobayashi, S., Kitamura, T., Wada, Y., Yanagida, S., 2005b. Versatile preparation method for mesoporous TiO<sub>2</sub> electrodes suitable for solid-state dye sensitized photocells. *Bulletin of Materials Science* 28(6), 635-641.

Sharma, H., Nguyen, D., Chen, A., Lew, V., Khine, M., 2011. Unconventional low-cost fabrication and patterning techniques for point of care diagnostics. *Ann Biomed Eng* 39(4), 1313-1327.

Shih, T.R., Chung, C.K., 2008. A high-efficiency planar micromixer with convection and diffusion mixing over a wide Reynolds number range. *Microfluid. Nanofluid.* 5(2), 175-183.

Silva, L.B., 2010. New portable system development for specific detection of DNA/RNA sequences using gold nanoprobe integrated with optical sensors based on nanocrystalline silicon technology. *Materials Science. Universidade Nova de Lisboa, Caparica*.

Silva, L.B., Baptista, P., Raniero, L., Doria, G., Franco, R., Martins, R., Fortunato, E., 2007. Novel Optoelectronic Platform using an Amorphous/Nanocrystalline Silicon Biosensor for the Specific Identification of Unamplified Nucleic Acid Sequences Based on Gold Nanoparticle Probes, 935-938.

Silva, L.B., Baptista, P., Raniero, L., Doria, G., Martins, R., Fortunato, E., 2008. Characterization of optoelectronic platform using an amorphous/nanocrystalline silicon biosensor for the specific identification of nucleic acid sequences based on gold nanoparticle probes. *Sensors & Actuators B - Chemical* 132(2), 508-511.

Silva, L.B., Veigas, B., Doria, G., Costa, P., Inácio, J., Martins, R., Fortunato, E., Baptista, P.V., 2011. Portable optoelectronic biosensing platform for identification of mycobacteria from the Mycobacterium tuberculosis complex. *Biosensors and Bioelectronics* 26(5), 2012-2017.

Smestad, G.P., 1998. Education and solar conversion: Demonstrating electron transfer. *Solar Energy Materials and Solar Cells* 55(1-2), 157-178.

Snakenborg, D., Mogensen, K.B., Kutter, J.P., 2003. Optimization of Signal-To-Noise Ratio in Absorbance Detection by Integration of Microoptical Components. *Proc. Micro Total Analysis Systems*, pp. 841-844.

Soe, A.K., Nahavandi, S., Khoshmanesh, K., 2012. Neuroscience goes on a chip. *Biosens Bioelectron* 35(1), 1-13.

Sollier, E., Murray, C., Maoddi, P., Di Carlo, D., 2011. Rapid prototyping polymers for microfluidic devices and high pressure injections. *Lab Chip* 11(22), 3752-3765.

Soo, P.-C., Horng, Y.-T., Chang, K.-C., Wang, J.-Y., Hsueh, P.-R., Chuang, C.-Y., Lu, C.-C., Lai, H.-C., 2009. A simple gold nanoparticle probes assay for identification of Mycobacterium tuberculosis and Mycobacterium tuberculosis complex from clinical specimens. *Molecular and Cellular Probes* 23(5), 240-246.

Soper, S.A., Brown, K., Ellington, A., Frazier, B., Garcia-Manero, G., Gau, V., Gutman, S.I., Hayes, D.F., Korte, B., Landers, J.L., Larson, D., Ligler, F., Majumdar, A., Mascini, M., Nolte, D.,

Rosenzweig, Z., Wang, J., Wilson, D., 2006. Point-of-care biosensor systems for cancer diagnostics/prognostics. *Biosens. Bioelectron.* 21(10), 1932-1942.

Sparreboom, W., van den Berg, A., Eijkel, J.C.T., 2010. Transport in nanofluidic systems: a review of theory and applications. *New Journal of Physics* 12(1), 015004.

Storhoff, J.J., Elghanian, R., Mucic, R.C., Mirkin, C.A., Letsinger, R.L., 1998. One-Pot Colorimetric Differentiation of Polynucleotides with Single Base Imperfections Using Gold Nanoparticle Probes. *J. Am. Chem. Soc.* 120(9), 1959-1964.

Storhoff, J.J., Lucas, A.D., Garimella, V., Bao, Y.P., Muller, U.R., 2004. Homogeneous detection of unamplified genomic DNA sequences based on colorimetric scatter of gold nanoparticle probes. *Nat. Biotechnol.* 22(7), 883-887.

Stroock, A.D., Dertinger, S.K.W., Ajdari, A., Mezic, I., Stone, H.A., Whitesides, G.M., 2002. Chaotic Mixer for Microchannels. *Science* 295(5555), 647-651.

Sun, Y., Kwok, Y.C., 2006. Polymeric microfluidic system for DNA analysis. *Anal. Chim. Acta* 556(1), 80-96.

Sun, Y., Rogers, J.A., 2007. Structural forms of single crystal semiconductor nanoribbons for high-performance stretchable electronics. *Journal of Materials Chemistry* 17(9), 832-840.

Tabeling, P., 2006. *Introduction to Microfluidics*. Oxford University Press, Incorporated.

Taton, T.A., Mirkin, C.A., Letsinger, R.L., 2000. Scanometric DNA array detection with nanoparticle probes. *Science* 289(5485), 1757-1760.

Teichler, A., Perelaer, J., Schubert, U.S., 2012. Inkjet printing of organic electronics - comparison of deposition techniques and state-of-the-art developments. *Journal of Materials Chemistry C* 1(10), 1910-1925.

Thuo, M.M., Martinez, R.V., Lan, W.-J., Liu, X., Barber, J., Atkinson, M.B.J., Bandarage, D., Bloch, J.-F., Whitesides, G.M., 2014. Fabrication of Low-Cost Paper-Based Microfluidic Devices by Embossing or Cut-and-Stack Methods. *Chemistry of Materials* 26(14), 4230-4237.

Tran-Minh, N., Dong, T., Karlsen, F., 2013. An efficient passive planar micromixer with ellipse-like micropillars for continuous mixing of human blood. *Computer Methods and Programs in Biomedicine* 117(1), 20-29.

Tsai, R.-T., Wu, C.-Y., 2011. An efficient micromixer based on multidirectional vortices due to baffles and channel curvature. *Biomicrofluidics* 5(1), 014103-014113.

Utracki, L.A., 2002. *Polymer Blend Handbook*.

van den Berg, A., Craighead, H.G., Yang, P., 2010. From microfluidic applications to nanofluidic phenomena. *Chem. Soc. Rev.* 39(3), 899-900.

Veigas, B., Doria, G., Baptista, P.V., 2012. Nanodiagnostics for Tuberculosis. In: Cardona, P.-J. (Ed.), *Understanding Tuberculosis-Global Experiences and Innovative Approaches to the Diagnosis*, pp. 257-276. InTech.

Veigas, B., Jacob, J.M., Costa, M.N., Santos, D.S., Viveiros, M., Inacio, J., Martins, R., Barquinha, P., Fortunato, E., Baptista, P.V., 2012. Gold on paper-paper platform for Au-nanoprobe TB detection. *Lab Chip*.

Veigas, B., Machado, D., Perdigão, J., Portugal, I., Couto, I., Viveiros, M., Baptista, P.V., 2010. Au-nanoprobes for detection of SNPs associated with antibiotic resistance in *Mycobacterium tuberculosis*. *Nanotechnology* 21(41), 5101-5108.

Viskari, P.J., Landers, J.P., 2006. Unconventional detection methods for microfluidic devices. *Electrophoresis* 27(9), 1797-1810.

Wang, H., Iovenitti, P., Harvey, E., Masood, S., 2002. Optimizing layout of obstacles for enhanced mixing in microchannels. *Smart Mater. Struct.* 11(5), 662.

Wang, J., 2000. From DNA biosensors to gene chips. *Nucleic Acids Res.* 28(16), 3011-3016.

Watts, B.R., Kowpak, T., Zhang, Z., Xu, C.-Q., Zhu, S., Cao, X., Lin, M., 2012. Fabrication and Performance of a Photonic-Microfluidic Integrated Device 3(1), 62-77.

Weber, J.L., David, D., Heil, J., Fan, Y., Zhao, C., Marth, G., 2002. Human Diallelic Insertion/Deletion Polymorphisms. *Am. J. Hum. Genet.* 71, 854-862.

Weigl, B.H., Bardell, R.L., 2004. Microfluidics for Clinical Diagnostics—Promise and Current Reality. *Lab Medicine* 35(4), 233-237.

- Weigl, B.H., Bardell, R.L., Cabrera, C., 2007. Introduction to Microfluidic Techniques. In: Marks, R.S., Cullen, D.C., Karube, I., Lowe, C.R., Weetall, H.H. (Eds.), *Handbook of Biosensors and Biochips*, pp. 1(41)-19(41). John Wiley & Sons, Ltd., Chichester, England.
- Weigl, B.H., Bardell, R.L., Cabrera, C., 2008. Introduction to Microfluidic Techniques. *Handbook of Biosensors and Biochips*. John Wiley & Sons, Ltd.
- Whitesides, G.M., 2006. The origins and the future of microfluidics. *Nature* 442(7101), 368-373.
- Won-Jong, K., Rabe, E., Kopetz, S., Neyer, A., 2006. Novel exposure methods based on reflection and refraction effects in the field of SU-8 lithography 16(4), 821.
- Xiang, X., Chen, L., Zhuang, Q., Ji, X., He, Z., 2012a. Real-time luminescence-based colorimetric determination of double-strand DNA in droplet on demand. *Biosens Bioelectron* 32(1), 43-49.
- Xiang, X., Luo, M., Shi, L., Ji, X., He, Z., 2012b. Droplet-based microscale colorimetric biosensor for multiplexed DNA analysis via a graphene nanoprobe. *Anal. Chim. Acta* 751(2), 155.
- Yager, P., Domingo, G.J., Gerdes, J., 2008. Point-of-care diagnostics for global health. *Annu. Rev. Biomed. Eng.* 10, 107-144.
- Yang, M., Li, L., Zhang, S., Li, G., Zhao, H., 2010. Preparation, characterisation and sensing application of inkjet-printed nanostructured TiO<sub>2</sub> photoanode. *Sensors and Actuators B: Chemical* 147(2), 622-628.
- Yetisen, A.K., Akram, M.S., Lowe, C.R., 2013. Paper-based microfluidic point-of-care diagnostic devices. *Lab Chip* 13(12), 2210-2251.
- Yole Développement, 2011. *Emerging Markets for Microfluidic Applications (EMMA 2011)*.
- Zhai, J.H., Cui, H., Yang, R.F., 1997. DNA based biosensors. *Biotechnol. Adv.* 15(1), 43-58.
- Zhang, C., Xu, J., Ma, W., Zheng, W., 2006. PCR microfluidic devices for DNA amplification. *Biotechnol Adv* 24(3), 243-284.
- Zhang, J., Chan-Park, M., Miao, J., Sun, T., 2005. Reduction of diffraction effect for fabrication of very high aspect ratio microchannels in SU-8 over large area by soft cushion technology. *Microsystem Technologies* 11(7), 519-525.